Creation of ytterbium quantum gases with a compact 2D-/3D-MOT setup

Dissertation
zur Erlangung des Doktorgrades
des Department Physik
der Universität Hamburg

vorgelegt von
Sören Erik Dörscher
aus
Hamburg

Hamburg
2013

Gutachter der Dissertation:	Prof. Dr. Klaus Sengstock Prof. Dr. Henning Moritz
Gutachter der Disputation:	Prof. Dr. Klaus Sengstock Prof. Dr. Andreas Hemmerich
Datum der Disputation:	4. September 2013
Vorsitzender des Prüfungsausschusses:	Prof. Dr. Peter Schmelcher
Vorsitzender des Promotionsausschusses:	Prof. Dr. Peter Hauschildt
Dekan der Fakultät für Mathematik, Informatik und Naturwissenschaften:	Prof. Dr.Heinrich Graener

Abstract

In this thesis, a newly developed experimental apparatus for studies of ultracold quantum gases of ytterbium atoms in optical lattices using ultraprecise spectroscopy in the optical domain and first experimental results on the creation of bosonic and fermionic quantum-degenerate gases are presented. Two-dimensional magneto-optical trapping of ytterbium is demonstrated for the first time. Nearly pure Bose–Einstein condensates of ^{174}Yb and highly quantum-degenerate Fermi gases of ^{173}Yb with large particle numbers provide an excellent starting point for future experiments on novel strongly correlated quantum phases of ytterbium in optical lattices, *e.g.* Kondo insulators or SU(N)-symmetric systems.

The experimental setup is based on a novel 2D-/3D-MOT scheme using a miniaturised atom source in a compact glass cell. A 2D-MOT on the broad $^1S_0 \leftrightarrow {}^1P_1$ principal transition of ytterbium captures atoms directly from the atomic beam emitted by a dispenser and is used to load a 3D-MOT on the narrow intercombination transition $^1S_0 \leftrightarrow {}^3P_1$. The 2D-/3D-MOT setup provides excellent optical access for future experiments in optical lattices. It is well suited for experiments on ultracold mixtures, because it allows magneto-optical cooling of rubidium atoms in the same setup. Efficient loading of an intercombination 3D-MOT requires active broadening of the laser spectrum and large intensities to enhance its capture velocity, but temperatures of about 20 μK are achieved by a final single-frequency cooling phase. Loading rates of up to $1.5 \times 10^7\ \mathrm{s}^{-1}$ have been achieved for ^{174}Yb. They demonstrate that the performance of the 2D-MOT is comparable to or even exceeds that of Zeeman slowers for ytterbium.

Quantum-degenerate gases are produced by all-optical means in a crossed dipole trap. A deep horizontal trap with a maximum trap depth equivalent to 0.6 mK is used for initial trapping and evaporative cooling of atoms transferred from a strongly compressed 3D-MOT. A second, vertical dipole trap creates additional confinement in the crossing region. During forced evaporation by lowering of the trap depth atoms are first concentrated into and subsequently cooled to quantum degeneracy within the crossed region. The generation of nearly pure BECs of 1×10^5 ^{174}Yb atoms and degenerate Fermi gases of typically 2×10^4 ^{173}Yb atoms at temperatures of $T/T_\mathrm{F} = 0.15$ is demonstrated, but temperatures as low as $T/T_\mathrm{F} = 0.09$ have been observed. Therefore, the experimental setup presented herein is very well suited for future experiments studying novel quantum phases of ultracold mixtures of ytterbium atoms in the ground state $^1S_0$ and metastable state $^3P_0$ in tuneable optical lattice potentials.

Finally, concepts for the application of ultraprecise Doppler- and recoil-free spectroscopy on the ultranarrow $^1S_0 \leftrightarrow {}^3P_0$ clock transition in order to measure interaction and correlations in quantum gases, especially spin–spin correlations between the states $^1S_0$ and $^3P_0$ or adjacent lattice sites, are discussed.

Zusammenfassung

In der vorliegenden Arbeit wird ein neuentwickelter experimenteller Aufbau zur Untersuchung von ultrakalten Ytterbiumquantengasen in optischen Gitterpotentialen mit Hilfe von höchstpräziser Spektroskopie auf einem ultraschmalen Übergang im optischen Frequenzbereich vorgestellt. Dabei ist es im Rahmen dieser Arbeit erstmals gelungen Ytterbium aus einem thermischen Atomstrahl in einer zweidimensionalen magnetooptischen Falle zu fangen und zu kühlen. Darüber hinaus werden erste experimentelle Resultate zur Erzeugung von quantenentarteten Bose- und Fermigasen der Isotope ^{174}Yb und ^{173}Yb in diesem Aufbau präsentiert. Die Verfügbarkeit ultrakalter Quantengase mit großen Teilchenzahlen bildet hierbei einen hervorragenden Ausgangspunkt für die Untersuchung bislang wenig erforschter, stark korrelierter Quantensysteme und -phasen, die durch ultrakalte Ytterbiumatome in periodischen Potentialen realisiert werden können, beispielsweise Kondoisolatoren und Systeme mit SU(N)-Spinsymmetrie.

Das vorgestellte Experiment basiert im Kern auf einem neuartigen 2D-/3D-MOT-Konzept für Ytterbium. Hierbei wird zunächst eine 2D-MOT, die den breiten Übergang $^1S_0 \leftrightarrow {}^1P_1$ verwendet, direkt aus dem Atomstrahl eines Dispensers geladen. Der von ihr erzeugte Strahl kalter Ytterbiumatome wird seinerseits zum Laden einer 3D-MOT auf der Interkombinationslinie $^1S_0 \leftrightarrow {}^3P_1$ verwendet. Durch die Verwendung dieses schmalen Übergangs können minimale Temperaturen von etwa 20 µK in der MOT erzielt werden, allerdings ist für effizientes Laden aus der 2D-MOT eine anfängliche Erhöhung der Einfanggeschwindigkeit durch die spektrale Verbreiterung sowie höchstmögliche Intensität des Kühllasers notwendig. Die in diesem 2D-/3D-MOT-Aufbau erzielten Laderaten sind mit typischerweise $1.5 \times 10^7\ \mathrm{s}^{-1}$ für das bosonische Isotop ^{174}Yb ähnlich hoch wie in Yb-MOTs, die aus einem Zeemanslower geladen werden, oder sogar höher. Darüber hinaus bietet er exzellenten optischen Zugang für zukünftige Experimente. Insbesondere erlaubt die Verwendung von Dispensern als Atomquellen den Betrieb der 2D-MOT in einer kompakten Glaszelle und damit Laserkühlung von Rubidium in demselben Aufbau, wodurch die Erzeugung ultrakalter Quantengasmischungen aus Ytterbium und Rubidium stark vereinfacht wird.

Zur Erzeugung quantenentarteter Gase wird das lasergekühlte Ytterbium anschließend aus der stark komprimierten MOT in eine gekreuzte optische Dipolfalle umgeladen. Diese besteht aus einer starken horizontalen Falle, deren anfängliche Tiefe einer Temperatur von 0.6 mK entspricht, sowie einer zweiten, vertikalen Falle, die zusätzlichen horizontalen Einschluss in der Kreuzungsregion erzeugt. Im Zuge erzwungener evaporativer Kühlung des Gases durch fortlaufendes Senken der Fallentiefe werden die Atome, die anfangs ausschließlich in der horizontalen Falle gefangen werden, in der Kreuzungsregion konzentriert und dort wiederum weiter bis in das quantenentartete Regime gekühlt. Es wurden auf diese Weise Bose-Einstein-Kondensate aus 1×10^5 ^{174}Yb Atomen ohne erkennbaren thermischen Anteil und hochentartete Fermi-Gase von typischerweise 2×10^4 ^{173}Yb bei Temperaturen von $T/T_\mathrm{F} = 0.15$ sowie minimalen beobachteten Temperaturen von $T/T_\mathrm{F} = 0.09$ erzeugt. Der in dieser Arbeit vorgestellte experimentelle Aufbau ist daher bestens für die zukünftige experimentelle Untersuchung der neuen Quantenphasen, die in gemischten ultrakalten Quantengasen des Grundzustands $^1S_0$ sowie des metastabilen Zustands $^3P_0$ von Ytterbium erwartet werden, geeignet.

Abschließend werden mögliche Anwendungen doppler- und rückstoßfreier Spektroskopie auf dem ultraschmalen Uhrenübergang $^1S_0 \leftrightarrow {}^3P_0$ zur Messung von Wechselwirkungen und Korrelationen in jenen Quantengassystemen behandelt. Insbesondere wird hierbei auf Möglichkeiten zur Beobachtung von Spinkorrelationen zwischen den Zuständen $^1S_0$ und $^3P_0$ sowie zwischen angrenzenden Gitterplätzen eingegangen.

Contents

List of Publications

Journal articles

Im Rahmen der vorliegenden Arbeit sind die folgenden wissenschaftlichen Veröffentlichungen entstanden.

The following research articles have been published in the course of this thesis.

[1] Dörscher, S. *et al.* Creation of quantum-degenerate gases of ytterbium in a compact 2D-/3D-magneto-optical trap setup. *Review of Scientific Instruments* **84,** 043109 (Apr. 2013)

[2] de Angelis, M. *et al.* iSense: A Portable Ultracold-Atom-Based Gravimeter. *Procedia Computer Science* **7,** 334–336 (2011)

[3] Becker, C. *et al.* Ultracold quantum gases in triangular optical lattices. *New Journal of Physics* **12,** 065025 (June 2010)

Conference contributions

Im Rahmen der vorliegenden Arbeit wurden folgende wissenschaftliche Vorträge und Poster durch den Autor präsentiert.

The following talks and posters have been presented by the author in the course of this thesis.

DPG Spring Meeting S. Dörscher, *Production of Ultracold Gases of Ytterbium in a 2D-/3D-MOT Setup* (talk), Hannover, March 2013

DPG Spring Meeting A. Thobe, S. Dörscher, B. Hundt, and A. Kochanke, *Production of Yb Quantum Gases for Optical Lattice Experiments* (poster), Hannover, March 2013

Summer School of the 23rd International Conference on Atomic Physics S. Dörscher & A. Thobe, *2D/3D-MOT System for the Production of Quantum-Degenerate Gases of Ytterbium* (poster), Paris, July 2012

Workshop on Geodesy with Inertial Quantum Sensors S. Dörscher, *A Versatile System to Produce Ultracold Ytterbium* (talk), Hannover, June 2012

DPG Spring Meeting S. Dörscher and B. Hundt, *2D/3D-MOT System for the Production of Quantum-Degenerate Gases of Ytterbium* (poster), Stuttgart, March 2012

Evaluation of the planned Collaborative Research Centre 925 C. Becker, S. Dörscher, & A. Thobe, *Quantum phases probed on ultra-narrow transitions* (poster), Hamburg, February 2011

YAO Meeting S. Dörscher, *Dynamics of dark and dark-bright solitons in Bose–Einstein condensates* (talk), Vienna, February 2009

List of Figures

List of Tables

List of symbols

A Mass number of a nucleus. 7

a s-wave scattering length. xv, 24, 25, 27

a_{bg} Background s-wave scattering length of a Feshbach resonance. 27

a_{ee} s-wave scattering length of two excited-state atoms. 25, 35

a_{eg} s-wave scattering length of a ground-state and an excited-state atom. 96

a_{eg}^{+} s-wave scattering length of a ground-state and an excited-state atom in a symmetric superposition state. 25, 35

a_{eg}^{-} s-wave scattering length of a ground-state and an excited-state atom in an anti-symmetric superposition state. 25, 35

a_{gg} s-wave scattering length of two ground-state atoms. 25, 35, 96

$\boldsymbol{A}_{\mathrm{e}}$ Normal vector of the emitter surface in numeric simulations of the 2D-MOT. 120

B Scalar projection of the magnetic induction vector. 25, 27, 106, 107, 109

$\boldsymbol{B}$ Magnetic induction vector. 109, 110, 119

B_0 Resonance position of a magnetically induced Feshbach resonance. 27

B_i Projection of the magnetic induction vector onto the axis i. 53

c Speed of light. 9, 31, 124, 129

$\boldsymbol{d}$ Operator of the electric dipole moment. 109, 123

E Energy. 20, 123

$E_{\mathrm{rec}}^{(\mathrm{l})}$ Recoil energy of photon of the optical lattice absorbed or emitted by an atom. 33, 103, 106

$E_{\mathrm{rec}}^{(\mathrm{s})}$ Recoil energy of a $^1\mathrm{S}_0 \leftrightarrow {}^3\mathrm{P}_0$ probe photon absorbed or emitted by an atom. 103

$\boldsymbol{E}$ Electric field vector. 109

$\boldsymbol{e}_i$ Unit vector along the axis i. 109, 119, 120, 130

$\mathscr{F}$ Finesse of a resonator. 107

F Total angular momentum quantum number of an atom, including nucleus and electrons. 9–14, 18, 19, 60, 71, 105

f Focal length. 80, 82

g Scalar projection of the acceleration due to gravity. 130, 131

g_F Landé factor of an eigenstate of the total angular momentum operator of an atom, including nucleus and electrons. xv, 11, 13, 14, 106

g_I Landé factor of an eigenstate of the nuclear spin operator. 7, 11, 106

g_J Landé factor of an eigenstate of the total angular momentum operator. 11, 15, 22

$\boldsymbol{g}$ Gravity acceleration vector. 130

h Planck constant, see compilation of CODATA recommended values by Mohr *et al.*[4] 9

H_{MIS} Hamiltonian of the linear Zeeman effect used for level-mixing in magnetically induced spectroscopy. 109

$\hbar$ Reduced Planck constant, see compilation of CODATA recommended values by Mohr *et al.*[4] 9, 11, 31, 91, 92, 96, 97, 103, 106, 109, 123

I Nuclear spin quantum number. 6, 7, 9, 11, 35, 70, 91, 106

I_{C} Electric current. 53

I_{L} Intensity of a laser beam. 31, 76, 105, 108, 109, 121, 124

$I_{\mathrm{L},0}$ Peak intensity of a laser beam. 62

$I_{\mathrm{L,sat}}$ Saturation intensity of an atomic transition. 9, 11, 62, 108, 121

$\boldsymbol{I}$ Nuclear spin operator. 13, 17

J Total angular momentum quantum number. 9, 11, 17, 18, 20, 22, 25, 33, 35, 106, 123, 124, 129

J_{nn} Nearest-neighbour tunnelling parameter of the Hubbard model. 99

$\boldsymbol{J}$ Total angular momentum operator. 13, 17

$\boldsymbol{j}$ Total angular momentum operator of a single electron. 8

k Wave number. 11

k_{B} Boltzmann constant, see compilation of CODATA recommended values by Mohr *et al.*[4] 9, 73, 74, 76, 77, 88, 91, 92, 120

k_{s} Wave number a probe photon close to the clock transtion $^1\mathrm{S}_0 \leftrightarrow {}^3\mathrm{P}_0$. 103

L Orbital angular momentum quantum number. 9

l Orbital angular momentum quantum number of two particles, *e.g.* two atoms or a single electron in an atom. 27

$\boldsymbol{L}$ Orbital angular momentum operator. 8, 11

m Mass of a particle. 7, 120, 130, 131

M^2 M^2 factor of a real beam, *i.e.* the ratio of its divergence angle and that of an ideal Gaussian beam. 82

m_F Magnetic quantum number of the total angular momentum of an atom, including nucleus and electrons. 14, 70, 71, 105–107

M_{HD} Magnification of the imaging system along the x-axis. 86

m_J Magnetic quantum number of the total angular momentum. 20, 25, 27, 109, 123, 124

m_l Magnetic quantum number of the orbital angular momentum of two particles, *e.g.* two atoms or a single electron in an atom. 27

M_{LA} Magnification of the imaging system along the z-axis. 63

m^o_{Yb} Standard atomic mass of ytterbium (see Wieser & Coplen, 2011[5]). 6, 11

N Total number of atoms. 89, 91, 92

N_0 Number of condensed atoms in a Bose gas. 89, 91

N_{sat} Saturated maximum number of atoms in the 3D-MOT. 61

$\bar{n}$ Mean density of atoms within the effusive atom source in numeric simulations of the 2D-MOT. 120

P Power. 129

p_{2D} Pressure measured by the 2D-MOT cell gauge. 48

p_{3D} Pressure measured by the science cell gauge. 48

$P^{(\mathrm{h})}$ Power in the horizontal dipole trap beam. 77

$P^{(\mathrm{s})}$ Power of the probe beam used to interrogate the clock transition $^1\mathrm{S}_0 \leftrightarrow {}^3\mathrm{P}_0$. 108

$P^{(\mathrm{sc})}$ Power in the planned science dipole trap beam. 93

$P^{(\mathrm{v})}$ Power in the vertical dipole trap beam. 77

$P_{\mathrm{c}}^{(\mathrm{h})}$ Critical power in the horizontal dipole trap beam for support against gravity. 77, 88

$P_{\mathrm{c}}^{(\mathrm{sc})}$ Critical power in the planned science dipole trap beam for support against gravity. 93

$P_{\mathrm{f}}^{(\mathrm{h})}$ Final power in the horizontal dipole trap beam at the end of the forced evaporation ramp. 88

$P_{\mathrm{f}}^{(\mathrm{v})}$ Final power in the vertical dipole trap beam at the end of the forced evaporation ramp. 88

$P_{\mathrm{i}}^{(\mathrm{h})}$ Initial power in the horizontal dipole trap beam during trap loading. 88

P_{max} Maximum power in a laser beam. 76

$P_{\mathrm{max}}^{(\mathrm{h})}$ Maximum power in the horizontal dipole trap beam. 78

$P_{\mathrm{max}}^{(\mathrm{v})}$ Maximum power in the vertical dipole trap beam. 78

$P_{\mathrm{tr}}^{(\mathrm{h})}$ Power in the horizontal dipole trap beam between at transition from the first to second phase of forced evaporation. 88

p_{vap}^{*} Asymptotic vapour pressure in the Clausius–Clapeyron equation. 6

p_{vap} Vapour pressure. 6

q Quasi momentum. 103

R Universal gas constant, see compilation of CODATA recommended values by Mohr *et al.*[4] 6

R_i Thomas–Fermi radius of a Bose–Einstein condensate along the axis i. 91

S Spin quantum number. 7, 9, 20

$\boldsymbol{S}$ Spin operator. 8, 11

T Temperature. iii, v, 6, 73, 74, 91–93, 111

T_{c} Critical temperature of Bose–Einstein condensation. 91

T_{D} Doppler cooling limit. 9, 11

T_{e} Temperature of the atom source. 120, 121

t_{e} Duration of the forced evaporation ramp in the elongated dipole trap. 88

T_{F} Fermi temperature. iii, v, 3, 73, 92, 93, 111

t_{h} Hold time of the atomic sample in the trap, *e.g.* after inducing an oscillation. 90, 91

t_{x} Duration of the forced evaporation ramp in the crossed dipole trap. 88, 92

U Interaction parameter of the Hubbard model. 96, 97, 99

U_{ee} Interaction parameter of two excited-state atoms. 97

U_{eg} Interaction parameter of a ground-state and excited-state atom. 97

U_{eg}^{-} Interaction parameter of a ground-state and an excited-state atom in an anti-symmetric superposition state atom. 98, 113

U_{eg}^{+} Interaction parameter of a ground-state and an excited-state atom in a symmetric superposition state. 98, 113

U_{gg} Interaction parameter of two ground-state atoms. 97

v Velocity. 120

$\boldsymbol{v}$ Velocity vector. 120

V_0 Maximum depth of the optical dipole potential induced by a laser field. 74, 76, 129–132

$V_0^{(\mathrm{v})}$ Nominal depth of the vertical optical dipole trap. 87

$V^{(\mathrm{t})}$ Tensor term of the second-order AC–Stark shift. 105

$V^{(\mathrm{v})}$ Vector term of the second-order AC–Stark shift. 105

V_c Critical depth of an optical dipole potential for support against gravity. 130–132

v_c Capture velocity of the 3D-MOT. 68, 120

V_D Optical dipole potential depth. 31, 124, 129

V_eff Effective depth of a optical dipole potential under the influence of gravity. 73, 75, 77, 87, 91, 131, 132

$V_\mathrm{eff}^{(\mathrm{i})}$ Initial effective depth of the crossed dipole trap during trap loading. 88

$V_\mathrm{eff}^{(\mathrm{tr})}$ Effective depth of the crossed dipole trap at the transition from the first to second step of the forced evaporation ramp. 88

V_g Gravity potential. 130

W Lambert W-function. 131

w_0 Minimal $1/\mathrm{e}^2$ waist of a Gaussian beam. 76, 79, 82, 87, 93, 129–132

$w_0^{(\mathrm{s})}$ Minimal $1/\mathrm{e}^2$ waist of the probe beam used to interrogate the ${}^1\mathrm{S}_0 \leftrightarrow {}^3\mathrm{P}_0$ clock transition. 108

$w_{0,i}$ Minimal $1/\mathrm{e}^2$ waist of a Gaussian beam along the axis i. 75

$W^{(s)}$ Spontaneous rate of a specific transition. 8, 13, 123, 124

w_i $1/\mathrm{e}^2$ waist of a Gaussian beam at a specific position along the axis of propagation. 129

y_bar Position of the outer potential barrier of an optical dipole trap under the influence of gravity. 131

y_cm Vertical centre-of-mass position the atomic sample. 90

y_sag Sag of the trap centre of an optical dipole trap under the influence of gravity. 131, 132

Z Charge number of a nucleus. 8

z_nn Number of nearest neighbours of a lattice site. 99

z_R Rayleigh range of a Gaussian beam. 76, 129, 130, 132

α Second-order AC–Stark polarisability. 123, 124, 129

$\alpha^{(\mathrm{v})}$ Vector term of the second-order AC–Stark polarisability. 106

β_{in} Inelastic two-body loss rate coefficient. 20

Γ Line width of a transition or rate of a process, *e.g.* decay of an atomic state. 9, 11, 18, 31, 32, 65, 68, 71, 102, 108, 124

Γ_{sc} Photon scattering rate of an atom in an optical dipole potential. 31, 76, 77

Δ_{2D} Detuning of the 2D-MOT beams from the $^1S_0 \leftrightarrow {}^1P_1$ resonance frequency. 65, 68

Δ_{3D} Detuning of the 3D-MOT beams from the $^1S_0 \leftrightarrow {}^3P_1$ resonance frequency. 66

$\Delta_{3D}^{(sf)}$ Detuning of the 3D-MOT beams from the $^1S_0 \leftrightarrow {}^3P_1$ resonance frequency during the single-frequency phase. 69

Δ_{FS} Fine structure splitting frequency of the $^3P_0$ and $^3P_1$ states. 109

Δ_{push} Detuning of the pushing beam from the $^1S_0 \leftrightarrow {}^1P_1$ resonance frequency. 67

ΔB Width of a magnetically induced Feshbach resonance. 27

δg Differential Landé factor of $^3P_0$ and $^1S_0$states. 106

ΔH_{sub} Sublimation enthalpy. 6

$\Delta\omega_s^{(B)}$ Magnetic shift of the $^1S_0 \leftrightarrow {}^3P_0$ resonance frequency. 106

$\Delta\omega_s^{(coll)}$ Collisional shift of the $^1S_0 \leftrightarrow {}^3P_0$ resonance frequency. 96, 97

ε Polarisation state of a photon. 105, 123, 124, 129

η Lamb–Dicke parameter. 103

θ_c Capture angle of the 3D-MOT. 68, 120

θ_{div} Asymptotic divergence angle of a Gaussian beam. 76

θ_{DPS} Acceptance angle of the differential pumping stage. xiii, 47

θ_{pol} Angle of the electric field of a linearly polarised laser to the quantisation axis. 105, 109

κ Characteristic parameter for the Rabi frequency of an atom as a function of laser intensity and magnetic field strength in magnetically induced spectroscopy. 109

λ Wavelength in vacuum. 8, 9, 11, 23, 32–35, 76, 94, 129

λ_s Wavelength of the $^1S_0 \leftrightarrow {}^3P_0$ clock transition. 21, 107

λ_m Near-infrared magic wavelength of the states $^1S_0$ and $^3P_0$. 9, 33

λ_{ODT} Wavelength of the crossed dipole trap. 76

μ Reduced mass in the centre-of-mass frame of two colliding particle. 25, 29

ε_0 Vacuum permittivity, see compilation of CODATA recommended values by Mohr *et al.*[4] 123, 124, 129

μ_B Bohr magneton, see compilation of CODATA recommended values by Mohr *et al.*[4] 11, 14

μ_N Nuclear magneton, see compilation of CODATA recommended values by Mohr *et al.*[4] 11, 106

$\boldsymbol{\mu}$ Operator of the magnetic dipole moment. 109

μ_r Residual magnetic susceptibility. 115

Ξ Abundance of an isotope. 7

ξ FWHM amplitude of the spectral broadening of the 3D-MOT laser. 66

ξ_max Maximum FWHM amplitude of the spectral broadening of the 3D-MOT laser. 65

ξ_opt Optimum FWHM amplitude of the spectral broadening of the 3D-MOT laser. 64, 66

τ Lifetime, *e.g.* of an atomic state, or time constant of an exponential process in general. 13, 18

τ_MOT Loading time constant of the 3D-MOT. 61

Φ Flux emitted by the atom source. 120

χ Aspect ratio of the minimal $1/e^2$ waists of a Gaussian beam. 76, 79, 82, 87, 93, 129–132

Ω On-resonance Rabi frequency. 108, 109

ω Angular frequency. 11, 15, 31

ω_0 Resonance frequency of an atomic transition. 31, 32, 123, 124

Ω_B Rabi frequency induced by the magnetic field in magnetically induced spectroscopy. 109

ω_ho Harmonic oscillator frequency. 102, 103

ω_i Harmonic trapping frequency of a potential along the axis *i*. 75–77, 87, 90, 91, 93, 130–132

$\omega_i^{(\mathrm{max})}$ Maximum harmonic trapping frequency of the crossed dipole trap along the axis *i*. 76

Ω_L Rabi frequency induced by the laser field in magnetically induced spectroscopy. 109

ω_L Frequency of a laser field. 31, 123, 124, 129

ω_m Magic frequency of the states $^1\mathrm{S}_0$ and $^3\mathrm{P}_0$. Refers to the near-infrared magic wavelength of the clock transition in ytterbium unless stated otherwise. 33

ω_s Carrier frequency of the clock transition $^1\mathrm{S}_0 \leftrightarrow {}^3\mathrm{P}_0$ (between specific nuclear spin states in the fermionic isotopes) for precision spectroscopy in optical lattices. 97, 98, 100

$\omega_z^{(\mathrm{h})}$ Axial trapping frequency of the horizontal dipole trap. 87
$\bar{\omega}$ Geometric mean value of the harmonic trapping frequency of a potential. 90–92

Acronyms

AC	alternating current. xiii, 1, 7, 30–35, 103–105, 109, 110, 123, 124
AEL	alkaline earth–like. xv, 1, 2, 5–8, 13, 16–18, 20–23, 26–28, 30, 32, 34–37, 39, 41, 59, 60, 70, 74, 100, 111–113
AOM	acousto-optic modulator. 78, 79, 107
AR	anti-reflection. 45, 47, 86, 108
BBR	black-body radiation. 19, 108
BEC	Bose–Einstein condensate. iii, xiv, 3, 25, 73, 88–91, 93, 96, 111
CCD	charge-coupled device. 63
CF	Conflat. 47, 115
DC	direct current. 17
DPS	differential pumping stage. xiii, 38, 45, 47, 48, 115, 117, 119–121
E1	electric dipole. 15, 17–19, 32
E2	electric quadrupole. 18, 19
ECDL	external-cavity diode-laser. 107
EDM	electric dipole moment. 17, 30
EMCCD	electron multiplying charge-coupled device. 86
FSC	fine structure–changing. 20
FWHM	full width a half maximum. xxiii, 59, 64, 65
HFI	hyperfine interaction. 17, 19
IUPAC	International Union of Pure and Applied Chemistry. 7
KLM	Kondo-lattice model. 2, 21, 22, 35, 112

M1 magnetic dipole. 16, 18, 19
M2 magnetic quadrupole. 18, 19, 21
MI Mott insulator. 1, 35, 96, 97, 99, 112
MIS magnetically induced spectroscopy. 17, 21, 106, 109, 110
MOT magneto-optical trap. iii, v, xiii–xv, 2, 3, 6, 9–11, 13, 15, 16, 23, 28, 37–40, 43–55, 58–71, 73, 77, 79, 85–88, 92, 111, 115, 117, 119–121, 155

NIR near-infrared. 32, 35, 54, 104, 106
NIST National Institute of Standards and Technology. 107

ODT optical dipole trap. xiv, 10, 20, 30, 31, 40, 52, 53, 55, 58, 69, 73, 74, 76–79, 81–86, 93, 94, 102
OFR optical Feshbach resonance. 23, 26
OLC optical lattice clock. 1, 2, 9, 20, 23, 32, 33, 95, 96, 99, 101–107

PA photoassociation. 23, 26, 29, 30
PDH Pound–Drever–Hall. 107
PMF polarisation-maintaining, single-mode optical fibre. 62, 73, 78, 82, 85, 94
PNC parity non-conservation. 5, 17
PQNC principal quantum number–changing. 20
PTFE polytetrafluoroethylene. 108
PZT piezoelectric transducer. 107

RF radio-frequency. 27

SF superfluid. 1, 97, 99, 112
SMF single-mode optical fibre. 54, 55, 62

UV ultra-violet. 32, 35

VXDT vertical crossed optical dipole trap. xiii, 73–75, 77–79, 81, 83, 85, 86, 89–92, 111

XDT crossed optical dipole trap. 41, 43, 55, 73, 74, 78, 111

ZSLC Zeeman sublevel–changing. 20, 27

"Yet all experience is an arch wherethrough
Gleams that untravelled world, whose margin fades
For ever and for ever when I move
How dull is it to pause, to make an end,
To rust unburnished, not to shine in use!"

—Alfred Tennyson, *Ulysses*

Chapter 1

Introduction

Following the celebrated realisation of Bose–Einstein condensation[6,7] in dilute atomic vapours and of Fermi degeneracy[8] only a few years later, studies of ultracold atomic and molecular gases have developed into a thriving, highly diverse field of research. Ultracold atoms in optical lattices are one of the main interests, for they allow the investigation of problems that are well known from solid-state physics, but are difficult to study both experimentally in condensed-matter systems and theoretically. The remarkable purity of quantum gases in optical lattice potentials and the unprecedented control over the parameters of these systems make them ideal candidates for a quantum simulation[9] of such systems.

Soon after the advent of quantum degeneracy, it was pointed out[10] that ultracold atoms in the periodic potential of an optical lattice can be described by the Hubbard model, and over the past decade a series of seminal experiments have studied its physics in the lowest Bloch band, *e.g.* the realisation of the quantum phase transition from a superfluid (SF) state to the Mott insulator (MI) in bosons[11] and fermions,[12] its modification by the presence of impurities in ultracold mixtures,[13] creation of ultracold molecules[14–17] or the observation of second-order tunnelling and superexchange processes,[18,19] to name only a few examples. In the process, a number of novel experimental techniques have been developed or adapted, *e.g.* single-site-resolved imaging[20,21] or the detection of noise correlations.[22] The use of the latter technique to observe anti-bunching in a fermionic band insulator[23] demonstrates how these new techniques shift boundaries to allow direct observation of new quantities, such as correlations, and hence the signatures of novel quantum phases. Several recent studies have concentrated on multi-orbital physics beyond the lowest-band Hubbard model[24–31] or studies of artificial magnetism[32] in novel types of optical lattices, to name only a few examples.

In the field of frequency metrology, on the other hand, optical lattice clocks (OLCs)[33–74] have been developed as a novel type of optical frequency standard for alkaline earth–like (AEL) atoms and to search for drifts of fundamental constants within the same timeframe, following the advent of octave-spanning frequency combs.[75] These OLCs are based on an ultranarrow transition from the ground state $^1S_0$ to the metastable excited state $^3P_0$ in the optical domain, but most importantly atoms are trapped in a deep optical lattice without disturbing the clock transition by the light shifts of the optical potential. A feature first pointed out by Katori,[33] the differential AC–Stark shift of these two states may be cancelled to leading order by tuning the optical lattice to a special, the so-called "magic" wavelength. In consequence, OLCs allow tight confinement of atoms at individual sites of the optical lattice and hence probing of the clock transition free of Doppler of photon recoil shifts, as in ion clocks, but also massively parallel probing of thousands of individual oscillators. The first OLC was realised for strontium (Sr) almost a decade ago, and recent experiments[65,66] have

reported systematic shift controlled down to relative uncertainties of a few 10^{-16} as well as instabilities of a few 10^{-18} after only a few hours of averaging, demonstrating the extraordinary potential of these clocks with respect to both microwave clocks and ion clocks in the optical domain.

At the same time, cooling of this new class of atoms to quantum degeneracy was studied by several groups around the world. While it has already been achieved for ytterbium (Yb) back in 2003 by the Kyoto group,[76] ytterbium quantum gases have only been reported[1,77,78] recently in other laboratories – including the experiment presented herein. Moreover, quantum degeneracy of other AEL elements has only been achieved recently for calcium (Ca)[79,80] and strontium.[81,82]

Owing to the presence of two valence electrons in an ns^2 orbital, AEL elements are quite different from the traditional alkali element, which have a single valence electron, and possess several highly intriguing features, *e.g.* metastable excited electronic states or a nuclear spin that is decoupled from the electron shell. Therefore, AEL elements are extremely promising candidates to study a large number of novel phenomena and systems that are difficult to study in alkali elements – or cannot be studied at all. To name no more than a few examples, they have been proposed for studies of quadrupolar anisotropic interactions,[83] alternative ways of creating artificial gauge potentials[84–87] for neutral atoms, novel quantum computation schemes,[88–91] the Kondo-lattice model (KLM) and heavy-fermion materials,[92–96] as well as two-orbital SU(N)-symmetric spin Hamiltonians[92] with $N > 2$.

Ytterbium is a particularly versatile one among the AEL elements, *e.g.* it has the largest number of stable isotopes among these elements. Five bosonic and two fermionic isotopes not only allow various combinations of isotope mixtures to be studied, but also provide a variety of different interaction strengths, nuclear spins and other isotope-dependent properties to choose from for specific experiments. A fine example of this flexibility are the fermionic isotopes, where one, ^{171}Yb, is particularly interesting for precision measurements in optical frequency standards or matter-wave interferometry due to its small nuclear spin and weak s-wave interactions, whereas the other, ^{173}Yb, is a prime candidate for studying strongly correlated quantum phases, because it has a large nuclear spin and strong interactions.

In this thesis, I present the setup and first results of a newly developed apparatus for studies of ultracold ytterbium in optical lattices. In future experiments, we intend to use the well-proven techniques of OLCs to perform Doppler- and Stark-free spectroscopy of quantum-degenerate gases in optical potentials for the first time in the optical domain. The ultranarrow clock transition has the potential to become a powerful tool in probing and preparing quantum gases of ytterbium in different electronic states, and it will allow the detection of signatures of the novel quantum phases expected in these systems.

Our apparatus is based on a novel 2D-/3D-magneto-optical trap (MOT) scheme for ytterbium, where the 2D-MOT is not loaded from a background gas[97] , but directly from a dispenser that emits atoms transversely to the emerging beam of precooled atoms. We have shown that this setup allows loading rates that are similar to or even exceed the performance of previously reported setups using Zeeman slowing[98] of thermal beam for loading of a three-dimensional MOT. It is both the first time that a 2D-MOT has been created for ytterbium or any other of the high-melting AEL elements and that the concept of transverse loading has been demonstrated in a glass cell, which represents a substantial simplification of the setup as compared to previous demonstrations of transverse loading.[99] In particular, it results in a highly flexible system that is very well suited for studies of ultracold mixtures composed from different chemical elements, since the second species,

in our case rubidium (Rb), may be cooled and trapped magneto-optically in the same 2D-MOT setup.

Furthermore, I discuss the setup of a crossed optical dipole trap for all-optical cooling of ytterbium to quantum degeneracy and the generation of Bose–Einstein condensates (BECs) of ^{174}Yb and degenerate Fermi gases of ^{173}Yb in our apparatus. Large atom numbers of nearly pure BECs and Fermi gases at very low temperatures of down to $0.1\,T_{\mathrm{F}}$ are highly encouraging and our system provides excellent starting conditions for future experiments in optical lattices.

This thesis is organised as follows:

- Atomic properties of ytterbium are reviewed at length in chapter 2. In particular, its isotopes, relevant transitions for laser cooling, properties of the metastable states and ultranarrow transitions, as well as known interaction properties are discussed.
- The concept of our experimental setup from the 2D-/3D-MOT scheme to the all-optical generation of quantum-degenerate gases is presented briefly in chapter 3.
- Our 2D-/3D-MOT scheme and experimental results for loading of large ytterbium samples into a 3D-MOT as well as subsequent magneto-optical cooling to temperatures of a few tens of microkelvins are presented in chapter 5. Transverse loading of the 2D-MOT is examined with respect to both experimental results and extensive numeric simulations of the 2D-MOT.
- The setup of a crossed optical dipole trap for subsequent evaporative cooling and the demonstration of Bose–Einstein condensation of ^{174}Yb as well as Fermi degeneracy of ^{173}Yb are discussed in chapter 6.
- Concepts and ideas of using the clock transition in order to probe or prepare ytterbium quantum gases are presented in chapter 7, and the current status of the spectroscopy laser system is reviewed briefly.
- A final summary of the experimental results obtained in the framework of this thesis and a discussion of the current status of on-going experimental work and possible future experiments based on the results of this thesis are given in the concluding chapter 8.

Chapter 2

Ytterbium in a nutshell

Alkaline earth–like (AEL) atoms have become a focus of interest by the atomic physics community over the past decade. Their characteristic feature is the presence of two s-shell valence electrons, which gives rise to a number of common properties and provides novel opportunities, *e.g.* for precision measurements and the simulation of condensed-matter systems. Beyond the actual alkaline-earth elements, such as calcium and strontium, this group also contains several transition metals, *e.g.* mercury (Hg), and the rare-earth element ytterbium, which is studied in this thesis.* While the first, and for a long time only, quantum-degenerate gases of ytterbium were reported[76,100–103] by the Kyoto group from 2003 onwards, several research groups have started experiments on ultracold ytterbium in the past few years, *e.g.* at Düsseldorf, Seattle, Tokyo, Hamburg, Florence, and Munich. However, only three of them – the groups at Seattle,[77] Tokyo[78] and we[1] – have reported quantum-degeneracy to date.

This chapter is intended to provide a survey of the properties of ytterbium. Its vapour pressure is discussed briefly (see section 2.1), because it becomes important later in thesis. Ytterbium provides a rich variety of isotopes, which is presented in more detail in section 2.2, and the combination of a broad principal transition $^1S_0 \leftrightarrow {}^1P_1$ with a narrow intercombination transition $^1S_0 \leftrightarrow {}^3P_1$ (see section 2.4). Besides the $^1S_0$ ground state, there are several metastable excited electronic states, $^3P_0$and $^3P_2$, accessible via ultranarrow transitions (see section 2.5). In combination with state-dependent optical potentials (see section 2.8) these may be used for precision spectroscopy in an optical lattice or to study a variety of novel systems, especially because the nuclear spin decouples from the electron shell in $^1S_0$ and $^3P_0$ (see section 2.9). However, while the s-wave scattering lengths are well known for the ground state, the interactions of the metastable state $^3P_0$ are still largely unexplored (see section 2.6). Finally, mixtures of ytterbium and rubidium provide both the means to achieve extremely low temperatures and to realise new systems in optical lattices or as molecules (see section 2.7).

Although the discussion in this thesis focuses exclusively on quantum gases of neutral ytterbium, it is used in several other areas of research as well, *e.g.* singly ionised ytterbium is used in many ion trap experiments, while multiply ionised Ytterbium is widely used as dopant in active laser media of solid-state as well as fibre lasers. Furthermore, ytterbium is used in experiments on quantum non-demolition measurements,[104–106] precision measurements of parity non-conservation (PNC) effects,[107–113] and the search for permanent electric dipole moments of atoms or molecules.[114–118]

*Helium (He) is not an AEL element, however. Because its valence electrons occupy the 1s-shell and low-energy excitations populate the 2s-shell, the level structure of helium differs significantly from AEL elements. Furthermore, other elements, like the actinide nobelium (No), do not occur naturally and have therefore been neglected.

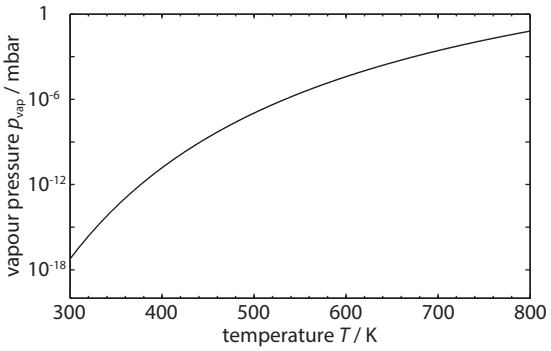

Figure 2.1 | Vapour pressure of ytterbium according to the parameters discussed in section 2.1. Sufficient vapour pressure for the operation of a beam apparatus, for instance, are achieved at temperatures of about 700 K.

2.1 Vapour pressure

Similar to many of the AEL elements, ytterbium has a high standard melting point[119] of 1097 K, and its low vapour pressure of ytterbium at room temperature is one of the major differences to many of the traditional alkali elements, *e.g.* rubidium or potassium (K). As I am going to discuss in more detail in chapter 3, this requires a novel approach to implement a 2D-MOT. Nevertheless, atomic beams of sufficient flux for spectroscopy or loading of MOTs can be produced in an oven or even a dispenser source at temperatures well below the melting point.

The vapour pressure of solid ytterbium as a function of temperature is illustrated by figure 2.1 and described by the Clausius–Clapeyron equation

$$p_{\mathrm{vap}}(T) = p^{*}_{\mathrm{vap}} \exp\left(-\Delta H_{\mathrm{sub}}/RT\right), \tag{2.1}$$

where $\ln\left(p^{*}_{\mathrm{vap}}/\mathrm{torr}\right) = 8.295(43)$ and $\Delta H_{\mathrm{sub}}/R = 7696(33)$ K have been determined by Habermann & Daane.[120] Ytterbium in its metallic form is relatively inert at room temperature. In contact with oxygen it oxidises slowly in a matter of weeks, but it becomes highly reactive, when heated to temperatures of several hundreds of degrees Celsius.[121]

2.2 Isotopes

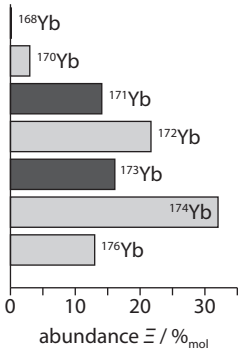

Figure 2.2 | Representative isotope composition of ytterbium. Dark (light) shades represent fermionic (bosonic) isotopes. See also table 2.1.

One of the most remarkable features of ytterbium is its multitude of seven stable and mostly abundant isotopes, as shown figure 2.2.[122] Among these are two fermionic isotopes, ^{171}Yb and ^{173}Yb, with nuclear spins of $I = 1/2$ and $I = 5/2$, respectively. The remaining five isotopes, including the most abundant isotope ^{174}Yb, are bosons that have no nuclear spin ($I = 0$). Therefore, ytterbium allows the realisation of ultracold Bose–Bose, Bose–Fermi as well as highly interesting (*cf.* section 2.9) Fermi–Fermi isotope mixtures[123] and provides a rich selection of properties, *e.g.* with respect to atomic interactions, even for quantum gases of a single isotope.

The basic properties of the stable ytterbium isotopes are summarised in table 2.1. The representative isotope composition shown there yields a standard atomic mass[5] $m^{o}_{\mathrm{Yb}} = 173.054(5)$ u. Further details, like isotope shifts and hyperfine structures of the relevant transitions (see section 2.4) or atomic interactions (see section 2.6), are presented during the discussion of the properties of ytterbium throughout the remainder of this chapter.

Table 2.1 | Abundances and nuclear properties of ytterbium isotopes. Nuclear spin I, Landé factors g_I, atomic masses m and abundances Ξ in a representative composition as recommended by the IUPAC are summarised for the stable isotopes of ytterbium with mass number A.

A	I	g_I[a]	m/u[b]	$\Xi/\%_{\mathrm{mole}}$[b]
168	0		167.933 897(5)	0.123(3)
170	0		169.934 761 8(26)	2.982(39)
171	1/2	+0.4919	170.936 325 8(26)	14.09(14)
172	0		171.936 381 5(26)	21.68(13)
173	5/2	−0.6776	172.938 210 8(26)	16.103(63)
174	0		173.938 862 1(26)	32.026(80)
176	0		175.942 571 7(28)	12.996(83)

[a] Sansonetti & Martin, 2005[124]

[b] Audi *et al.*, 2003[125]

[c] Berglund & Wieser, 2011[126]

2.3 Electronic structure

Owing to its two valence electrons occupying the 6s-orbital, the electronic structure of ytterbium is similar to AEL elements rather than other rare-earth elements, such as dysprosium (Dy)[127] and erbium (Er),[128] which have been Bose-condensed recently. Therefore, most atomic states of ytterbium belong to either the singlet ($S = 0$) or triplet ($S = 1$) electronic spin manifolds. The intercombination transitions between these spin configurations are extremely weak and give rise to many of the important features of ytterbium, such as narrow-line laser cooling (see section 2.4.2) and the existence of metastable excited electronic states (see section 2.5). A partial level scheme including the relevant transitions used in this thesis is shown in figure 2.3 (see figure C.1 for a comprehensive diagram).*

As the penultimate element of the lanthanide series, however, the full electronic configuration of ytterbium in its ground state reads [Xe] $4f^{14}6s^2$. Possible excitations of electrons from this closed shell have to be taken into account in some cases, *e.g.* for the determination of the AC–Stark effect, where these states cause additional resonances mainly due to two-photon transitions.

Angular momentum coupling in AEL elements, and especially in ytterbium, as well as the aforementioned excitations from the 4f-shell are discussed in more detail in the following subsections.

2.3.1 Angular momentum coupling

Angular momentum coupling in ytterbium is mostly governed by Russell–Saunders coupling, which gives rise to the aforementioned separation into singlet ($S = 0$) and triplet ($S = 1$) states of the combined electronic spin, as shown in figure 2.3. It is this manifestation of the two-electron character of AEL atoms in general that gives rise to all of their characteristic features discussed below. Nev-

*For the sake of brevity, the electronic configuration of an atomic state is omitted, when referring to the configuration with the lowest energy (see figure C.1).

Table 2.2 | Spin–orbit interaction in AEL atoms increases towards larger proton numbers and results in larger spontaneous transition rates $W^{(s)}$ of the respective intercombination transitions $^1S_0 \leftrightarrow {}^3P_1$ at wavelengths λ.

Element	Z	λ / nm	$W^{(s)}$ / s^{-1}
calcium	20	675 [a]	2.3×10^{3} [a]
strontium	38	689 [b]	4.8×10^{4} [b]
ytterbium	70	555.802 [b]	1.15×10^{6} [b]
mercury	80	254 [b]	8.0×10^{6} [b]

[a] Degenhardt *et al.*, 2005[129]

[b] Sansonetti & Martin, 2005[124]

ertheless, ***j***–***j***-coupling becomes dominant in some cases, *e.g.* for highly excited states, as ytterbium is rather heavy an element ($Z = 70$).

While alkali elements can usually be treated as effective single-electron atoms, the transitions in ytterbium reflect its multi-electron character. Intercombination transitions, which connect spin-singlet to spin-triplet states and *vice versa*, are strongly suppressed compared to ordinary transitions, *i.e.* within each of the spin manifolds, because a photon cannot couple to the spin state of an atom directly. They are forbidden for pure ***L***–***S***-coupling, but acquire small transition amplitudes in the case of intermediate mixing: spin–orbit coupling perturbs the atomic eigenstates and admixes small fractions of states from the opposite spin manifold. Owing to this coupling mechanism, intercombination transitions are stronger in heavy AEL elements than in lighter ones as shown in table 2.2.

2.3.2 Excitations of f-shell electrons

Although the valence electrons in the outer 6s-shell are responsible for the alkaline earth–like electronic properties of ytterbium, excitations of electrons from its closed 4f-shell cannot be neglected entirely. Some of these excited states are shown in figure C.1, a concise list can be found in the compilation by Martin *et al.*[130]

The resulting atomic states are, of course, neither part of the singlet, nor triplet manifolds, but subject to a different coupling regime altogether. If only a single electron is excited and both valence electrons remain in the 6s-shell, the single hole in the 4f-shell usually gives rise to a $^2F_{7/2}$ state according to Hund's fourth rule and couples with the excited electron via ***j***–***j***-coupling. However, most of the resulting states exhibit severe admixtures of different configurations (see Martin *et al.*,[130] pp. 375ff.). In some publications (*cf.* Bowers *et al.*[131]) the notation of ***L***–***S***-coupling is used instead. No states with multiple electrons excited from the 4f-shell have been reported below the ionisation threshold,[130] but multiply excited states where a valence electron has been excited in addition to a 4f-electron do exist and give rise to yet more complicated coupling of the individual electrons and holes.

These excitations of 4f-electrons are usually spectrally well resolved and thus not a problem for laser cooling or even precision spectroscopy itself, but they are a potential complication in the case

of state-dependent or magic optical potentials (see section 2.8), *i.e.* optical traps that need to be operated at a particular wavelength to cancel specific light shifts. Although most of the states resulting from the excitation of a 4f electron are not accessible via single-photon transitions from the metastable states and have relatively large excitation energies, there may still be resonances – especially due to two-photon transitions – close to the wavelength of the optical trap. The presence of such a resonance not only modifies the polarisability, but also causes substantial photon scattering in its vicinity. While the potential light shifts are not critical in the context of this thesis, resonant heating may nevertheless become a severe problem. Due to their importance for OLCs, several two-photon resonances around the magic wavelength $\lambda_\mathrm{m} \approx 759\,\mathrm{nm}$ have been investigated both theoretically[132] and experimentally,[133] and they were found to be sufficiently far-detuned from this magic wavelength (see also the discussion of hyperpolarisability in section 7.2.3).

2.4 Ground state properties

The ground state of ytterbium is the spin-singlet state $^1\mathrm{S}_0$. Without any net angular momentum of the electron shell ($L = S = J = 0$), its total angular momentum F arises solely from the nuclear spin I (see section 2.2). Therefore, the ground state gives rise to a number of highly intriguing features such as the decoupling of the nuclear spin (see section 2.9).

Its insensitivity to magnetic fields is particularly useful for some applications, *e.g.* precision spectroscopy on ultranarrow transitions (see chapter 7) or matter-wave interferometry. However, it also prevents magnetic trapping of ground-state atoms, and thus all-optical methods are required to generate quantum-degenerate gases (see chapter 3). Moreover, the vanishing nuclear spin of the bosonic isotopes prevents control of the interactions between atoms in the $^1\mathrm{S}_0$ state via magnetically tuned Feshbach resonances as well as sub–Doppler cooling,[134] since techniques like Sisyphus cooling[135] rely on the substructure in the ground state. In the case of the fermionic isotopes, this substructure is provided by the nuclear spin and evidence of Sisyphus cooling has been reported[121] for ytterbium.

Fortunately, two-stage laser cooling on the $J = 0 \leftrightarrow J' = 1$ cycling transitions $^1\mathrm{S}_0 \leftrightarrow {}^{1,3}\mathrm{P}_1$ allows efficient magneto-optical trapping and cooling of ytterbium down to temperatures of a few 10 µK. Here, the large line width of the singlet transition $^1\mathrm{S}_0 \leftrightarrow {}^1\mathrm{P}_1$ provides a strong radiation force, while the achievable MOT temperatures are severely limited in the absence of sub–Doppler cooling.* Owing to the suppression of spin-changing transitions, on the other hand, the intercombination transition $^1\mathrm{S}_0 \leftrightarrow {}^3\mathrm{P}_1$ in ytterbium has a line width of only 182 kHz. Its radiation pressure is hence strongly reduced and the Doppler cooling limit is only about 4 µK. The properties of both transitions for laser cooling are summarised in more detail in table 2.3. The Doppler cooling limit and saturation intensity of each transition is given by[137]

$$k_\mathrm{B} T_\mathrm{D} = \frac{\hbar\Gamma}{2} \text{ and} \tag{2.2}$$

$$I_\mathrm{L,sat} = \frac{\pi h c}{3\lambda^3}\Gamma \tag{2.3}$$

where λ and Γ are wavelength of the transition and decay rate of the excited state, respectively.

*Temperatures on the order of 100 µK have been reported[136] for the fermionic isotopes.

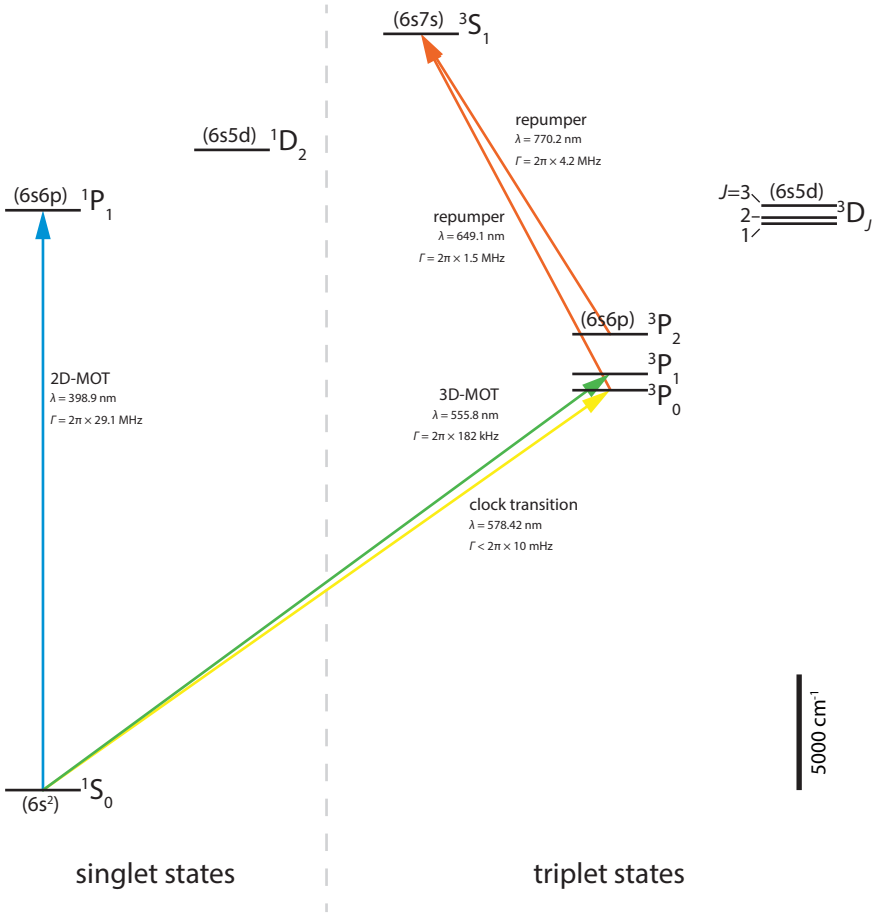

Figure 2.3 | Partial level scheme of ytterbium showing its low-energy states and transitions which are relevant for laser cooling, precision spectroscopy and optical pumping as discussed in this thesis. See also figure C.1 for an extended term diagram, including the exact electronic configurations.

Therefore, the $^1S_0 \leftrightarrow {}^1P_1$ transition is well suited for initial two-dimensional magneto-optical trapping and cooling of atoms from a thermal beam in our 2D-/3D-MOT scheme or a Zeeman slower. Subsequently, the $^1S_0 \leftrightarrow {}^3P_1$ is used for further magneto-optical trapping and cooling to the microkelvin regime that allows transfer into a deep optical dipole trap (ODT) and subsequent evaporative or sympathetic cooling.*

Further details about the laser cooling transitions are discussed in the subsequent sections 2.4.1 and 2.4.2. In particular, the hyperfine structure of the $^1S_0 \leftrightarrow {}^1P_1$ transition impedes the operation of a 2D-MOT due to the proximity of the $F = 5/2 \leftrightarrow F' = 3/2$ to the $F = 5/2 \leftrightarrow F' = 7/2$ hyperfine transition, which is used to magneto-optical trapping (see section 5.9 for further details). Another transition that is used for precision measurements in ytterbium is discussed briefly in the final section 2.4.3.

*Direct loading from a MOT on the $^1S_0 \leftrightarrow {}^1P_1$ transition into an optical lattice has been demonstrated[39] for strontium, using the enhancement of the lattice depth by a cavity and "drain" lasers for selective transfer to the lattice.

Table 2.3 | Parameters of the laser cooling transitions $^1S_0 \leftrightarrow {}^1P_1$ and $^1S_0 \leftrightarrow {}^3P_1$ in ytterbium. See the text for a definition of the Doppler cooling limit and saturation intensity. The last two columns represent the maximum radiation force on these transitions and the typical velocity for a Doppler shift equal to the line width of the transition.

Transition	λ/nm	$\Gamma/2\pi$ MHz	$I_{\mathrm{L,sat}}$/mW cm^{-2}	T_{D}/μK	$\frac{\hbar k\Gamma}{2m^{o}_{\mathrm{Yb}}}$/m s^{-2}	$\frac{\hbar\Gamma}{k}$/m s^{-1}
$^1S_0 \leftrightarrow {}^1P_1$	398.9[a]	29.13(3) [b]	59.97(5)	699.0(6)	5.3×10^5	11.6
$^1S_0 \leftrightarrow {}^3P_1$	555.8[a]	0.1823(3)[c]	0.1388(3)	4.37(1)	2.4×10^3	0.101

[a] Sansonetti & Martin, 2005[124]

[b] Takasu *et al.*, 2004[138]

[c] Blagoev & Komarovskii, 1994[139]

2.4.1 Principal transition

The principal transition $^1S_0 \leftrightarrow {}^1P_1$ is well suited for initial trapping of ytterbium due to its large line width. Decay from the excited state $^1P_1$ into metastable states (see section 2.5) is possible, but weak enough to be negligible in our 2D-/3D-MOT scheme. Different isotopes and the hyperfine structure of the fermionic isotopes can be resolved spectrally in most cases, but it is not ideal for operation of a MOT in the case of ^{173}Yb. Furthermore, the magnetic insensitivity of the ground state $^1S_0$ causes a peculiar Zeeman splitting of the transition for the fermionic isotopes, since the magnetic dipole moment of the excited state is much larger. All of these subjects are discussed in more detail in the remainder of this subsection.

Isotope and hyperfine shifts

The isotope shifts and hyperfine structure of the $^1S_0 \leftrightarrow {}^1P_1$ transition are summarised in table 2.4 and illustrated in figure 2.4a with respect to the transition frequency[140]

$$\omega(^1S_0 \leftrightarrow {}^1P_1, {}^{174}\mathrm{Yb}) = 2\pi \times 751\,525\,987.561(60)\,\mathrm{MHz}$$

of the most abundant isotope ^{174}Yb. These and further results regarding this transition have been reported by Das *et al.*[140] The isotope shifts of the principal transition are sufficiently large compared to the line width for selective addressing of individual isotopes in MOTs and imaging. However, the $F = 5/2 \leftrightarrow F' = 3/2$ transition frequency is separated by only about -2.5Γ from the $F = 5/2 \leftrightarrow F' = 7/2$ transition, which is the relevant hyperfine transition for the operation of a MOT (see section 5.9).

Magnetic substructure

As discussed above, any magnetic moment of the ground state arises solely from the nuclear spin. Hence, the Zeeman shifts of the $^1S_0 \leftrightarrow {}^1P_1$ transition are dominated by the magnetic moment of the excited state. Due to the vanishing nuclear spin of the bosonic isotopes, their effective Landéfactor in the excited state is that of the electron shell[130] ($g_J = 1.035$) in weak and moderate magnetic fields, *i.e.* unless $\boldsymbol{L}$–$\boldsymbol{S}$-coupling is broken in the Paschen–Back regime. In contrast, the coupling of the nuclear and electronic magnetic moments in the fermionic isotopes gives rise to a combined Landé factor[142]

$$g_F = g_J \frac{F(F+1) - I(I+1) + J(J+1)}{2F(F+1)} + g_I \frac{\mu_N}{\mu_B} \frac{F(F+1) + I(I+1) - J(J+1)}{2F(F+1)} \tag{2.4}$$

Table 2.4 | Isotope shifts and hyperfine structure of the $^1S_0 \leftrightarrow {}^1P_1$ and $^1S_0 \leftrightarrow {}^3P_1$ transitions of ytterbium, which are used for laser cooling. The frequency shifts are given with respect to ^{174}Yb and ^{176}Yb, respectively.

Transition		Frequency shift / MHz	
Isotope	$F \rightarrow F'$	$^1S_0 \leftrightarrow {}^1P_1$ [a]	$^1S_0 \leftrightarrow {}^3P_1$ [b]
^{168}Yb		1887.400(50)	4609.960(80)
^{170}Yb		1192.393(66)	3241.177(60)
^{171}Yb	*(centroid)*	939.523(39)	2780.55
	$1/2 \rightarrow 3/2$	832.436(50)	4759.440(80)
	$1/2 \rightarrow 1/2$	1153.696(61)	−1177.231(60)
^{172}Yb		533.309(53)	1954.852(60)
^{173}Yb	*(centroid)*	291.516(54)	1510.61
	$5/2 \rightarrow 3/2$	515.975(200)	4762.110(120)
	$5/2 \rightarrow 5/2$	−253.418(50)	3266.243(60)
	$5/2 \rightarrow 7/2$	587.986(56)	−1431.872(60)
^{174}Yb		0	954.832(60)
^{176}Yb		−509.310(50)	0

[a] Das *et al.*, 2005[140]

[b] Pandey *et al.*, 2009[141]

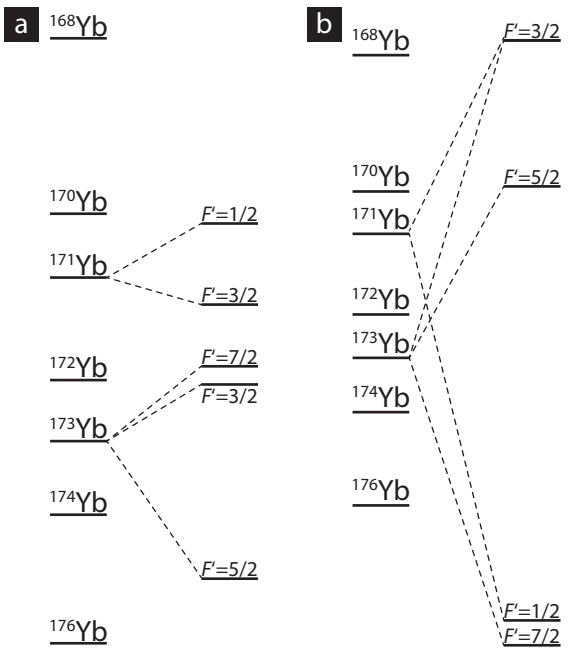

Figure 2.4 | Line structure of the $^1S_0 \leftrightarrow {}^1P_1$ and $^1S_0 \leftrightarrow {}^3P_1$ transitions of ytterbium. The isotope shifts and hyperfine structures summarised in table 2.4 are illustrated for the laser cooling transitions **(a)** $^1S_0 \leftrightarrow {}^1P_1$ and **(b)** $^1S_0 \leftrightarrow {}^3P_1$ of ytterbium.

Table 2.5 | Landé factors g_F of $^1P_1$ and $^3P_1$ hyperfine states for fermionic isotopes ^{171}Yb and ^{173}Yb.

Isotope	F	$g_F\left(^1P_1\right)$	$g_F\left(^3P_1\right)$
^{171}Yb	1/2	1.380	1.990 34
	3/2	0.690	0.995 30
^{173}Yb	3/2	−0.415	−0.597 64
	5/2	0.118	0.170 28
	7/2	0.295	0.426 26

in the weak-field regime. The resulting effective Landé factors are summarised in table 2.5. Figure 2.5 illustrates the resulting Zeeman splitting of the cooling transition for both bosonic and fermionic isotopes of ytterbium or any other AEL element. While the splitting is trivial and similar to that of the well known alkali elements for bosons, fermionic isotopes exhibit a distinctly different behaviour in the weak field regime. Its consequences for laser cooling will be discussed in more detail in chapter 5. Nevertheless, the splitting in the respective Paschen–Back regime, where ***I***–***J***-coupling is broken, is once again similar to figure 2.5b for the fermionic isotopes. Here, the additional nuclear spin degree of freedom of the fermions is left unchanged by absorption or emission of a photon, which is exploited in a proposed[143] scheme for nuclear spin–preserving sideband-cooling.

Decay into metastable states

The $^1S_0 \leftrightarrow {}^1P_1$ transition is not entirely closed. An atom decays from the excited state into the long-lived triplet states $^3P_0$ and $^3P_2$ (*cf.* section 2.5) via the triplet states $^3D_1$ or $^3D_2$ with a finite probability, as illustrated by figure 2.6a. As it is initiated by intercombination transitions, the overall leakage is small. Moreover, a fraction of the atoms branching into these ^3D states decays back to the ground state indirectly via $^3P_1$ and is usually not lost, *e.g.* from a MOT. A recent experimental study[146] has reported transition rates $W^{(s)}(^1P_1 \rightarrow {}^3P_0) = 5.96(197)\,s^{-1}$ and $W^{(s)}(^1P_1 \rightarrow {}^3P_2) = 0.42(14)\,s^{-1}$ which correspond to an overall branching probability into the metastable states of 3.5×10^{-8}.* A 3D-MOT can be operated without repumping atoms from the long-lived triplet states. Nevertheless, the presence of loss channels from the excited states constitutes a power-dependent contribution to the total loss rate of a MOT which has been studied by Loftus *et al.*,[147] who have observed a lifetime approaching $\tau = 800$ ms for weak excitation of the $^1S_0 \leftrightarrow {}^1P_1$ transition.

The composition of the available decay channels from the excited state $^1P_1$ varies greatly among the AEL elements, because it depends critically on the energies of the lowest D-states with respect to $^1P_1$. The main quantum numbers of the lowest available electronic d-orbitals in different elements can be lower than, equal to or – in the case of beryllium (Be) – even greater than that of the s-orbitals in the ground state. Decay of the excited state via any of the D-states is absent both in the light alkaline earth elements beryllium and magnesium (Mg), and in the transition metals, *e.g.* mercury, where the lower d-shells have already been filled, whereas for the heavy alkaline earth

*Unlike earlier experiments by Loftus *et al.*[147] and Honda *et al.*[148] these results are in agreement with the *ab initio* calculations of Porsev *et al.*[144] (see also figure 2.6).

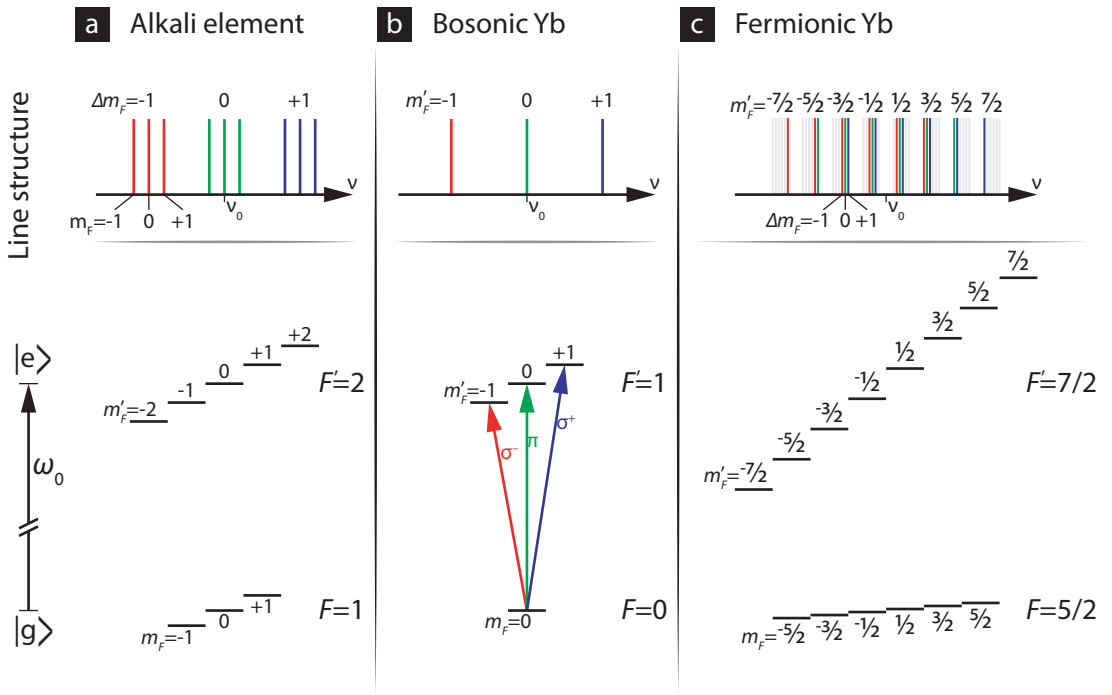

Figure 2.5 | Zeeman splitting of cooling transitions in ytterbium. The top row schematically shows the Zeeman splitting of transitions used for laser cooling in different elements, between states $|g\rangle$ and $|e\rangle$ with $F' = F + 1$ in a weak magnetic field. Sketches of the corresponding energy shifts of the magnetic substates are given in the bottom row. The colour of the individual spectral components indicates their polarisation as σ^+ (blue, $\Delta m_F = +1$), σ^- (red, $\Delta m_F = -1$) or π (green, $\Delta m_F = 0$). The subfigures represent different combinations of Landé factors g_F in the states $|g\rangle$ and $|e\rangle$. **(a)** In alkali elements the D-lines typically split into three groups with $\Delta m_F = 0, \pm 1$ as the Landé factors of the two states are nearly equal; their residual difference and nonlinear effects lift the degeneracy of these transitions. **(b)** A similar structure is found for the laser cooling transitions $^1S_0 \leftrightarrow {}^1P_1$ and $^1S_0 \leftrightarrow {}^3P_1$ in the bosonic isotopes of ytterbium, where $F = 0$ in the ground state. **(c)** For the fermionic isotopes, the large difference in the Landé factors results in a splitting of the line into $2F' + 1$ groups with a common magnetic substate m'_F in $|e\rangle$ governed by the magnetic moment of the excited state, which is on the order of the Bohr magneton μ_B, and a further splitting depending on the magnetic substate m_F in $|g\rangle$. A given substate of $|e\rangle$ can be addressed from no more than three substates in $|g\rangle$ ($|\Delta m_F| \leq 1$); nevertheless, the remaining energy differences are indicated in the top row in light grey, for clarity. The systems shown here corresponds to the $F = 5/2 \rightarrow F' = 7/2$ transitions in ^{173}Yb, but it is representative for all $^1S_0 \leftrightarrow {}^1P_1$ and $^1S_0 \leftrightarrow {}^3P_1$ hyperfine transitions of the fermionic isotopes ^{171}Yb and ^{173}Yb.

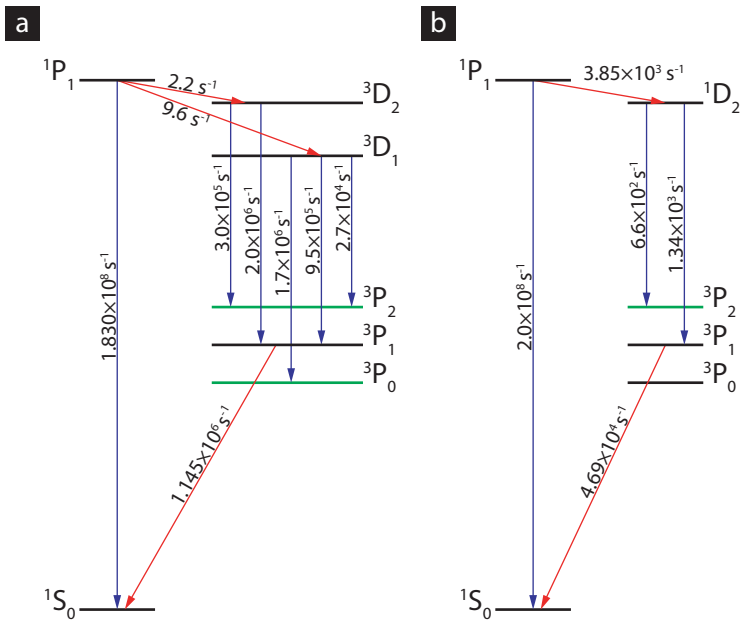

Figure 2.6 | Decay channels of the $^1P_1$ state in ytterbium and strontium allow leakage to the metastable states $^3P_0$ and $^3P_2$ through various intermediate D-states. **(a)** For ytterbium, shelving in the metastable states initiated by decay to $^3D_2$ and $^3D_1$ via intercombination transitions is the dominant leakage process. Transition rates are given for ytterbium.[138,139,144] **(b)** In the case of strontium, the singlet transition to $^1D_2$ causes far greater leakage, but predominantly populates the metastable state $^3P_2$. The transition rates reported[145] for strontium are given here. In both cases, a fraction of the atoms decays back to the ground state from the respective D states via $^3P_1$.

element barium (Ba), these states are actually the excitations with the lowest energies. In the case of the alkaline-earth elements calcium and strontium, the dominant loss channel is decay via the singlet state $^1D_2$. It is not only more than two orders of magnitude stronger than the decay to the triplet D-states, but qualitatively different as $^1D_2$ cannot decay into the non-magnetic long-lived state $^3P_0$ via an electric dipole (E1) transition – a third of the atoms decays into $^3P_2$, while the remainder returns to the ground state via $^3P_1$.[145] Although repumping of the $^3P_2$ state (see section 2.5) is often used to operate a MOT on the principal transition despite the presence of this leakage channel, the accumulation of atoms in $^3P_2$ has been exploited for magnetic[149,150] as well as magneto-optical trapping of metastable calcium using the $^3P_2 \leftrightarrow {}^3D_3$ transition,[151] and a similar technique is used for strontium.[81] Clearly, ytterbium is situated in an intermediate regime where the leakage from $^1P_1$ does not pose a significant problem, *e.g.* for the operation of a MOT, but can hardly be exploited either.

2.4.2 Intercombination transition

The isotope shifts and hyperfine structure of the $^1S_0 \leftrightarrow {}^3P_1$ transition are summarised in table 2.4 and illustrated in figure 2.4b with respect to the transition frequency[141]

$$\omega(^1S_0 \leftrightarrow {}^3P_1, {}^{176}\mathrm{Yb}) = 2\pi \times 539\,385\,606(10)\,\mathrm{MHz}$$

as reported by Pandey *et al.*[141] in a detailed investigation of this transition. Due to its narrow line width, all isotopes and hyperfine transitions are well resolved spectrally, and the Zeeman splitting of the intercombination transition is similar to that of the principal transition. Owing to the coupling of orbital angular momentum and spin, the total electronic Landé factor is given by[130] $g_J = 1.49282$. Therefore, operation of a MOT is not impeded by the hyperfine structure as in the

former case, but the unusual Zeeman splitting reduces the effective restoring force of the MOT (see section 5.9 for details). Furthermore, the intercombination transition $^1S_0 \leftrightarrow {}^3P_1$ is a near-perfect cycling transition.*

Temperature of an ytterbium intercombination MOT

Lowest temperatures of typically about 20 μK are observed[1,77,153,154] in intercombination MOTs of ytterbium. While temperatures as low as 12 μK have been reported,[155] other experiments[76,78,101,156–164] report slightly higher minimum temperatures, up to 70 μK, albeit not all of the latter were actually aimed at creating quantum-degenerate gases.

In stark contrast to the singlet transition, temperatures reported for intercombination MOTs of the fermionic isotopes[100,165] are comparable to those observed in the bosonic isotopes.† It has been found for both ytterbium and strontium that the MOT dynamics are consistent with Doppler cooling theory, but extra heating mechanisms exist, which cause the temperature of the MOT to rise an order of magnitude more strongly with intensity than expected in Doppler cooling theory.[121,167,168] Maruyama[121] attributes this behaviour to the non-trivial structure of the light field in a 3D-MOT[169] and trapping of atoms in light-shift micropotentials.[170] A study of heating mechanisms in strontium[171] concluded that the excess heating arises from sampling of intensity fluctuations, caused by imperfections in the MOT beams, by the atoms.

Magneto-optical trapping on a narrow transition

The strength of the intercombination transition $^1S_0 \leftrightarrow {}^3P_1$ varies significantly across the AEL elements, due to the different strengths of spin–orbit interaction (see section 2.3.1). For the lighter AEL elements, it is too weak to support a MOT against gravity,‡ whereas its line width is comparable to the alkali D-lines for mercury. In the case of ytterbium and strontium the intercombination transition is narrow, but still broad enough for magneto-optical trapping under the influence of gravity.

Nevertheless, MOTs using these narrow transitions exhibit a peculiar behaviour at large detuning. Here, the Doppler broadening is much smaller than the detuning and the trapped atoms become resonant only in a thin shell, where the detuning is balanced by the Zeeman shift of the trap. Under the influence of gravity, the sample occupies only the lower region of the enclosed volume. In extreme cases, some lasers do not even participate in cooling and trapping anymore. The temperature in this regime is nearly independent of the detuning, since it mainly determines the radius of the resonance shell. This kind of behaviour may be observed for ytterbium, but usually relatively small detuning and large magnetic field gradients, which suppress this behaviour, are used in the intercombination MOT. It is much more pronounced in strontium due to its narrower intercombination transition.[166]

---

*Other than via the intercombination transition to the ground state, the excited state can only decay into the metastable state $^3P_0$ via a very weak[152] magnetic dipole (M1) transition; this loss channel is usually completely negligible, *e.g.* during loading of a MOT.

†However, temperatures of down to 400 nK, *i.e.* below the photon recoil limit and close to the Doppler limit, have been observed[166] for an intercombination MOT of fermionic ^{87}Sr.

‡This problem can be overcome by quenching the excited state, which increases the retarding force significantly.[172]

2.4.3 Parity-violating transitions

Heavy AEL elements like ytterbium are studied intensively in the search for permanent electric dipole moments (EDMs) using atoms[114–116] or molecules.[117,118] Furthermore, it has been proposed by DeMille[107] that the nearly forbidden transition $^1S_0 \leftrightarrow {}^3D_1$ has a large E1 transition amplitude arising from PNC. Ytterbium is very favourable to study these effects due to its large number of stable isotopes. Several theoretical[107–109] and experimental[110–113] studies have investigated this transition, but experiments are not necessarily performed on cold atoms, but often in vapour cells. The transition amplitude caused by PNC is measured via interference with an additional amplitude induced by an electric field via the DC–Stark effect (see the publication by DeMille[107] for a detailed summary), and alternative methods, *e.g.* via polarisation rotation,[173] have been proposed. These studies demonstrate that atomic ytterbium is of great interest for precision measurements well beyond the scope of ultracold gases discussed in this thesis, but they require highly specialised setups.

2.5 Metastable states

The most interesting feature of ytterbium, and AEL elements in general, is the existence of the long-lived excited electronic states $^3P_0$ and $^3P_2$ that are connected to the ground state by ultranarrow transitions with line width of at most a few 10 mHz. The expected lifetimes of these states are summarised in table 2.6, and their decay mechanisms are discussed in more detail in sections 2.5.1 and 2.5.2.

While the ultranarrow $^1S_0 \leftrightarrow {}^3P_0$ clock transition may be used for ultraprecise spectroscopy of ultracold ytterbium in optical lattice potentials (see also chapter 7) and other applications, *e.g.* the creation of artificial gauge field[84,85] (see section 2.5.3), the metastable state $^3P_0$ itself allows the study of novel, strongly correlated quantum systems in periodic potentials (see section 2.5.4).

2.5.1 Radiative decay

The long natural lifetimes of the excited electronic states $^3P_0$ and $^3P_2$ stem from the lack of any strong E1 transitions to energetically lower states. Several theoretical studies[132,144,152,174] have investigated residual radiative decay of the metastable states in AEL atoms, but no experimental results have been reported for ytterbium, yet. Table 2.6 summarises the predictions of the most recent studies by Porsev *et al.*[144] and Porsev & Derevianko,[174] the former yielding similar results as the earlier publication by Migdalek & Baylis.[152] Considering radiative decay, the non-magnetic state $^3P_0$ is more stable than $^3P_2$, and aside from their lifetimes the features of both states are distinctly different.

As $^3P_0$ is the excited state with the lowest energy in ytterbium, it may only decay back into the ground state; however, the transition $^1S_0 \leftrightarrow {}^3P_0$ connects two states with total angular momentum $J = 0$. In the bosonic isotopes of any AEL element, it is thus strictly forbidden as a single-photon transition of any kind. In contrast, hyperfine interaction (HFI) between the total angular momentum $\boldsymbol{J}$ and nuclear spin $\boldsymbol{I}$ of the fermionic isotopes quenches the state $^3P_0$, as the eigenstates are perturbed and a small fraction of the radiatively decaying unperturbed eigenstate $^3P_1$ is admixed to the perturbed eigenstate $^3P_0$ (*cf.* the magnetically induced spectroscopy (MIS) method discussed in section 7.4). This results in a finite transition strength of the $^1S_0 \leftrightarrow {}^3P_0$ transition in fermionic

Table 2.6 | Natural lifetimes of the metastable states in ytterbium resulting from predicted[144] radiative decay rates of the triplet states $^3P_0$ and $^3P_2$, including quenching due to hyperfine interaction in the fermionic isotopes.[174] A compatible lifetime of 14.5 s for the unquenched $^3P_2$ has been predicted by a preceding work.[152] The natural lifetime of the state $^3P_0$ in bosonic isotopes arises solely from multi-photon decay processes.

State	Radiative lifetime τ/s		
	^{171}Yb	^{173}Yb	other
$^3P_0$	23 [a] ($F = 1/2$)	26 [a] ($F = 5/2$)	see text
$^3P_2$	15 [b] ($F = 5/2$)	15 [b] ($F = 9/2$)	15 [b]
	6.3[a,b] ($F = 3/2$)	7.2[a,b] ($F = 7/2$)	
		8.3[a,b] ($F = 5/2$)	
		11.4[a,b] ($F = 3/2$)	
		15 [b] ($F = 1/2$)	

[a] Porsev & Derevianko, 2004[174]

[b] Porsev *et al.*, 1999[144]

isotopes of AEL elements – in the particular case of ytterbium line widths of $\Gamma = 2\pi \times 7$ mHz and $\Gamma = 2\pi \times 6$ mHz have been predicted[174] for the isotopes ^{171}Yb and ^{173}Yb, respectively.* Radiative decay of this state in bosonic ytterbium isotopes is only possible via multi-photon processes, *e.g.* an E1–M1 two-photon transition[174] as indicated in figure 2.7a. The lifetime in these cases is therefore much longer than for any of the other cases of metastable states discussed in this section; to the author's best knowledge, neither experimental results nor any theoretical predictions have been published to date.

In contrast to $^3P_0$, the transition from the ground state to the second metastable state, $^1S_0 \leftrightarrow {}^3P_2$ ($\Delta J = 2$), is allowed, albeit only as a magnetic quadrupole (M2) or higher transition.† However, it is the state with the highest energy among the (6s6p) triplet states and may hence decay radiatively both into the metastable state $^3P_0$ via an electric quadrupole (E2) transition and into $^3P_1$ by an M1 transition. Figure 2.7b illustrates the available radiative decay channels including theoretical predictions of the transition rates.[152]‡ The magnetic dipole transition to $^3P_1$ is expected to be the

*In disagreement with these values, Porsev & Derevianko state these line widths as 43.5 mHz and 38.5 mHz both in the conclusion and abstract of their article.[174] This is in stark contrast to the results of a preceding publication[132] by Porsev *et al.* Comparison of the aforementioned line widths to the transition rates given in table IV therein suggests that the former are actually given as angular rather than ordinary frequencies, *i.e.* the correct units would have to be ms^{-1}. This conclusion is corroborated further by cross-referencing to transition rates from other studies cited in the table, *e.g.* the aforementioned publication[132] by Porsev *et al.* Therefore, I disregard the line widths explicitly stated by the authors in their publication[174] and instead use the values resulting from the transition rates listed in table IV therein.

†The summary discussion in this chapter is restricted to the dominant transition. Of course, higher-order transitions do exist, but they are mostly of negligible strength compared to the dominant channels (see also the publication by Derevianko[175]).

‡Throughout this thesis, in particular in table 2.6, the more recent publication[144] by Porsev *et al.* is used as reference. Its predictions are compatible with the preceding study[152] by Migdalek & Baylis. However, transition rates from the latter publication are given in figure 2.7b, because the former does not state any transition rates within the triplet system.

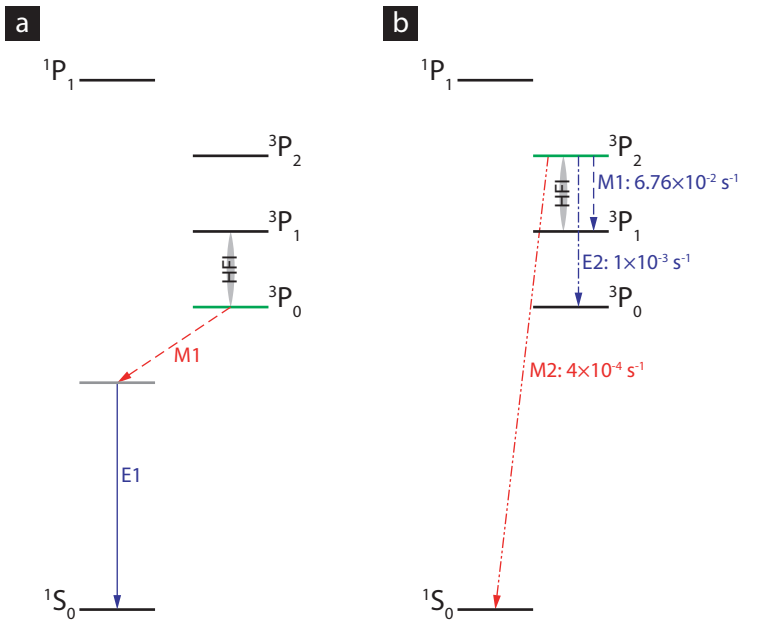

Figure 2.7 | Decay channels of the metastable states in ytterbium. (a) Radiative decay of the lowest triplet state $^3P_0$ is strictly forbidden as a single photon–decay in the bosonic isotopes. It is possible only via multi-photon processes, *e.g.* the indicated E1–M1 two photon decay.[174] For the fermionic isotopes, its lifetime is governed by hyperfine interaction (see section 2.5 for details). Coupling to $^3P_1$ is indicated as a grey ellipsis. **(b)** The other metastable state $^3P_2$ can decay to each of the energetically lower states via weak M1, M2 or E2 transitions as illustrated. Theoretical predictions[152] of the transitions rates are given for each transition. As in the case of $^3P_0$, hyperfine interaction (HFI) quenches the metastable state.

dominant decay channel compared to the much weaker quadrupole transitions. The metastable state is quenched due to hyperfine interaction in the fermionic isotopes, and the predicted transition rates[174] are of the same order of magnitude as the strongest decay channel of the unperturbed eigenstate (see table 2.6). Unlike the previously discussed state $^3P_0$, however, not all hyperfine states have a counterpart among the $^3P_1$ states that has the same total quantum number F, and those remain unaffected by quenching, because F is still a good quantum number. This results in the peculiar situation that the lifetime of the metastable state depends substantially on its total angular momentum F.

In conclusion, radiative lifetimes between seven and fifteen seconds are expected for the metastable state $^3P_2$. The lower state $^3P_0$ is expected to live for more than twenty seconds for the fermionic isotopes and much longer than that in case of the bosonic isotopes.

2.5.2 Non-radiative decay

Although the preceding discussion has been focussed on radiative decay, the environment of an atom naturally gives rises to a series of additional decay mechanisms. For instance, it has been reported[176] that quenching of the $^3P_2$ state by black-body radiation (BBR) – via excitation of the nearby ^3D states – reduces its lifetime in strontium by almost an order of magnitude at room temperature. However, the effect of BBR quenching is expected[174] to be negligible for ytterbium.

More importantly, losses from the metastable states arise from inelastic collisions with other ultracold atoms.* Understanding the prevalent processes is greatly simplified in the bosonic isotopes due to their lack of hyperfine structure, but their nature and strength depend sensitively on

*De-excitation of $^3P_0$ by collisions with background gas atoms has been studied experimentally,[111] but is of little relevance for ultracold gases, as collisions with atoms from the background gas are a limiting factor for the lifetime of any ultracold gas.

the internal states of the colliding atoms. Furthermore, they differ significantly between the AEL elements.

Early theoretical studies[177–179] investigated collisions of spin-polarised bosonic atoms in $^3P_2$. In particular, Kokoouline *et al.*[179] predicted inelastic losses due to Zeeman sublevel–changing (ZSLC) collisions, *i.e.* an inelastic relaxation of the Zeeman substates into a state with high moitonal angular momentum via an avoided crossing in the long-range molecular potential. However, experimental studies of ultracold calcium,[180] ytterbium,[181] and strontium[182] observed much higher inelastic collision rates than predicted by theory. A recent study[183] of $^3P_2$—$^3P_2$ collisions in ytterbium reported an average inelastic collision rate coefficient of $\beta_{in} = 4 \times 10^{-17}\ \mathrm{m^3\ s^{-1}}$. It was concluded from the weak spin-dependence of inelastic losses that they are not caused by ZSLC collisions, but rather by fine structure–changing (FSC) collisions to either of the energetically lower triplet states, $^3P_1$ and $^3P_0$, as well as principal quantum number–changing (PQNC) collisions.

In contrast, collisions of ground and metastable atoms, $^1S_0$—$^3P_2$, were found to exhibit usually much weaker inelastic collisions consistent with dominant ZSLC processes in the same study.[183] Since these inelastic collisions comprise the relaxation into a Zeeman sublevel of lower energy, they do not affect the lowest diatomic Zeeman substate, while the collision rate for the remaining states shows a clear dependence on the magnetic field. Uetake *et al.*[183] report inelastic collision rate coefficients β_{in} on the order of $10^{-18}\ \mathrm{m^3\ s^{-1}}$ for $m_J > -2$ at low magnetic field strengths and $10^{-20}\ \mathrm{m^3\ s^{-1}}$ for the lowest substate $m_J = -2$.

As of date, no similar investigations of inelastic processes involving the non-magnetic state $^3P_0$ have been reported for ytterbium, although collisions of fermionic ^{171}Yb in the metastable state $^3P_0$ have been studied in an OLC using a deep 2D optical lattice with a focus on elastic p-wave collisions.[184] Nevertheless, such inelastic collisions have been investigated for strontium. Traverso *et al.*[182] studied $^3P_0$—$^3P_0$ and $^3P_2$—$^3P_2$ collisions of metastable strontium in an ODT and found the $^3P_0$—$^3P_0$ inelastic collision rate coefficient to be about an order of magnitude smaller than for $^3P_2$—$^3P_2$ collisions. They point out that this suppression does not result solely from an absence of FSC collisions, because $^3P_0$ is the lowest of the ^3P states, but additionally from a suppression of PQNC processes as compared to $^3P_2$—$^3P_2$ collisions. A typical PQNC process for these states reads

$$(n\mathrm{s}\,n\mathrm{p})\,^3\mathrm{P}_J + (n\mathrm{s}\,n\mathrm{p})\,^3\mathrm{P}_{J'} \rightarrow (n\mathrm{s}^2)\,^1\mathrm{S}_0 + (n\mathrm{s}\,n{+}1\mathrm{s})\,^{2S+1}\mathrm{S}_S + \Delta E$$

where n is the principal quantum number of the valence shell, $J, J' = 0, 1, 2$ the total quantum numbers of the input states, $S = 0, 1$ the spin of the excited output state and ΔE the excess energy, *i.e.* of two colliding ^3P atoms one exits in the ground state $^1S_0$ and the other in either a singlet or triplet excited S-state. In the case of strontium, the conversion of two $^3P_2$ atoms into a ground $^1S_0$ state and a (5s6s) $^3S_1$ atom is energetically favourable, whereas the other channel, which yields a (5s6s) $^1S_0$ atom, as well as both channels in $^3P_0$—$^3P_0$ collisions are energetically unfavourable and hence suppressed. Therefore, the PQNC contribution to the inelastic collision rate is expected to be larger for $^3P_2$ than for $^3P_0$. Following this same line of thought in the case of ytterbium, using the energies listed in figure C.1, immediately leads to the conclusion that none of the aforementioned channels is suppressed there. The impact of these open PQNC channels remains subject to future investigations of inelastic collisions in ytterbium. Fortunately though, the inelastic $^3P_2$—$^3P_2$ collision rates reported[183] for ytterbium are much smaller than those observed[182] in strontium.

In another study, Lisdat *et al.*[185] observed an order of magnitude suppression of $^1S_0$—$^3P_0$ col-

lisions as compared to $^3P_0$—$^3P_0$ in a 1D optical lattice. Interestingly, there is a large discrepancy between the $^3P_0$—$^3P_0$ collision rate coefficients reported therein and by Traverso *et al.*,[182] which may – as suggested by Lisdat *et al.* – be a result of the different dimensionalities of the trap potentials.

With respect to the focus of this thesis on the metastable $^3P_0$ state, an investigation of both elastic and inelastic $^3P_0$—$^3P_0$ and $^1S_0$—$^3P_0$ collisions in ytterbium is a vital aspect of evaluating the feasibility and restrictions of experiments involving this metastable state. However, it is generally advisable to avoid large densities or multiple-occupancies in optical lattices for the metastable states, *e.g.* using $^3P_0$ or $^3P_2$ as the localised species for a realisation of the Kondo-lattice model (see chapter 8).

2.5.3 Ultranarrow transitions

The ultranarrow transitions $^1S_0 \leftrightarrow {}^3P_0$ and $^1S_0 \leftrightarrow {}^3P_2$ in the optical domain are one of the most important features of ytterbium and other AEL elements. As discussed in section 2.5.1, their finite transition strength arises from hyperfine interaction in the fermionic isotopes and – in the case of $^1S_0 \leftrightarrow {}^3P_2$ – a weak M2 amplitude. Furthermore, it may be created artificially by methods like magnetically induced spectroscopy (see section 7.4). The lifetimes of the metastable stats result in natural linewidth of no more than a few 10 mHz for ytterbium, and both transitions allow highly sensitive spectroscopy of ytterbium in the optical domain using the Rabi or Ramsey technique.

The $^1S_0 \leftrightarrow {}^3P_0$ transition ($\lambda_s = 578.42\,\mathrm{nm}$) is well suited as a clock transition, and it allows spectroscopy of neutral atoms trapped in optical lattices with unprecedented precision, *e.g.* in novel optical frequency standards. We plan to use this transition to probe and manipulate ytterbium quantum gases as discussed in more detail in chapter 7. Furthermore, ytterbium has been proposed for a variety of applications, ranging from the creation of artificial gauge potentials by dressing $^1S_0$ and $^3P_0$ with a single laser,[84,85] to an optical frequency knife[186] in forced evaporation or studies of atom–wall interactions[187] using laser-induced tunnelling between Wannier–Stark states.

In contrast, the $^1S_0 \leftrightarrow {}^3P_2$ transition exhibits a much higher sensitivity to external fields due to its highly susceptible excited state. While this is an undesired trait for optical frequency standards and ultrahigh precision spectroscopy, it allows local tuning of the resonance condition via magnetic field gradients. It has been proposed[89] for single-site addressing in a novel quantum computation scheme based on $^3P_2$ atoms, but also for addressing, detection and the implementation of quantum gates in several other proposed quantum computation schemes.[88,91] Furthermore, the recent realisation of optical magnetic resonance imaging (OMRI) by Kato *et al.*[188] demonstrates the adaption of well-proven precision spectroscopy techniques from other fields to the optical domain, *e.g.* for the study of quantum gases.

2.5.4 Applications of the metastable states

The metastable states provide a wealth of interesting opportunities, even without any direct use of the ultranarrow transitions. Similar to the different hyperfine ground states in alkali elements, they provide additional degrees of freedom, but in contrast to them the metastable states of ytterbium are excited electronic states. Therefore, many of their atomic properties, *e.g.* interactions, can be radically different from the ground state, and state-dependent potentials (see section 2.8) allow

simple and robust realisation of different optical potentials for either species.

Several proposed quantum computation schemes[88–91,189] use the metastable states, *e.g.* for storing or movinq qubits[88] as well as quantum gates including exchange,[190] interaction,[90] and lossy blockade schemes.[88,91] The lower metastable state $^3P_0$ shares some important features with the ground state $^1S_0$, such as the decoupling of its nuclear spin (see section 2.9), and has thus been proposed as an ideal candidate for the investigation of two-orbital SU(N)-symmetric spin Hamiltonians[92] or a prospective realisation of the KLM and studies of heavy-fermion materials in ultracold gases,[92–96] to name only a few examples. Furthermore, the metastable state in combination with dressing on the clock transition and laser induced-tunnelling in an anti-magic optical lattice (see section 2.8.3) has been proposed[84] as an alternative system for studies of artificial magnetic fields in periodic potentials. Therefore, the metastable state $^3P_0$ allows the investigation of a variety of systems and quantum phases that are also highly relevant *e.g.* for condensed-matter systems.

The other metastable state $^3P_2$ is quite different from $^3P_0$. For instance, it has a large magnetic dipole moment[130] ($J = 2$, $g_J = 1.50$) that has been used for magnetic trapping in other AEL elements.[149,150] However, $^3P_2$ is especially interesting due to the anisotropy of its interactions. Several theoretical studies[83,177–179] have investigated the effects of anisotropic electric quadrupole–quadrupole interaction, which is expected in addition to magnetic dipole–dipole interaction among $^3P_2$ atoms. They predict magnetic resonances of its elastic scattering length, caused by the appearance of bound state in the long-range potential itself. These resonances are in stark contrast to magnetically induced Feshbach resonances, which are familiar from alkali elements and result from the resonance with a bound state in another channel. These resonances may provide another way of controlling atomic interactions in quantum gases of AEL atoms (see section 2.6). Another recent theoretical study[83] has investigated the quantum phases arising from these quadrupolar interactions in optical lattices.

2.5.5 Pumping and cycling transitions

Several allowed dipole transitions from the $^3P_0$ and $^3P_2$ states into higher excited states provide the means to selectively address and manipulate the metastable states, *e.g.* to repump them to the ground state for detection. Here, mainly transitions to the ^3S and ^3D states are discussed in more detail, but applications of other transitions have been proposed, *e.g.* the use of the $^3P_0 \leftrightarrow {}^1P_1$ transition for a spin-preserving repumping mechanism in the Paschen–Back regime proposed for the fermionic isotopes by Reichenbach & Deutsch.[143]

The $^3P_{0,2} \leftrightarrow {}^3S_1$ transitions shown in figure 2.3 may be used to repump both metastable states back to the ground state via an intermediate decay to $^3P_1$. However, both transitions need to be driven, even if only a single metastable state is initially populated, since the excited state $^3S_1$ decays into all three triplet states $^3P_{0,1,2}$ with a ratio of 1: 3: 4.[144] Furthermore, the strong coupling of both metastable states to a common excited state may be used to engineer coherent coupling between the two metastable states, *e.g.* by a Raman transition or stimulated Raman adiabatic passage (StiRAP).

Furthermore, each of the metastable states $^3P_2$ and $^3P_0$ can be repumped to the ground state $^1S_0$ individually by a single laser using transitions to the ^3D states. The $^3P_2 \leftrightarrow {}^3D_2$ transition repumps atoms from the upper metastable state to the ground state via $^3P_1$, and the $^3P_0 \leftrightarrow {}^3D_1$ may be used for repumping from $^3P_0$ to $^1S_0$ in the same fashion, because the branching ratio of $^3D_1$ is favourable and less than three per cent of the atoms are expected[144] to decay into $^3P_2$ (see figure 2.6). This

convenient repumping mechanism for $^3P_0$ has already been demonstrated[59] for ^{171}Yb in an OLC. Recently, Olmos *et al.*[192] have predicted the emergence of strong dipolar interactions mediated by the exchange of photons on the $^3P_0 \leftrightarrow {}^3D_1$ transitions between AEL atoms in a suitable optical lattice.

The cycling transition* $^3P_2 \leftrightarrow {}^3D_3$ may be used for direct absorption or fluorescence imaging of the metastable state without any repumping to the ground state. It is especially interesting, if the visible transition to (6s6d) $^3D_3$ at $\lambda = 494$ nm can be used instead of the infrared transition to (6s5d) $^3D_3$ ($\lambda = 1798$ nm), since it allows a much higher resolution as well as use of the same camera as for absorption imaging from the ground state. An assessment of the branching ratios from that excited state into other potential decay channels is beyond the scope of this thesis; however, the analogous transition in strontium has been discussed by Stellmer[193] in some detail.

2.6 Atomic interactions

Atomic interactions† are critical both for the generation of and subsequent experiments with quantum-degenerate gases, *e.g.* fast rethermalisation during evaporative or sympathetic cooling requires large collision rates, but not large enough to cause excessive three-body losses. While magnetically induced Feshbach resonances are used to control the s-wave scattering length in many alkali elements, they are not available in the ground state of the AEL elements. However, different methods, *e.g.* optical Feshbach resonances (OFRs), may be used to control and provide novel ways of modifying the scattering length (see section 2.6.3).

The s-wave scattering lengths of ytterbium in its ground state are well known and summarised in table 2.7 (see also section 2.6.1). The large number of ytterbium isotopes provides a rich variety of interaction strengths and allows the investigation of quantum gases with a wide range of s-wave scattering lengths even without any active modification. Quantum-degeneracy may be achieved directly by evaporative cooling for many isotopes, especially ^{173}Yb and ^{174}Yb, and by sympathetic cooling with another isotope for most of the others.

In contrast, the interaction parameters of atoms in the metastable states are largely unknown (see section 2.6.2). In order to study novel quantum phases and phenomena proposed for these states, their interaction among each other and with ground state needs to be characterised in more detail in future experiments.

2.6.1 Interaction of ground state atoms

A comprehensive study of scattering properties in the ground state $^1S_0$ of ytterbium has been reported by Kitagawa *et al.*[194] Rather than performing direct measurements, they deduced the s-wave scattering lengths of all collision pairs from measurements of molecular binding energies via two-photon photoassociation (PA) spectroscopy. Their findings are summarised in table 2.7 and in reasonable agreement with the previous studies in individual isotopes (see their publication for details). As illustrated by figure 2.8, these scattering lengths can be described very well by a simple mass scaling model (see *ibid.*) using a single molecular potential for all isotopes.

*In calcium, the respective transition has been used to operate a MOT from the metastable state.[151]

†They are usually restricted to s-wave scattering in the ultracold regime, because higher partial waves are frozen out due their centrifugal barrier.

Table 2.7 | s-wave scattering lengths *a* of ytterbium at zero energy for all homo- and heteronuclear combinations.

a/nm	^{168}Yb	^{170}Yb	^{171}Yb	^{172}Yb	^{173}Yb	^{174}Yb	^{176}Yb
^{168}Yb	13.33(18)	6.19(8)	4.72(9)	3.44(10)	2.04(13)	0.13(18)	−19.0(16)
^{170}Yb		3.38(11)	1.93(13)	−0.11(19)	−4.30(36)	−27.4(27)	11.08(12)
^{171}Yb			-0.15(19)	−4.46(36)	−30.6(32)	22.7(7)	7.49(8)
^{172}Yb				-31.7(3.4)	22.1(7)	10.61(12)	5.62(8)
^{173}Yb					10.55(11)	7.34(8)	4.22(10)
^{174}Yb						5.55(8)	2.88(12)
^{176}Yb							-1.28(23)

Source: Kitagawa *et al.,* 2008[194]

Detailed knowledge of the scattering lengths readily allows an assessment of the most suitable candidates for achieving quantum degeneracy and optimal cooling strategies. ^{168}Yb, ^{170}Yb, ^{173}Yb, and ^{174}Yb are well suited for evaporative cooling, and the latter two have actually been cooled to quantum degeneracy in the course of this thesis (see sections 6.5 and 6.6). For two more isotopes, the weakly attractive* bosonic ^{176}Yb and the almost non-interacting fermionic ^{171}Yb, sympathetic cooling is required, *e.g.* with the most abundant isotope ^{174}Yb. Other suitable coolant species are the remaining three isotopes which can be cooled evaporatively, but they typically suffer from lower initial particle numbers, partially due to their lower abundances. Naturally, sympathetic cooling is not restricted to isotope mixtures, but may be implemented using a second species, and it may be an interesting option for other isotopes, as well. All of the aforementioned isotopes have first been cooled to quantum degeneracy in the group of Yoshiro Takahashi[76,100–103] using these strategies. However, the last isotope, ^{172}Yb, has never been cooled to quantum degeneracy despite being the second-most abundant one, because it suffers from strong attractive interactions, which result in low critical particle numbers for an interaction-induced collapse.

With respect to the study of ultracold gases, ytterbium provides a variety of interaction strengths to work with, in particular regarding the spinless bosonic isotopes. Moreover, the two fermionic isotopes exhibit quite complementary interaction strengths. While the spin components of ^{171}Yb are almost non-interacting, strong interactions are readily realised in ^{173}Yb. However, to ascertain their suitability for specific applications, a careful and detailed analysis is required. For most applications, interactions beyond the ground state are highly relevant and the fermionic nature of these two isotopes has to be kept in mind.†

2.6.2 Interaction of metastable atoms

Elastic interactions of atoms in the metastable state $^3P_0$, either among each other or with atoms in the ground state, have not yet been investigated in detail for ytterbium (see also section 2.5.2). In general, the s-wave scattering lengths of $^3P_0$ atoms can be expected to be virtually independ-

*In an isotope mixture with ^{174}Yb, the repulsive interaction of both species actually stabilises ^{176}Yb against an interaction-induced collapse.[195]

†In particular, the interaction shifts of atomic transitions are not as might be expected naïvely (see the Varenna lecture notes of Ketterle & Zwierlein[196] for a detailed discussion).

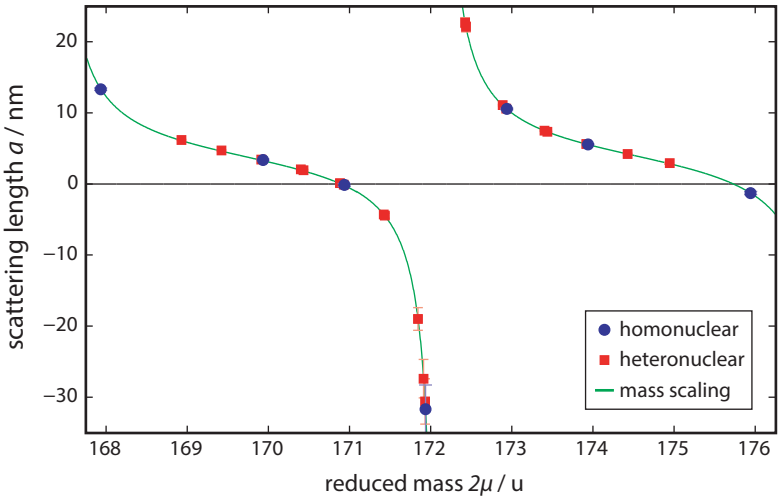

Figure 2.8 | Mass scaling of the s-wave scattering lengths in ytterbium. Plotted as a function of the reduced mass μ of the colliding atoms, the s-wave scattering lengths a deduced by Kitagawa *et al.*[194] coincide well with a simple mass scaling model (see *ibid.*). The resonance near $2\mu \approx 172$ u signals the appearance of a 72nd bound state in the scattering potential.

ent from those of the ground-state atoms, since different electronic states are involved. For instance, Yamaguchi *et al.*[162] used high-precision spectroscopy of a bulk BEC on the ultranarrow $^1S_0 \leftrightarrow {}^3P_2$transition to detect interaction shifts of the transition frequency and deduced a scattering length of $a = -33(10)$ nm for $^1S_0$—$^3P_2(m_J = 0)$ interactions in ^{174}Yb (*cf.* table 2.7). This measurement for the metastable state $^3P_2$ clearly demonstrated the potential of using the clock transition to detect interaction shifts (see chapter 7), as it benefits directly from such large differences of the s-wave scattering lengths.

Interactions in a $^1S_0$—$^3P_0$ system are less complex than those involving $^3P_2$ atoms, because the total angular momentum J of both states vanishes and the nuclear spin is expected[92] to be decoupled rather well in both states for the fermionic isotopes, *i.e.* interactions are independent of their nuclear spin state (see section 2.9). However, two fermionic atoms of the same isotope are indistinguishable and may be in an anti-symmetric electronic superposition state if their nuclear spin state is symmetric and *vice versa*. In contrast, bosonic ytterbium atoms may only be in symmetric superposition state, since they have no nuclear spin degree of freedom. Therefore, the s-wave interactions of $^1S_0$ and $^3P_0$ atoms are expected to be characterised by up to four scattering parameters a_{gg}, a_{ee}, and $a_{eg}^{\pm}$ (see Gorshkov *et al.*[92] for details). A thorough investigation of $^1S_0$—$^3P_0$ and $^3P_0$—$^3P_0$ interactions in order to measure these interaction parameters for the different isotopes and verify their independence from the nuclear spin state will be essential for further studies of multi-component quantum gases of ytterbium.

Kato *et al.*[197] have recently studied the $^1S_0$—$^3P_2$ interactions in a three-dimensional optical lattice and demonstrated the existence of magnetic Feshbach resonances in particular collision channels (see section 2.6.3). Their findings correspond to scattering lengths at vanishing magnetic field of $a(B = 0) = -25(14)$ nm for $^1S_0$—$^3P_2(m_J = +2)$ interactions in ^{174}Yb and $a(B = 0) = 18(3)$ nm for $^1S_0$—$^3P_2(m_J = -2)$ interactions in ^{170}Yb. Several theoretical studies[177–179] have investigated $^3P_2$—$^3P_2$ collisions, although not specifically for ytterbium, and predict substantial dipolar and quadrupolar contributions.

2.6.3 Modification of the scattering lengths

In many alkali elements, magnetic Feshbach resonances are routinely used to tune the scattering length across a large range. Feshbach resonances occur when a rovibrational bound state of a closed channel is tuned into resonance with a colliding pair of atoms, and in most cases a magnetic field is used to control the detuning of a different dimer state of ground state atoms (see the review by Chin *et al.*[198]). This well-proven technique cannot be used for bosonic ytterbium in the ground state,[199] but OFRs[200] allow laser-induced tuning of the scattering length. Furthermore, several types of magnetic resonances have been proposed or demonstrated for the metastable state $^3P_2$.

Optical Feshbach resonances

In the case of ground state atoms, OFRs can be used to modify the scattering lengths. The closed channel of an OFR is an excited electronic dimer state. A near-resonant laser beam may be used to tune it into resonance with the input channel of the colliding ground state atoms, as is readily understood in a dressed state picture. Unlike in magnetic Feshbach resonances, where the closed channel dissociates into a pair of ground state atoms, the finite lifetime of the closed channel due to spontaneous decay introduces losses, *i.e.* the scattering length becomes complex in the vicinity of the resonance (see the review by Chin *et al.*[198]). After the original proposal,[200] initial experiments were performed for alkali elements,[201–203] but these systems suffer from strong losses, as the employed transitions are rather broad. Using the narrow intercombination transitions of AEL atoms, OFRs introduce much smaller losses, as first pointed out by Ciuryło *et al.*[199] and later demonstrated for ytterbium by Enomoto *et al.*[204] However, efficient implementation requires an intimate knowledge of the PA spectra of the respective transition, as this figure of merit is determined by the detuning from the resonance and ultimately limited by other nearby PA transitions (see the article by Ciuryło *et al.*[199] for instance). Borkowski *et al.*[205] have published a detailed theoretical study focussing on possible OFRs in ytterbium.

Although the losses induced by OFRs are a drawback compared to magnetic Feshbach resonances, they have great potential. Global modification of the scattering length using an OFR was recently demonstrated[206] for ^{88}Sr, but they also provide the means to engineer the scattering length locally by shaping the intensity of the light field accordingly. This novel degree of control allows a vast number of applications, *e.g.* by local quenching of a quantum gas in an optical lattice using a focussed beam. Yamazaki *et al.*[207] have proposed the use of standing-wave OFR laser fields to introduce spatial modulation of the interaction at a sub-wavelength scale. In combination with the well known techniques to create optical lattices and far-detuned optical lattices themselves this allows great experimental flexibility, *e.g.* to create disorder by modulation of interactions or dynamically shift the modulation by modulating the phases of the beams forming the standing wave. Furthermore, the use of OFRs has been proposed to mediate nuclear spin exchange in fermionic isotopes of AEL elements and thereby implement entangling quantum gates.[208]

OFRs are not restricted to s-wave interactions, however. p-wave OFRs in fermionic ^{171}Yb have been proposed to study novel quantum phases and types of superfluidity,[209] and their existence has recently been demonstrated experimentally.[210]

Hence, OFRs are a highly intriguing feature in AEL atoms with numerous prospective applications, especially if they are combined with optical lattices, ultrahigh-precision spectroscopy (see chapter 7), and other techniques of engineering and probing quantum gases.

Magnetic resonances in the metastable state $^3P_2$

Beyond its large magnetic dipole moment, the anisotropy of atomic interactions, caused by a sizeable electric quadrupole contribution (see also section 2.5), is one of the intriguing features of the metastable state $^3P_2$, and it gives rise to several novel methods of using magnetic fields to modify the collision properties in ytterbium resonantly. Several theoretical studies[177–179] of $^3P_2$—$^3P_2$ collisions (see *ibid.*) in AEL atoms have predicted magnetic resonances of the scattering lengths due to the appearance of bound states in the long-range molecular potential of the metastable atoms. This phenomenon has not been observed experimentally for any AEL element yet, but its investigation is highly interesting, as this phenomenon is a characteristic effect of the anisotropic interactions of atoms in the $^3P_2$ state, despite its apparent similarity to the well known Feshbach resonances.

In an investigation of $^1S_0$—$^3P_2$ interactions using high-precision spectroscopy, Kato *et al.*[197] have recently observed another type of Feshbach resonance in several bosonic isotopes of ytterbium. In this case, the anisotropy of interactions, which is introduced by the metastable state $^3P_2$, allows coupling of partial waves of different motional angular momenta l, if the total projection of angular momenta onto the quantisation axis is preserved, *i.e.* $m_{J,1} + m_{J,2} = m'_{J,1} + m'_{J,2} + m_l$ for an s-wave entrance channel. A bound state within the centrifugal barrier of a channel with higher angular momentum may thus cause a Feshbach resonance in the entrance channel and modify the scattering length according to[198]

$$a(B) = a_{\mathrm{bg}} \cdot \left(1 - \frac{\Delta B}{B - B_0}\right) \tag{2.5}$$

where a_{bg}, ΔB, and B_0 are the background scattering length, the width of the resonance, and the resonance field strength. Kato *et al.*[197] report two resonances, for interactions of the ground state with $^3P_2(m_J = +2)$ in ^{174}Yb and $^3P_2(m_J = -2)$ in ^{170}Yb. Although they are rather narrow ($\Delta B \approx 2$ G), both resonances occur at remarkably low magnetic fields ($B_0 \sim 1$ G) and thus modify the scattering lengths in weak fields considerably (*cf.* also the derived scattering lengths given in section 2.6.2). If inelastic collisions are kept small, *e.g.* in spin states which are immune to ZSLC collisions (see section 2.5.2), these resonances may allow tuning of the scattering lengths in a variety of applications. As pointed out by Kato *et al.*,[197] these include the case of spin-polarized fermionic gases and mixtures of AEL atoms in the metastable state $^3P_2$ with alkali atoms, such as rubidium (*cf.* the predicted magnetic Feshbach resonances of ground state AEL and alkali elements discussed in section 2.7.3).

2.7 Mixtures of ytterbium and rubidium

Ultracold mixtures of ytterbium and alkali atoms are highly interesting systems due to the fundamentally different electronic structure of these elements. The apparatus presented herein has been developed to study ultracold mixtures of ytterbium and rubidium in future experiments. In addition to species-specific optical potentials (*cf.* the discussion of state-dependent optical potentials in section 2.8), which have already been proposed for heteronuclear alkali mixtures,[211] a unique feature of these systems is the ability to selectively confine and manipulate rubidium by means of magnetic and RF fields that affect ytterbium neither in its ground state nor in the metastable state $^3P_0$. For instance, a magnetic field gradient may not only be used to compensate their differential

gravitational sag, but also allows dynamic control of their spatial overlap, as has been demonstrated by Hansen *et al.*[212]

2.7.1 Assisted cooling of ytterbium

Combining ytterbium with rubidium provides an intriguing route to accessing extremely low-temperature or low-entropy regimes, in addition to the investigation of ultracold mixtures. Sympathetic cooling of ytterbium by rubidium has already been demonstrated experimentally[164] and may be used to produce larger and colder samples of ytterbium. Here, rubidium may be used either as a substitute for ^{174}Yb in sympathetic cooling of the weakly interacting isotopes (see section 2.6.1), or to cool the other isotopes sympathetically instead of evaporatively and suppress particle loss in the final cooling stages.[*] The latter is especially appealing for isotopes that usually suffer from low initial particle numbers, *e.g.* due to low abundances. Another, highly interesting option is the use of entropy exchange[213] to actively reduce the entropy of an ytterbium quantum gas, *e.g.* after loading into a deep, but species-selective optical lattice, by transfer to a rubidium reservoir.

2.7.2 Laser cooling of ytterbium and rubidium

Several effects inflicting significant losses on either species unfortunately hinder simultaneous magneto-optical trapping of ytterbium and rubidium.

An ytterbium MOT using the principal transition $^1S_0 \leftrightarrow {}^1P_1$ is capable of photoionising rubidium by excited-state absorption (see the compendium by Sansonetti & Martin[124]) and thus causes additional losses from the rubidium MOT. It has been demonstrated[136,214] in the research group of Axel Görlitz that simultaneous MOTs may still be operated, but in those experiments the presence of ytterbium cooling light reduced the particle number of the rubidium MOT by about a factor of two. Similar photoionisation-induced losses and a measurement of its cross-section have recently been reported for Rb-Sr mixtures.[215] In fact, the problem occurs for quite a few combinations of AEL and alkali elements, *e.g.* the ionisation threshold of the rubidium $5^2P_{3/2}$ state corresponds to a wavelength of 479 nm, whereas in lithium (Li) it is large enough to prevent similar ionisation processes for the principal transitions of ytterbium and most other AEL elements.

Although the intercombination transition $^1S_0 \leftrightarrow {}^3P_1$ of ytterbium does not cause photoionsiation of rubidium, severe losses of ytterbium have been observed[216] in a simultaneous MOT of both species. Nemitz *et al.*[216] report a reduction of the ytterbium particle number by more than an order of magnitude and attribute these losses to light-induced collisions of excited Yb* with rubidium.[†]

Concerning the 2D-/3D-MOT discussed in this thesis, we therefore expect a simultaneous operation of MOTs for ytterbium and rubidium to be impractical and plan to prepare both species sequentially. Photoionisation of rubidium in the 2D-MOT stage of our setup is avoided in this scheme as well, but it may become a significant problem for simultaneous operation of the 2D-MOTs, because the ytterbium cooling beams are operated at high intensities.

[*] Evaporation in magnetic traps typically takes much longer than in optical traps, whereas lifetimes in deep optical traps are shorter than in magnetic traps. Sympathetic cooling with rubidium is thus mostly an option for the final steps of cooling.

[†] Nemitz *et al.*[216] use ^{87}Rb and two different bosonic isotopes of ytterbium, ^{174}Yb and ^{176}Yb, in their measurements. It is not reported whether any isotope-dependence has been observed.

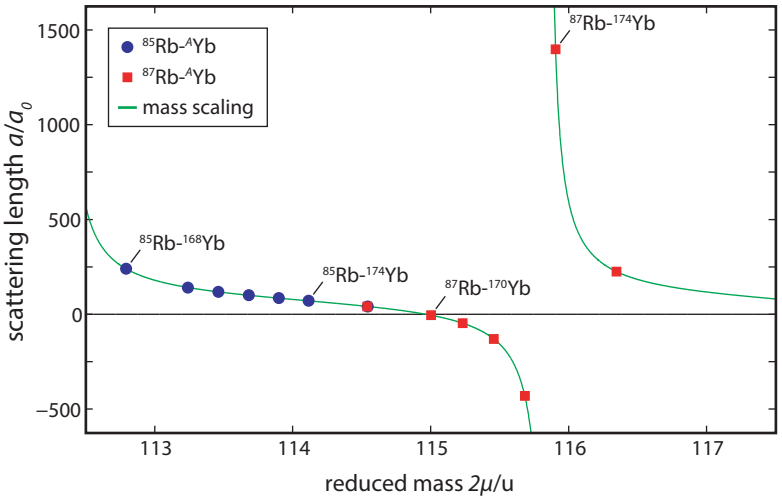

Figure 2.9 | s-wave scattering lengths of rubidium and ytterbium reported by Münchow[219] are plotted as a function of the reduced mass μ. As illustrated by a simple mass scaling model (see figure 2.8) the anomalously large scattering length of ^{87}Rb—^{174}Yb interactions is caused by the appearance of an additional bound state.

2.7.3 Interactions of ytterbium and rubidium

Mixing ytterbium and rubidium introduces another set of atomic interactions. They are essential for experimental applications of these mixtures, ranging from sympathetic cooling to the stability of quantum-degenerate mixtures, and knowledge of the interaction parameters is crucial for assessing the prospects of specific combinations of isotopes.

Thermalisation rates of ^{87}Rb and the five isotopes ^{170}Yb, ^{171}Yb, ^{172}Yb, ^{174}Yb, ^{176}Yb at temperatures of several 10 µK have been studied by Tassy *et al.*,[164] concluding that sympathetic cooling is possible for ^{174}Yb and ^{176}Yb (see also Tassy[214]). However, later experiments by Baumer *et al.*[217] have found ^{87}Rb and ^{174}Yb to be immiscible at temperatures of a few microkelvins indicating an extremely large s-wave scattering length. Several extensive studies of s-wave interactions in Rb-Yb mixtures based either on thermalisation rate measurements or PA spectroscopy to deduce the molecular potential parameters have been reported,[218–220] and they agree quite well with each other and with other experimental data. As illustrated in figure 2.9, the scattering lengths of ^{87}Rb with different isotopes of ytterbium vary strongly, crossing zero in the vicinity of ^{87}Rb—^{170}Yb, whereas moderate, positive scattering lengths are expected for interactions of ^{85}Rb with all ytterbium isotopes.

The existence of magnetic Feshbach resonances of rubidium and ytterbium atoms in the ground state has been expected in the community for some time. While they have not yet been observed experimentally, several studies[219,220] have predicted the positions of a series of Feshbach resonances in various isotope combinations. Resonances involving ^{87}Rb are expected to occur only at very large field strengths of typically several kilogauss, whereas most ^{85}Rb resonances are predicted at moderate magnetic field strengths of one kilogauss and less. Unfortunately, all of these resonances have relative widths on the order of a few 10^{-6} or less, corresponding to widths of no more than a few 10 mG, and especially the accessible ^{85}Rb resonances are much narrower according to these predictions.[220] Accessing any of these resonances experimentally will therefore be extremely challenging.

Interactions of rubidium and ytterbium in any of its metastable states have not been investigated of date, but Kato *et al.*[197] point out the possibility of magnetic Feshbach resonances similar to those found in $^1S_0$—$^3P_2$ interactions of ytterbium (see section 2.6.3).

2.7.4 Related research

Several research groups study Rb-Yb and other mixtures of AEL and alkali elements. Many of these experiments are focussed on the creation and study of ultracold polar molecules formed by AEL and alkali atoms, which are fundamentally different from those created by either group on its own. In particular, it is the presence of an unpaired electron that gives rise to a $^2\Sigma$ ground state configuration and thus a residual spin degree of freedom of the molecular ground state. Open-shell molecules like these are excellent candidates for the realisation of lattice-spin models, and topologically ordered states in these systems have been proposed for a new type of quantum computing.[221] Due to this spin degree of freedom, these molecules have a magnetic dipole moment in addition to the EDM, which is familiar from heteronuclear alkali molecules. A large EDM of almost one debye has been predicted for YbRb,[222] whereas LiYb is expected to exhibit a fairly small EDM in comparison.[223,224]

In the on-going search for an EDM of the electron, it has been realised early that heavy polar molecules[225] are well suited for these experiments due to the enhancement of the EDM by s–p-hybridisation, as observed previously for single atoms.[226] First experimental results have been reported for YbF using a thermal beam,[117] but YbRb as well as other molecules of ytterbium and neutral atoms or ions with single valence electron have been proposed for experiments at ultralow temperatures. The production of YbRb in an excited electronic state by PA using the D1-transition of rubidium at 795 nm has already been demonstrated experimentally.[216]

Simultaneous quantum degeneracy has been realized in Li-Yb mixtures[77,227] and more recently in Rb-Sr mixtures.[228] These experiments demonstrate the wide range of mass ratios that is accessible by this family of mixtures. In particular, Li-Yb mixtures are expected to be well suited to study novel phenomena arising in mixtures with large mass ratios, such as the influence of mass ratios on three-body dynamics,[229] novel trimer states,[230] and novel quantum phases, *e.g.* a crystalline phase in mass-mismatched Fermi mixtures.[231]

2.8 State-dependent potentials

The potential experienced by an atom in ODT or lattice depends on its electronic state (see section 2.8.1). Owing to its metastable states, the resulting state-dependent potentials are a powerful tool in any experiment using ytterbium quantum gases. The AC–Stark shifts of the ground state $^1S_0$ and metastable state $^3P_0$ are illustrated in figure 2.10. A wide range of relative potential depths can be realised by tuning the laser wavelength. The most interesting special cases of equal depths at magic wavelengths (see section 2.8.2), equal but opposite depths at anti-magic wavelengths (see section 2.8.3), and state-selective potentials ,where one of the states in unaffected by the ODT (see section 2.8.4), are discussed below. Similar, species-dependent potentials have been proposed[211] in the more general context of ultracold mixtures, *e.g.* of alkali elements.

In combination with shelving of atoms in the metastable states and coherent coupling to the ground state via ultranarrow transitions, state-dependent potentials are a crucial part of many potential applications of ytterbium, including ultraprecise spectroscopy on the clock transition in an optical lattice (see also chapter 7), quantum simulation of the Kondo lattice model[93,94] or two-orbital SU(N) magnetism,[92] studies of artificial gauge potentials in optical lattices,[84,85,232] and schemes for quantum computation with AEL atoms.[88,91]

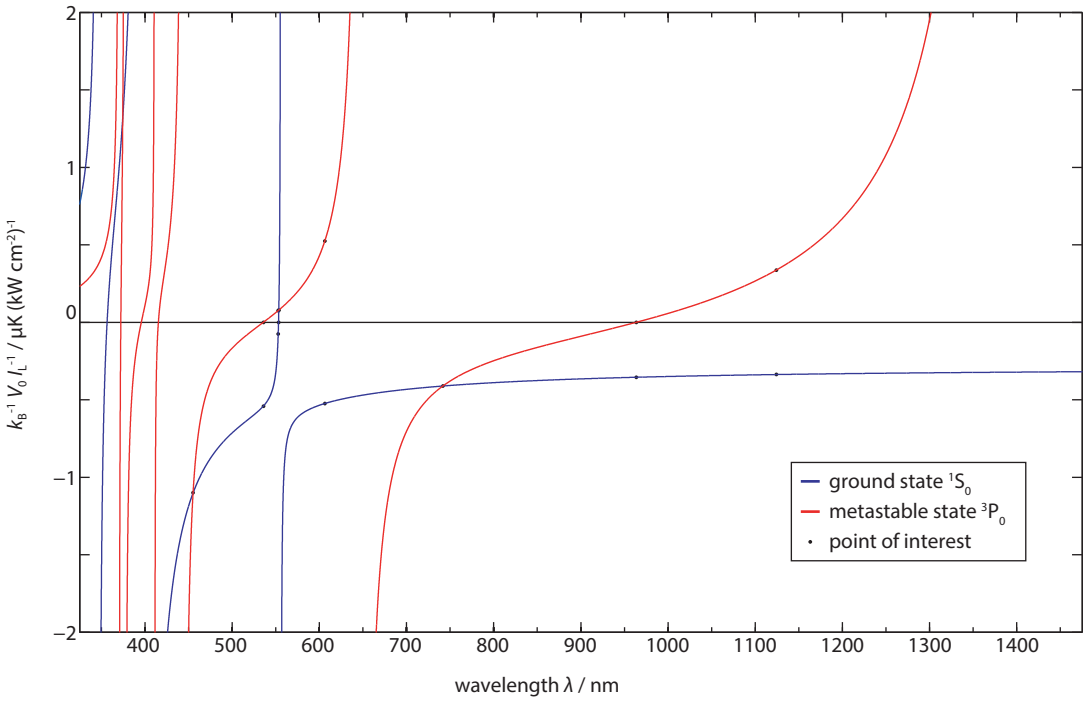

Figure 2.10 | AC–Stark shifts of $^1S_0$ and $^3P_0$ in bosonic ytterbium have been calculated as discussed in appendix C including the contributions of the lowest-energy and several higher transitions as compiled by Barber.[158] Some examples of magic, anti-magic and state-selective wavelengths have been marked as points of interest, but the exact wavelengths are not predicted very accurately. Nevertheless, the model is sufficient to determine the absolute depths of optical potentials, *e.g.* the ODTs discussed in chapter 6, with reasonable accuracy.

2.8.1 AC–Stark polarisabilities of ground and metastable states

Optical potentials have become a ubiquitous and well known tool in studies of quantum gases. These potentials, ranging from simple trapping to multi-dimensional lattice potentials, may be engineered precisely and nearly free of any defects by focussing and interfering laser beams. (A detailed introduction is given in the review by Grimm *et al.*[233])

The second-order AC–Stark effect, which is proportional to the intensity $I_\mathrm{L}(\boldsymbol{r})$ of the laser field, is the dominant source of these potentials, and in a perturbative approach it may be understood as a stimulated absorption from and immediate re-emission of a photon into the laser field. The contribution of a single excited state $|\gamma'\rangle$ to the AC–Stark shift of an atomic state $|\gamma\rangle$ in the electromagnetic field of a laser with frequency ω_L and the rate of spontaneous photon scattering from the beam are given by[142,233]

$$V_\mathrm{D}(\boldsymbol{r}) = -\frac{3\pi c^2}{2{\omega_0}^3}\left(\frac{\Gamma}{\omega_0-\omega}+\frac{\Gamma}{\omega_0+\omega}\right) I_\mathrm{L}(\boldsymbol{r}) \tag{2.6}$$

$$\Gamma_\mathrm{sc}(\boldsymbol{r}) = \frac{3\pi c^2}{2\hbar{\omega_0}^3}\left(\frac{\omega}{\omega_0}\right)^3\left(\frac{\Gamma}{\omega_0-\omega}+\frac{\Gamma}{\omega_0+\omega}\right)^2 I_\mathrm{L}(\boldsymbol{r}) \tag{2.7}$$

where ω_0 and Γ are the resonance frequency and line width of the transition to the excited state, provided that $|\gamma'\rangle$ predominantly decays back into $|\gamma\rangle$ (see appendix C for a detailed and more formal discussion of atomic polarisabilities). In the case of far–off-resonant detuning, and in particular in order to predict the magic wavelengths, the counter-rotating terms in equations (2.6) and (2.7) must not be neglected (*cf.* the discussion for a moderately detuned laser in the review paper by Grimm *et al.*[233]). For a qualitative understanding of the AC–Stark shifts in the ground and metastable states of ytterbium at visible and near-infrared (NIR) wavelengths, it is hence sufficient to consider only the least-energetic allowed dipole transitions from these states.

Figure 2.10 illustrates the results of a quantitative estimation of AC–Stark shifts in the ground and lower metastable states as a function of wavelength in this spectral region. The polarisability of the ground state is dominated by its principal transition $^1S_0 \leftrightarrow {}^1P_1$at the violet edge of the visible spectrum. In the spectral region of interest, it gives rise to an attractive, slowly varying optical potential, whereas the metastable state $^3P_0$ has two E1 transitions, $^3P_0 \leftrightarrow {}^3S_1$ at $\lambda = 649\,\mathrm{nm}$ and $^3P_0 \leftrightarrow {}^3D_1$ at $\lambda = 1389\,\mathrm{nm}$, in this spectral region. Hence, its AC–Stark shift varies across a wide range, it usability is limited solely by the tolerable rates of photon scattering. Furthermore, both a magic and an anti-magic wavelength as well as a zero-crossing, *i.e.* a state-selective wavelength, exist in between these resonances.

The $^1S_0 \leftrightarrow {}^3P_1$transition of the ground state gives rise to a sharp spectral feature. Due to its narrow line width, its contribution to the overall AC–Stark shift far off resonance is minor. Nevertheless, optical traps may be operated at small absolute detuning from the intercombination transition without excessive photon scattering, for the diverging terms in equations (2.6) and (2.7) are functions of the relative detuning from a transition with respect to its line width. In combination with the background contribution of the principal transition, another state-selective wavelength exists on the blue-detuned side of the resonance, where the ground-state polarisability crosses zero.

Although the qualitative picture presented above is obviously able to predict the existence of several notable wavelengths, their exact positions depend sensitively on the background contributions of transitions in ultra-violet (UV) region, *i.e.* to higher excited states. They are best measured experimentally by extrapolating from a wavelength scan, since most calculations are only able to provide an initial estimate (*cf.* the results reported by Dzuba & Derevianko[234] and Guo *et al.*[235]). For the purposes of this thesis, in particular designing the optical dipole traps (see chapter 6), a calculation of the AC–Stark shift based on available experimental and theoretical data is sufficient.

2.8.2 Magic-wavelength lattices

Optical lattices at magic wavelengths are essential for ultrasensitive spectroscopy of ultracold gases. Regarding AEL elements, magic wavelengths usually refer to crossings of the AC–Stark shifts of ground and metastable states. While ordinary optical potentials induce both line pulling and broadening of the ultranarrow transition between those states, its main differential light shift is cancelled at these wavelengths, and spectroscopic measurements may be performed with ultrahigh-precision even in extremely deep optical lattice potentials. As first pointed out by Katori[33] in his proposal for an optical lattice clock (OLC), the magic optical lattice may then in turn be used to confine atoms in the Lamb–Dicke regime,[236] *i.e.* both recoil- and Doppler-free spectroscopy is possible (see chapter 7 for further details).

When low-dimensional anti-magic or state-selective lattices are employed, a magic lattice may

Table 2.8 | Measured magic frequencies for the clock transition $^1S_0 \leftrightarrow {}^3P_0$ **in ytterbium isotopes.**

Isotope	$\omega_m/2\pi$ THz
^{171}Yb	394.798 329(10) [a]
^{174}Yb	394.799 475(35) [b]

[a] Barber *et al.,* 2008[133]

[b] Lemke *et al.,* 2009[59]

provide additional, uniform confinement of ground- and metastable-state atoms in the remaining directions. In these situations, a deep, magic confinement lattice even allows Doppler-free spectroscopy along its axis, although the achievable level of precision may be adversely affected by the light shifts arising from the presence of the non-magic potentials.

Nevertheless, optical lattices near a magic wavelength are not restricted to their obvious role of providing uniform confinement of the $^1S_0$ and $^3P_0$ states of a single ytterbium isotope. A scheme for entangling bosonic ytterbium atoms held in a magic lattice has been proposed by Weinstein *et al.*[237] Here, the vanishing vector polarisability of the ytterbium atoms (see chapter 7) is exploited to transport a "head" atom with $J = 1/2$ in the lattice by changing its polarisation, analogously to Archimedes' screw. On-site interactions between ytterbium atoms and the head atom may then be used to engineer entangled states or for read-out of the clock. Unfortunately, this scheme is not applicable to Rb-Yb mixtures. Weinstein *et al.*[237] point out that the vector polarisabilities of alkali elements of their $nS_{1/2}$ ground states are not strong enough, and they propose using an aluminium head atom with an $nP_{1/2}$ ground state, instead.

The magic wavelength in between the two low-frequency transitions $^3P_0 \leftrightarrow {}^3S_1$ and $^3P_0 \leftrightarrow {}^3D_1$ has been proposed first for ultrahigh-precision spectroscopy, and it is used in current OLCs based on ytterbium as well as the apparatus presented herein. At a wavelength of $\lambda_m \approx 759.35$ nm, narrow, high-power laser sources to produce deep optical lattice potentials, *e.g.* Ti:sapphire lasers, are readily available. The magic frequencies are isotope-dependent and measurements with 10^{-7} precision have been reported for several ytterbium isotopes (see table 2.8). In addition, Barber *et al.*[133] report a slope of $22(1) \times 10^{-12}$ for each recoil energy $E_{rec}^{(l)}$ of lattice depth for the differential light shift of the clock transition in ^{174}Yb. Hence, even at a detuning of 1 GHz from the magic frequency and a peak lattice depth of $50E_{rec}^{(l)}$, the residual differential light shift induced by the lattice is only about one hertz. The goal of achieving hertz-level sensitivity in the spectroscopy of ultracold quantum gases thus requires only moderate control over the lattice frequency. In particular, it is compatible with the well-established technique of creating multidimensional lattices with stable topology from individual lattices detuned from each other by frequencies of several tens of megahertz.

Multiple other magic wavelengths exist at shorter wavelengths and the positions of some have been predicted by Dzuba & Derevianko[234] and Guo *et al.*,[235] *e.g.* in the vicinity of the intercombination transition near $\lambda' \approx 550$ nm. While the net optical potential is attractive at most of them, one of magic wavelengths investigated by Dzuba & Derevianko[234] is possibly located in a region of repulsive AC–Stark shift. Blue-detuned magic lattices are particularly interesting, because atoms

are trapped in regions of minimal intensity and residual light shifts may hence be reduced substantially.[56]

2.8.3 Anti-magic wavelengths

At anti-magic wavelengths the AC–Stark shifts of ground and metastable state are equal in magnitudes, but have opposite signs. In contrast to magic and state-selective wavelengths, this condition may often be relaxed, if the lattice depths are required to be similar, but not necessarily equal in magnitudes. Prospective wavelengths ranges for anti-magic optical traps are found around $\lambda \approx 619\,\mathrm{nm}$ and $\lambda' \approx 1120\,\mathrm{nm}$,[84] and in both cases the ground state potential is attractive (see figure 2.10).

Optical lattices at these wavelengths trap atoms in the ground or metastable state in separate sublattices, at the nodes and anti-nodes of the field, respectively. As the overlap of neighbouring sites from different sublattices is greatly enhanced in comparison to each of these sublattices on their own, they are prospective candidates for studying off-site interactions, *e.g.* using ultrahigh-precision spectroscopy. Moreover, sublattices of different geometries may be realised. For instance, if the ground state is trapped in a triangular lattice at an anti-magic wavelength, the sublattice experienced by metastable state will be of hexagonal geometry.

The combination of far off-resonant anti-magic lattices with dressing of the clock states $^1\mathrm{S}_0$ and $^3\mathrm{P}_0$ via near-resonant lasers allows the realisation of addressable sub-wavelength lattices.[238] The lattices may be used to dynamically control the lattice spacing and even the geometry of the lattice in multiple dimensions. Moreover, they allow the creation state-dependent lattices for the fermionic isotopes and hence controlled breaking of the SU(N)-symmetry of the nuclear spin. In a similar fashion, optical lattice that are near-resonant with the clock transition have been proposed for quantum information processing in state-selective potentials,[91] as well as the creation of sub-wavelength lattices via additional dressing lasers,[238] *e.g.* to create arrays of controllable double-well potentials.

As mentioned earlier (see section 2.5.3), the clock transition provides a convenient means of inducing artificial gauge potentials in ytterbium quantum gases. In an anti-magic lattice, it may be used to assist tunnelling between adjacent sites of the $^1\mathrm{S}_0$ and $^3\mathrm{P}_0$ sublattices and to create staggered or uniform artificial magnetic fields.[84] Their unique features make both bosonic and fermionic AEL atoms prospective candidates for the implementation of artificial gauge potentials, *e.g.* to study the Harper Hamiltonian[239,240] (see the proposals by Gerbier & Dalibard[84] and Dalibard *et al.*[85] for details).

2.8.4 State-selective potentials

Ytterbium atoms in the ground state $^1\mathrm{S}_0$ and the metastable state $^3\mathrm{P}_0$ may be trapped in independent optical lattices using state-selective wavelengths, *i.e.* wavelengths at which the AC-Stark shift of either state vanishes. Engineering of separate optical lattice potentials for each state is an extremely powerful tool, as it allows individual control of lattice depths or controlled transport of a single state in the lattice. State-dependent lattices have been proposed as storage and transport lattices in novel quantum computation schemes for AEL atoms, using the spin of the fermionic isotopes as qubits to encode information.[88]

Several state-selective wavelengths are found in the visible and NIR spectral region, *e.g.* the polarisability of $^3P_0$ vanishes near $\lambda \approx 540\,\mathrm{nm}$ and $\lambda' \approx 950\,\mathrm{nm}$ (see figure 2.10). In the case of $^1S_0$, the AC–Stark shift vanishes close to the intercombination resonance; however, the polarisability of $^3P_0$ at this wavelength is relatively weak and high intensities are required to create deep lattice potentials. As this particular state-selective wavelength is rather close to transitions of both the ground and metastable state, spontaneous photon scattering may impose a substantial limitation for ytterbium. Due to the spectrum of $^1S_0$, any other wavelength that selectively traps $^3P_0$ is located in the UV region beyond the $^1S_0 \leftrightarrow {}^1P_1$transition.

Even single, state-dependent lattices with mismatched AC–Stark shifts of ground and metastable states provide a variety of highly interesting application. Suitable lattices may be realised readily in the vicinity of the aforementioned state-selective wavelength at $\lambda \approx 540\,\mathrm{nm}$, where $^1S_0$ experiences an attractive potential, whereas $^3P_0$ is subjected to a much weaker potential whose sign and magnitude may be tuned via the lattice wavelength. Here, a ground state MI may coexist and interact with a fraction of mobile $^3P_0$ atoms in a shallow lattice. Furthermore, a state-dependent lattice like this may be used for entropy exchange[213] between the localised and mobile fraction of a state-mixture, even without the need of a second chemical element. However, losses due to inelastic collisions of $^3P_0$ atoms or photon scattering in deep lattices near the $^1S_0 \leftrightarrow {}^3P_1$ intercombination transition may pose problems to these experiments and require careful experimental evaluation. Therefore, it is rather advisable to realise the reverse situation, where $^1S_0$ is the mobile species, *e.g.* close to the intercombination tranisiton as mentioned above despite the large intensities that are required.

2.9 Nuclear spin decoupling

A particularly interesting aspect of the fermionic isotopes of AEL atoms is the decoupling of their nuclear spin[46] from the electronic degrees of freedom in both the ground state $^1S_0$ and in the metastable state $^3P_0$ due to the absence of total electronic angular momentum ($J = 0$). As a consequence, the four s-wave scattering lengths a_{gg}, a_{ee}, a_{eg}^+ and a_{eg}^- describing interactions in this two-orbital system are independent of nuclear spin of the colliding atoms,[92] and unlike in alkali quantum gases there are no spin-changing collisions.[94] Near-perfect decoupling is expected for the ground state with a nuclear-spin-dependent variation of a_{gg} on the order 10^{-9} ; however, the same admixture of P_J-states with $J \neq 0$ to $^3P_0$ that gives rise to a finite transition strength of the clock transition for the fermionic isotopes (see section 2.5.1) breaks the decoupling of their nuclear spin slightly and a variation of the scattering lengths on the order of 10^{-3} is expected.[92]

In consequence, AEL atoms are promising candidates for quantum simulation of spin Hamiltonians with SU(N) symmetries up to $N = 2I + 1$, *i.e.* any $N \leq 6$ in the case of ^{173}Yb. These well-known, but challenging models are studied in solid-state physics, *e.g.* the Kugel–Khomskii model in transition-metal oxides or the KLM in manganese oxide perovskites and heavy-fermion materials (see the article by Gorshkov *et al.*[92] and references therein). Their unique features and the generic advantages of quantum gas experiments, like their extraordinarily high degree of control or the availability of various lattice geometries, have recently inspired a multitude of theoretical investigation and proposals.[92–96,241–245] Hence, experimental studies of these systems in quantum gases of AEL atoms are highly interesting to investigate physics beyond the lowest-band Hubbard

model, and they may contribute substantially to the understanding of complex condensed-matter systems.

Furthermore, the nuclear spin is used as a qubit in several quantum computation schemes proposed[88,91,191] for the AEL elements, and it may even be used as a quantum register.[90]

Chapter 3

A novel 2D-/3D-MOT concept for studies of ultracold ytterbium

In the framework of this thesis, the first 2D-MOT for ytterbium,[1] or any other high-melting AEL element, has been realised and quantum-degenerate Bose and Fermi gases of ^{174}Yb and ^{173}Yb have been generated in this novel 2D-/3D-MOT setup. It allows experiments on ytterbium quantum gases, ultracold Yb-Yb and Rb-Yb mixtures, which exploit the unique features of this species (see chapter 2), and in particular precision spectroscopy in optical lattices (see chapter 7). Conception and development of the entire experimental apparatus have been a major part of this thesis, as have its assembly and a subsequent characterisation of the novel 2D-MOT of ytterbium. The subsequent four chapters give a concise review of the experiment from the design phase to its current status as an operational quantum gas apparatus.

The initial goal has been to develop a concept for a 2D-/3D-MOT system for ytterbium, which matches or even exceeds the performance of setups based on Zeeman slowers and loads a 3D-MOT on the intercombination transition directly from a 2D-MOT. As loading a 2D-MOT from a background vapour is highly impractical due to the low vapour pressure of ytterbium (see section 2.1), we have developed the novel concept – based on a previous design reported[99] for lithium – of a transversely loaded ytterbium 2D-MOT in a glass cell as shown in figure 3.1, where atoms are trapped directly from the atomic beam emitted by a dispenser. In consequence, our 2D-/3D-MOT setup is highly compact, and like traditional setups for alkali metals it uses two separate glass cells for the MOTs. Based on a numeric simulation, we expect the 2D-MOT to yield a sufficient flux of cold atoms and a suitable velocity distribution for direct loading of a 3D-MOT, if a spectrally broadened laser is used for the latter. Subsequent cooling of ytterbium to quantum-degeneracy requires an all-optical approach using deep optical dipole traps.

In this chapter our initial experimental concept for these challenges is presented briefly. The prospects of realising a 2D-MOT for ytterbium in the first place are discussed in section 3.1, followed by the presentation of our concept of a transversely loaded 2D-MOT scheme for ytterbium in section 3.2. Potential problems and possible solutions for loading a 3D-MOT near the intercombination transition from the 2D-MOT are discussed in the subsequent section 3.3. Finally, our concept for all-optical generation of quantum-degenerate gases is formulated briefly in section 3.4.

In the following chapters, our apparatus is presented in detail (see chapter 4), and our 2D-/3D-MOT of ytterbium as well as the creation of quantum degenerate gases are discussed (see chapters 5 and 6).

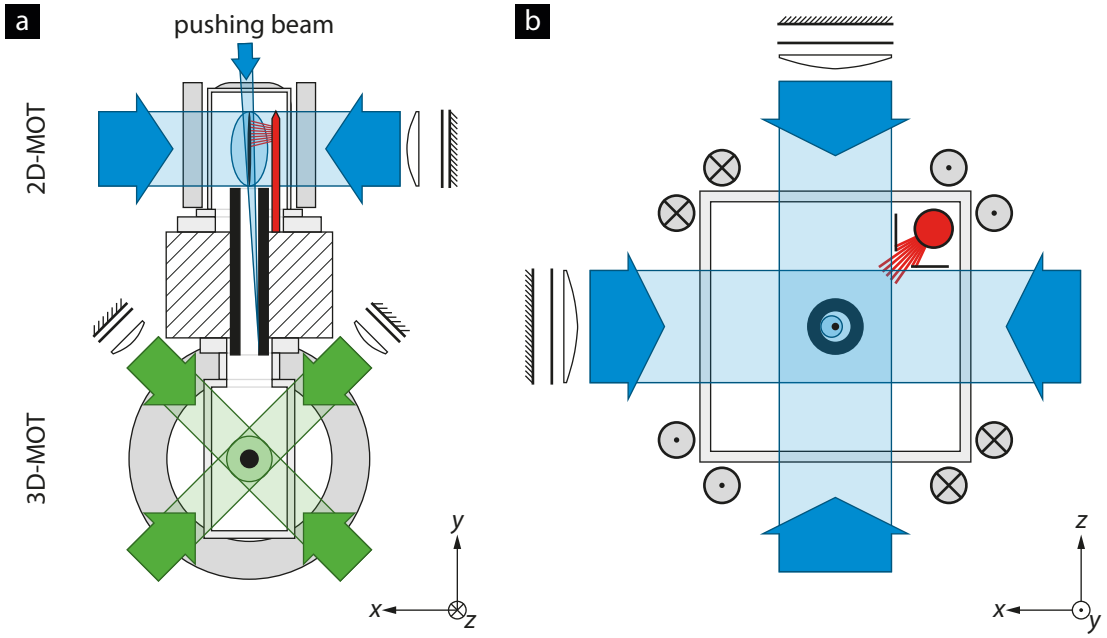

Figure 3.1 | Schematic view of the 2D-/3D-MOT setup. **(a)** The 3D-MOT using the intercombination transition $^1S_0 \leftrightarrow {}^3P_1$ is loaded from a 2D-MOT operated close to the principal transition $^1S_0 \leftrightarrow {}^1P_1$ in a separate glass cell. Both cells are mounted to a central vacuum chamber and connected by a dual differential pumping stage. A pushing beam enhances the loading rate of the 3D-MOT. **(b)** Top-view of the 2D-MOT and transverse loading from the beam of atoms emitted by a dispenser.

3.1 Benefits and challenges of a 2D-MOT for ytterbium

Two-dimensional MOTs[97] are well known sources of cold atoms for loading a subsequent 3D-MOT[246] and widely used for the traditional alkali elements.* A variety of different configurations have been devised, and often a "pushing" beam or a moving molasses is used to enhance their yield. In contrast to Zeeman slowers[98] or chirp cooling,[247] the setup of a 2D-MOT is fairly simplistic, yet achieves similar fluxes of atoms. It does not require powerful slowing beams passing in the vicinity of the 3D-MOT, nor exceedingly large magnetic fields. In fact, alkali 2D-MOTs are usually loaded from a background vapour produced by dispensers. These small reservoirs are heated by an electric current to sublimate the respective element from its metallic or a compound form. In contrast to an actual oven, they allow these 2D-MOTs to be set up in a compact glass cell. This cell is connected with the 3D-MOT cell only via a differential pumping stage (DPS) to ensure the excellent vacuum that can hardly be achieved in vapour-cell MOTs[248] directly, but is required for quantum gas experiments. Beyond their smaller form factor, 2D-MOTs are highly flexible, as glass cells provide excellent optical access, and a set of coils in an anti-Helmholtz configuration is used to produce and control the required magnetic field gradients. Therefore, multiple elements may readily be cooled in a single 2D-MOT setup, either simultaneously or sequentially. Due to this

*2D-MOTs differ from simple beam-brightening, *e.g.* via transverse laser cooling in Zeeman slowers, as there is no co-axial initial beam of thermal atoms, but the beam of cold atoms is created solely by the 2D-MOT.

flexibility, 2D-MOTs are inherently well suited for studies of ultracold mixtures.

Many of these and other traditional benefits of 2D-MOTs apply to ytterbium and other AEL elements as well, even though Zeeman slowers for these elements are typically much shorter, because their principal transition $^1S_0 \leftrightarrow {}^1P_1$ is much broader. Until the first realisation of a 2D-MOT in the framework of this thesis, however, most experiments since the early demonstrations of laser cooling and trapping for calcium,[249] strontium,[249] and ytterbium[148] have been based on Zeeman slowers, including all of those that have actually reported quantum-degenerate gases of AEL atoms.*

The fundamental problem of AEL elements considering a traditional 2D-MOT is their extremely low vapour pressure (see section 2.1), which effectively prevents the creation of any background vapour under practicable conditions.† Some of the transition metals among the AEL elements are more favourable than the actual alkaline earth elements and ytterbium. For mercury, which remains in its liquid state until well below room temperature, a 2D-MOTs has been reported,[251,252] and the MOT reported recently for cadmium (Cd) is loaded from a background vapour.[253] However, these elements are not well suited for quantum gas experiments, as most relevant transitions are deep in the UV. Therefore, a novel approach is necessary to construct a 2D-MOT for one of the other AEL elements, which have favourable transition wavelengths, but high melting temperatures.

3.2 Transverse loading of a 2D-MOT

The aforementioned novel concept for loading a 2D-MOT without the convenience of a background vapour has been demonstrated by Tiecke *et al.*[99] for lithium. Like most of the AEL elements, the lightest of the alkali elements has a low vapour pressure that is insufficient for a traditional 2D-MOT. In contrast, the side-loaded 2D-MOT of Tiecke *et al.*[99] uses an atomic beam emitted by an oven perpendicular to the axis of the MOT for loading. Here, atoms below a certain threshold velocity are slowed and captured by the 2D-MOT upon entering the illuminated volume, whereas – in stark contrast to loading from a vapour background – atoms that miss or which are not captured during the first pass through the 2D-MOT volume are essentially lost.

Transverse loading works well for ^{6}Li with reported loading rates on the order of $10^9\ s^{-1}$,[99] but their 2D-MOT relies on an oven, and it is built from standard Conflat vacuum components. For ytterbium, such a design is not particularly favourable, as the advantages over a Zeeman slower, *e.g.* in terms of form factor, are marginal at best, and incorporation of an additional species is hindered by its limited optical access.

Therefore, we have devised a hybrid design that aims at combining the concept of transverse loading with the traditional setup of a 2D-MOT in a glass cell. It consists of a large glass cell that provides sufficient optical access even for large MOT beams as well as pushing beams from a variety of angles from above. The magnetic field gradient is generated by a set of four rectangular coils encasing the glass cell. Due to its similarity to 2D-MOT setups used for rubidium and potassium, rubidium dispensers, which have been installed in a remote part of the cell, readily allow laser cooling of this second species from a background vapour. In contrast to the alkali dispensers whose

*Several experiments that are not aimed at producing quantum-degenerate gases use direct loading of a 3D-MOT from a thermal beam, *e.g.* as reported by Barber[158] using an additional slowing beam.

†Loading from a background vapour in a heated ceramics cell has been reported for strontium.[250]

orientation is of little consequence, the ytterbium dispensers have been oriented to emit directly into the 2D-MOT volume and on average perpendicular to its axis. Furthermore, they have been placed as close to the 2D-MOT as possible without obstructing the cooling beams to minimise the effect of divergence of the atomic beam. The counterpropagating laser beams then decelerate atoms emitted by the dispenser. Similar to a Zeeman slower, the magnetic field gradient enhances the deceleration of fast atoms by compensating large Doppler shifts via Zeeman shifts on the near side of the MOT. The natural choice as a cooling transition is the principal transition $^1S_0 \leftrightarrow {}^1P_1$, as it yields an extremely strong radiation pressure due to its short wavelength and large saturation intensity (see section 2.4.1).

We have performed a series of numeric simulations of our 2D-MOT setup (see appendix B) to assess the feasibility of this concept and determine the optimal cooling parameters (see chapter 5). Initial results for an effusive emitter* were positive, as they suggested that a sizeable fraction of atoms could be cooled and subsequently captured in a 3D-MOT under practical conditions. Our experimental realisation of the 2D-/3D-MOT (see chapter 5) has shown that a dispenser allows substantial loading rates. In fact, an investigation of the 3D-MOT loading rate as a function of the 2D-MOT parameters has revealed a remarkable agreement between these initial simulations and our experimental results, as discussed in more detail in section 5.5.

3.3 Direct loading of an intercombination MOT

The beam of precooled atoms produced by the 2D-MOT is transferred into another cell via a differential pumping stage to be recaptured in a 3D-MOT. In the case of ytterbium, this second MOT may be operated on either the principal transition $^1S_0 \leftrightarrow {}^1P_1$ or the narrow intercombination transition $^1S_0 \leftrightarrow {}^3P_1$. Clearly, it is desirable to capture atoms directly in the intercombination MOT that is required to achieve sufficiently low temperatures for subsequent evaporative cooling in an ODT.

The range of velocities addressable by a single-frequency laser near the intercombination transition is severely limited by its narrow line width (see table 2.3). While quenching the excited state with an additional laser grants control over the line width of the transition, additional frequency sidebands introduced by active modulation of the laser frequency provide a simple means to weaken its frequency selectivity and hence to expand the capture range of the MOT (see section 5.3).[153] Our numeric simulation of the transversely loaded 2D-MOT suggests that an intercombination MOT is capable of capturing the bulk of atoms emitted by the 2D-MOT into its volume (see appendix B). Nevertheless, contingency plans for an additional 3D-MOT on the principal transition were prepared during the design phase.

3.4 Evaporative cooling

As has been discussed in section 2.4, the ground state of ytterbium cannot be trapped magnetically and an all-optical approach is required to achieve quantum degeneracy. In the case of ^{174}Yb and ^{173}Yb (see section 2.6.1), evaporative cooling is possible and quantum gases may be produced

*The actual velocity distribution of atoms emitted by a dispenser has not been characterised, but an effusive Maxwell-Boltzmann distribution was assumed instead (see appendix B for details), because we were mostly interested in qualitative results.

without the need of a second species for sympathetic cooling. Combined with their importance for subsequent experiments in optical lattices, these two species are thus ideal candidates to demonstrate the creation of BECs and degenerate Fermi gases in our setup.

A crossed optical dipole trap (XDT) is required for efficient forced evaporation in an all-optical approach and two different fundamental configurations have been used to create quantum-degenerate gases of AEL atoms to date. As discussed in section 6.2 we use a trap configuration consisting of a deep horizontal trap and a weaker vertical confinement beam. Here, atoms are initially trapped predominantly in the horizontal trap. They accumulate in the crossed region during the initial stages of evaporation, and only the final evaporation stage leading to the creation of a quantum-degenerate gas is performed in a genuinely crossed trap. In the alternative approach the XDT is formed by two roughly horizontal beams of comparable depths. Although the former option has been implemented, the experimental setup has been designed to allow retrofitting in order to use the latter configuration if needed.

Chapter 4

Experimental setup

A new experimental apparatus for studies of ytterbium quantum gases and ultracold mixtures using ultrahigh-precision spectroscopy has been designed and constructed during a major part of this thesis. The existing setups for studies of K-Rb mixtures[254,255] and rubidium spinor condensates[256–259] have been reviewed carefully with respect to the requirements of the novel 2D-/3D-MOT and all-optical cooling scheme for ytterbium discussed in the previous chapter and state-of-the-art manufacturing techniques. This evolutionary approach has resulted in a design that retains as much backwards compatibility as possible, but takes advantage of the unique features provided by ytterbium as the primary species.*

This chapter provides a detailed summary of the vacuum system and mechanical setup of our apparatus in section 4.1, the generation of magnetic fields in section 4.2. A brief introduction to the optical setup is given in section 4.3, and more details are found in the subsequent chapters on the ytterbium 2D-/3D-MOT (see chapter 5) and the generation of quantum-degenerate gases in a crossed optical dipole trap (see chapter 6). Further details on the vacuum chamber are presented in appendix A.

The setup presented in this chapter – with the sole exception of the primary magnetic field coils discussed in section 4.2.2 – has been designed and constructed by the author. The components have been assembled in a collaborative effort by the entire project team.

4.1 Vacuum system

The vacuum system is literally at the centre of our setup. Here, ytterbium is precooled in a 2D-MOT in one glass cell and then transferred to another, "science" glass cell for laser cooling in a 3D-MOT, further evaporative cooling and eventually experiments on and detection of a quantum-degenerate sample. A well constructed and carefully assembled vacuum system is crucial for achieving the extremely high vacuum in the science cell that is required to prevent excessive loss of atoms from quantum gases by collisions with the background gas, *i.e.* pressures on the order of a few 10^{-11} mbar or less. At the same time, it needs to allow efficient transfer of an atomic beam from the 2D-MOT cell, with its much higher pressures of a few 10^{-9} mbar, and provide an optimum of optical access to the science cell.

Figure 3.1 shows the core components of our vacuum system in a CAD model. The 2D-MOT and science cells are mounted to a single vacuum chamber. It serves as a central hub that connects

*Its core components have been designed for generic, 2D-/3D-MOT-based quantum gas experiments. Two recent projects, studying K-Rb mixtures and coupling of a BEC to a nanomechanical oscillator, use central components developed during this thesis.

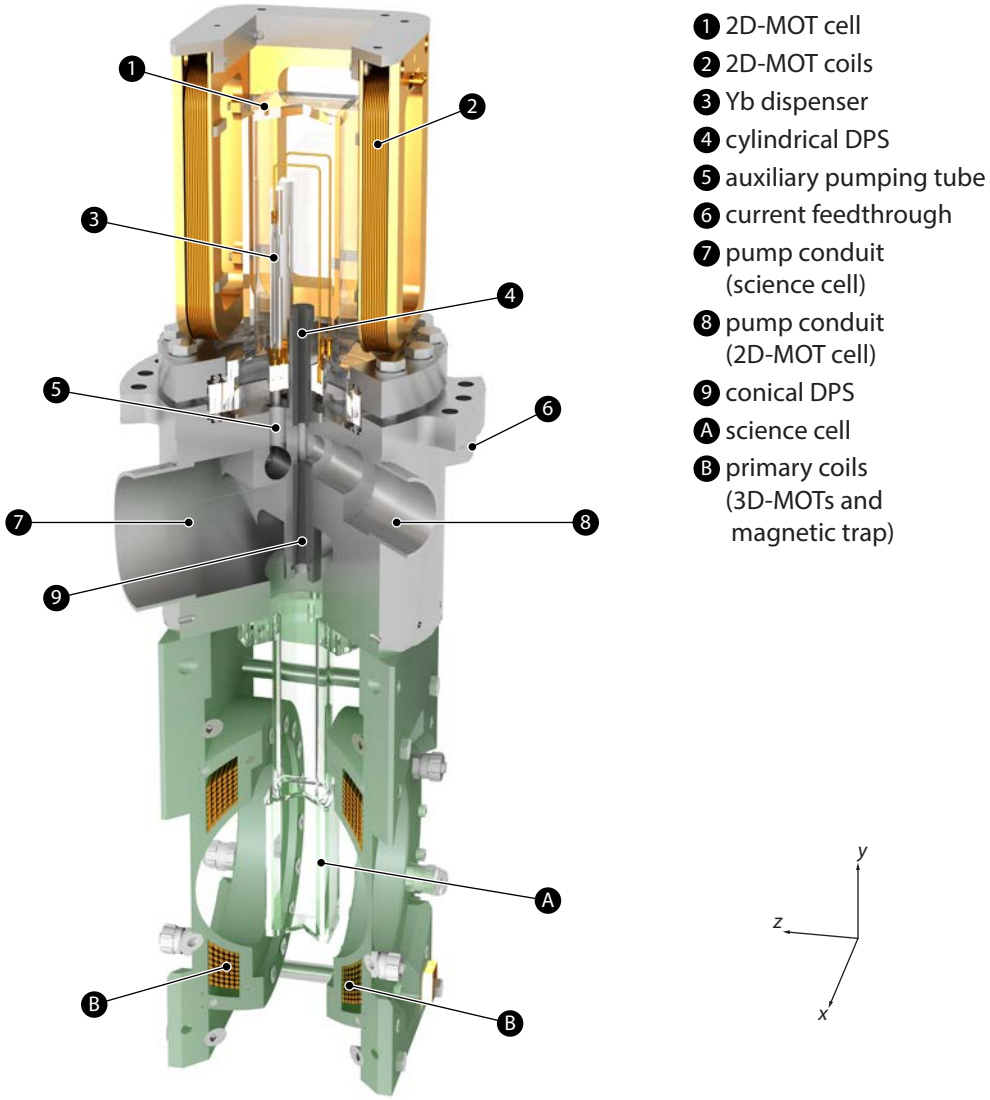

Figure 4.1 | CAD model of the 2D-/3D-MOT setup illustrating the central components of the vacuum system and the magnetic coils which generate the magnetic fields for the MOTs. In order to show the internal layout of the central vacuum chamber in more detail, the chamber itself – and the science cell, but not the dispenser setup – have been rotated by 90° around the *y*-axis. The coordinate system in the lower right corner refers to their actual orientation, which is retained by the coils in the rendered image above, and it is used when referring to the apparatus throughout this thesis.

the cells with each other, as well as to vacuum pumps, an electrical feedthrough and so forth. A dual DPS provides an effective decoupling of the vacua in both cells, but allows the atomic beam produced by the 2D-MOT to be transferred into the science cell. In combination with a highly compact chamber, it reduces the transfer distance between these two MOTs to 30 cm. During operation of the 2D-MOT, vacua of currently about 2×10^{-9} mbar (see below) and 3×10^{-11} mbar are achieved in the 2D-MOT and science cells, respectively. The pressure ratio of about one hundred and more maintained by the DPS is sufficient to ensure background-limited lifetimes on the order of several tens of seconds in the science cell.[257]

Ytterbium dispensers in the upper glass cell (see figure 4.2a) produce the atomic beam loading the 2D-MOT and have been set up in an upright position facing towards the 2D-MOT. Apertures have been inserted in front of each ytterbium dispenser. They effectively protect the glass cell from being coated with ytterbium, whereas no deterioration of the MOT loading rates is observed. Moreover, several rubidium dispensers have been installed at the bottom of the cell to load a rubidium 2D-MOT from a background vapour. The apparatus is thus well prepared for future ytterbium-rubidium mixture experiments – as well as other mixtures, since the dispensers may be replaced easily.

Each of the components of the vacuum system or installed within is discussed in more detail in the subsequent subsections.

4.1.1 2D-MOT cell

For maximum optical access, the actual 2D-MOT cell (50 mm × 50 mm × 120 mm) atop the chamber has been manufactured entirely from Spectrosil 2000 synthetic fused-silica glass, and broadband anti-reflection (AR) coatings have been applied to its external surfaces.[*] A pedestal made from Vitreosil is used to mount the entire cell to the chamber via Helicoflex gaskets (see appendix A for further details).

Several ytterbium and rubidium dispensers have been installed within the 2D-MOT cell on an electrically and thermally insulating MACOR ring as illustrated in figure 4.2. For resistive heating, they are connected to a high-power electric current feedthrough.[†] Each dispenser is powered via a separate wire, but connected to a ground wire shared by an ytterbium and a rubidium dispenser, and it may effectively be operated at currents up to 17 A.[‡]

Two ytterbium dispensers,[§] have been installed in an upright position and emit ytterbium towards the central axis of the cell through a slit cut into their mantle as shown in figure 4.2. Although they are specified for operation at heating currents from 9 A to 16 A by the manufacturer, we have observed substantial emission of ytterbium starting at currents slightly below 6 A, and we typically operate a single dispenser at a current of 6.4 A.[¶]

[*] Manufactured by Hellma Analytics GmbH & Co. KG. Residual reflectivities of less than 1.2 % (2.2 %) have been specified for the lateral (top) external surfaces at wavelengths from 390 nm to 950 nm. Internal surfaces have not been coated due to technical reasons.

[†] Manufactured by Trinos Vakuum-Systeme GmbH (8 pins, max. current: 50 A per pin).

[‡] Wires of different diameters are used for the power (diameter: 0.91 mm, max. current: 17 A) and ground connections (diameter: 1.3 mm, max. current: 30 A). They are made from a ZrCu alloy and insulated by ceramic beads.

[§] Alvatec, AS-4-Yb-500-S (Yb net weight: 500 mg).

[¶] The dispenser is usually operated at a constant voltage of about 1.63 V rather than a constant current. It is one of several safeguards that have been implemented to protect the dispenser from being operated at excessively high currents

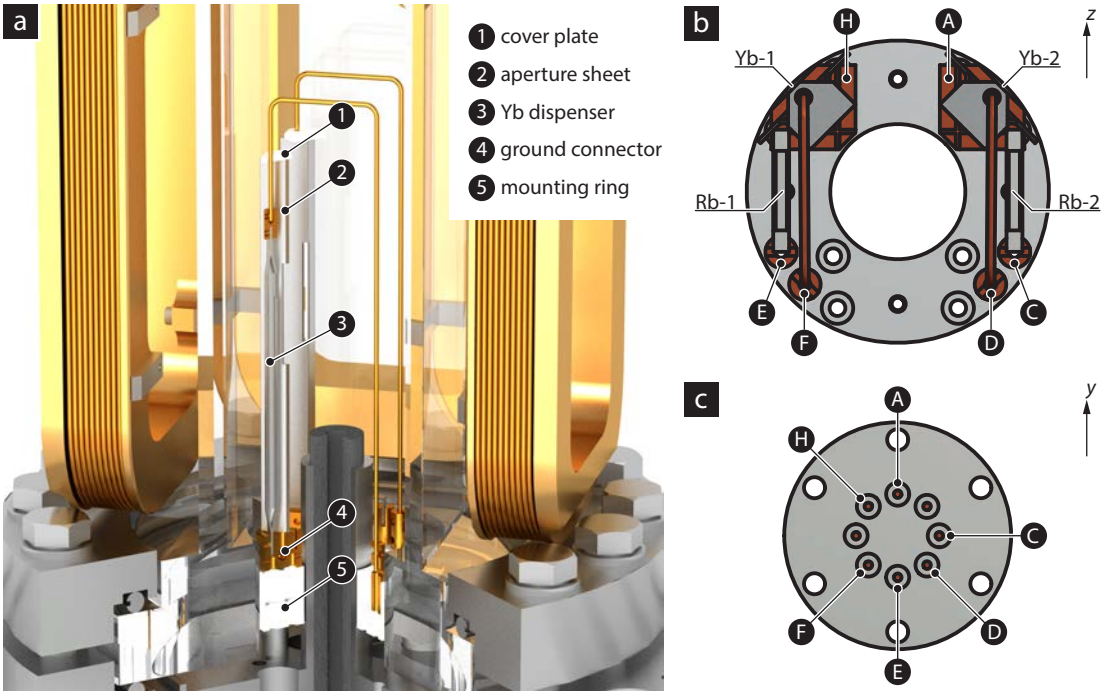

Figure 4.2 | Setup of ytterbium and rubidium dispensers. **(a)** A close-up of figure 4.1 illustrates the mechanical and electrical setup of the ytterbium dispensers, as well as the apertures shielding the glass cell from the atomic beam. **(b)** The configuration of all four dispensers within the 2D-MOT cell is shown in top view. Each of them is powered via a separate connection (C-F), but each pair of dispensers shares a common ground conductor (A,H). **(c)** For reference, the pin assignment of the high-power feedthrough with respect to the labels used in (b) is illustrated. The two unlabelled pins (B,G) have been connected to the mounting structure in (b), but the respective wires are not used.

As discussed in section 2.1, the vapour pressure of ytterbium is extremely small, and it is efficiently adsorbed to any surface at room temperature. Because the dispenser emits substantial amounts of ytterbium into a solid angle of almost 2π, critical areas within the 2D-MOT cell like its windows need to be protected, lest they be coated with ytterbium within a matter of weeks. Rectangular apertures made from aluminium have been installed in front of each ytterbium dispenser to block the direct lines of sight from its emitting surface to the critical areas of the glass cell, *i.e.* the areas where 2D-MOT and pushing beams are transmitted by the windows, without obstructing the emission of ytterbium into the 2D-MOT cell. Additional MACOR cover plates on top of these apertures provide additional shielding to the top surface of the cell. After more than twelve months of regular operation no degradation of the transmission of a probe beam through the cell has been ovserved,* whereas the corners of the cell opposing the currently used dispenser, which are of course not protected by the apertures, have been visibly coated with ytterbium. Since ytterbium is efficiently adsorbed within the vacuum system, we attribute the pressure rise observed during operation (see below) mostly to the emission of spurious elements with a larger vapour

by accident.

*A transmission of about 95 % has been measured at a wavelength of 399 nm.

pressure by the dispenser.

For later studies of Rb-Yb mixtures, two more rubidium dispensers* have been installed at the bottom of the cell to produce a background vapour of rubidium in the 2D-MOT cell.

4.1.2 Transfer stage

The science cell below the central chamber is connected to the 2D-MOT cell by a DPS to transfer atoms between the cells, but maintain a large pressure ratio during operation. The dual-stage DPS consists of two separate graphite tubes along the central axis of the chamber. As illustrated by figure 4.3, a vacuum pump is attached to the intermediate region between these tubes, which greatly enhances the overall effectiveness of the two design.† The upper section is cylindrical, and at its nominal conductance[260] of 0.12 L s^{-1} it is capable of maintaining a pressure ratio of nominally up to 440 between the 2D-MOT cell and the intermediate region between both tubes.‡ In contrast, the lower tube has a novel, conical inner wall which increases the geometrically acceptable angle of divergence of the atomic beam generated by the 2D-MOT to a half-angle of $\theta_{\mathrm{DPS}} = 1.8°$ (see figure 4.3), and its conductance of 0.20 L s^{-1} corresponds to a nominal maximum pressure ratio of 270 from the aforementioned intermediate region to the science cell (*cf.* the discussion of the observed pressure ratio below).

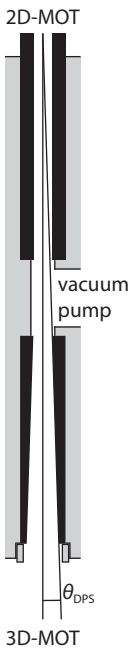

Figure 4.3 | Maximum divergence angle θ_{DPS} in the DPS illustrated by a sketch at a scale of 1: 2.

4.1.3 Science cell

The science cell (26 mm × 36 mm × 80 mm) itself is made from the same fused-silica glass as the 2D-MOT cell and with identical AR coatings. Unlike the other cell, however, it has been attached to a glass-to-metal transition with a standard CF flange. The science cell is hence mounted to the central vacuum chamber via CF gaskets made from silver-plated copper to ensure optimal sealing and longevity. An additional port in the vacuum chamber provides internal access to the science cell, but it is not used in the current setup. In comparison to previous chambers, the effective pumping speed of the science cell has been optimised by removing bottlenecks in its connection to the vacuum pumps.

Taking advantage of the all-optical creation of ytterbium quantum gases, the magnetic field coils around the science cell allow outstanding off-axis optical access in a cone of 88° opening angle around the z-axis, as well as in the x–y-plane (see section 4.2 and figure 4.5). Moreover, this enables high-resolution imaging and long times-of-flight along both the x- and z-axes. Indeed, we expect that imaging along the latter axis will ultimately be limited in resolution solely by the glass cell, whose broad side faces the z-axis to allow as large a numerical aperture as possible.

*SAES Advanced Technologies, RB/NF/4.8/17 FT10+10.

†Ideally, the individual tubes act as two individual DPSs, rather than as a single DPS with the total conductance of both tubes.

‡Conductance values depend on the mean velocity of the particles in a gas, and these values given here have been calculated for rubidium at room temperature.

4.1.4 Vacuum maintenance and monitoring

Under regular conditions, the vacua in both cells are maintained by a set of two ion pumps[*] via large-diameter tubes (see figure 4.4). The 2D-MOT cell is evacuated only indirectly via the upper DPS by one of these pumps. It is connected to the aforementioned intermediate region and hence an integral part of the DPS, which allows a significant vapour pressure in that cell for the operation of a rubidium 2D-MOT.

An auxiliary pumping tube within the chamber itself bypasses the upper DPS and may be opened gradually using a plug mounted on a linear manipulator (see figure 4.1). It allows a precise control of the effective pumping speed of the 2D-MOT cell.[†] The science cell is connected to the second ion pump directly, *i.e.* without a DPS, for maximum pumping speed.

An additional titanium sublimation pump cartridge[‡] with three filaments has been installed in one of the connection tubes, and it is fired occasionally in order to coat this section of the tube with a layer of titanium that acts as a highly efficient getter.

In order to evacuate or vent the vacuum system both cells are connected to a single turbomolecular pump[§] as illustrated by figure 4.4. Two high-quality, all-metal valves ensure excellent sealing of the cells even after many opening/closing cycles and may be used to selectively vent the system through either cell, *e.g.* to prevent contamination of the science cell during maintenance operations in the 2D-MOT cell. Following such maintenance it takes approximately two weeks to re-establish the typical pressure levels discussed below.

Cold-cathode vacuum pressure gauges[¶] have been installed in the vicinity of each of the ion pumps to complement their integrated pressure monitors. However, their readings should only be considered coarse indications of the actual pressure in the cells. In addition to possible calibration errors and their remote location to avoid excessive stray field caused by their magnets, the 2D-MOT gauge in particular is separated from the cell by the upper differential and auxiliary pumping stages.

4.1.5 Observed background pressures

We observe typical pressures of $p_{3D} < 1 \times 10^{-11}$ mbar and $p_{2D} \approx 5 \times 10^{-10}$ mbar in the science and 2D-MOT cells, respectively, when all dispensers are off-line. If a single ytterbium dispenser is operated at its regular current (see above), these pressures rise to typically $p_{3D} \approx 3 \times 10^{-11}$ mbar and $p_{2D} \approx 2 \times 10^{-9}$ mbar. Since the upper DPS has been bypassed by the open auxiliary tube, the observed pressure ratio agrees well with the expected, nominal performance (see above). Nevertheless, the differences of actual pressures in the cells and pressures measured by the gauges are largely unknown, and they may in particular be of significance for the apparent reduction of DPS performance during operation. Finally, we are still observing a continuing slow decline of pressures in both cells, and even better pressures are hence expected in future experiments.

[*] Varian, VacIon Plus 55 StarCell (nominal pumping speed: 55 L s^{-1}).

[†] As of the writing of thesis, the auxiliary pumping tube is usually operated in its fully open state. Closing the tube deteriorates the pressure in the science cell when the dispensers are in operation, if only slightly.

[‡] Varian, 916-0050 series

[§] Pfeiffer Vacuum, CompactTurbo TMU261 (nominal pumping speed: 250 L s^{-1}).

[¶] Pfeiffer Vacuum, IKR 270 (1×10^{-11} to 5×10^{-3} mbar).

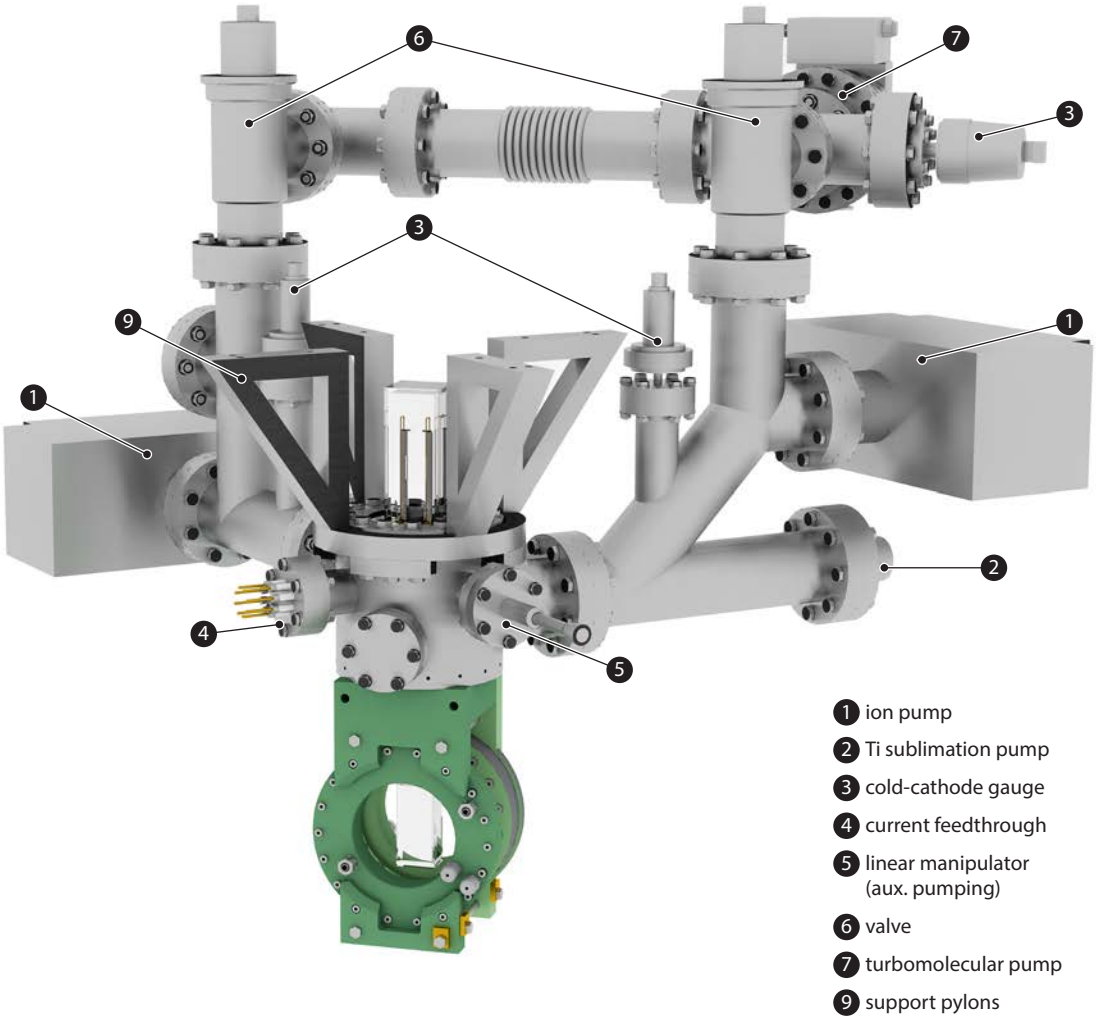

Figure 4.4 | CAD model of the vacuum system. Vacuum pumps and gauges are connected to the central vacuum system shown in figure 4.1. The branch on the right is connected to the science cell, whereas the 2D-MOT cell is pumped indirectly by the branch on the left. A linear manipulator may be used to open or close an auxiliary pumping tube to control the pumping speed of the 2D-MOT cell. Both branches are connected to a single turbomolecular pump and sealed individually by all-metal edge valves. The central vacuum chamber is mounted to support pylons attached to the superstructure shown in figure 4.7.

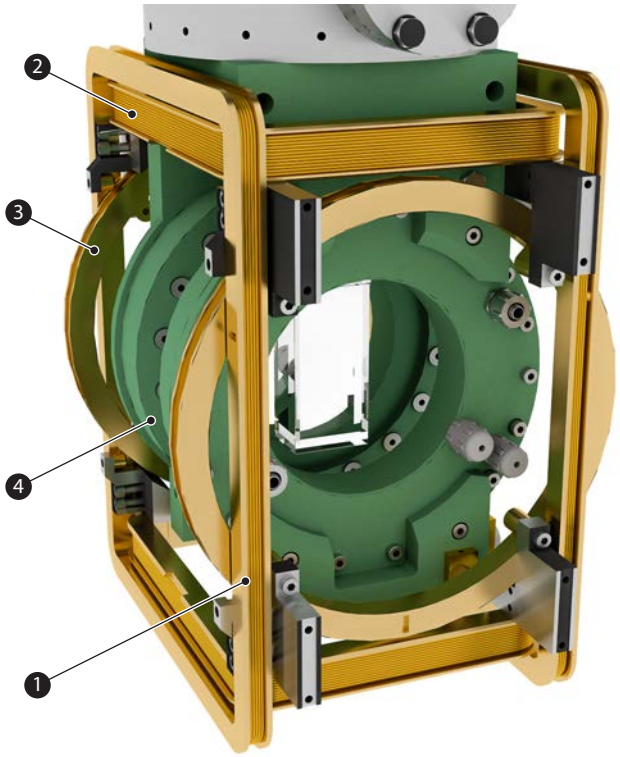

Figure 4.5 | CAD model of the compensation coils encasing the primary magnetic field coils and the science cell. The internal layout of these coils is shown in figure 4.6.

4.2 Magnetic fields

The coils shown in figure 4.1 generate the magnetic fields required for the 2D- and 3D-MOTs. Although the intercombination MOT of ytterbium requires only small field gradients, the primary pair of coils encasing the science cell has been developed to create large magnetic field offsets and steep gradients for any experiment requiring strong magnetic fields. Additional compensation coils (see figure 4.5) are used to cancel residual magnetic field offsets and gradients in all three dimensions, or to apply such small fields deliberately.

All three sets of coils are discussed in detail in the subsequent subsections, including considerations governing their design and performance.

4.2.1 2D-MOT coils

The magnetic field of the 2D-MOT is generated by a set of four rectangular coils that encase the glass cell as shown in figure 4.1 (see also figure 3.1). In contrast to permanent magnets, the 2D-MOT may readily be operated at different gradients for ytterbium and rubidium by adjusting the current running through the coils. A flexible set of coils is particularly important, since in the case of ytterbium, owing to the broad line width of $^1S_0 \leftrightarrow {}^1P_1$ transition (see section 2.4.1) used for laser cooling, significantly stronger magnetic field gradients than in a typical 2D-MOT of rubidium are required. To generate these strong fields each coil consists of 84 windings as illustrated by

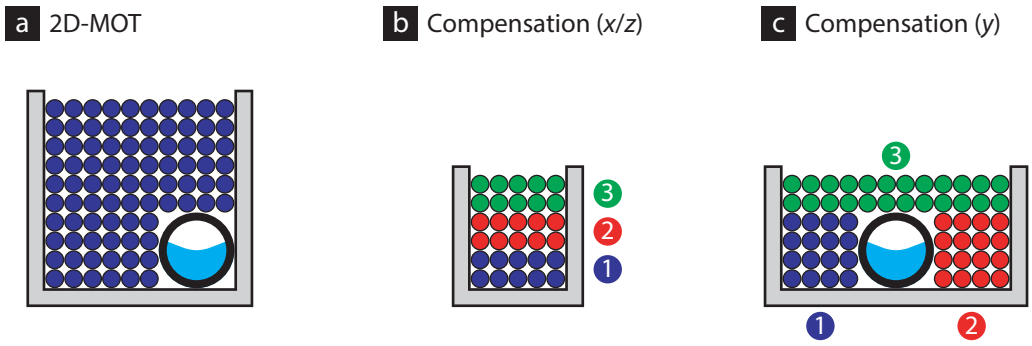

Figure 4.6 | Internal layout of the 2D-MOT and compensation coils. **(a)** Each of 2D-MOT gradient coils is water-cooled via a copper pipe soldered to its frame. **(b)** Each compensation/gradient coil frame in the *x*- and *z*-directions has been outfitted with three coils in separate layers. **(c)** The compensation/gradient coils in *y*-direction may optionally be water-cooled by central copper pipes that have been soldered to their frames. Each of them carries three separate coils as shown above. The left-hand sides of the coils shown above face the respective glass cells, and the individual layers listed in table 4.1 are labelled accordingly.

figure 4.6a, and the set of four coils creates a magnetic field gradient of nominally 4.61 G cm^{-1} per 1 A of current. All four coils have been connected in series to a single power supply,* and they are typically operated at a current of about 12.0 A for ytterbium, *i.e.* at a gradient of 54 G cm^{-1} (see section 5.5 for details). The attainable gradients are limited to approximately 64 G cm^{-1} by the total output power of the current source.

Since several hundreds of watts are dissipated thermally in the coils at high currents like these, they are water-cooled via copper pipes running along each of the coils (see figure 4.6a), and the pipes themselves have been soldered to the brass frames of the coils for optimum thermal contact. At a thermal power dissipation of 175 W distributed across all four coils and a water pressure of only 1 bar, a temperature rise of 4 K has been measured in the coil itself during initial off-site testing. Even at more than 350 W of total dissipated power, the temperature of the coils is not elevated substantially. Therefore, the magnetic field gradient of the 2D-MOT attainable in the current setup is limited by the maximum power delivered by the power supply.

All four coils are mounted rigidly to a common superstructure and fixed with respect to each other by additional stabilisers. For alignment of the 2D-MOT, position and attitude of the coil assembly may be fine-adjusted using a two-axis, horizontal translation stage and a mirror mount. The latter is used not only for tilting the assembly, but also to adjust its vertical position. In contrast, the entire module needs to be turned to achieve rotation around the vertical axis; however, this degree of freedom is far less important for the overall alignment of the 2D-MOT than the others.

4.2.2 Primary coils

A MOT operated on the intercombination transition of ytterbium requires only a small gradient field due to its narrow line width, but the primary coils around the science cell have nonetheless been designed for a multitude of roles, including magneto-optical and magnetic trapping of rubid-

*Hameg HMP-4040 (max. current (voltage) per channel: 10 ampere (32 V), max. combined output power: 385 W). Three channels are used in parallel.

ium, Zeeman splitting of the clock transition via large offset fields or magnetic addressing of the metastable $^3P_2$ state in optical lattices via magnetic field gradients.

As illustrated in figure 4.1, we take advantage of the all-optical creation of ytterbium quantum gases and use a pair of quadrupole coils instead of a more complex magnetic trap design, *e.g.* cloverleaf traps[261] or the 8-Dee design[262] used by the alkali experiments in our research group. This allows excellent optical access (see section 4.1.3), and we are going to use a combination of magnetic and optical dipole traps to produce BECs of rubidium. Since both blue-detuned and red-detuned strong ODTs may be implemented in our setup, such a hybrid technique may either use an optical plug[6] to avoid Majorana losses or use the quadrupole trap to load rubidium into an ODT.[263,264]

Each of the coils contains 48 windings of insulated copper wire in a coated fibreglass casing,* and they are cooled by water from a closed circuit, which is pumped through the cavities containing the wires. At their centre, the quadrupole coils produce either a magnetic field gradient of $1.3\,\mathrm{G\,cm^{-1}\,A^{-1}}$ or a nearly homogeneous offset field of $6\,\mathrm{G\,A^{-1}}$ along the z-axis. They may be switched between symmetric and anti-symmetric operation at will via two H bridges. Using a high-current power supply,† offset fields of more than 0.8 kG or gradients of up to $0.18\,\mathrm{kG\,cm^{-1}}$ may be produced, and they are still well below the maximum capacity of the cooling circuit.

4.2.3 Compensation coils

Stray magnetic fields are caused by the terrestrial magnetic field, vacuum pumps and gauges, or simply electrical devices in the vicinity of the science cell and need to be cancelled. Moreover, small offset or gradient fields are used for numerous purposes, *e.g.* to establish an axis of quantisation and induce specific, but small Zeeman splitting, or for magnetically induced spectroscopy (see section 7.4), to name only a few examples.

A triaxial array of compensation coils allows magnetic field offsets and residual gradients to be controlled along all three axes. These pairs of coils have been arranged tightly around the primary coils (see figure 4.5) in superstructures made from brass. Their geometry has been optimised to yield an optimal trade-off between minimal obstruction of optical access, magnetic field response and field homogeneity. Each superstructure contains three separate layers of insulated copper wire as illustrated by figure 4.6, which may be operated as separate coils. Currently, the compensation coils do not support dynamic reconfiguration during an experimental cycle, but each pair of layers in use has been connected manually to a programmable power supply.‡

Magnetic field offsets and gradients produced by these pairs of coils in symmetric and anti-symmetric operation, respectively, are summarised in table 4.1. The more complex layout of the compensation coils along the y-axis causes substantial differences in the responses of the individual layers in both configurations. These coils in particular have been optimised to produce large gradients in order to vertically shift the centre of a rubidium MOT away from a dipole trap storing cold ytterbium at the actual centre of the coils. Similar to the 2D-MOT coils, additional copper pipes have been installed for optional water-cooling (see figure 4.6), as high currents of up to 10 A are required to generate the necessary magnetic field gradients.

*Manufactured by E. Hippe KG from epoxy-fibreglass EP GC 201.

†Delta Elektronika SM45-140 (max. current: 140 A).

‡Hameg, HMP 4040 (see page 51).

Table 4.1 | Offset and gradient field responses of the compensation coils at each layer to an electric current. The nominal values given below for offset fields B_i/I_C and field gradients $(\partial B_i/\partial r_i)/I_C$ $(i = x, y, z)$ have been computed numerically from the geometry of the coils. Their layouts and individual layers are illustrated in figure 4.6.

Axis	Layer	Offset/G A^{-1}	Gradient/mG cm^{-1} A^{-1}
x	1	0.66	72
	2	0.66	70
	3	0.66	67
y	1	0.58	100
	2	0.49	82
	3	0.56	96
z	1	0.53	89
	2	0.53	88
	3	0.53	86

4.3 Optical setup

In order to exploit the excellent optical access provided by the science cell and magnetic coils, several optical breadboards have been set up around the core apparatus shown in figure 4.1 to install the optics for the MOTs, ODTs, spectroscopy, imaging laser systems and so forth. Figure 4.7

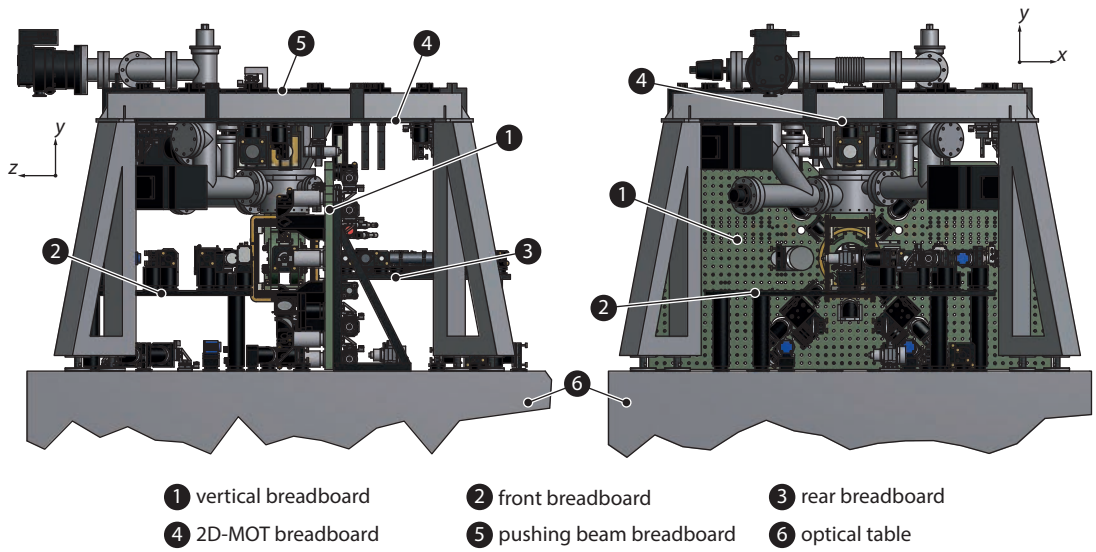

Figure 4.7 | Overview of the experimental setup. The CAD drawing of the apparatus shows the superstructure to which the vacuum system and several optical breadboards have been attached. As illustrated, an array of breadboards provides access to the science (1-3, 6) and 2D-MOT cell (4-5). Detailed, schematic optical layouts of the individual breadboards are shown in figures 4.8 through 4.10.

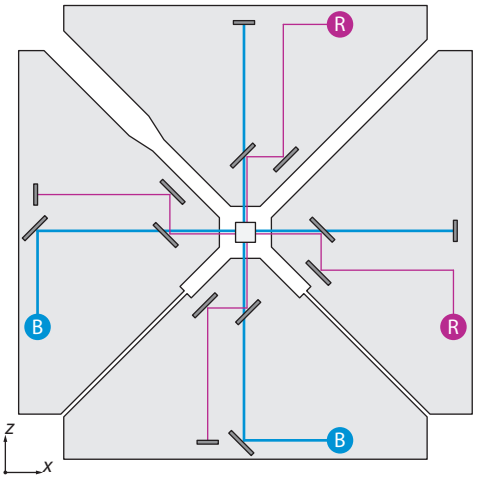

Figure 4.8 | Schematic setup of the 2D-MOT optics. Optical elements of the 2D-MOT are mounted upside down on four breadboards (see figure 4.7). The individual beams and their superposition are illustrated schematically in bottom view, more details may be found in the text. The sketch includes beams that have been planned, but not implemented yet. A summary of the symbols and colour coding is given in figure 4.9.

illustrates this setup, and this section briefly highlights the layout of beams in the science and 2D-MOT cells. Details on the individual laser systems and beams, *e.g.* the MOTs and optical traps, are found in the subsequent chapters 5 and 6.

The setup, which is discussed in more detail below, has been designed to provide all lasers used by a complete experiment for precision spectroscopy with adequate optical access to the science cell. Only a part of these lasers has been set up at the time of writing of this thesis, *e.g.* the optical lattices have only been set up recently. Therefore, both the current setup that has been used for the experiments discussed in this thesis and, subsequently, expansions, which have been implemented recently or will be implemented for future experiments, are presented for each plane of access. Although not yet implemented for the experiments described herein, the latter are essential for the aptitude of the apparatus constructed in the framework of this thesis to conduct a wide range of future experiments.

In particular, the wide variety of wavelengths used in Yb-Rb experiments and their close spacing in some spectral regions, *e.g.* in the green and NIR, represent a major challenge to these experiments. Special attention has thus been paid to the optical setup to provide all of these lasers with optimal access using state-of-the-art mirrors and filters.

4.3.1 2D-MOT

Four aluminium breadboards at the top of the frame shown in figure 4.7 carry the optics required to shape the beams for the 2D-MOT and others, *e.g.* to probe the transmission of the glass cell. At the current stage, it contains only the 2D-MOT beams for ytterbium which are delivered in free space (see section 5.1 for details), as well as several probe beams to monitor the transmission of the 2D-MOT cell. An additional, small breadboard (see figure 4.7) has been used to set up the pushing beam.

As outlined by figure 4.8, 2D-MOT beams for both ytterbium and rubidium will eventually be delivered via single-mode optical fibres (SMFs) or in free space. These individual beams are then shaped separately and superimposed or split by edge filters close to the cell.

4.3.2 Science cell — vertical plane

A vertically mounted breadboard made from the same fibreglass material as the casings of primary coils (see section 4.2.2) provides access to the science cell in the x–y-plane. Figure 4.9 schematically shows the optical setup on this breadboard, where all beams are delivered via SMFs.

As of the writing of this thesis, two arms of the retroreflected intercombination 3D-MOT for ytterbium have been set up along the diagonal axes. Imaging of ytterbium quantum gases is performed predominantly along the x-axis using the principal transition (see section 6.3.6). Finally, the breadboard contains a single steering mirror to reflect the vertical ODT (see section 6.3.3) towards the science cell.

Nevertheless, the complete setup shown in figure 4.9 has been designed to accommodate a variety of additional systems. Both triangular and square lattices may be set up, and in the latter case the lattice beams are superimposed onto the MOT beams and retroreflected in the lower part of the breadboard. In fact, the aforementioned steering mirror may be used to reflect one of the beams of a triangular lattice, but transmit light at any of the laser cooling transitions of ytterbium. Additional horizontal ODTs may be set up at wavelengths of 532 nm and 1064 nm along the x-axis to create a horizontal XDT. Moreover, lasers for clock spectroscopy and repumping or coherent control at both repumping transitions of ytterbium may be superimposed along this axis as well.

For mixture experiments, rubidium 3D-MOT branches may be superimposed onto the existing ytterbium branches, and both MOTs may be set up as part of a retroreflected or six-beam MOT configuration, *i.e.* using separate beams for counterpropagating directions. In a similar fashion, resonant light at either the principal transition of ytterbium or the D2 transition of rubidium may be superimposed and used for imaging of the respective species along the x-axis. Finally, the ytterbium MOT branches support 3D-MOT or imaging beams on the principal transition in addition to the regularly used intercombination transition. In this case, optional imaging optics may be installed along the diagonal axes in the lower sections of the breadboard, *e.g.* for alignment of an optical lattice.

As illustrated in figure 4.9, the beams are prepared either on the rear plane of the breadboard, on a horizontal breadboard or the optical table. Therefore, its front plane may be used for additional expansions, *e.g.* probe beams for later experiments or monitoring equipment, like a photomultiplier tube that has been installed to monitor the fluorescence of the ytterbium MOT.

4.3.3 Science cell — horizontal plane

In the horizontal x–z-plane, two aluminium breadboards provide direct access to the science cell and sufficient space to prepare a large number of beams superimposed along the z-axis as illustrated in figure 4.10. As in the case of the vertical breadboard, all beams – with one exception – are delivered via SMFs.

For the experiments discussed below, a retroreflected 3D-MOT beam at the intercombination transition of ytterbium has been set up along the z-axis. A strong horizontal dipole trap at a wavelength of 532 nm is delivered in free space to the breadboard beyond the vertical plate and superimposed onto the z-axis (see section 6.3). For imaging along this axis, another beam at the principal transition has been superimposed onto the MOT beam along positive z-direction. An imaging system on the opposite breadboard is used to monitor the 3D-MOT (see section 5.1.4).

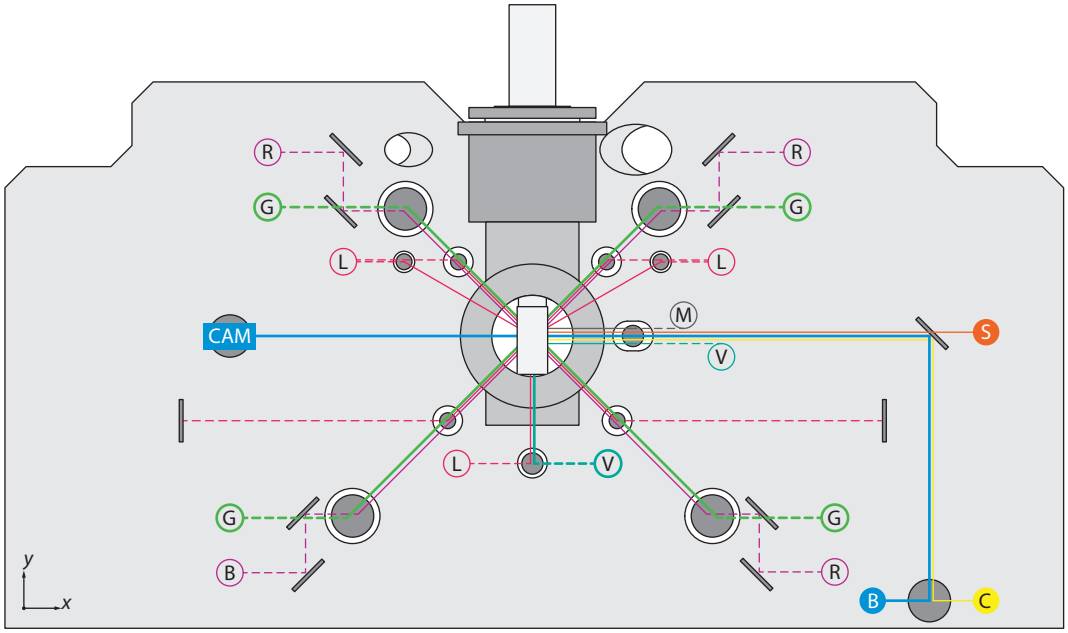

| Wavelengths

- B cooling (2D-MOT) & imaging | 399 nm
- V dipole trap | 532 nm
- G cooling (3D-MOT) | 556 nm
- C clock spectroscopy | 578 nm
- S metastable state repumping & coupling | 649 nm & 770 nm
- L magic lattice | 759 nm
- R cooling & imaging (Rb) | 780 nm*
- M dipole trap | 1064 nm

*Beams may include repumping laser.

| Symbols

- CAM camera system
- X beam shaping optics
- (X) beam shaping optics, behind breadboard
- —— beam
- ---- beam, behind breadboard

| Status

- —— implemented
- —— not yet implemented

Figure 4.9 | Schematic setup of optics in the *x*–*y*-plane. All beams entering the science cell in this vertical plane and their successive superposition are shown schematically in a front view of the experimental setup, more details on these lasers may be found in the text. From this perspective, the vacuum chamber is located in front of the vertical fibreglass (see figure 4.7). Several branches shown above have been planned, but not yet implemented. The legend summarises the line styles used to indicate these two types of beams, as well as other symbols and the colour coding used to identify the individual beams.

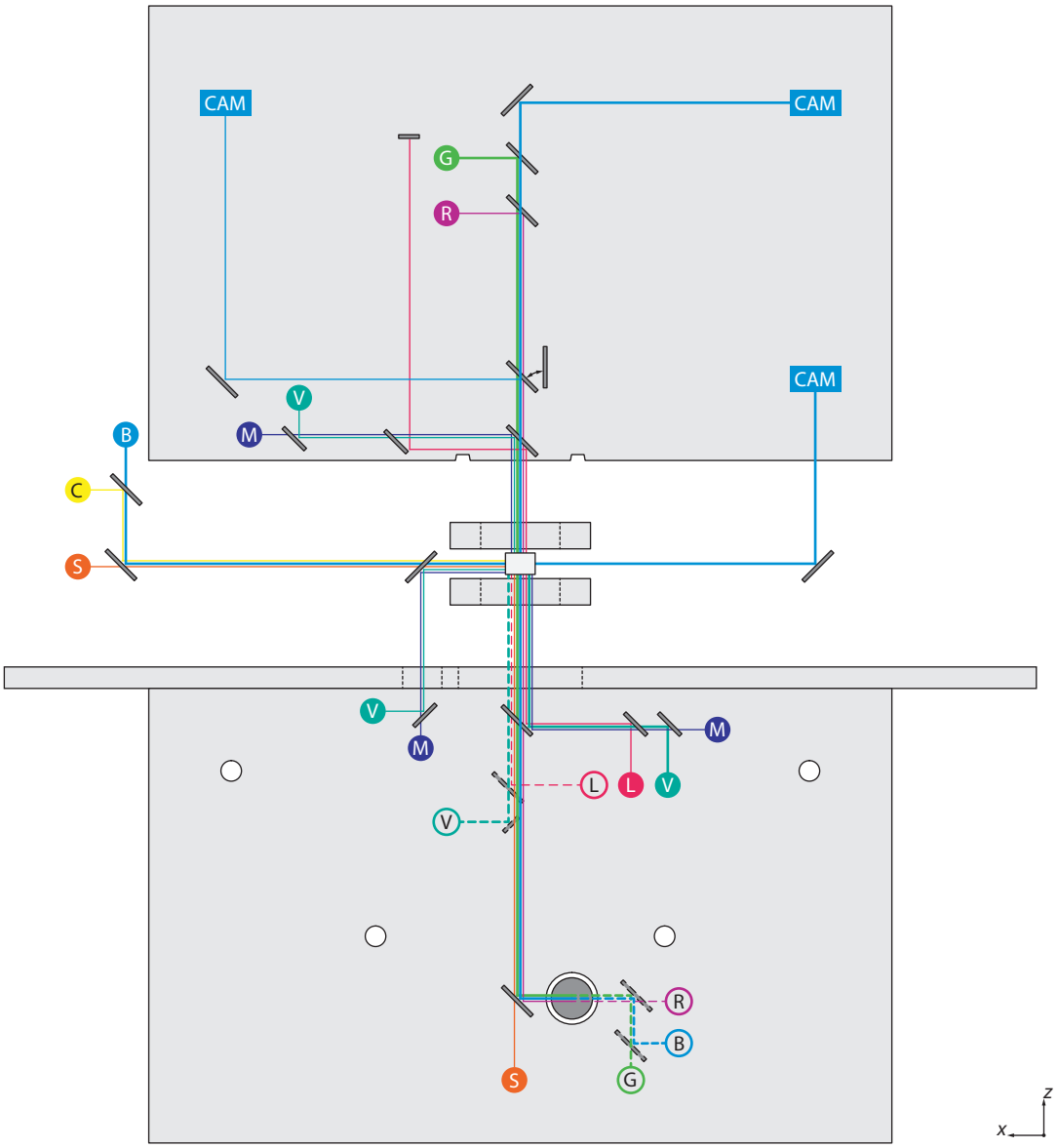

Figure 4.10 | Schematic setup of optics in the *x*–*z*-plane. Beams entering the science cell from any direction within the horizontal plane and their step-by-step superposition are shown schematically in a top view of the experimental setup, more details may be found in the text. The majority of the required optical elements is mounted on two horizontal breadboards, but along the *x*-axis the vertical breadboard is used as well. As in the case of the vertical breadboard, several of the branches shown above have not yet been implemented. A summary of the symbols and colour coding is given in figure 4.9.

Moreover, the camera of the imaging system along the x-axis has been mounted on this breadboard.

Recently, a 1D optical lattice at the magic wavelength and an additional beam for clock spectroscopy have been implemented on the z-axis as well. A second ODT at 1064 nm may eventually be set up and superimposed to the existing trap, *e.g.* to create a bichromatic trap for Rb-Yb mixtures,[217] and another pair of traps at these wavelengths may readily be implemented from the opposite direction (see also section 6.7). Beyond optical traps, beams at both repumping transitions of ytterbium may be superimposed onto the MOT beams in positive z-direction.

For mixture experiments, rubidium MOT beams may be superimposed to the existing beams of the ytterbium MOT. As in the case of the vertical breadboard, both sets of beams may be set up either in a retroreflection or as part of a six-beam configuration.

As illustrated in figure 4.10, the optical table, peripheral regions of the breadboards or even their bottom plane may be used to set up the initial superposition of beams, beam shaping or imaging optics, and the camera systems for detection. In fact, parts of the steering optics of the vertical ODT have been mounted to the horizontal breadboard from below.

Chapter 5

Laser cooling of ytterbium in a 2D-/3D-MOT system

In the experimental setup presented in the previous chapter, we have demonstrated 2D magneto-optical trapping of ytterbium for the very first time. A subsequent 3D-MOT using the intercombination transition of ytterbium is loaded directly from this 2D-MOT. Our 2D-/3D-MOT setup yields typical 3D-MOT loading rates of more than $1.5 \times 10^7\ s^{-1}$ for ^{174}Yb, and about 10^9 atoms may be collected in total (see figure 5.1). Based on these figures of merit, we have therefore successfully demonstrated that an ytterbium 2D-MOT is not only on a par with previously reported setups using Zeeman slowers,[76,77] but even achieves a substantially better performance in a highly compact, multi-species setup. As temperatures of a few 10 µK are achieved on the intercombination transition even in the absence of sub–Doppler cooling mechanisms, the 3D-MOT provides an ideal starting point for the subsequent creation of quantum-degenerate gases. Its large loading rates result in highly flexible overall cycle times, because quantum-degenerate gases of substantial size may be created at MOT loading times of only about 2 s, while longer loading times of typically 15 s result in slightly larger samples with strongly suppressed shot-to-shot number fluctuations.

In this chapter, the results obtained for our 2D-/3D-MOT setup are discussed in more detail. The fundamental setup of our 2D- and 3D-MOTs has been introduced briefly in the previous chapter. As presented in more detail in a brief summary (see section 5.1) of our setup, we are using retroreflected configurations for both MOTs. This is in stark contrast to the six-beam configuration used in many alkali 3D-MOTs, and we attribute the lack of advantages of this configuration in the case of ytterbium to its lack of efficient sub–Doppler cooling, especially in the bosonic isotopes, and the resulting insensitivity of the intercombination MOT to small imbalances of the MOT beams.

Spectral broadening of the 3D-MOT laser to a spectral width of 7 MHz full width a half maximum (FWHM) ameliorates the frequency selectivity of the intercombination transition and enhances the loading rate by more than a factor of six (see section 5.3). This comes at the expense of a temporary increase of temperature, but a brief single-frequency cooling phase concluding the loading cycle rapidly cools the 3D-MOT to temperatures of 20 µK and less (see section 5.6). A discussion of several pushing beam configurations is going to show that a simple red-detuned pushing beam at the principal transition enhances the loading rate by another factor of three (see section 5.4).

Besides being the first to trap and cool ytterbium or any other of the AEL elements with comparably high melting points, our 2D-MOT also demonstrates transverse loading 2D-MOT from a dispenser in a glass cell for the first time. Our experimental apparatus thus preserves many of the traditional benefits of 2D-MOTs that are loaded from background vapours, and the concept may be applied to other elements – especially other AEL element – as well. To assess the feasibility of transverse loading in an ytterbium 2D-MOT and direct loading of an intercombination 3D-MOT

we initially performed numeric simulations of Doppler cooling in our setup at different parameter sets (see appendix B). The results of this simulation supported our concept on both accounts, but already indicated the necessity of spectral broadening, which has turned out to be essential for efficient 3D-MOT loading. In an effort to characterise the performance of our 2D-MOT in more detail, we have therefore performed an extensive comparison of experimental loading rates to the results of our simulation covering a broad range of 2D-MOT parameters (see section 5.5). As a central conclusion, we found them to be in remarkably good agreement, and the simulation has accurately predicted the optimal operating parameters, which have been the foundation of our conception of the experimental setup. This result is particularly important for any possible transfer of the concept to other, similar AEL elements, and it once again emphasises that transverse loading may be an option to implement 2D magneto-optical trapping in other elements as well.

All of these initial experiments have been performed using ^{174}Yb, for it is the most abundant isotope and generally convenient to work with. Following the realisation of Bose–Einstein condensation in this isotope, however, we studied the performance of our 2D-/3D-MOT for ^{173}Yb, the promising fermionic, spin-5/2 isotope. As a detailed discussion (see section 5.9) is going to show, it is affected by the properties of the fermionic isotope in general and this one in particular. The most important of these is specific to the 2D-MOT, as it arises from the hyperfine splitting of the principal transition in ^{173}Yb. As discussed in section 5.9 (see also section 2.4), there is another hyperfine transition little more than two times the line width away from the $|^1\mathrm{S}_0, F = 5/2\rangle \leftrightarrow |^1\mathrm{P}_1, F' = 7/2\rangle$ transition used by the 2D-MOT. Although this allows operation of the 2D-MOT only within a small window of detuning and – even taking into account the lower abundance of ^{173}Yb – reduces the 3D-MOT loading rate substantially, the 3D-MOT itself is not affected significantly, and longer loading times may be used to balance its reduced loading rates. In conclusion, we will show that – despite these caveats – the overall performance of our 2D-/3D-MOT is comparable to systems based on Zeeman slowers, and that our setup is well suited for the creation and subsequent studies of degenerate Fermi gases.

The MOT laser systems have originally been set up by Hans Keßler[265] in the course of his diploma thesis ($^1S_0 \leftrightarrow {}^1P_1$ laser) and the author ($^1S_0 \leftrightarrow {}^3P_1$ laser). Both systems were later modified extensively by various team members. The entire team has been involved in performing the experiments discussed in this chapter. Data analysis and the numeric simulations reported below have been developed and performed by the author.

5.1 Laser systems

Operation of the 2D- and 3D-MOTs requires lasers at wavelengths of 399 nm ($^1\mathrm{S}_0 \leftrightarrow {}^1\mathrm{P}_1$) as well as 556 nm ($^1\mathrm{S}_0 \leftrightarrow {}^3\mathrm{P}_1$). Both of these laser systems will be reviewed in the subsequent subsections, including shaping of the MOT beams and other relevant technical details. The third subsection discusses the absorption imaging system along the z-axis, which is used to monitor the 3D-MOT. A second imaging system has been implemented with a focus on imaging ultracold samples (see section 6.3.6). Nevertheless, some measurements of small, compressed MOTs that are presented below have used this system.

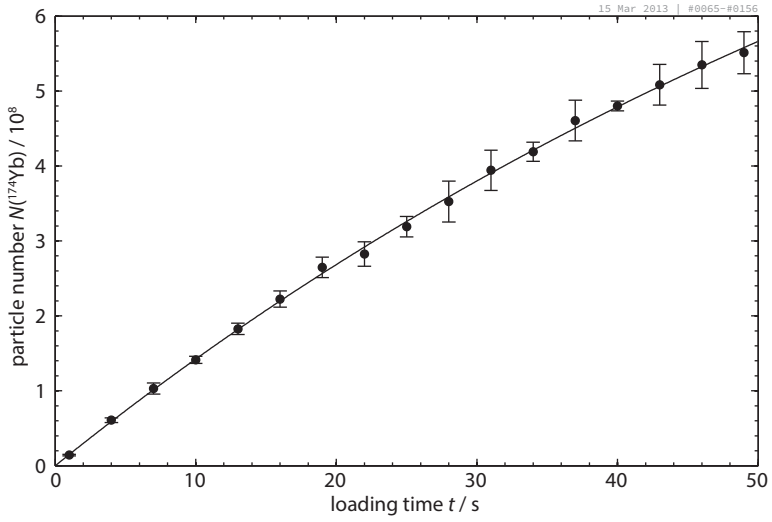

Figure 5.1 | Loading curve of the 3D-MOT for ^{174}Yb. The atom number of the 3D-MOT determined by a two-dimensional Gaussian fit after 5 ms time of flight is plotted as a function of loading time for the most abundant bosonic isotope ^{174}Yb. The solid line shows a fit of an exponential loading curve that yields a saturated atom number of $N_{\mathrm{sat}} = 1.24 \times 10^9$ and a time constant $\tau_{\mathrm{MOT}} = 82.0(15)$ s.

5.1.1 2D-MOT laser system (399 nm)

Light for the 2D-MOT and absorption imaging is generated by a composite laser system. An extended-cavity, GaN diode-laser* (ECDL) is locked to an atomic beam via fluorescence spectroscopy (see section 5.1.3) and serves as a master laser to inject several slave diodes for absorption imaging. Light for the 2D-MOT beams is generated by a commercial, high-power frequency-doubled diode-laser† with a tapered amplifier that is offset-locked to the master ECDL at a variable frequency offset.

The laser system has originally been set up by Hans Keßler, and a detailed discussion may be found in his diploma thesis.[265] At that time two injection-locked slave laser diodes were used to power each of the 2D-MOT beams at powers of approximately 50 mW per beam, and a series of acousto-optic modulators (AOMs) devised by Rodolphe Le Targat and the author allowed the detuning to be varied by several times the line width of the transition. In the process of setting up the 2D-/3D-MOT system, however, the slave diodes were replaced by the aforementioned commercial system for its higher output power. By offset-locking this laser, the 2D-MOT detuning may be varied on-line across an extremely wide range around resonance without any readjustments. Finally, the laser system has recently been moved to the same optical table as the experimental apparatus and retrofitted to allow free-space delivery of the beams. Beyond the mere increase in power available at the experiment, this modification had become necessary, as the optical fibres were damaged by the focussed beam and degraded significantly over time. In the current setup, typically 180 mW of laser power are available per 2D-MOT beam, and additional beams, *e.g.* for imaging and pushing, are produced by an injection-locked slave laser diode at variable detuning and powers.

The beam is delivered directly to the 2D-MOT breadboard where it is split into two branches. Each of them is shaped by a series of telescopes and waveplates to create an elliptic beam of approx-

*Nichia NDV4312 and NDV4313 diodes selected for wavelengths close to 400 nm are used.
†Toptica, TA-SHG pro (typ. output power: 375 mW).

imately 1 cm × 4 cm in diameter, where the long axis is oriented vertically.* After passing through the 2D-MOT cell the beams are retroreflected in a cat's eye configuration and reversing their circular polarisations. Razor blades on both sides of the cell are used to create defined lower edges of the beam and thus prevent the atomic beam from being deflected before entering the differential pumping stage.†

The additional pushing beam is delivered to the top breadboard shown in figure 4.7 and shaped by a custom fibre collimator that creates a focus within the DPS (see section 5.4). As discussed below, the alignment of the beam is highly delicate. The fibre collimator is mounted on a two-axis translation stage that provides full control in combination with a large-diameter steering mirror.

5.1.2 3D-MOT laser system (556 nm)

Two laser systems are currently available for laser cooling at the intercombination transition of ytterbium, the use of optical Feshbach resonances, and advanced techniques, *e.g.* the separation of spin components via the optical Stern–Gerlach effect[266] that has recently been demonstrated for ytterbium[267] and strontium.[268] Therefore, the setup of the 3D-MOT laser system has been and will be modified extensively to implement these additional features. The configuration described below has been used for all quantitative measurements reported herein, and changes with respect to the previous setup that has been used in early stages of our setting up the 3D-MOT are highlighted briefly.

Light for the 3D-MOT is generated by a commercial, frequency-doubled fibre-laser.‡ A few milliwatts are split off the primary beam and sent to the beam apparatus (see section 5.1.3) for stabilisation of the laser via fluorescence spectroscopy as in the case of the violet laser. The major part of the beam is passed through an AOM in a double pass and the differential detuning with respect to another, fixed-frequency AOM in the spectroscopy branch may be used to dynamically vary the common detuning of all 3D-MOT beams across a range of more than 10 MHz – allowing nearly arbitrary detuning given the narrow line width of the intercombination transition. Subsequently, the light is delivered to the optical table via a polarisation-maintaining, single-mode optical fibre (PMF), split into six beams using a commercial beam splitter cluster,§ and sent to the apparatus itself via individual non–polarisation-maintaining SMFs. The cluster allows precise, but variable distribution of power into each of the three 3D-MOT branches and among the two beams in each arm. In the current configuration nearly all light is passed to a single beam of each branch.

After adjusting its polarisation within the SMF via fibre polarisation controllers,[269] each beam is collimated to a diameter of 1.5 cm and sent to the science cell. Once again, two-axis translation stages carrying the collimators and steering mirrors allow complete geometric alignment of the beams. In the current setup, three beams are used and each of them is retroreflected in a cat's eye configuration set up in place of an opposed fibre coupler. The power is not distributed equally among the axial (z) and radial (x–y) beams. Typically, 16 mW are available in each radial beam, whereas 6 mW are diverted into the axial beam.¶

*At the aforementioned typical laser powers, this corresponds to a peak intensity of $I_{L,0} = 1.9 I_{L,sat}$.

†Alternatively, the upper DPS tube may be used to create such edges, but the results are inferior to using razor blades.

‡Menlo, orange one-SHG.

§Schäfter+Kirchhoff, Fiber Optical Beam Port Cluster $1 \rightarrow 6$. Designed for a wavelength of 556 nm.

¶This corresponds to maximum intensities of $I_{L,0} = 130 I_{L,sat}$ and $I_{L,0} = 45 I_{L,sat}$, respectively.

Because the aforementioned double-pass AOM is used to control the power in the 3D-MOT beams, it is currently not possible to vary the intensities of the beams independently; nor may any of the beams be turned on or off individually.

Initial experiments were performed in a similar configuration, but using a commercial frequency-doubled diode-laser* with a fibre amplifier and a six-beam MOT configuration. Here, additional low-power beams were available, *e.g.* for use as pushing beams. The setup was then successively modified by switching to the aforementioned fibre laser and later a retroreflected MOT configuration during optimisation of the 3D-MOT.

5.1.3 Beam apparatus

A simple vacuum apparatus is used to stabilise both MOT lasers to the resonant fluorescence of an atomic beam detected by photomultiplier tubes and using a lock-in technique to generate a dispersive signal. The ytterbium beam is produced by an oven at a temperature of about 425 degrees Celsius and collimated by two apertures. Further details on the locking scheme are found in the diploma thesis of Hans Keßler.[265] The residual Doppler broadening due to divergence of the atomic beam is about 50 MHz. Owing to the large line width of the principal transition $^1S_0 \leftrightarrow {}^1P_1$, we use Doppler-broadened spectroscopy for stabilisation of the 2D-MOT laser system, whereas the probe beam is retroreflected and Doppler-free spectroscopy is used for stabilisation of the 3D-MOT laser to the narrower intercombination transition $^1S_0 \leftrightarrow {}^3P_1$.

5.1.4 MOT imaging system (*z*)

Due to its limited field of view, the primary absorption imaging system, which has been set up mainly for imaging of quantum-degenerate ytterbium (see section 6.3.6), is inadequate for monitoring or even characterising large 3D-MOTs. A dedicated imaging system has been set up along the *z*-axis for this purpose, and the imaging beam is superimposed onto the axial MOT beam as shown in figure 4.10. An objective made from two commercial achromatic lenses produces an image of the MOT at a reduced scale ($M_{\mathrm{LA}} \approx 0.4$), which is then detected by a CCD camera† that acquires absorption and reference image in rapid succession.

5.2 Basic 2D-/3D-MOT of ytterbium

Even in a basic configuration, *i.e.* without the optimisations presented below, we have been able to demonstrate two-dimensional magneto-optical trapping of ytterbium emitted by the dispenser and subsequent loading of ytterbium into an intercombination 3D-MOT, albeit at very small loading rates. It has been particularly useful in identifying critical aspects of 2D- and 3D-MOT alignment as well as a viable range of operating parameters, both of which are summarised briefly in this section.

*Toptica, DL-FA SHG

†pco, pixelflyqe double shutter. Different cameras with anti-reflection coatings for wavelengths of either 399 nm or 780 nm have been used.

Due to stray light from the cooling laser beams, the 2D-MOT itself is hardly visible with the naked eye,* and we use inexpensive CCTV cameras to capture images of the MOT fluorescence.

For the most abundant, bosonic isotope ^{174}Yb, geometric alignment of the beams and external adjustment to the correct circular polarisations are sufficient to observe magneto-optical trapping of ytterbium emitted by the dispenser. It is strongest at magnetic field gradients around 54 G cm^{-1} and with the laser red-detuned by one to two times the line width (see the detailed analysis below).

During basic alignment, we then optimise the shape of the 2D-MOT and align it to the differential pumping stage. The MOT may be distorted significantly by imbalances of the radiation pressures exerted by the incoming and reflected beams, and careful alignment of the cooling beams is essential for an optimal shape. Due to the inevitable power loss of the reflected beam, a delicate balance of focussing and displacing the retroreflected beams needs to be found to produce an optimal 2D-MOT and an atomic beam that may be transferred through the differential pumping stage. To this end, the 2D-MOT needs to be aligned to the DPS by translating the magnetic coils, although its position and relative angle depend critically on the aforementioned local balance of radiaton pressures as well.

Once the 2D-MOT is aligned to the differential pumping stage, magneto-optical trapping of ytterbium at the intercombination transition may be observed in the science cell. Magnetic field gradients of a few gauss per centimetre or less are sufficient for the intercombination MOT due to its narrow line width. If the 3D-MOT laser is not broadened (see below), large detuning of several megahertz is required for trapping, however. For initial observation of a MOT, the laser is best ramped from large red detuning closer to resonance in several steps. It is clearly visible by the naked eye, and we use absorption imaging (see section 5.1.4) for alignment of the 2D- and 3D-MOTs using the loading rate as the figure of merit.

The 3D-MOT is fine-adjusted such that we observe loading of the 3D-MOT, even if the diameters of individual beams are reduced to a few millimetres. However, it is generally quite insensitive to imperfect alignment and rarely needs to be readjusted. In contrast, the alignment of the 2D-MOT

* Since the human eye is much more sensitive at 556 nm than at 399 nm, an additional laser beam at the intercombination transition may be sent through the DPS from below to produce clearly discernible fluorscence without introducing significant stray light.

Table 5.1 | Parameters of the 2D-/3D-MOT system. Power and detuning of the cooling and pushing beams as well as the magnetic field gradients in the MOTs, which are used during different stages of laser cooling discussed in this chapter, are summarised.

Component		Transition	Power / mW		Detuning / MHz	Gradient / G cm^{-1}
2D-MOT		$^1S_0 \leftrightarrow {}^1P_1$	180		−35	54
pushing beam		$^1S_0 \leftrightarrow {}^1P_1$	0.35		−20	n/a
3D-MOT	(loading)	$^1S_0 \leftrightarrow {}^3P_1$	16	(radial)	−6.7 [a]	1.9
			6	(axial)		
	(final)		0.17	(radial)	−0.74	7.1
			0.06	(axial)		

[a] Laser spectrum actively broadened to an FWHM ξ_{opt} = 6.9 MHz around this frequency.

is much more critical. Fine-adjustment may increase the 3D-MOT loading rate substantially and occasional readjustment is required.

In conclusion, a basic configuration is sufficient to demonstrate the feasibility of our 2D-/3D-MOT concept and MOT lifetimes on the order of a minute have been observed. As expected, however, the loading rate may be increased greatly in a more sophisticated setup – especially by spectrally broadening the 3D-MOT laser and implementing a pushing beam.

5.3 Broadband MOT

It has already been pointed out that the intercombination transition of ytterbium is highly velocity-selective due to its narrow line width and severely limits the capture range of a MOT using this transition (see sections 2.4.2 and 3.3). Its capture velocity is only about 2 m s^{-1} under typical circumstances.[153]

Efficient loading from the 2D-MOT requires much larger capture velocities, however. Results of our numeric simulation of two-dimensional magneto-optical trapping (see appendix B) for the loading rate of a 3D-MOT as a function of its capture velocity are shown in figure 5.2. According to their predictions, a capture velocity of about 10 m s^{-1} or more is required to achieve substantial loading rates. Furthermore, the results clearly indicate that optimal 2D-MOT parameters for loading a 3D-MOT depend on its capture velocity as well. The simulation suggests that the greater overall flux at large field gradients comes at the cost of reduced flux of slow atoms, *i.e.* for a specific capture velocity there will be an optimal combination of magnetic field gradient and laser detuning (see section 5.5).

To extend the capture range of the intercombination MOT, we spectrally broaden the cooling light by rapidly modulating its detuning using the double-pass AOM in the laser system (see section 5.1.2). It allows modulation of the laser frequency with an effective maximum FWHM $\xi_{\max} \geq 15$ MHz. We typically use a modulation frequency of 200 kHz, *i.e.* on the order of the transition line width. The additional frequency components create radiation pressure across a broader range in frequency space than a single component and thus increase the capture velocity of the MOT. The bias detuning is matched to keep the minimum absolute detuning from resonance constant and to enhance the effect of broadening the laser. Moreover, substantial power spectral density on resonance would introduce additional heating in the MOT itself.

Experimental results demonstrating the effect of spectral broadening are shown in figure 5.3.

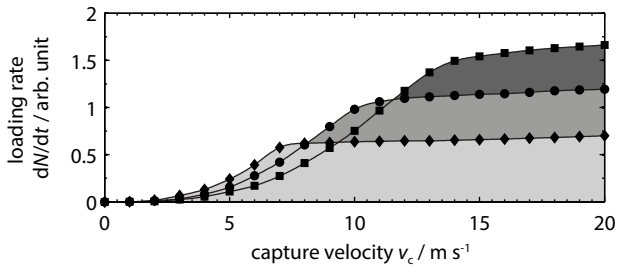

Figure 5.2 | Influence of the capture velocity on the 3D-MOT loading rate. Loading rates of a 3D-MOT have been plotted as a function of its capture velocity based on numerical simulations of the 2D-MOT. Results are shown for three selected magnetic field gradients of 40 G cm^{-1} (⧫), 55 G cm^{-1} (●) and 70 G cm^{-1} (■), at laser detuning of $\Delta_{2D}/\Gamma = -1.4$, -1.2 and -1.1, which yields optimal maximum loading rates. They reveal a distinct dependence of the 3D-MOT's loading efficiency and optimal parameters on its capture velocity.

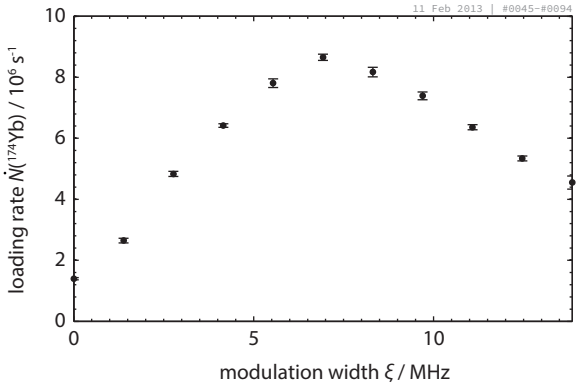

Figure 5.3 | Enhancement of the loading rate by spectral broadening. Loading rates of the ^{174}Yb 3D-MOT have been measured for a sequence of spectral broadening amplitudes. The high-frequency edges of the spectrum have been kept at a constant detuning of $\Delta_{3D}/2\pi = -3.2$ MHz from the intercombination transition $^1S_0 \leftrightarrow {}^3P_1$ by adjusting the bias detuning accordingly. The loading rate has been calculated from the atom number in the MOT after 2 s of loading assuming a linear loading behaviour at these time scales.

The loading rate initially increases steeply with modulation amplitude ξ and reaches a distinct maximum near $\xi_{opt} = 6.9$ MHz where the loading rate is enhanced by a factor of 6.2(2). At larger detuning $\xi > \xi_{opt}$, however, the loading rate declines slowly. While figure 5.2 implies that the loading rate eventually saturates with increasing capture velocities, this behaviour is readily understood considering the experimental situation. The same amount of total laser power is distributed among an increasing number of spectral sidebands, and the power spectral density inevitably decreases. Beyond ξ_{opt}, additional broadening thus decreases the effective capture velocity.

In conclusion, spectral broadening of the laser is a highly efficient means of increasing the loading rate. Although the capture velocity may be increased further by using larger broadening amplitudes at increased laser power, the loading rate will eventually saturate and may possibly increase only slightly. The optimum loading rate of the measurement shown in figure 5.3 is $8.66(10) \times 10^6$ s^{-1}. Recent optimisations, have increased this figure further to $15.1(3) \times 10^6$ s^{-1} as shown in figure 5.1, and it represents the typical loading rate for ^{174}Yb as of the writing of the thesis, *i.e.* including other improvements like as the pushing beam.

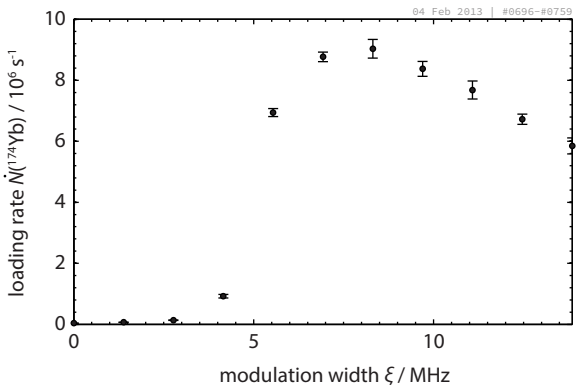

Figure 5.4 | Effect of spectral broadening without matched bias detuning. Loading rates of the ^{174}Yb 3D-MOT have been measured for the same sequence of spectral broadening amplitudes as in figure 5.3. During these measurements, however, the bias detuning was kept at a constant value, which had been chosen to yield a near-optimal maximum loading rate. Below its optimal broadening amplitude, the inappropriate bias value reduces the loading rate substantially.

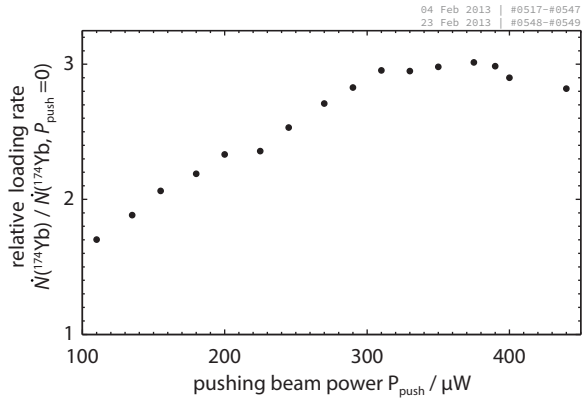

Figure 5.5 | Enhancement of the loading rate by a pushing beam. Loading rates of the spectrally broadened 3D-MOT for ^{174}Yb have been measured for a number of pushing beam powers with respect to the loading rate without any pushing beam. Details on the setup of the beam are given in the text.

5.4 Pushing beam

It is well known from alkali 2D-MOTs that additional pushing beams or even a moving molasses ($2D^+$-MOT[97]) may be used to enhance the transfer efficiency from 2D- to 3D-MOTs substantially. The additional radiation pressure of a pushing beam is used to match the velocity distribution emerging from the 2D-MOT to the capture range of the 3D-MOT and to enhance the transfer of axially slow atoms. We have tested several configurations of pushing and optional slowing beams in our 2D-MOT and found up to a three-fold enhancement of the loading rate.

The best results have been obtained with a single pushing beam near the principal transition $^1S_0 \leftrightarrow {}^1P_1$. Although the pushing beam itself is dumped within the differential pumping stage in order not to disturb the 3D-MOT at the weaker intercombination transition, it pushes the atomic beam of the 2D-MOT through the differential pumping stage. As shown schematically in figure 3.1, the beam has a diameter of a few millimetres within the 2D-MOT volume, but it is focussed into the lower graphite tube and has been aligned slightly off its axis to be dumped. Light for the pushing beam is derived from one of the slave diodes (see section 5.1.1). Its intensity and detuning may be controlled independently from the 2D-MOT beams, and the laser is typically detuned by $\Delta_{\mathrm{push}}/2\pi = -20$ MHz from resonance.

A pushing beam as presented in the previous paragraph enhances the loading rate of the intercombination typically by a factor of three, as is illustrated by figure 5.5. However, the alignment of the beam is extremely delicate – in particular, similar enhancement factors may be achieved for different alignments at different beam powers. The power values given in figure 5.5 should thus be considered mainly an example intended to demonstrate that the optimal effect of the pushing beam in a given alignment does not depend critically on its power.

In contrast, we have observed no discernible effect of similar pushing beams near the intercombination transition in our setup. Another alternative configuration used a pushing beam that passed through the differential pumping tube and a counterpropagating "slowing" beam to achieve an overall enhancement. While it did yield an overall increase in loading rate, the presence of these beams – tuned close to the strong principal transition – in the science cell disturbed the 3D-MOT significantly and limited its size. Therefore, this configuration was abandoned in favour of the simple, yet more efficient single pushing beam that avoids noticeable disturbance of the 3D-MOT altogether.

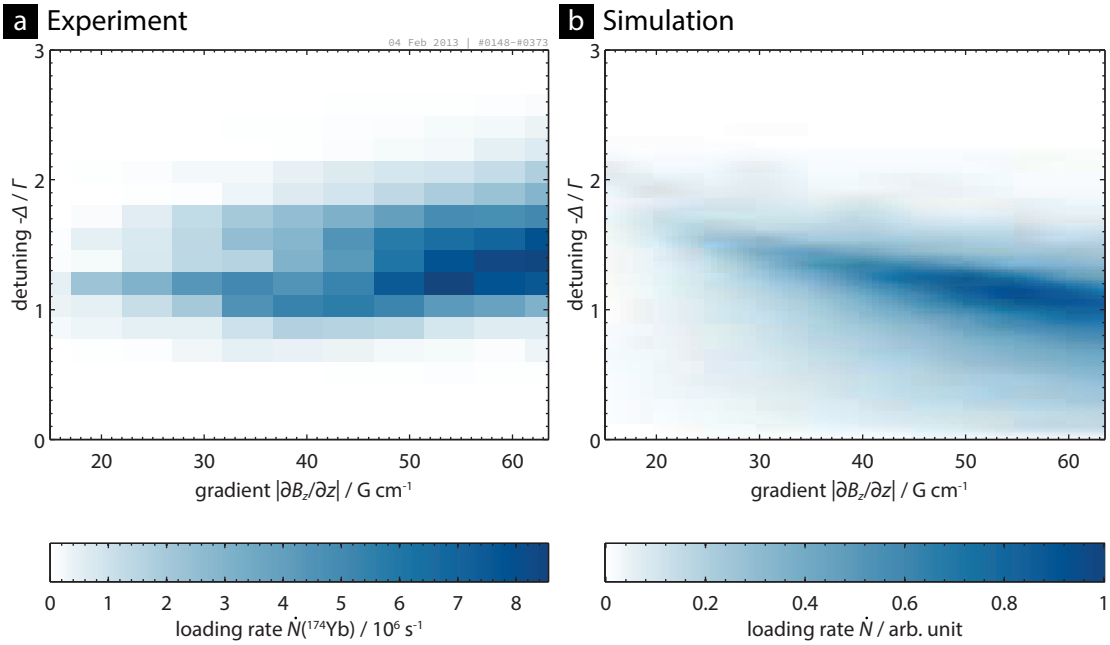

Figure 5.6 | Optimal 2D-MOT parameters. Experimental data for ^{174}Yb **(a)** and loading rates of the intercombination 3D-MOT obtained from a numeric simulation **(b)** are plotted as a function of the 2D-MOT parameters, detuning and magnetic field gradient. Optimal loading is achieved at a gradient of 54 G cm^{-1} and a detuning of $\Delta_{2D}/\Gamma = -1.2$ in both cases. For the evaluation of the simulation, a capture velocity $v_c = 10$ m s^{-1} and an accepted angle $\theta_c = 1.8°$ (*cf.* figure 4.3) have been assumed for the intercombination MOT. A detailed discussion of the numeric simulation is given in appendix B.

5.5 Optimal 2D-MOT parameters

Optimal detuning and magnetic field gradient, which yield a maximum loading rate of the 3D-MOT, are determined both by the 2D-MOT setup itself and by the properties of the 3D-MOT. As discussed briefly in section 5.3, our numeric simulation of the 2D-MOT indicates that the low-velocity fraction of the atomic beam produced by the 2D-MOT is actually suppressed at too large a magnetic field gradient. Results of this simulation have been used to estimate the required magnetic field gradients during the construction of the 2D-MOT coils and as an initial estimate of the best 2D-MOT parameters.

In order to determine these optimal parameters exactly for our 2D-/3D-MOT setup, we have measured the loading rates of the intercombination 3D-MOT, including spectral broadening and the pushing beam, across a broad range of 2D-MOT parameters, and the results are shown in figure 5.6a. Optimal loading of the 3D-MOT is achieved at a magnetic field gradient of 54 G cm^{-1} and a 2D-MOT detuning $\Delta_{2D}/\Gamma = -1.2$, and we usually operate the 2D-MOT at these parameters. Nevertheless, loading rates are reasonably large across a wide range of magnetic field gradients around this optimum, whereas the 2D-MOT only works within a small window of detuning.

It is highly interesting to compare these experimental results to our numeric simulation of the 2D-MOT. Results for equivalent conditions, including the geometry and average intensity of the MOT beams, are shown in figure 5.6b. Their overall agreement with the experimental data is quite

remarkable – especially if the simplified model that the simulation is based upon as well as the delicate influence of experimental imperfections are taken into account. For instance, the simulation's failure to reproduce the dependence of the optimal detuning on the magnetic field gradient may be owed to its assuming homogeneous intensity profiles instead of Gaussian distribution for the 2D-MOT beams. Most importantly, however, the optimal 2D-MOT parameters predicted by the simulation are in excellent agreement with the experimental results. In conclusion, the numeric simulation has proven itself a valuable tool for analysing the performance of the 2D-MOT. The effect of major modifications of the 2D-MOT may be estimated in advance, and it may even provide an assessment of similar 2D-MOTs for similar elements like strontium.

5.6 Temperatures and the single-frequency MOT

While the broadband 3D-MOT discussed in section 5.3 is ideal for fast, highly efficient loading from the 2D-MOT, low temperatures cannot be realised in this configuration, for it needs to be operated at maximum laser power to take the most advantage of spectral broadening. We have found typical temperatures of some 570 µK, *i.e.* two orders of magnitude larger than the Doppler limit of the intercombination transition. Clearly, efficient transfer of the atomic sample into an ODT for subsequent evaporative cooling is not possible directly from the broadband MOT, but much lower temperatures are required.

To achieve this goal, the loading phase using a broadband MOT is followed by a final, single-frequency cooling phase of the 3D-MOT, in which the temperature is reduced as close to the Doppler temperature (see section 2.4.2) as possible. Compared to typical 3D-MOT loading durations of up to several 10 s, it is extremely brief. First, the broadening amplitude is gradually decreased to zero over the course of typically 200 ms. Both the bias detuning and the laser power are reduced as well to match the reduced broadening. For another 200 ms, the atomic sample is then held in the single-frequency MOT at a detuning of typically $\Delta_{3D}^{(sf)}/2\pi = -740\,\mathrm{kHz}$ and minimal powers of 170 µW (60 µW) in the diagonal (axial) MOT beams. Its temperature is reduced to typically 20 µK for strong compression as required by subsequent transfer to the dipole trap (see section 5.7). In moderately compressed MOTs, slightly lower temperatures of about 13 µK have been observed.

Although temperatures like these are still larger than the Doppler temperature, they are more than sufficient for loading the atomic sample into a deep ODT (see section 6.4). Furthermore, they are similar to the best values reported for other ytterbium MOTs (*cf.* section 2.4.2), possibly due to common practical limitations of Doppler cooling on a narrow transition.

5.7 Compression

In parallel to the single-frequency cooling phase, the MOT is usually compressed by increasing the magnetic field gradient from its value of typically $1.9\,\mathrm{G\,cm^{-1}}$ (1.5 A) used during the broadband MOT stage. A steep final gradient of about $7.1\,\mathrm{G\,cm^{-1}}$ (5.5 A) is applied for subsequent transfer to the crossed dipole trap. It results in a highly compressed MOT and yields optimal transfer efficiency into the optical trap (see section 6.4.1). However, lower final gradients resulting in moderate compression are used frequently, *e.g.* for loading rate measurements and other measurements on the MOT itself.

5.8 Intercombination MOT at large detuning

At large detuning and small magnetic fields gradients, atoms trapped by a MOT using a narrow intercombination transition experience radiation pressure from the trapping beams only within a thin shell around its centre, where the detuning is balanced by the Zeeman shift (see 2.4.2). Under the influence of gravity, the atomic sample is then trapped at the bottom of the cell. The effect is well known from the particularly narrow intercombination transition of strontium,[166] and we have observed a similar behaviour in our ytterbium 3D-MOT.

This regime is quite peculiar, for the atomic sample is supported against gravity and cooled mainly by the up bound diagonal beams, whereas the counterpropagating down bound beams do not participate positively in magneto-optical trapping anymore. Here, the temperature of the MOT is insensitive to detuning that merely determines the radius of the aforementioned shell. However, we have found this regime unfit for subsequent loading of ytterbium into our crossed dipole trap due to the low density and large displacement of the MOT.

5.9 Fermion MOT

All of the various optimisations and characterisations of the 2D- and 3D-MOTs discussed in the previous sections have been initially been performed using the most abundant, bosonic isotope ^{174}Yb. Owing to the similarity of all bosonic isotopes, we expect magneto-optical trapping of the other four bosons to work along the same lines and produce similar results. As illustrated by figure 5.1 their lower abundances may readily be balanced by a longer loading cycle of the 3D-MOT. In contrast, the two fermionic isotopes, ^{171}Yb and ^{173}Yb, are not only more interesting for future experiments, but may require modification of the 2D- and 3D-MOT due to their nuclear spin. For instance, sub–Doppler cooling of these isotopes (see section 2.4.2) may lead to a reduction of the final MOT temperature and thus enhance the efficiency of evaporative cooling in the crossed dipole trap.

Following our initial experiments to realise quantum-degenerate gases of the bosonic isotope ^{174}Yb, magneto-optical trapping of fermionic ^{173}Yb in our 2D-/3D-MOT setup has recently been demonstrated. Transitioning to ^{174}Yb requires extensive realignment of the 2D-MOT, and its initial alignment is more difficult than for ^{174}Yb, because it is not readily visible on CCD cameras due to its much weaker fluorescence. Optimisation of the 3D-MOT loading rates works along the same lines as for its bosonic counterpart. Both a broadband MOT and a pushing beam are used for ^{173}Yb as well, albeit at modified parameters.

Initial results revealed that the loading rates of ^{173}Yb are much smaller than those of ^{174}Yb even if its lower abundance is taken into account. This behaviour was not unexpected, and may possibly be owed to a relative insensitivity of the bosonic 2D-MOT to experimental imperfections. In fact, these results suggested that even more power in the 2D-MOT beams is required for ^{173}Yb than for the bosons. Nevertheless, several fundamental effects may impede operation of the MOTs, and they are discussed briefly in this paragraph. In general, the effective restoring force of a MOT is reduced in most fermionic AEL atoms.* Owing to the unusual Zeeman splitting of their cooling transitions for these isotopes (see figure 2.5), almost half of the magnetic substates do not experience any

*Notably, this is not the case for ^{171}Yb, which has only magnetic substates in $^1S_0(I = 1/2, m_F = \pm 1/2)$.

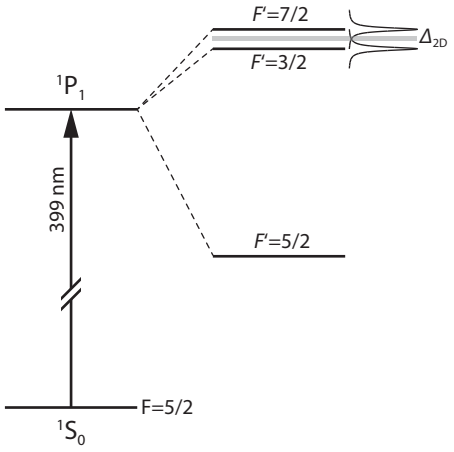

Figure 5.7 | Hyperfine structure of the $^1S_0 \leftrightarrow {}^1P_1$ transition in ^{173}Yb. Due to the proximity of the $F = 5/2 \leftrightarrow F' = 3/2$ hyperfine transition to the $F = 5/2 \leftrightarrow F' = 7/2$ transition used for magneto-optical trapping, the performance for the 2D-MOT is degraded. A range of detuning from $-\Gamma$ to -1.6Γ for operation of the 2D-MOT has been highlighted. Lorentz profiles with the natural line width of the transition are shown next to the $F' = 7/2$ and $F' = 3/2$ levels and illustrate the overlap of both transitions at this detuning.

restoring force on the $F \leftrightarrow F' = F + 1$ hyperfine transition, but optical pumping is sufficiently rapid in ytterbium MOTs to give rise to a reduced average restoring force.*

Cooling in the 2D-MOT is complicated in the specific case of ^{173}Yb by the hyperfine structure of its principal transition $^1S_0 \leftrightarrow {}^1P_1$. As discussed in 2.4.1, its $F = 5/2 \leftrightarrow F' = 3/2$ hyperfine transition is close to the $F = 5/2 \leftrightarrow F' = 7/2$ transition used by the 2D-MOT. At typical detuning, the 2D-MOT lasers are therefore blue-detuned from the other hyperfine transition by about one line width.† However, optical pumping in the MOT suppresses scattering of photons on this transition, since atoms pumped into one of the stretched states $m_F = \pm 5/2$ by $\sigma^\pm$ light may only absorb photons of the opposite circular polarisation on the $F = 5/2 \leftrightarrow F' = 3/2$ transition.

Early results for ^{173}Yb have been included in our recent publication.[1] They have motivated a number of modifications to our experimental setup, *e.g.* the relocation of the 2D-MOT laser system discussed in section 5.1.1, most of which have been implemented during the writing of this thesis. As a preliminary result, the typical loading rate of the 3D-MOT has been increased to about $2 \times 10^6\ s^{-1}$. Our 2D-/3D-MOT setup is thus comparable or even superior to previously reported Zeeman slower–based setups.[100] More details on the performance of the ^{173}Yb-MOTs may be found in the doctoral thesis of Alexander Thobe, who has performed most of the recent experimental work on the fermionic MOTs.

*In contrast, the much narrower intercombination transition of strontium requires use of a "stirring" laser.[270]

†Due to the reversed sign of the Landé factors in the $F' = 3/2$ and $F' = 3/2$ hyperfine states of $^1P_1$, the second hyperfine transition gives rise to a restoring force in the same magnetic field at blue detuning.

Chapter 6

All-optical creation of quantum-degenerate gases

After preparing laser-cooled ytterbium at temperatures of a few 10 µK in a compressed MOT, we generate quantum-degenerate gases of ytterbium by forced evaporative cooling in a crossed optical dipole trap (XDT). As discussed in section 6.1, all-optical methods are necessary to achieve quantum degeneracy in ytterbium, but they allow highly efficient evaporative cooling from large initial phase-space densities. In our setup, atoms are transferred into a vertical crossed optical dipole trap (VXDT) that consists of a deep horizontal ODT with an effective trap depth of up to $V_{\mathrm{eff}}/k_{\mathrm{B}} = 0.61$ mK, which initially traps the atomic sample, and a vertical ODT creating the crossed region (see section 6.2). These beams are delivered to the apparatus either via free space or a PMF and shaped by compact objectives as presented in section 6.3.

Forced evaporative cooling of ytterbium in our XDT is carried out by lowering the trap depths in two phases over the course of about 5 s (see section 6.4). Atoms are first cooled in the horizontal trap only and successively concentrate in the crossed region, where they are cooled to quantum degeneracy in a second step. We routinely produce nearly pure BECs of 1×10^5 ^{174}Yb as well as quantum-degenerate Fermi gases of 2×10^4 ^{173}Yb atoms at $T = 0.15T_{\mathrm{F}}$, although temperatures as low as $T = 0.09T_{\mathrm{F}}$ have been achieved at the expense of lower particle numbers. These figures in general and the low temperature of our degenerate Fermi gases in particular are extremely promising for future experiments in optical lattices, *e.g.* studies of fermionic systems by ultrahigh-precision spectroscopy. In comparison to other recently published experiments,[77,227,271] our experimental apparatus based on a novel 2D-/3D-MOT has thus proven itself highly competitive.

Owing to the necessity of providing initial trap depths equivalent to several 100 µK, the VXDT has been designed as a compromise between large initial depths and small final trapping frequencies in the ultracold regime – even more so, as the trap depths and initial trapping frequencies of both beams have been planned conservatively. However, our apparatus supports the realisation of various ODT configurations (see section 4.3), and we have planned the implementation of additional dipole trap at a later stage (see section 6.7). These traps will be designed specifically for the ultracold regime, *i.e.* with a focus on small trapping frequencies, but not large initial depths, and to allow optimal transfer into optical lattices that are being set up as of the writing of this thesis.

The VXDT presented in this chapter has been designed and set up by the author. Experimental work on evaporation, Bose–Einstein condensation of ^{174}Yb, and Fermi degeneracy of ^{173}Yb has been performed by the entire project team, but the recent experiments on Fermi degenerate gases have been conducted during the writing of this thesis and hence without active participation of the author. The measurements of collective excitations for the determination of trapping frequencies have been performed by the author. Data analysis of the experimental results has been developed and performed by the author.

6.1 Evaporative cooling in optical dipole traps

Since the ground state of ytterbium cannot be trapped magnetically (see section 2.4), optical dipole traps (ODTs) have to be used to produce quantum-degenerate gases. Although a variety of all-optical cooling methods[272–275] have been demonstrated, quantum gases of AEL elements are usually created in crossed optical dipole traps (XDTs) following similar procedures.

Evaporative cooling in an ODT mainly exploits the finite depth of the trap, which allows atoms of sufficient energy, *e.g.* resulting from a collision, to escape from the trap and remove a large amount of energy in the process. Forced evaporative cooling may then be achieved by continuously decreasing the power of the beam and thereby the trap depth V_0. The procedure is highly efficient, *i.e.* a large increase of phase-space density is achieved by a small decrease in atom number, if the trap depth V_0 is kept much larger than the average thermal energy $k_\mathrm{B}T$ of a trapped atom. A detailed analysis of evaporation in optical traps is given by O'Hara *et al.*[276] The collision rate, *i.e.* rethermalisation, decreases during evaporation in a static geometry, but actual experiments use trap geometries that effectively change during evaporation (see below) to achieve fast rethermalisation in the final stages of evaporation.

Elastic collisions are crucial for fast rethermalisation during evaporation. Several isotopes of ytterbium, including the fermionic ^{171}Yb, are not suitable for direct evaporative cooling due to their weak atomic interactions at low temperatures, and sympathetic cooling, *e.g.* by another isotope, may be used in these cases (see section 2.6 for details). Owing to their favourable scattering properties and large abundances, we have therefore chosen the bosonic isotope ^{174}Yb as well as fermionic ^{173}Yb for demonstrating and optimising the production of ytterbium quantum gases in our setup, as discussed below.

6.2 A vertical crossed dipole trap

Evaporative cooling of AEL elements has been demonstrated in several basic configurations of XDTs,[76,77,79] and either of these configurations may in principle be implemented at our experimental setup (see section 4.3). This flexibility notwithstanding, we have decided to implement a vertical crossed optical dipole trap (VXDT), as illustrated by figure 6.1, for several reasons (see appendix D for a brief summary of ODT potentials).

In this configuration, the horizontal beam primarily supports the trapped atoms against gravity, but provides little confinement along its axis of propagation (z). In contrast, the restoring force of the vertical trap against gravity is negligible, but it provides confinement in both horizontal directions, and together both beams create a tightly confined crossed region. Since the effective trap depth is dominated by the horizontal beam and initial potential depths equivalent to several 100 µK are required, a tightly focussed, high-power beam needs to be used in the horizontal direction. Therefore, it has been designed as a trade-off between large initial trap depths and suitable trapping frequencies on the order of 100 Hz in the ultracold regime. In contrast, substantially larger waists and less power may be used for the vertical beam, since only moderately large nominal potential depths and trapping frequencies are required to sustain a suitably high density for fast rethermalisation.

Due to its single high-power beam and asymmetric design, the VXDT allows great flexibility,

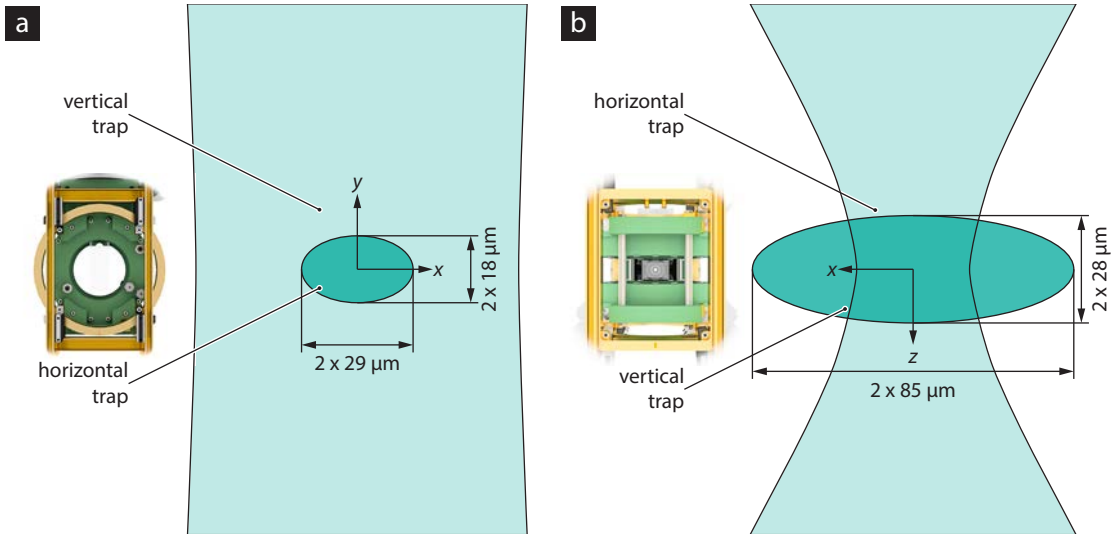

Figure 6.1 | Vertical crossed optical dipole trap. The configuration of the crossed dipole trap is shown in focal plane of **(a)** the horizontal and **(b)** the vertical dipole trap. The CAD images on the left illustrate the perspective.

e.g. in balancing initial trap depth and final trapping frequencies, and largely independent control of certain trapping frequencies and the trap depth.

6.2.1 Elliptic beams

The performance of the VXDT configuration in the ultracold regime is improved substantially by using elliptic beams for both of its branches.

In the case of the horizontal trap, the beam is focussed more tightly in the vertical than in the horizontal direction, as illustrated in figure 6.1. In comparison to a circularly shaped beam of the same maximum trap depth, the horizontal trapping frequency ω_x (see section D.2) is thus reduced at the cost of a larger vertical frequency ω_y. In deep traps, where gravity is negligible, the scaling of these trapping frequencies follows equation (D.7), *i.e.* $\omega_i \propto \sqrt{{w_{0,i}}^{-1}}$ $(i = x, y)$. However, an elliptic trap as described above provides a stronger restoring force to balance gravity, and its lateral trapping frequencies are reduced with respect to that scaling law at small effective trap depths V_{eff} (see section D.3 for details). A moderate aspect ratio of about two has been planned for this trap. Larger aspect ratios may effectively deteriorate the overall performance of the trap, since the vertical trapping frequency is increased even further and the anharmonicity of the potential is more pronounced at small waists. Moreover, the influence of technical imperfections is expected to become a serious limitation at this level due to the increased sensitivity of the trap to aberrations, mechanical vibrations and power fluctuation (*cf.* section 6.3).

In contrast, choosing an aspect ratio for the vertical trap is a subtler process, since this trap primarily affects the horizontal trapping frequencies, but not the trap depth. The horizontal beam provides little confinement along its axis of propagation, and the frequency ω_z is consequently dominated by the vertical trap, whereas the contributions of the two traps to the second frequency

ω_x may well be comparable. As illustrated in figure 6.1, we have designed the vertical ODT to use an elliptic beam of a moderate aspect ratio where the short axis is oriented along z, *i.e.* the axis dominated by this trap. In consequence, the large waist along x strongly suppresses its influence on the trapping frequency along that axis. The intention of this choice has been to achieve almost independent control over the two trapping frequencies. For example, the vertical trap may be used to match the two horizontal frequencies without significantly increasing ω_x in the process. In particular, trap geometries ranging from highly prolate to moderately oblate along z may be realised by varying ω_z via the power of the vertical trap.

These advantages notwithstanding, the effect of a particular choice of minimal waists for the elliptic vertical beam and their orientation on evaporative cooling of ytterbium remains to be investigated experimentally. In the elongated trap created by the horizontal beam, its orientation as shown in figure 6.1 creates a strong axial confinement at a given depth of the crossed region along z. Its effect may range from enhancing density-dependent losses, *e.g.* due to three-body collisions, to enhancing evaporation if large densities are required to achieve fast thermalisation of less strongly interacting isotopes.

6.2.2 Choice of wavelength

Our optical setup has been constructed to support ODTs at wavelengths of both 532 nm and 1064 nm (see section 4.3), and high-power laser systems for both wavelengths are available in our laboratory. For evaporative cooling of ytterbium, we have nevertheless decided to use dipole traps at the former wavelength ($\lambda_{\mathrm{ODT}} = 532\,\mathrm{nm}$), because the angle of divergence ($\theta_{\mathrm{div}} = w_0/z_{\mathrm{R}} = \lambda/\pi w_0$) of the horizontal beam may otherwise become problematic. For simplicity, the same wavelength has been selected for the vertical trap, but there is no practical reason not to use the latter wavelength for this or other traps in the future.

As discussed in section 2.8, the traps are sufficiently far detuned from any ground state transition of ytterbium to create deep optical potential without significant photon scattering. A reasonable estimate of the photon scattering rate is given by the contribution of the principal transition ${}^1\mathrm{S}_0 \leftrightarrow {}^1\mathrm{P}_1$ of $\Gamma_{\mathrm{sc}}/I_{\mathrm{L}} = 0.16\,\mathrm{s}^{-1}/(\mathrm{MW\,cm}^{-2})$ according to equation (2.7). Due to its narrow line width, the contribution of the intercombination transition is about three orders of magnitude smaller, while the laser is detuned even further from all other transitions.

Table 6.1 | Parameters of the crossed dipole trap as illustrated by figure 6.1. Measured minimum waists and maximum powers as discussed in section 6.3 are summarised and have been used to compute the trap depth and trapping frequencies at maximum power (see equations (D.2), (D.7), and (D.8)).

Axis	P_{max}/W	w_0/μm	χw_0/μm	$k_{\mathrm{B}}^{-1} V_0$/μK	$(2\pi)^{-1}\omega_i^{(\mathrm{max})}$/Hz		
					x	y	z
horizontal	9.0	17.7(8)	29.5(7)	620	1.9×10^3	3.1×10^3	16
vertical	1.35	28.4(8)	85.0(2)	20	348	1.0	116

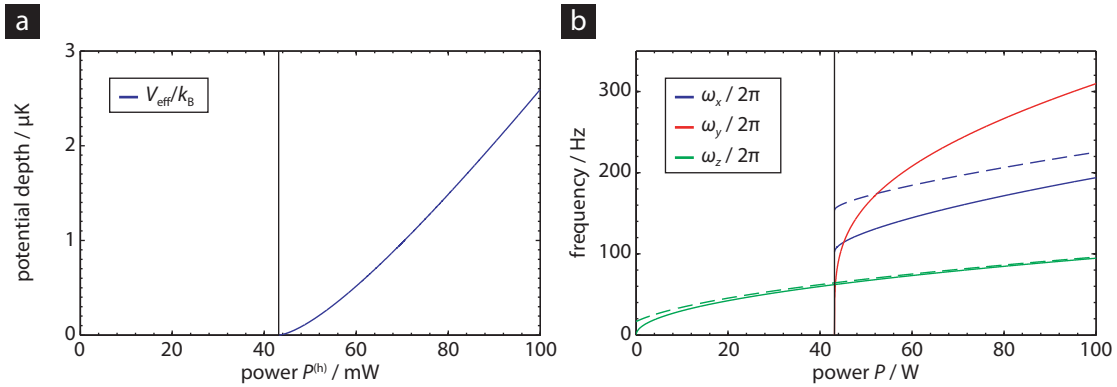

Figure 6.2 | Effective depth and trapping frequencies of the crossed dipole trap at low powers. **(a)** The effective potential depth V_{eff}/k_B of the trap is determined by the horizontal beam, whereas the contribution of the vertical beam is negligible. Here, it has been plotted as a function of power in the horizontal trap close to the critical power, which is represented by a solid black line. **(b)** Trapping frequencies $\omega_i/2\pi$ have been plotted as a function of power in the dominant beam. For the cases of $\omega_{x,y}$ the power $P^{(h)}$ of the horizontal beam is varied at constant power $P^{(v)} = 35$ mW (solid line) and 1.35 W (dashed line), respectively. In contrast, ω_y is plotted as function of the power $P^{(v)}$, whereas $P^{(h)}$ is kept constant at 45 mW (solid line) and 10 W (dashed line).

6.2.3 Trap parameters

The result of all of these considerations is the VXDT configuration shown schematically in figure 6.1, and table 6.1 summarises its parameters based on the measured waists of the actual ODT beams (see section 6.3 for details). The effective depth $V_{eff}/k_B = 0.61$ mK of the horizontal trap is more than sufficient to transfer atoms from an intercombination MOT of few 10 μK. The crossed region created by the vertical branch has a maximum potential depth equivalent to 20 μK within this elongated trap. Finally, estimated photon scattering rates at full power of $\Gamma_{sc}^{-1} \approx 5.6$ s and 172 s for the horizontal and vertical trap, respectively, are more than sufficient for evaporation as well as working with ultracold samples, especially as they will be reduced proportionally at lower laser intensities.

The relevant properties of the VXDT in that regime are illustrated by figure 6.2. The excellent degree of independent control over ω_z and $\omega_{x,y}$ via the individual laser powers is demonstrated in figure 6.2b. For the horizontal trap, a critical power $P_c^{(h)} = 43$ mW is expected as shown in figure 6.2a, and the corresponding trap frequencies $\omega_{x,y}$ are still on the order of 100 Hz reasonably close to this threshold. This not ideal for experiments on ultracold gases, and it clearly shows the nature of the horizontal trap as a compromise between large initial trap depths and low final trapping frequencies. However, several options have been considered to achieve lower final trap frequencies (see section 6.7 below).

6.3 Implementation of the optical dipole traps

The implementation of the VXDT discussed in the previous section 6.2 in our experimental setup is presented in more detail in this section. Optical access to the science cell has already been surveyed

briefly in section 4.3; the beams for the VXDT are injected along the positive z- and y-axes, respectively. Both ODT branches are powered by a single high-power laser system (see section 6.3.1), and the beam-shaping optics used to produce foci with the required minimal waists are discussed in sections 6.3.2 and 6.3.3. Specific aspects of the alignment procedures are presented in sections 6.3.4 and 6.3.5. Finally, the imaging system used for absorption imaging of ultracold samples is summarised briefly in section 6.3.6.

6.3.1 Dipole trap laser system (532 nm)

A frequency-doubled solid-state laser* that is located on the same table as the experimental setup itself (see figure 4.7) generates the laser light for the ODTs. Its inherent frequency noise is sufficiently low for operation of an XDT, and we have not taken any measures to actively stabilise its frequency, as of date. The preparation of the beams for the individual branches of the trap is illustrated schematically by figure 6.3. Partially reflecting mirrors coated in-house are used to split them from the primary beam. We operate the laser at a total output power of 18 W, but roughly 4 W have been reserved to implement additional ODTs at a later point (see section 6.7).†

Each of the beams is subsequently passed through an AOM‡ in order to control its power and shift its frequency. The resulting frequency difference of about 2.5 MHz is used to suppress the effects of possible interference of the beams regardless of their polarisations, as the atomic sample experiences a time-averaged effective potential. Logarithmically amplified photodiodes monitor the power leaking through one of the steering mirrors§ in each of the beams, and sample-and-hold regulators are used to control and stabilise the intensities of the individual beams.

Quartz crystals are used in the AOMs instead of the more common TeO_2 crystals, specifically, because they can handle laser intensities of several 100 W cm^{-2} at this wavelength. In contrast, we have observed an irreversible, severe degradation of beam quality for the latter after being operated at laser powers of a few watts or more, although these intensities are well within their specifications. Instead of nearly pure TEM_{00}, the profile of the beam after the AOM had become doughnut-shaped with a central minimum. Especially with respect to the horizontal trap, these AOMs are therefore completely unfit for operating any high-power ODT at this wavelength.

Subsequently, the beam for the horizontal trap is enlarged by a pair of spherical singlet lenses and up to $P_{\mathrm{max}}^{(\mathrm{h})} = 9.0\,\mathrm{W}$ are delivered directly, *i.e.* in free space, to the rear breadboard of the experimental setup (see figure 4.10). In contrast, the second beam is coupled into a short PMF¶ that delivers up to $P_{\mathrm{max}}^{(\mathrm{v})} = 1.35\,\mathrm{W}$ to the vertical branch. These values reflect the maximum powers used for each of the traps in a typical experimental cycle, but especially in the case of the vertical trap substantially larger powers may be achieved. The polarisations of the beams are adjusted by half- and quarter-waveplates in the respective branches of the laser system (see figure 6.3).

*Coherent, Verdi-V18

†As of date, no such mirror has been installed to use this power reserve, and the resulting excess power in the vertical branch is dumped into the blocked 0$^{\mathrm{th}}$ order of its AOM.

‡Crystal Technologies, model 3080-292 (quartz crystal, centre frequency: 80 MHz, aperture: 2.5 mm).

§In the case of the vertical trap, a mirror after the beam shaping optics is used, whereas one of the mirrors delivering the beam to the experimental setup is used for the horizontal beam.

¶Nufern, PM-S405-HP. Assembled in-house.

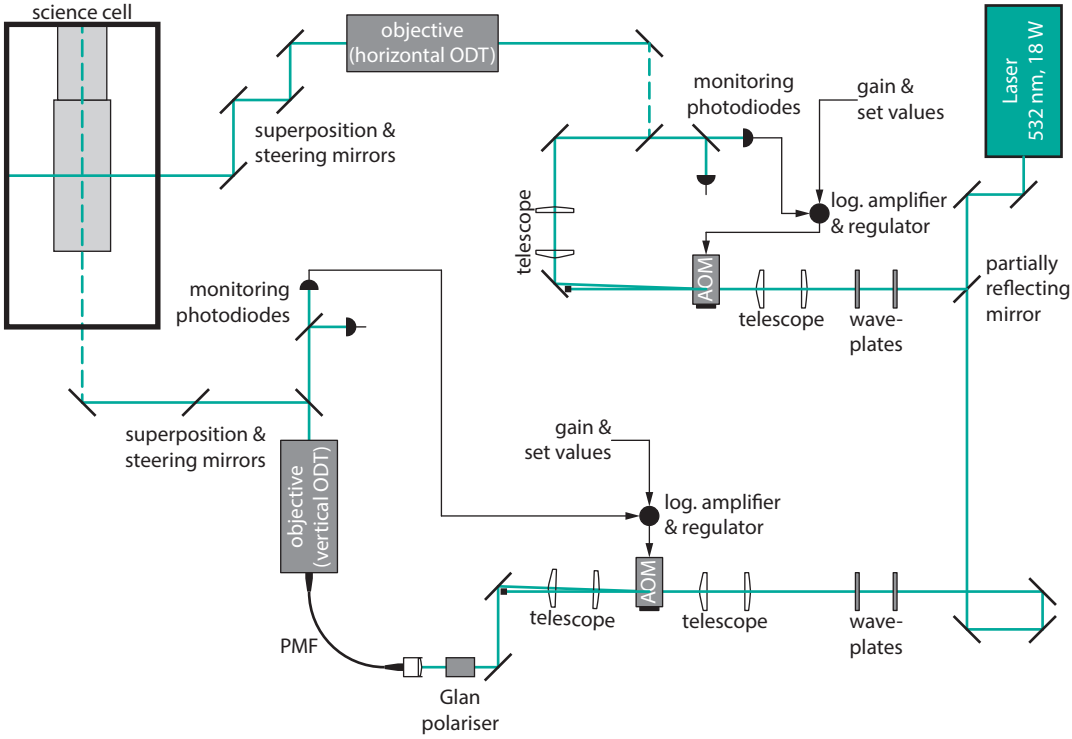

Figure 6.3 | A sketch of the dipole trap laser system summarises the generation of a VXDT in the science cell (see the inset on the left). As discussed in the text, the beam of a single laser is split into horizontal (upper part) and vertical dipole trap branches (lower part). The sketch schematically shows the setup of the photodiodes and AOMs used to control the intensities of the beams. Furthermore, delivery of the beams to the science cell is illustrated. Vertically propagating beams are indicated by dashed lines, and the objectives shown in more detail in figures 6.4 and 6.6 are represented by grey boxes.

6.3.2 Horizontal trap

As mentioned in the previous section, the beam of the horizontal trap is delivered to the rear breadboard (see figure 4.10) in free space. There the beam is enlarged by a beam-shaping telescope and focussed into the science cell at a working distance of about 0.5 m. Its shape around the focus has been measured *in-situ* with a knife-edge beam profiler by reversing the last steering in front of the cell. Minimum waists of $w_0 = 17.7(8)\,\mu\text{m}$ ($\chi w_0 = 29.5(7)\,\mu\text{m}$) have been found along y (x), as illustrated by figure 6.5.

The polarisation of the beam is adjusted to be linear and s-polarised with respect to the horizontal plane of the breadboard prior to shaping the beam (see figure 6.3). This particular choice of polarisation minimises possible interference with the vertical trap. Moreover, the last filter used to superimpose the ODT onto the MOT beams (see figure 4.10) is highly reflecting only at this polarisation for technical reasons.

The beam-shaping objective has been mounted in a tube system for stability. Its layout is shown schematically in figure 6.4. The input beam has a diameter of 2 mm, but a telescope after the AOM (see the previous section 6.3.1) may be used to modify the initial diameter and hence the final waist

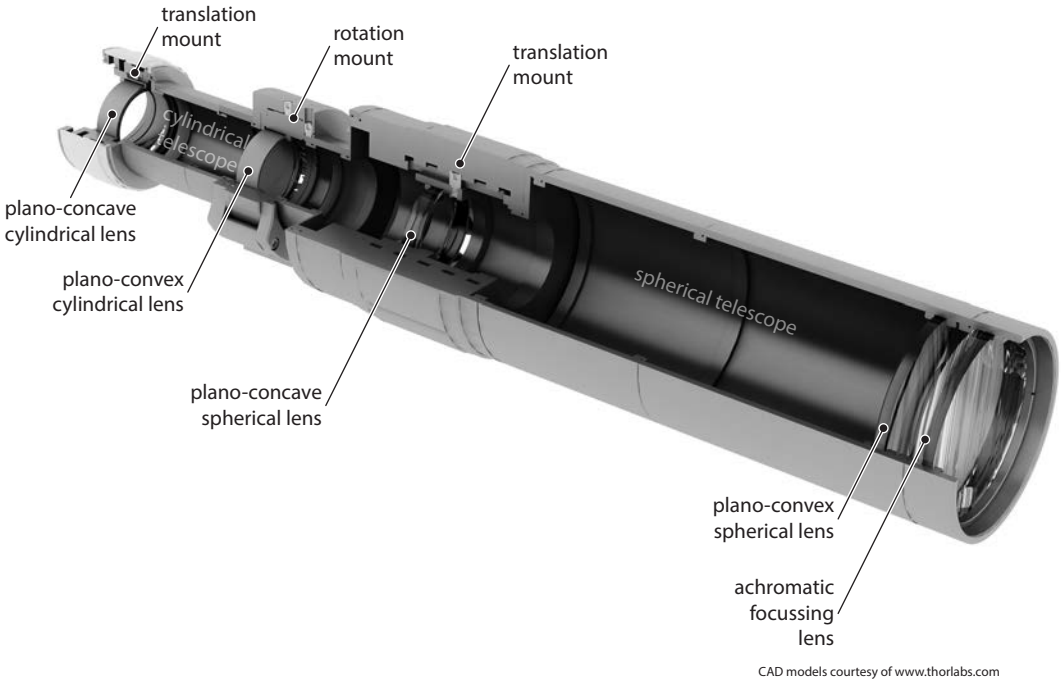

Figure 6.4 | Layout of the horizontal telescope illustrated by a CAD model. Translation and rotation mounts allow complete adjustment of the cylindrical and spherical telescopes as indicated above. More details are given in the text below.

of the horizontal trap without exchanging any lenses of the beam-shaping optics. The beam has been aligned carefully to the axis of the tube. It is enlarged by two pairs of plano-concave/plano-convex singlet lenses – first in the vertical direction by a pair of cylindrical lenses[*] and subsequently by another pair of spherical lenses.[†] Finally, the elliptic beam is focussed by an achromatic lens.[‡] Owing to the large diameter of the collimated beam in the vertical direction, these last two lenses have a diameter of two inches.

Several compromises were made in the choice of lenses for this objective and a variety of different lenses have been tested. Spherical or cylindrical lenses are used for all three telescopes (see section 6.3.1). We have refrained from using achromatic lenses for these telescopes, since maximum intensities of more than 100 W cm^{-2} at every lens in the objective but the last two exceed the damage thresholds, which are typically specified for these lenses, significantly. Large-diameter aspheres have been tested, but we have found their optical quality to be clearly unfit for this purpose. We observed much larger minimum waists than expected and strong distortions in the far field of tightly focussed beams. In contrast, the effective aberrations of spherical lenses in a plano-concave/plano-convex telescope can be kept at a reasonable level, whereas they become noticeably

[*]Thorlabs, LK1336RM-A (plano-concave cylindrical lens, $f = -50$ mm, 1 in diameter) and LJ1567RM-A (plano-convex cylindrical lens, $f = 100$ mm, 1 in diameter).

[†]Thorlabs, LC1259-A (plano-concave lens, $f = -50$ mm, 1 in diameter) and LA1979-A (plano-convex lens, $f = 200$ mm, 2 in diameter).

[‡]Thorlabs, AC508-500-A-ML (achromatic lens, $f = 500$ mm, 2 in diameter).

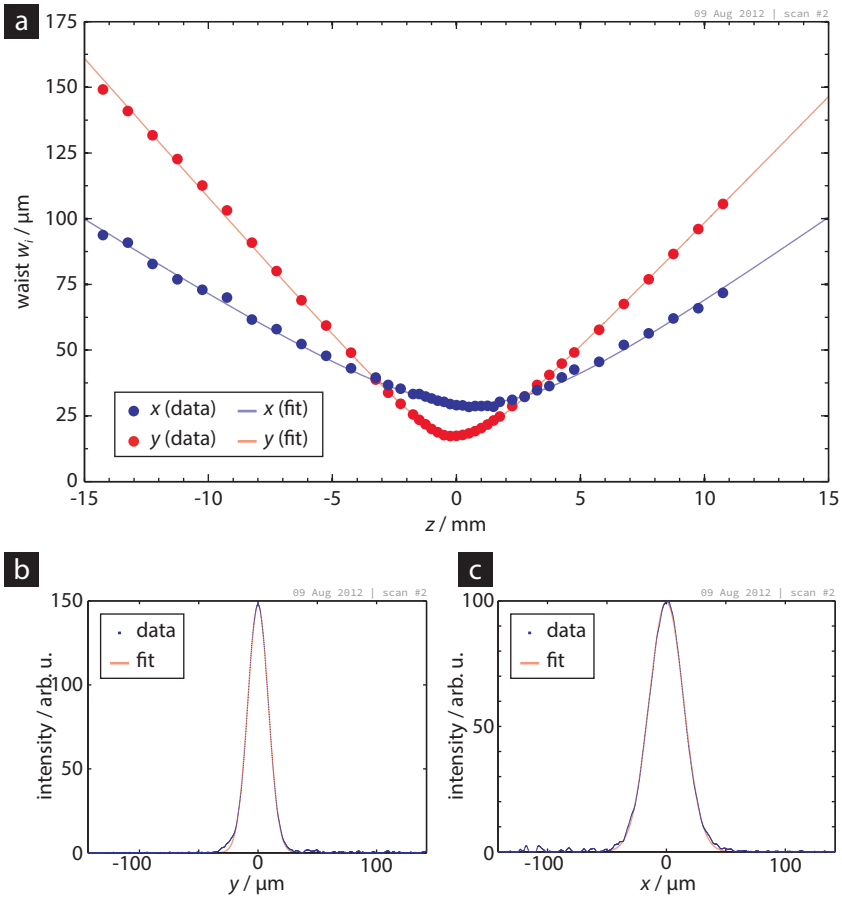

Figure 6.5 | Measurement of the horizontal dipole trap waists using the knife-edge beam profiler. **(a)** The waists of the horizontal ODT beam have been extracted from lateral profiles measured at various positions near the foci along its axis of propagation (z) and fits of a modified waist profile of a Gaussian beam (see the footnote on page 82) have been performed to determine the minimal waists of the trap. Slightly different divergence is observed on either side of the foci, which suggests the presence of minor residual spherical aberrations. However, the estimated Rayleigh ranges are still compatible with an ideal Gaussian beam within two standard errors of the fit or less. The vertical and horizontal foci in this measurement are displaced by 1.2 mm. **(b,c)** The beam profiles measured closest to the vertical focus ($z = 0$) in the vertical (a) and horizontal (b) directions illustrate that the lateral intensity distribution is very close to a Gaussian, especially in the vicinity of the focus, where atoms are held in the VXDT.

stronger in a plano-convex/plano-convex configuration.

The profile of the beam has been characterised with a knife-edge beam profiler* at regular intervals during alignment. A final, fine-spaced measurement of the beam profile is shown figure 6.5. Only minor, most likely spherical[277] aberrations are discernible despite the extensive use of spherical and cylindrical singlet lenses in the objective and the laser system itself. Moreover, the lateral intensity distributions are very close to a Gaussian, as illustrated by figures 6.5b and 6.5c at the focus. The characterisation yields a residual displacement of the foci of about 1.2 mm, and it has not been possible to reduce residual astigmatism below this level, because precision rotation mounts cannot be used for reasons of mechanical stability of the tube and manual adjustments are highly delicate. However, the residual displacement found in figure 6.5 is smaller than either Rayleigh range and thus at an acceptable level. Therefore, the beam as characterised in figure 6.5 is fit for implementation of the horizontal ODT.

6.3.3 Vertical trap

Light for the vertical trap is delivered by a PMF† to an objective that images the output of the fibre onto minimum waists of $w_0 = 28.4(8)\,\mu\text{m}$ ($\chi w_0 = 85.0(2)\,\mu\text{m}$) along z (x) at a working distance of 49 cm in the science cell (see figure 6.7). The optical fibre has been oriented to yield linear polarisation of the beam along the z axis in the science cell. However, the objective itself has been mounted on the optical table below the rear horizontal breadboard, and a steering mirror is used to reflect it onto the vertical axis, as indicated in figure 4.10.

Like the beam-shaping optics of the horizontal trap, it has been assembled in a tube system to achieve a stable and compact optical setup. Figure 6.6 illustrates its layout schematically. The PMF is mounted rigidly to the backplate of the tube. The beam emerging from the fibre has a mode-field diameter of 3.9 µm, and it is collimated by an achromatic lens.‡ The focal length has been selected such that the final achromatic focussing lens§ yields the desired waist along x. In order to create the smaller waist along the other axis, a plano-concave/plano-convex cylindrical telescope¶ has been placed in between these two lenses in order to enlarge the beam along its axis of polarisation.

Various lenses have been tested to collimate the output of the PMF, and the achromatic lens has been selected, after several aspheric lenses of comparable focal lengths had produced insufficient results. The alternative of using a moulded aspheric lens would have required a second spherical telescope to enlarge the beam to a similar diameter. It was abandoned due to the excellent results

*A Coherent BeamMaster BM-7 (UV) knife-edge beam profiler with a resolution of 0.1 µm for beams smaller than 100 µm has been used to measure the beam profiles within an axial range of 25 mm, limited by the translation stages carrying the objectives, because comparable results could only be obtained for a fixed knife edge profiler for technical reasons. The waists at each position were extracted by fits of a Gaussian distribution to the lateral profiles. Subsequently, waists and axial positions were fitted using equation (D.4) to determine the minimum waists and focus position, but the Rayleigh ranges on either side of the focus were used as empirical free parameters to check for possible aberrations. Note that, especially for large beams, these measurements do not yield a reliable estimate of the M^2 parameter, as this requires measurements of the waist several Rayleigh ranges away from the focus.

†The high-power optical fibres for the dipole traps have kindly been assembled and tested in-house by our colleague Ortwin Hellmig.

‡Thorlabs, AC064-013-A-ML (achromatic lens, $f = 13$ mm, 6.35 mm diameter).

§Thorlabs, AC254-250-A-ML (achromatic lens, $f = 500$ mm, 1 in diameter).

¶Thorlabs, LK1336RM-A (plano-concave cylindrical lens, $f = -50$ mm, 1 in diameter) and LJ1629RM-A (plano-convex cylindrical lens, $f = 150$ mm, 1 in diameter).

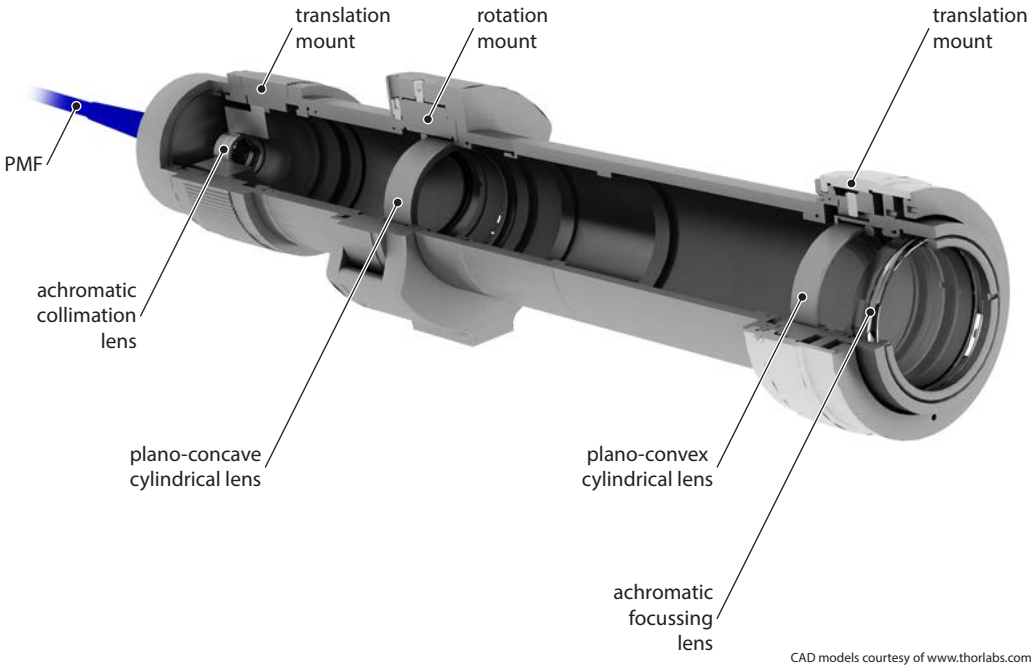

Figure 6.6 | Layout of the vertical telescope illustrated by a CAD model. Translation and rotation mounts allow complete adjustment of the initial collimation and the cylindrical telescope as indicated. More details are given in the text below.

obtained with the achromatic lens. Moreover, cylindrical singlet lenses are used for the telescope due to limited space despite possible aberrations. However, the plano-concave/plano-convex configuration is used to minimise spherical aberrations.

As in the case of the horizontal trap, the beam was monitored using a knife-edge profiler during alignment. A final characterisation of the objective is shown in figure 6.7. In contrast to the horizontal trap, signs of substantial aberrations are observed in the divergence of the beam on either side of its foci; the observed increased (decreased) divergence behind (in front of) the focus suggests the presence of negative spherical aberrations.[277] Since several attempts at realigning the objective resulted in similar beams as shown in figure 6.7, the problem is probably related to some of the lenses, most likely the collimation lens, or their mounts. Nevertheless, the lateral intensity distributions are very close to a Gaussian (see figures 6.7b and 6.7c), and the axial curvature of this beam is of little concern regarding the overall VXDT potential, especially due its role as a horizontally confining beam and large Rayleigh range. Therefore, the beam characterised by figure 6.7 is suitable for implementation of the vertical ODT, and we have refrained from investigating the origin of these aberrations in more detail.

6.3.4 Alignment of the cylindrical telescopes

Alignment of the cylindrical telescope in either objective is highly delicate, because even minute misorientation of the lenses introduces astigmatism of the focussed beam and limits its minimum

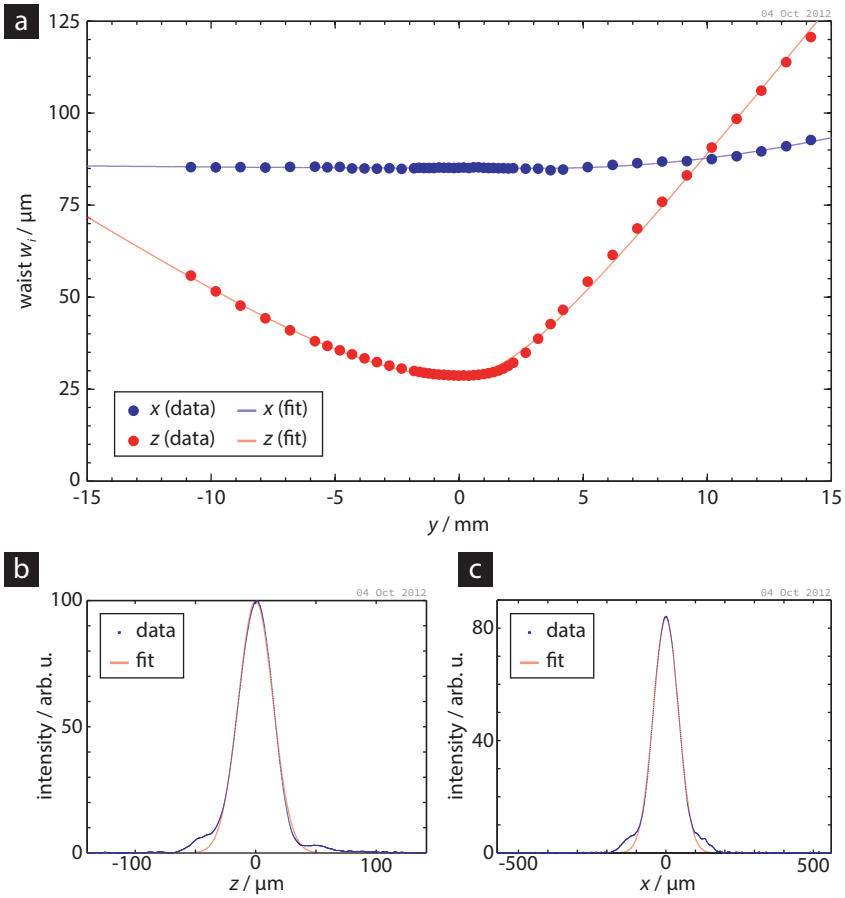

Figure 6.7 | Measurement of the vertical dipole trap waists using the knife-edge beam profiler. **(a)** The waists of the vertical ODT beam have been extracted from lateral profiles measured at various positions near the foci along its axis of propagation (y) and fits of a modified waist profile of a Gaussian beam (see the footnote on page 82) have been performed to determine the minimal waists of the trap. Substantial aberrations are observed in the vicinity of the foci, since the fits yield substantially smaller (larger) Rayleigh ranges than expected for an ideal Gaussian beam behind (in front of) the focus. **(b,c)** The beam profiles measured closest to the vertical focus ($y = 0$) along the z (a) and x (b) axes illustrate that the lateral intensity distribution is nonetheless very close to a Gaussian in the vicinity of the focus. Therefore, this beam may be used for the vertical ODT despite the observed signs of aberrations.

waists. Especially in the case of the horizontal trap, the acceptable level of astigmatism is extremely small due to its small waist and the resulting short Rayleigh ranges.

As illustrated in figures 6.4 and 6.6, the second lens of each cylindrical telescope has been placed in a rotation mount to adjust its orientation. The cylindrical telescope is initially aligned coarsely, *e.g.* by minimising the rolling motion of the collimated beam along its axis, but this is not sufficient to produce reasonably low astigmatism of the focussed beam. Therefore, an iterative procedure is used to align the relative orientation and distance of the lenses more precisely. In each step, the distance of the foci is measured using a knife-edge profiler and minimised by either rotating the second lens or translating the first lens to adjust the collimation of the telescope.

Usually, this procedure reduces the residual astigmatism to acceptable levels after a few iterations, but rotation of the lens is delicate and not reproducible, since a precision rotation mount cannot be used due mechanical limitations of available models. Nevertheless, this procedure allows systematic and efficient alignment of the most critical degrees of freedom in the objectives.

6.3.5 Alignment of the crossed dipole trap

Position and orientation of either beam in the science cell are adjusted by means of two steering mirrors per beam, and one of each pair has been equipped with differential micrometer screws to allow precise, reproducible adjustments at a micrometer scale. In the case of the horizontal trap, both of these mirrors have been placed in front of any optics superimposing the ODT with other beams as illustrated in figure 4.10, allowing completely independent adjustment of the horizontal dipole trap. Due to limited space, the last mirror reflecting the beam upwards towards the science cell (see figure 4.9) is used for adjustment of the vertical trap. However, the steering mirror for fine adjustments has been placed in front of any optics to superimpose other beams, *e.g.* a vertical optical lattice beam, and the precise alignment may therefore be performed independently of other beams in any case. Finally, both objectives are mounted on translation stages that allow axial adjustment of the focus position.

Initial alignment of the horizontal beam is straightforward, since it may be imaged using the MOT detection optics (see section 5.1.4) and thus aligned precisely to the MOT. Alignment of the axial focus position may be readily performed by imaging the trapped atoms along the x axis. However, coarse alignment is possible by eye due to its large divergence and intense Rayleigh scattering outside the glass cell.

The situation is more difficult for the vertical trap. We initially aligned its beam laterally to be transmitted by the differential pumping stage and axially using the measured working distance of the objective, but it cannot be aligned to the MOT by an imaging-based procedure like the horizontal beam. Instead, we couple near-resonant light at the intercombination transition $^1\mathrm{S}_0 \leftrightarrow {}^3\mathrm{P}_1$ into the PMF, and the distortion of the MOT by its intense radiation pressure readily visualises the position of the beam. The vertical beam is then aligned iteratively to a compressed MOT.

Precise alignment of the ODTs and their crossed region in particular is then performed by optimising evaporative cooling of ytterbium. Moreover, absorption imaging at brief times-of-flight readily reveals the positions of the beams. We have found the axial focus position to shift substantially at high power, likely due to thermal lensing, but these shifts may readily be minimised by operating the trap at maximum power as briefly as possible (see section 6.4).

Owing to its tightly focussed beams, the final alignment of the VXDT is prone to residual vibra-

tions of the experimental setup. Although transfer of mechanical vibrations to the setup is strongly suppressed by the optical table, which may be suspended on a hover cushion, we have strategically placed additional bags of quartz sand, especially on the optics of the horizontal trap, to dampen out any residual vibrations. Their effect is readily observed, as the number of condensed atoms is reduced by about a factor of two if they are removed. Furthermore, we have identified and, if possible, removed sources of mechanical noise in the vicinity of the experimental setup. However, some sources, *e.g.* water cooling and the controllers of the high-power lasers, may not be relocated readily.

6.3.6 Imaging of ultracold ytterbium

In addition to the MOT imaging system discussed in section 5.1.4, we have set up another imaging system along the perpendicular horizontal axis (x) as illustrated schematically in figures 4.9 and 4.10. As for the former branch, one of the slave lasers (see section 5.1.1) produces resonant light at the principal transition $^1S_0 \leftrightarrow {}^1P_1$ for this detection branch. Standard commercial achromatic lenses are used to image the region of interest onto the sensor chip of an EMCCD camera* at a magnification of $M_{HD} = 4.4(1)$. In order to suppress interference fringes, one half of its sensor has been covered to allow acquisition of two images in rapid succession, and an improved version of the standard post-processing technique[278,279] used in our research group has been implemented.

6.4 Experimental sequence

The basic concept of evaporatively cooling ytterbium to quantum degeneracy in our crossed dipole trap has already been discussed briefly in sections 6.1 and 6.2. Here, we present the experimental sequence, from loading of the VXDT to the eventual onset of quantum-degeneracy, and its optimisation in more detail.

6.4.1 Trap loading

The crossed dipole trap is loaded from the single-frequency 3D-MOT that has been compressed to maximise transfer efficiency and initial phase-space density. Both beams of the VXDT are switched abruptly to full power at the end of the loading cycle (see section 5.6) without substantially disturbing the uncompressed single-frequency MOT. We have found that overlapping compressed MOT and VXDT for an additional period beyond the single-frequency MOT phase (see section 5.6) does not enhance transfer efficiency, neither does additional Doppler cooling in an optical molasses, which even reduces the transfer efficiency due to the rapidly decreasing density. Therefore, the beams and magnetic field of the MOT are extinguished and atoms not trapped by the VXDT escape.

The transfer efficiency depends strongly on the detuning and compression of the single-frequency MOT as well as the alignment of the horizontal ODT. Optimal results are achieved for parameters given in chapter 5, and the ODT is not aligned to the centre, but rather to the lower perimeter of

*Andor, iXon 3A-DU888-DC-QBB. Its front window has been AR-coated for wavelengths 399 nm and 780 nm.

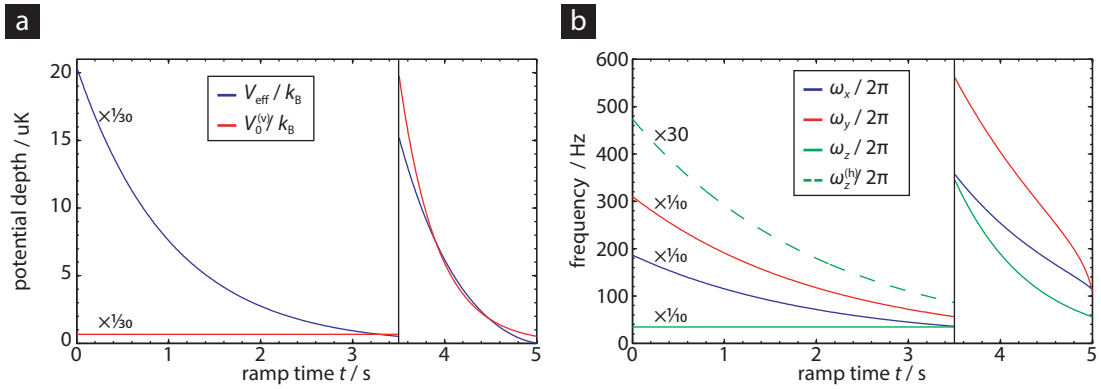

Figure 6.8 | A typical evaporation ramp consists of two segments as indicated by the black vertical lines (see the text for details). **(a)** Effective trap depth V_{eff} and depth $V_0^{(v)}$ of the crossed region along the axis of the horizontal trap over the course of the ramp have been plotted. The former is reduced continuously throughout the ramp, whereas the latter is kept constant in the first segment, while atoms concentrate in the crossed region. **(b)** All three trapping frequencies of the crossed region are plotted as a function of elapsed time during the ramp. Atoms trapped in the elongated horizontal trap experience a much smaller trapping frequency $\omega_z^{(h)}$ than in the crossed region, as indicated by the dashed line in the first segment. In contrast, ω_x and ω_y are dominated by the horizontal beam and hence virtually identical in the elongated trap. All quantities have been rescaled by the factors specified next to each line in the first segment, the axis label thus apply to the second segment.

the MOT. We typically transfer 1.2×10^7 ^{174}Yb into the dipole trap, and we have found their temperature to be about the same as in the single-frequency MOT after a few tens of milliseconds (see section 6.4.2 below).

Additional loading of the MOT does not increase the number of transferred atoms substantially beyond this number, but reduces number fluctuations from shot to shot. A rapid loss of atoms is observed in the first few 10 ms after switching off the MOT beams. It suggests that the density in the trap is limited mainly by three-body losses. The total number of atoms may be increased by enlarging the volume of trap. In fact, initial experiments using smaller waists of the horizontal beam ($w_0 = 13\,\mu m$, $\chi w_0 = 23\,\mu m$) yielded a lower maximum number of atoms in the trap.* We subsequently adjusted these waists and arrived at the configuration presented above, which yields an optimal maximum number in our setup.

6.4.2 Evaporation ramp

As expected due to the small potential depth of vertical trap, the remaining atoms, *i.e.* after the MOT has been shut off, are trapped only by the horizontal beam, and they form a dense, highly elongated cloud. We typically keep the trap beams at maximum power for a few 100 ms to have the ensemble settle by plain evaporation, before forced evaporation is carried out in two steps.

In the first step of evaporation, atoms are cooled in the horizontal trap. In a typical evaporation ramp for ^{174}Yb as it is shown in figure 6.8, we reduce the power of the horizontal trap exponentially

*This is consistent with observations of Takasu *et al.*[160] who have reported a significantly smaller maximum number of atoms for a much more tightly focussed trap.

from $P_{\mathrm{i}}^{(\mathrm{h})} = 9.0\,\mathrm{W}$ ($V_{\mathrm{eff}}^{(\mathrm{i})}/k_{\mathrm{B}} = 0.61\,\mathrm{mK}$) to $P_{\mathrm{tr}}^{(\mathrm{h})} = 0.30\,\mathrm{W}$ ($V_{\mathrm{eff}}^{(\mathrm{tr})}/k_{\mathrm{B}} = 17\,\mu\mathrm{K}$) over the course of $t_{\mathrm{e}} = 3.5\,\mathrm{s}$. As the temperature of the sample decreases, atoms are gradually concentrated in the crossed region.* The depth of the vertical trap is kept constant during this first ramp. At its conclusion, the depth of the crossed region is comparable to the effective depth of the potential, and the vast majority of atoms are located therein.

The second phase of evaporative cooling is then performed in the crossed region, where the atomic density and hence rethermalisation are enhanced due to the additional confinement along z (*cf.* section 6.1). Within typically $t_{\mathrm{x}} = 1.5\,\mathrm{s}$ for ^{174}Yb, we decrease the power of the horizontal trap further, but simultaneously ramp down the power of the vertical beam to about $P_{\mathrm{f}}^{(\mathrm{v})} = 35\,\mathrm{mW}$. The latter is essential to limit the density of the sample and avoid severe losses during this stage of evaporation. Eventually the temperature is reduced to below the critical temperature for Bose–Einstein condensation – or the Fermi temperature in the case of fermions – and we observe the emergence of a condensate for ^{174}Yb. The final power of horizontal trap is close to its critical value ($P_{\mathrm{f}}^{(\mathrm{h})} \gtrsim P_{\mathrm{c}}^{(\mathrm{h})}$, see section 6.2), and its exact value of course depends on the desired final temperature of the sample. Furthermore, the final power of the vertical trap may be varied across a wide range to adjust the trapping frequencies of the trap without significantly affecting evaporative cooling. The resulting quantum-degenerate gases are discussed in more detail in sections 6.5 and 6.6.

For optimisation, each ramp segment has initially been subdivided in up to three sub-segments whose durations and final parameters were optimised separately. Nevertheless, we have later found two long segments to be sufficient for stable and reproducible evaporation, and additional shorter segments at the end of the ramp are used to adjust the final parameters of the trap without affecting the main part of the evaporation ramp. Initial ramps contained steep sections that indicated increased loss from the trap at certain frequencies, but we have been able to eliminate them by stabilisation of the mechanical setup as discussed in the previous section 6.3.5.

6.5 Bose–Einstein condensates

Using the experimental sequence discussed in the previous section 6.4, we routinely produce BECs of ^{174}Yb that contain some 1×10^5 atoms. Figure 6.9 illustrates the emergence of the BEC towards the end of the evaporation ramp, and it yields nearly pure condensates without any discernible thermal fraction remaining.

Number fluctuations of the condensate from shot to shot are reasonably low at 10 s or more of MOT loading duration. Therefore, we typically operate the experiment at a cycle duration of slightly below 16 s, including evaporation and all other steps. However, substantial condensate sizes and moderate number fluctuations may be achieved even at MOT loading durations of only 2 s, *i.e.* a cycle duration of about 8 s. These figures clearly demonstrate that our experimental setup as a whole is highly competitive in terms of both condensate sizes and repetition rates (*cf.* the recent reports by Hansen *et al.*[77,212] for instance). As it allows seamless transition from highly stable atoms numbers to fast cycle times, it is well suited for future experiments the first of which are being prepared as of the writing of this thesis (see chapter 8).

*It has been shown by Takasu *et al.*[160] that this concentration process is entirely due to atomic collisions.

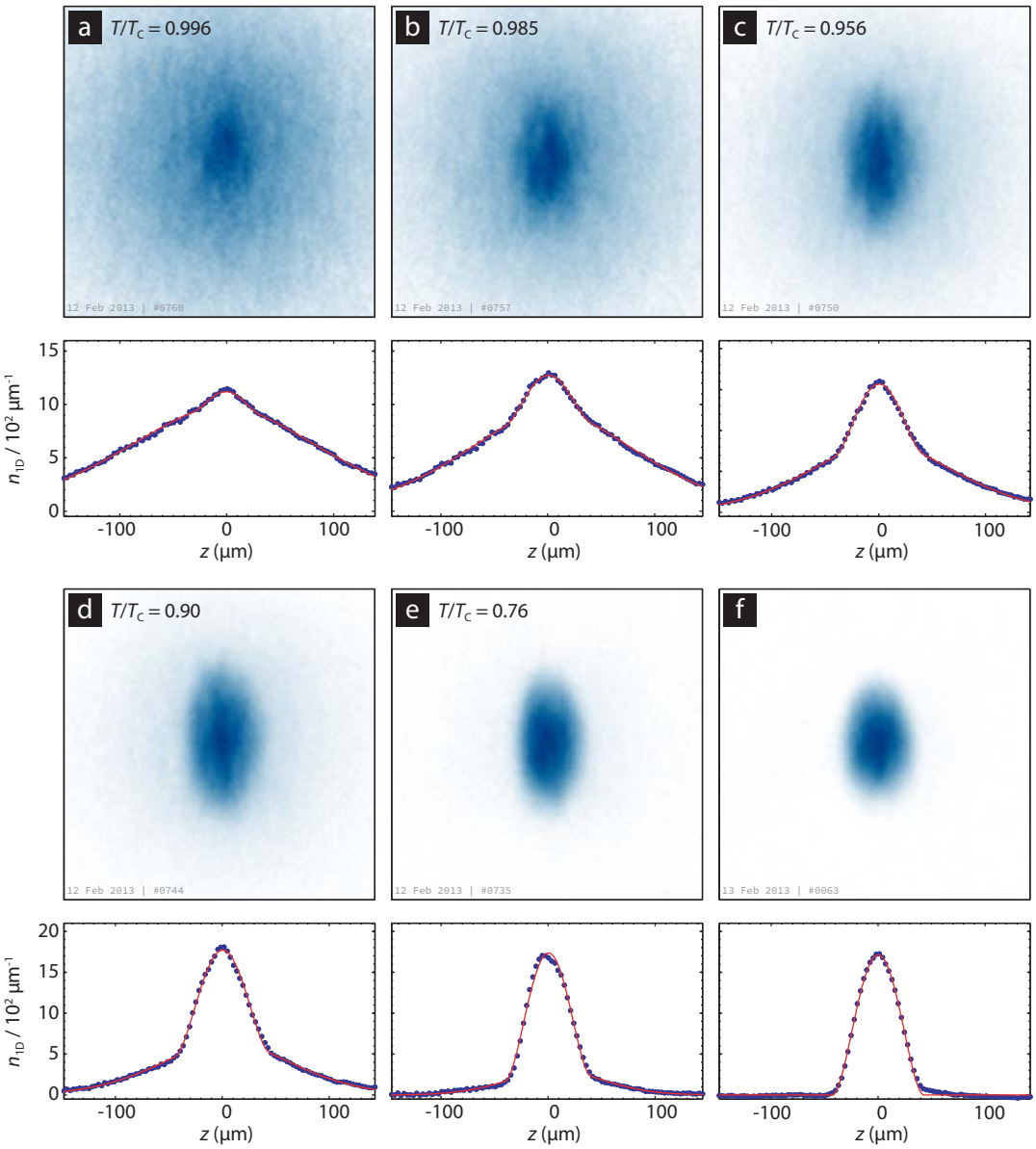

Figure 6.9 | Emergence of a Bose-Einstein condensate of ^{174}Yb. A series of absorption images demonstrates the emergence of a BEC of ^{174}Yb towards the end of the evaporation ramp. These images were taken after abruptly switching off the VXDT and allowing 20 ms of ballistic expansion. Condensate fractions N_0/N of **(a)** 1.1(1) %, **(b)** 4.4(2) %, **(c)** 12.5(5) %, **(d)** 26(1) %, and **(e)** 56(2) % have been determined by fitting a two-dimensional bimodal distribution to the data, where the BEC is assumed to be in the Thomas-Fermi regime. The last image **(f)** shows a nearly pure BEC with no discernible thermal fraction, and only a Thomas-Fermi profile has been used for the fit. The plots below each of the absorption images show the 1D densities obtained by integrating them along *y* (black circles), as well as the 1D density profiles resulting from the aforementioned fits (red solid line).

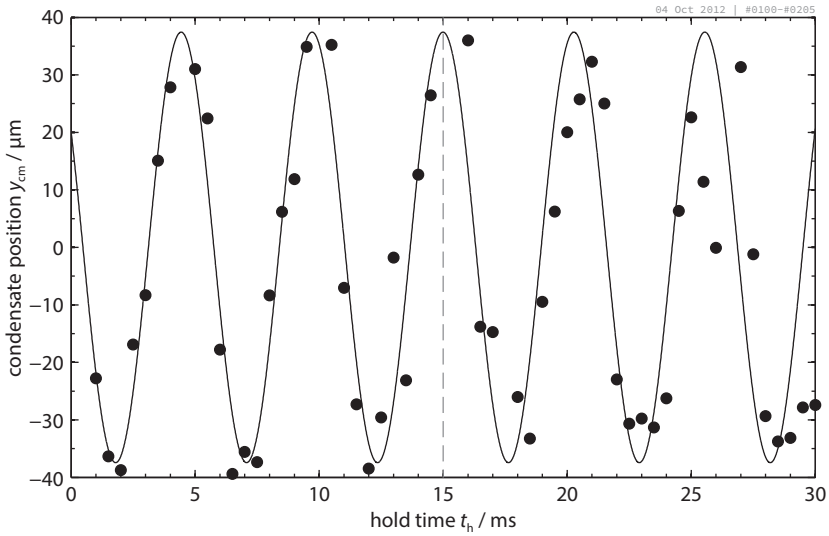

Figure 6.10 | Centre-of-mass oscillation of a ^{174}Yb-BEC along the vertical axis *y* used to determine the vertical trapping frequency ω_y as discussed in the text. The observed vertical positions y_{cm} of the condensates (black circles), after a variable hold time t_h and a subsequent ballistic expansion of 20 ms, as well as a sinusoidal fit (solid black line) of the oscillation are shown. The upper boundary of the time interval of the fit is indicated by a dashed vertical line.

6.5.1 Observation of collective excitations

In order to determine the trapping frequencies, especially ω_y and ω_z, of our VXDT in this regime, we have induced several low-lying collective excitations of these BECs of ^{174}Yb by abruptly changing the power of either trap.

Figure 6.10 illustrates our observation of the dipole mode along the vertical axis, *i.e.* an oscillation at the respective trapping frequency[280] ω_y that may readily be induced by quenching the horizontal beam. A sinusoidal fit to the first few periods (see figure 6.10) yields an oscillation frequency of $\omega_y/2\pi = 189(11)$ Hz. However, jitter gradually washes out the oscillation at hold times longer than some 15 ms. It is likely caused by shot-to-shot fluctuations of the trapping frequency that may be induced *e.g.* by residual power fluctuations of the beam.

In contrast, quenching the vertical trap excites the quadrupole or "breathing" mode at a oscillation frequency[280] of $\sqrt{5/2}\omega_z$. Figure 6.11 shows the resulting oscillation of the condensate width at a frequency of 87(3) Hz ($\omega_z/2\pi = 55(3)$ Hz). Although dampening of its amplitude is noticeable at hold time larger than 50 ms, the oscillation is observed for more than 100 ms, and the stability of the vertical dipole trap is demonstrated quite well.

These trapping frequencies are as expected for the low-power regime of our trap (see section 6.2). The third trapping frequency, ω_x, could not be measured at the time due to pending modifications of the imaging system along that axis. However, from the vertical trapping frequency given above $\omega_x/2\pi = 137(4)$ Hz may be estimated (see figure 6.2), and the resulting estimated geometric mean frequency is $\bar{\omega}/2\pi = 113$ Hz.

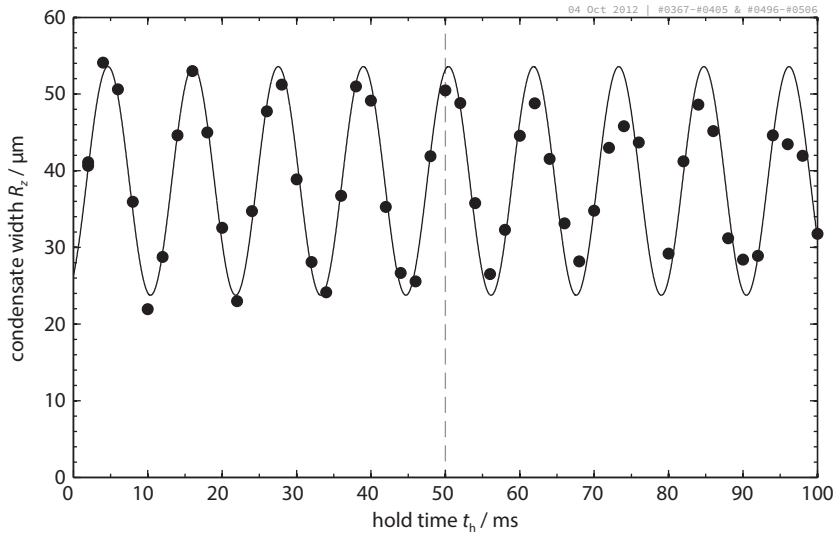

Figure 6.11 | Breathing mode oscillation of a ^{174}Yb-BEC used to determine the trapping frequency ω_z as discussed in the text. The observed lateral radii R_z of a Thomas-Fermi distributions fitted to the condensates (black circles), after a variable hold time t_h and a subsequent ballistic expansion of 20 ms, as well as a sinusoidal fit (solid black line) of the oscillation are shown. The upper boundary of the time interval of the fit is indicated by a dashed vertical line.

6.5.2 Final temperatures

The effective depth $V_{\mathrm{eff}}/k_{\mathrm{B}} = 0.3\,\mu\mathrm{K}$ of the VXDT during frequency measurements of the previous section 6.5.1 readily establishes an upper limit to the final temperatures of our ^{174}Yb samples, but a better estimate is provided by the critical temperature for Bose–Einstein condensation in a harmonic potential and condensate fraction given by[280]

$$k_{\mathrm{B}}T_{\mathrm{c}} \approx 0.94\hbar\bar{\omega}N^{1/3} \text{ and} \tag{6.1}$$

$$\frac{N_0}{N} = 1 - \left(\frac{T}{T_{\mathrm{c}}}\right)^3 . \tag{6.2}$$

The critical temperature is $T_{\mathrm{c}} \approx 0.24\,\mu\mathrm{K}$ for $N \approx 10^5$ atoms at the parameters found in section 6.5.1,* and we conservatively assume $N_0/N > 0.9$ for a nearly pure BECs as shown in figure 6.9f. Therefore, we achieve estimated final temperatures $T/T_{\mathrm{c}} < 0.5$ or $T < 0.12\,\mu\mathrm{K}$.

6.6 Degenerate Fermi gases

Following our initial experiments on Bose–Einstein condensation of ^{174}Yb, we have investigated cooling of the most abundant fermionic isotope, ^{173}Yb, as well. Due to its large nuclear spin ($I = 5/2$) this isotope is highly promising for the investigation of novel quantum phases in optical lattices

*Again, this is only an upper boundary to the actual critical temperature in our final trap, because the trap powers were raised for the measurements of the trapping frequencies discussed in section 6.5.1.

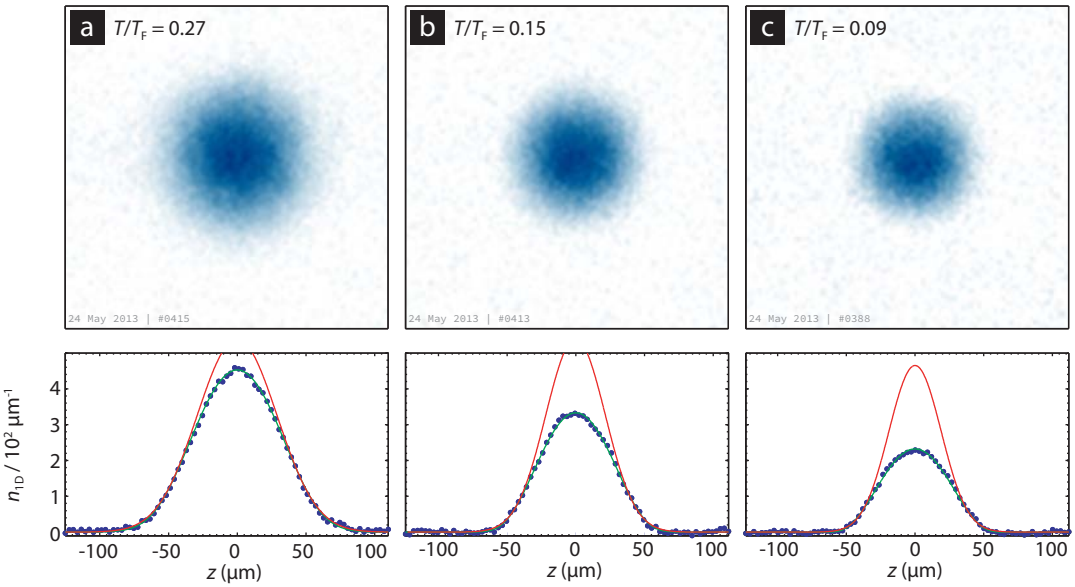

Figure 6.12 | Degenerate Fermi gases of ^{173}Yb. These absorption images show examples of quantum-degenerate Fermi gases of ^{173}Yb with atom numbers and temperatures of **(a)** $N = 3.5 \times 10^4$, $T/T_F = 0.27$, **(b)** $N = 2.1 \times 10^4$, $T/T_F = 0.15$, and **(c)** $N = 1.4 \times 10^4$, $T/T_F = 0.09$ as determined by fits of two-dimensional Fermi distributions. The images were taken with a time of flight of 8 ms after abruptly release from the VXDT and 2 ms of ballistic expansion. 1D density profiles of the Fermi gases, obtained by integrating the column densities along y, are shown in the plots below each of the images (black circles) along with those resulting from the fit used to determine their temperature (solid green line). For comparison, Fermi distributions with $T/T_F = 1$ (solid red line) have been fitted to the wings of the distribution in 2D, *i.e.* the region where the density is less than a quarter of its maximum value. They clearly overestimate the central density of the cloud.

as discussed briefly in chapter 2 (see also chapter 8), and achieving quantum-degeneracy of this isotope is a major milestone on the way to these future experiments.

The experimental sequence is very similar to the case of ^{174}Yb. We start by transferring atoms from a compressed 3D-MOT (see section 5.9) into the VXDT and subsequently perform evaporative cooling in two steps. The optimal parameters of the transfer differ slightly from those used for ^{174}Yb. Most importantly however, we load a maximum number of only 2×10^6 ^{173}Yb atoms into the VXDT, owing to the smaller 3D-MOTs and stronger interactions of the fermions (see section 2.6.1). Nevertheless, the MOT provides a mixture of all six spin states and evaporation is hence highly efficient despite the lower initial number of atoms. The evaporation ramp is very similar to that used for the bosons as discussed in section 6.4.2, and the first segment, *i.e.* evaporation in the elongated trap, is even steeper with a duration of only $t_x = 2.5$ s. As pointed out by O'Hara *et al.*[276] the cooling efficiency is not decreased severely by Fermi statistics.

We have successfully obtained quantum-degenerate Fermi gases of ^{173}Yb using this experimental sequence. Early results that have been published[1] were limited to $T/T_F \gtrsim 0.3$, but improvements of the overall setup and sequence for the fermions have recently allowed us to produce much colder Fermi gases of typically $N = 2 \times 10^4$ ^{173}Yb at $T/T_F \approx 0.15$. The Fermi temperature is given by[196]

$$k_B T_F = \hbar\bar{\omega}(6N)^{1/3}, \tag{6.3}$$

corresponding to an estimated $T_F = 0.15\,\mu K$ or less for each spin component in our trap.* We can decrease the temperature further at the cost of reduced particle numbers or vice versa. Examples of quantum-degenerate Fermi gases are shown in figure 6.12, demonstrating the achievement of temperatures down to $T/T_F = 0.09$. All of these results are nevertheless preliminary, and more details may be found in the doctoral thesis of Alexander Thobe, who has performed most of the recent experimental work on ultracold fermions.

In conclusion, these early results demonstrate that the experimental apparatus implemented within the framework of this thesis is well suited for the production of ultracold fermions and future experiments investigating their quantum phases in optical lattices.

6.7 A science dipole trap

The present horizontal ODT has been designed explicitly as a compromise between large initial trap depth and small final trapping frequencies (see section 6.2), and the measurement of the vertical trapping frequency discussed in section 6.5.1 clearly demonstrates that – as expected – values far smaller than 100 Hz simply cannot be realised in this trap alone. At present, the quantum-degenerate gases produced in our setup are hence limited to comparably large peak densities that are not ideal for studying bulk gases or quantum gases in optical lattices at moderate occupation numbers.

In order to generate quantum gases at lower densities, the implementation of a secondary horizontal trap has been planned. Since this "science" trap does not participate actively in forced evaporation, it may operate at a constant power, and a combination of large waists and high power may be used to create much lower trapping frequencies than in the current setup. As in the case of the horizontal ODT that is used for evaporation, an elliptic beam with its short axis along the vertical direction provides better support against gravity. Furthermore, it allows a significant reduction of the horizontal trapping frequency, especially as larger aspect ratios may be used for the science trap.

The science trap is to be injected nearly counter- or co-propagating to the current horizontal ODT to avoid an inversion of the horizontal aspect ratio of the effective trapping potential. If it is injected at a right angle towards the latter, each of the traps provides strong confinement along the propagation axis of the other, and the ratio ω_x/ω_z of the horizontal trap frequencies is eventually inverted at the end of evaporation. Therefore, we plan to use the aforementioned direction for the science trap to avoid potential problems arising from this inversion. As discussed in section 4.3 our setup supports a counterpropagating second trap at 532 nm and traps in either direction at 1064 nm.

As an example, a trap using the remaining spare power of the current dipole trap laser system at a wavelength of 532 nm and a minimal waist of $w_0 = 50\,\mu m$ ($\chi w_0 = 200\,\mu m$) in the vertical (horizontal) direction has a critical power of about $P_c^{(sc)} = 2.35\,W$. Operated at a slightly larger power of $P^{(sc)} = 2.5\,W$ its potential has an effective depth equivalent to little more than 100 nK. The resulting trapping frequencies are about $\omega_y/2\pi \approx 75\,Hz$ and $\omega_x/2\pi \approx 30\,Hz$. Even smaller

*In this estimate, the aforementioned total number of 2×10^4 atoms equally distributed across all nuclear six spin states and the trapping frequencies determined in the previous section 6.5 for BECs of ^{174}Yb have been assumed. The actual trapping frequencies may be lower in this regime and reduce the Fermi temperature accordingly.

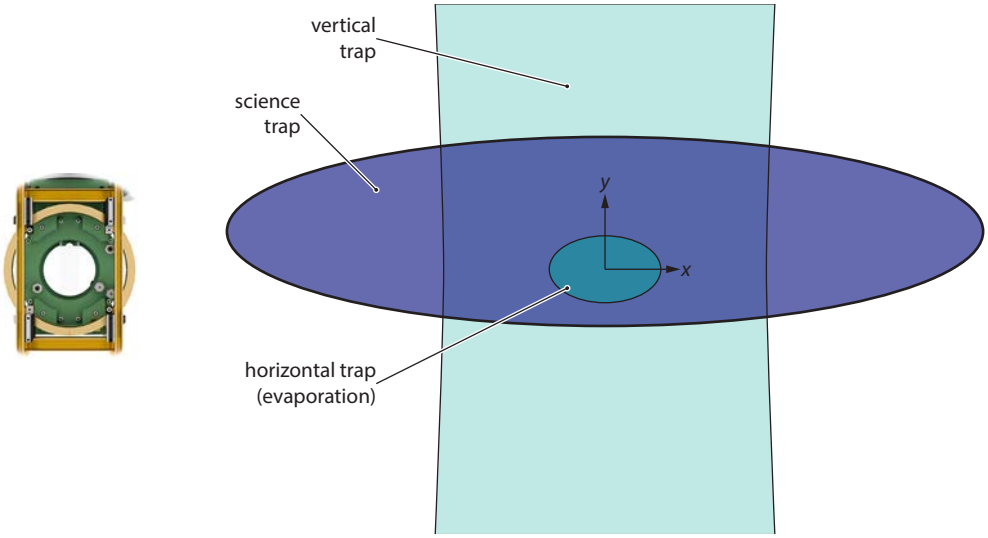

Figure 6.13 | Possible configuration of a science ODT. A science dipole trap may be set up as a second horizontal trap with larger waists, as shown schematically above in the focal plane of the horizontal traps (*cf.* figure 6.1a). The use of a trap like this allows lower final trapping frequencies to be achieved. As illustrated above the science trap is best aligned off-centre with respect to the trap used for evaporation to match their sags.

trapping frequencies are hard to realise for ytterbium. Of course, a separate laser system may be used to provide more power to the science trap and hence allow larger waists. Another high-power laser* is available, and it has been designated to produce a second dipole trap at a wavelength of 1064 nm as part of a bichromatic dipole trap for Rb-Yb mixtures. However, the polarisability of ytterbium in its ground state at that wavelength is about forty per cent smaller than at 532 nm and much lower than *e.g.* for rubidium. At either wavelength, the optical fibres used to deliver light for a stable high-power trap may ultimately prove to be a bottleneck.

We have therefore favoured the option of using the power reserve of the current laser system (see section 6.3.1) to implement a science trap of moderate power, and the infrastructure of our system has been prepared accordingly. In particular, another PMF like the one used in the vertical trap (see section 6.3.3) has been tested for up to 5 W of output power, and a fibre-coupled objective may be used instead of free-space delivery in order to enhance the mechanical stability and beam quality of the science trap with respect to the current horizontal ODT.

We are going to implement the science trap at a later stage, since it is used mainly for loading into and confinement in an optical lattice that is currently being set up (see chapter 8). Therefore, its implementation has been delayed in order to optimise its parameters for efficient loading into the lattice and to test several other transfer methods.

*InnoLight, Mephisto MOPA 25 (λ = 1064 nm, max. output power 25 W).

Chapter 7

Optical precision spectroscopy

Ultraprecise spectroscopy of the $^1S_0 \leftrightarrow {}^3P_0$ clock transition is one of the most essential novel features of ytterbium. We plan to use it as a tool to probe and manipulate quantum gases in the optical domain with unprecedented sensitivity. As discussed below, this transition provides the means to both observe energy shifts down to a few hertz, *e.g.* from atomic interactions, and engineer coherent coupling of two stable or metastable internal states directly, instead of resorting to multi-photon schemes as in the case of alkali elements. These features have been proposed for a variety of experiments on quantum gases and beyond. In particular, the development of optical lattice clocks[35] as novel optical frequency standards using neutral atoms has pioneered ultraprecise optical spectroscopy in optical potentials over the past decade. Many of the experimental techniques first demonstrated for OLCs may be readily adapted to the investigation of quantum gases, whereas some other requirements may be relaxed to afford greater flexibility in such studies.

This chapter is intended to survey possible uses of the $^1S_0 \leftrightarrow {}^3P_0$ clock transition in future experiments on ytterbium quantum gases and point out the differences with respect to OLCs.

Several proposals of using the frequency shifts of the clock transition to detect multiple occupancies or correlations of ytterbium in optical lattices and prepare atoms in the metastable state $^3P_0$ are discussed in section 7.1. The role of the magic optical lattice that allows spectroscopy of the clock transition free off frequency shifts due to atomic motion or the optical potential, both in OLCs and in our case, is discussed in section 7.2. Special emphasis will be placed on the different goals and requirements of studies of quantum gases in contrast to OLCs, which are targeted on accurate absolute frequency measurements of the clock transition. Moreover, Zeeman splitting of the nuclear spin states in the fermionic isotopes and residual light shifts due to the optical potential are surveyed briefly. The current status of the laser system for spectroscopy on the clock transition is summarised in section 7.3. Finally, the coupling strengths achievable for the individual isotopes and a scheme to induce a finite transition strength of the clock transition in the bosonic isotopes, where it is strictly forbidden as a single photon transition (*cf.* chapter 2), are presented in the concluding section 7.4.

Experimental work on the clock laser has been performed in the framework of the diploma theses of Thomas Rütze l and Jan-Henrik Carstens with support from Rodolphe Le Targat as well as the doctoral thesis of Alexander Thobe. The author has contributed to the design of the ultrastable resonator setup and initial installation of the laser system.

7.1 Applications of the clock transition in quantum gases

The ultranarrow transitions in ytterbium (see section 2.5.3) have the potential to probe quantum gases spectroscopically in the optical domain, *e.g.* for energy shifts due to atomic interactions, and to exert coherent control using a single laser. Spectroscopic probing of interactions in a Mott insulator has been demonstrated in the microwave domain for alkali elements.[281] In ytterbium, Yamaguchi *et al.*[162] have studied the frequency shifts induced by interaction in a bulk BEC using the $^1S_0 \leftrightarrow {}^3P_2$ transition. Furthermore, Bishof *et al.*[63] have studied interaction-induced sidebands of the clock transition in ^{87}Sr and observed spectrally resolved sidebands corresponding to different occupation numbers in a non-degenerate sample.

We are mainly interested in the $^1S_0 \leftrightarrow {}^3P_0$ transition, because the metastable state $^3P_0$ allows studies of novel correlated quantum phases in quantum-degenerate gases (see chapter 8) and the transition itself is well suited as a clock transition. In order to harness its full potential, we plan to adapt experimental techniques used in optical lattice clocks,[35] which have been developed as novel optical frequency standards over the past decade, to the study of quantum-degenerate gases in optical lattices (see the subsequent section 7.2 for details). We expect to achieve spectral resolutions on the order of a few hertz* and shifts of the resonance frequency to be generally much larger than for alkali elements, because different electronic states are used in ytterbium. Naturally, this concerns Doppler shifts, due to the large photon recoil in the optical domain, and differential light shifts in optical potentials as well, but tightly confining optical lattices at a magic wavelength may be used to overcome these effects as discussed in section 7.2.

The clock transition hence allows us to avoid or suppress any effects that strongly broaden the resonance and to resolve residual shifts, which may induced by atomic interactions or external potentials spectrally with hertz-level precision, *e.g.*

7.1.1 Probing quantum gases

An exciting prospect of ytterbium is to exploit ultraprecise spectroscopy near its $^1S_0 \leftrightarrow {}^3P_0$ transition as a novel means to probe and detect interactions or correlation effects in a quantum gas. The presence and strength of specific shifted resonances – or even their absence – in the excitation spectrum provide information, both qualitative and quantitative, on the system, and they may be used as a signature to detect specific quantum phases, for instance. Interrogation of the clock transition by a probe laser may then be used to either map its excitation spectrum or monitor the response of the system only at specific frequencies.

Frequency shifts caused by on-site interaction are expected to be on the order of several kilohertz and hence easily resolved in general. Deep in the bosonic MI regime, for example, the frequencies for excitation of a single atom in shells with $n$and $(n-1)$ atoms per site are obviously separated by[281]

$$\Delta\omega_s^{(\mathrm{coll})} = \frac{U}{\hbar}\left(\frac{a_{eg}}{a_{gg}} - 1\right) \tag{7.1}$$

where $|g\rangle = |{}^1S_0\rangle$ and $|e\rangle = |{}^3P_0\rangle$, U is the on-site interaction in the ground state, and a_{eg} (a_{gg}) is the s-wave scattering length of a ground-state atom with another ground-state atom (an atom in the

*The spectral resolution is limited in practice by experimentally feasible pulse durations, *i.e.* their Fourier-limited spectral bandwidth, when Rabi spectroscopy is used.

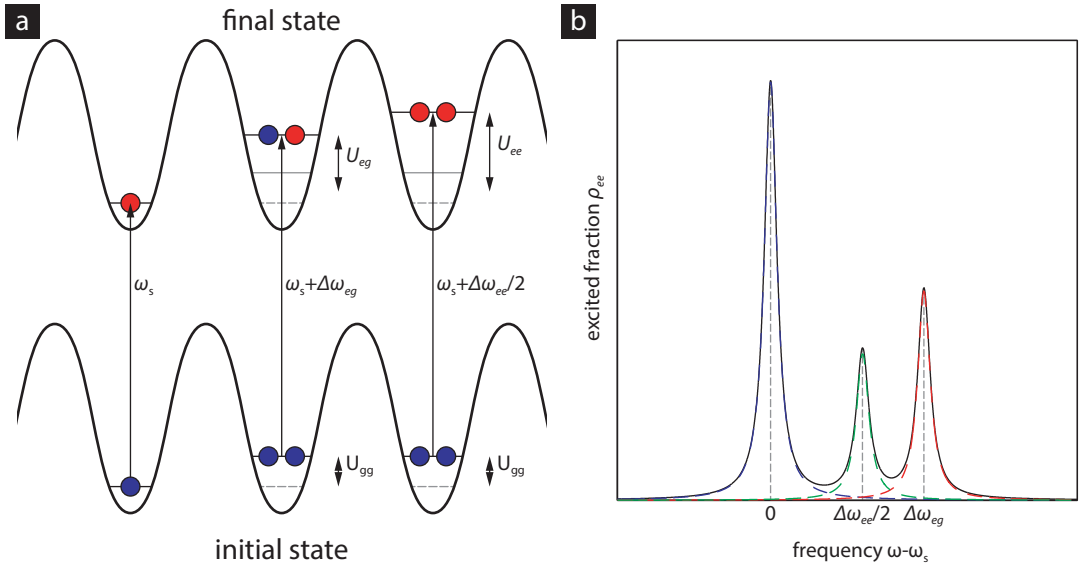

Figure 7.1 | Detection of multiply occupied sites via collisional frequency shifts. **(a)** A single ground-state atom (blue circles) at a lattice site is resonantly excited to the metastable state (red circles) at the carrier frequency ω_s. In contrast, the excitation frequencies of doubly occupied sites are shifted by the differences of interaction energies in the initial and final states. Moreover, different interactions energies of singly and doubly excited final states give rise to an interaction blockade of successive excitation of two atoms at a single site, and the two-photon resonance frequency is shifted accordingly. Note that, for indistinguishable particles, correct symmetrisation of the multi-particle states is required. **(b)** Excitation of one (dashed red line) or two atoms (dashed green line) at each doubly occupied site is observed as a sideband to the carrier (dashed blue line) in the excitation spectrum.

excited state). Since different electronic states are involved, these scattering lengths may differ substantially from each other, and the frequency shifts are on the order of the on-site interaction U. For the ultranarrow quadrupole transition, $^1S_0 \leftrightarrow {}^3P_2$, Fukuhara *et al.*[282] report expected interaction-induced frequency shifts of several 10 kHz in a MI of ^{174}Yb at reasonable lattice depths, whereas no elastic interaction parameters are known yet for the other metastable state $^3P_0$ (*cf.* section 2.5.2). Therefore, we plan to initially study the SF–MI quantum phase transition of bosonic ^{174}Yb in a magic optical lattice. Beyond refinement of our experimental technique, these first experiments will provide insight into interactions involving the exicted state $^3P_0$ in more detail.

Furthermore, the probe laser may be used to excite multiple atoms at a single lattice site as well.* Considering a single site within the $n = 2$ shell of a bosonic MI phase, for example, the probe laser may drive the transition from the initial state $|gg\rangle$ to a singly excited symmetric superposition state $(|ge\rangle + |eg\rangle)/\sqrt{2}$, but also to the doubly excited state $|ee\rangle$. As illustrated by figure 7.1, the differential collisional shifts of these transitions are generally not equal, but given by $\Delta\omega_s^{(\mathrm{coll})} = (U_{gg} - U_{eg})/\hbar$ and $\Delta\omega_s^{(\mathrm{coll})\prime} = (U_{gg} - U_{ee})/2\hbar$ in the former and latter case, respectively. Therefore, the interaction of excited-state atoms both with ground-state atoms and other excited-state atoms may be studied in the aforementioned initial experiments on bosonic Mott insulators – even if inelastic collisions

*However, excitation of multiple atoms in a single process may require intense probe beams due to its multi-photon character.

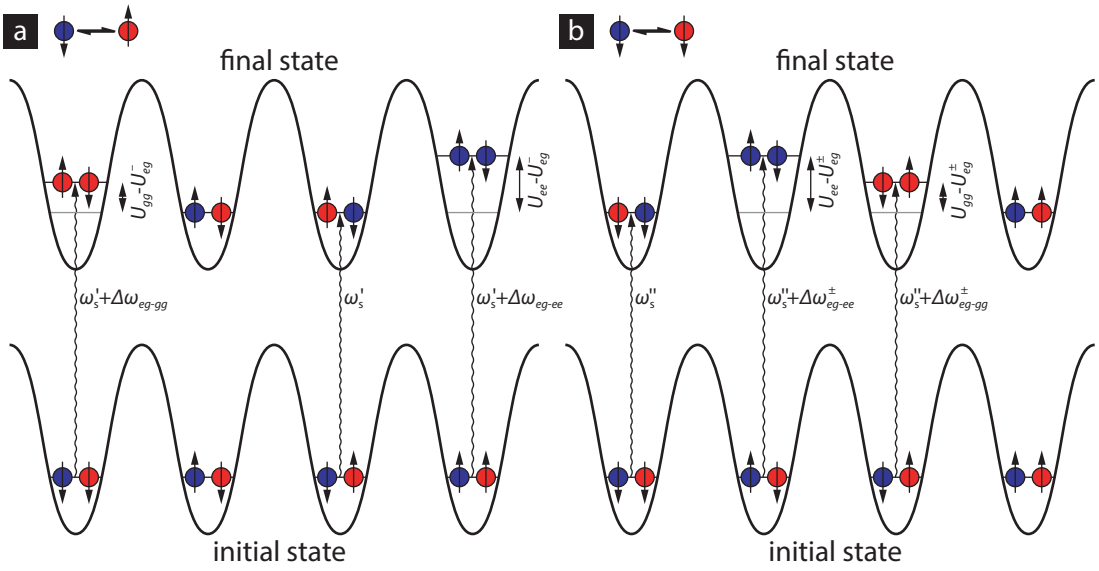

Figure 7.2 | Detection of spin–spin correlations of $^1S_0$ and $^3P_0$ atoms. A possible scheme to detect spin–spin correlations between fermionic ytterbium atoms in the ground and metastable state is illustrated for selective driving of a spin-changing **(a)** or spin-preserving **(b)** transition from a specific nuclear spin state. An effective spin-1/2 system is used as an example, *e.g.* ^{171}Yb or suitable two-component mixtures of ^{173}Yb. The carrier frequencies ω_s' and ω_s'' may be resolved spectrally *e.g.* by an appropriate bias magnetic field (see section 7.2.3). As shown above, the spin-changing (spin-preserving) transition effectively only excites or de-excites an atom if their spins are parallel (anti-parallel), and the two configurations may be distinguished by their different interaction energies, as both atoms end up either in the excited or ground state. Out of the remaining two spin–spin configuration one is unaffected by the probe pulse, while for the other ground and excited state are exchanged in the case of a π-pulse, *i.e.* the state acquires a phase of π due to anti-symmetrisation of the fermionic wave function. Note that correct anti-symmetrisation of the multi-particle states is required, since the particles are indistinguishable, and enforces a symmetric nuclear spin state in case of an anti-symmetric electronic state and vice versa. Both classes may be distinguished by their different interaction energies U_{eg}^{+} and U_{eg}^{-}.

occur at sites occupied by multiple excited-state atoms.

Regarding the fermionic isotopes, multiple occupancies are much more restricted than for bosonic systems, but collisional shifts arising from the interaction of atoms in different nuclear spin states provide a means to detect double occupancies directly.* Using the Zeeman effect of the nuclear spin (see section 7.2.3) and the polarisation of the probe laser, transitions between specific magnetic substates of the nuclear spin may be addressed selectively. As illustrated in figure 7.2, this addressability allows conditional excitation of an atom to the excited-state (or de-excitation into the ground state) as well as phase imprinting conditioned by the spin state of multiple particles. Especially in mixed systems of ground and excited state, which are one of the highly interesting prospects of studying ultracold fermionic ytterbium in optical lattices (see chapter 8), schemes like this may enable the detection spin-spin correlations between atoms in either electronic state. Fi-

*These measurements may even be performed locally either by focussing the probe beam or by imaging the spatial distribution of the atoms with high resolution. As discussed in chapter 4, our setup ought to allow an optimal resolution corresponding to a few lattice spacing in a magic-wavelength optical lattice.

nally, the isotope-dependence of collisional shifts provides the means to directly distinguish different combinations of isotopes at multiply occupied sites in ultracold mixtures of several ytterbium isotopes, *e.g.* to distinguish mixed from spatially separated phases.

In a long-term perspective, it is highly interesting to explore whether the clock transition can be used to detect off-site interaction or the effects of virtual tunnelling processes spectroscopically. These shifts are much smaller than the expected on-site shifts; as an order-of-magnitude estimate, consider the superexchange energy scale[283,284] ${J_{\mathrm{nn}}}^2/U$ in a system near the critical value[285] $(U/J_{\mathrm{nn}})_c \approx 5.8 z_{\mathrm{nn}}$ of the SF–MI ($n = 1$) quantum phase transition. Here J_{nn} and U are the nearest-neighbour tunnelling and on-site interactions parameters of the lowest-band Bose–Hubbard model and z_{nn} is the number of nearest neighbours. For a typical value of six nearest neighbour sites ($z_{\mathrm{nn}} = 6$), *e.g.* a triangular lattice in two or a cubic lattice in three dimensions, the superexchange energy scale is on the order of $10^{-3}U$, and frequency shifts of a few hertz to a few tens of hertz are to be expected. Therefore, a spectral resolution at the level of few hertz ought to be sufficient in order to detect the frequency shifts of the clock transition caused by these effects, *e.g.* to observe correlations arising from off-site spin–spin interactions.

Another intriguing option to detect inter-site correlations in an optical lattice is to exploit laser-induced tunnelling. An external potential gradient applied to a quantum gas in an optical lattices gives rise to a Wannier–Stark ladder of states.[286,287] Using the ultranarrow clock transition ${}^1\mathrm{S}_0 \leftrightarrow {}^3\mathrm{P}_0$, the energy differences between neighbouring sites are resolved spectrally. The probe laser may be used to couple the ground state at one site to the excited state at either the same or a different, *e.g.* neighbouring, site and vice versa, *i.e.* to induce tunnelling in the lattice as part of the excitation. The potential benefits of exploiting the Wannier–Stark ladder arising from gravity in OLCs was first pointed out by Lemonde & Wolf,[36] and Wolf *et al.*[187] have proposed to use Wannier–Stark states to probe the interaction of ultracold atoms with surfaces, *e.g.* to study Casimir forces. Nevertheless, rather than studying the external potential itself, laser-induced tunnelling may also be used in combination with selective addressing of nuclear spin states or different isotopes to selectively excite atoms and transfer them to another lattice site in the process. The collisional frequency shifts due to their interaction with atoms at that lattice site can be detected, and used to detect correlated states in an optical lattice, *e.g.* antiferromagnetic order as illustrated by figure 7.3.

7.1.2 Coherent control of quantum gases

Besides probing interactions and correlations in quantum gases, the clock transition may, of course, also be used to prepare atoms in the metastable state or in superposition states of ${}^1\mathrm{S}_0$ and ${}^3\mathrm{P}_0$. Since the quantum gas is usually created in the ground state, it is thus crucial for any experiments using the metastable state ${}^3\mathrm{P}_0$. Any effect that induces a frequency shift of the clock transition, *e.g.* collisional shifts, laser-induced tunnelling or selective addressing of transitions between specific nuclear spin states in the fermionic isotopes discussed in the previous section 7.1.1, in turn provides the means to selectively address and manipulate ytterbium atoms in an optical lattice. For instance, the signature collisional shift of multiply occupied sites may exploited to transfer one atom at each site with a specific occupation number to the excited state or to selectively remove atoms from these sites, *e.g.* by resonant light or inelastic collisions in the excited state. Owing to this addressability, the coupling of ytterbium ground-state atoms to the excited state and vice versa, and *e.g.* subsequent interaction, may be conditioned by the states of the manipulated and other atoms that

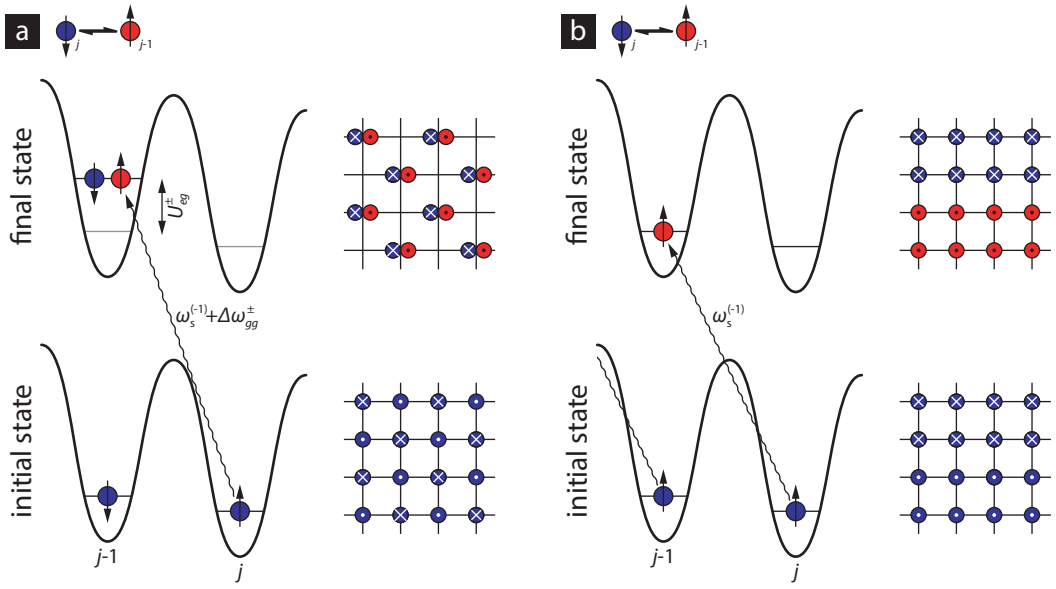

Figure 7.3 | Detection of nearest-neighbour spin–spin correlations. A possible scheme to exploit laser-induced tunnelling between Wannier–Stark states in order to detect off-site spin–spin correlations is illustrated for the cases of anti-ferromagnetic **(a)** and ferromagnetic order **(b)** in an effective spin-½ system of fermionic ground state atoms (see also figure 7.2). Here, the $^1S_0 \leftrightarrow {}^3P_0$ transition is driven selectively between specific nuclear spin states and the Wannier–Stark states of adjacent lattice sites at a carrier frequency $\omega_s^{(-1)}$ by using a bias magnetic field and an appropriate external force. As shown in the panels on the left, the resonance frequency incurs a collisional shift if an atom that is not affected by the probe laser pulse is present at the target site **(a)**, but not if the probe laser induces tunnelling of an atom at the target site to another adjacent site **(b)**. Therefore, the spin–spin correlation of adjacent sites may be observed as separate peaks at the carrier frequency and one or more sidebands. Note that correct anti-symmetrisation of the multi-particle states is required in the case of indistingushable fermions and, in general, interaction shifts of symmetric and anti-symmetric electronic state are different. The panels on the right illustrate the effect of a π-pulse on an antiferromagnetically ordered system **(a)** and a system with ferromagnetic domains and the same total spin **(b)**. The scheme may be applied analogously *e.g.* to isotope mixtures.

are present at the lattice sites involved. In consequence, a variety of schemes have been proposed to implement different kinds of quantum gates[88,90,190] (see the recent review article by Daley[191] for a survey of quantum computing with AEL atoms). Even without a focus on quantum information, these schemes are well worth investigating, for they allow the generation of entangled states in an optical lattice. Moreover, Reichenbach & Deutsch[143] have proposed a sideband-cooling scheme using the clock transition that preserves the nuclear spin state of fermionic atoms.

Owing to the large lifetime of the metastable state (see section 2.5.1), near-resonant coupling on the clock transition may readily be employed to generate artificial gauge potentials for ytterbium quantum gases (see the review article by Dalibard *et al.*[85] for details). Gerbier & Dalibard[84] have proposed a novel scheme that uses such coupling close to the clock transition in combination with an optical lattice at an anti-magic wavelength, using laser-induced tunnelling, to generate staggered or uniform artificial magnetic fields for AEL atoms in optical lattice potentials. Their proposal presents an intriguing alternative to another scheme for creating artificial gauge potentials, which

has recently been demonstrated.[32] The use of a similar triangular lattice in our setup (see chapter 8) allows us to investigate and combine the potential of both schemes.

Finally, the coupling strength between $^1S_0$ and $^3P_0$ can be engineered locally by appropriately shaping or modulating the probe laser beams itself. To name a few examples, the wings of a large probe beam may readily be used to generate nearly constant gradients of the coupling strength across the sample (see the article by Dalibard *et al.*[85] for a possible use in creating artificial gauge potentials), whereas a tightly focussed beam allows local addressing of specific regions within the system. Moreover, standing-wave probe or coupling laser fields offer a wealth of opportunities, since they allow modulation of the coupling strength at sub-wavelength scales. Recently, Daley *et al.*[91] have proposed the generation of nuclear-spin-state-dependent – as opposed to electronic-state-dependent (see section 2.8) – optical lattices using periodic modulation of the dressed states in a strong magnetic field.

Therefore, the clock transition $^1S_0 \leftrightarrow {}^3P_0$ is not only essential to prepare atoms in the metastable state $^3P_0$ and exploit its potential for studies of ultracold mixtures of $^1S_0$ and $^3P_0$, but it is a novel and extremely flexible tool for probing or manipulating ytterbium quantum gases itself. In particular, spectroscopy on the clock transition provides a wealth of means to detect interactions and correlations in quantum gases that will facilitate the detection of signatures of novel quantum phases expected in ytterbium quantum gases (see chapter 8).

7.2 Precision spectroscopy in optical lattices

Owing to its favourable properties (see section 2.5), the clock transition $^1S_0 \leftrightarrow {}^3P_0$ is an ideal candidate for frequency metrology in the optical domain. Optical lattice clocks (OLCs) are a novel type of optical frequency standards for neutral atoms that have developed over the past decade[33,35] and are currently approaching fractional instabilities of 10^{-18} after no more than a few hours of averaging.[66] In an OLC, atoms are trapped in a deep optical lattice at a magic wavelength to interrogate the clock transition free of frequency shifts due to atomic motion and differential light shifts induced by the optical potential to leading order. A detailed introduction to optical lattice clocks is found in the review articles by Lemonde[72] and Derevianko & Katori,[74] for example.

For studies of quantum-degenerate ytterbium in optical lattices, we plan to adapt many of the well-tried techniques known from optical lattice clocks. As discussed in section 7.1, our primary objectives are to probe quantum gases via Rabi spectroscopy for the effects of interaction or correlations and to use the clock transition for the preparation of superposition or mixed states of $^1S_0$ and $^3P_0$. Since residual Doppler shifts or excessive differential light shifts may easily wash out the spectral features that we strive to observe, the quantum gas is trapped in a deep optical lattice near a magic wavelength along the direction of the probe laser (see sections 7.2.1 and 7.2.2). Using a Rabi π-pulse, atoms are excited to metastable state $^3P_0$ on resonance, and the fractional excitation is measured by fluorescence or absorption imaging. For a balanced measurement, atoms from the excited state may be repumped using one of the repumping transitions discussed in section 2.5.5.

Although the planned spectroscopy scheme itself is nearly identical to that of an OLC, our requirements in terms of precision and accuracy are quite different from theirs, because we are solely interested in resolving frequency shifts and not in the absolute frequency of the transition. First of all, shifts well below a hertz can usually be ignored in our case, whereas they need to be controlled

down to much smaller energy scales in state-of-the art optical clocks. Moreover, reproducible shifts of the clock transition due to external fields may be ignored for the most part, but spatial inhomogeneity or global fluctuations, either at short time scales or from shot to shot, may still become a problem if they impede the required spectral resolution. However, strongly inhomogeneous, spectrally resolvable shifts provide additional means of probing or manipulating a quantum gas, *e.g.* laser-induced tunnelling between Wannier–Stark states (see section 7.1) or Zeeman shifts in a bias magnetic field (see section 7.2.3). Additionally, scans of the probe laser frequency to map the excitation spectrum of a quantum gas are particularly prone to shot-to-shot fluctuations or drifts, and reference measurements of the carrier at regular intervals will be required to correct for these drifts.

Owing to these requirements, some deviations from the strongly restricted setup of an OLC are possible without excessively sacrificing spectral resolution, and they allow greater experimental flexibility that may be exploited to study a wide range of systems, *e.g.* in optical lattices off the magic wavelengths (see chapter 8). Special emphasis is placed upon this aspect in the remainder of this section. In particular, section 7.2.3 briefly discusses a number of residual frequency shifts known from OLCs and their significance in our case.

7.2.1 Spectroscopy in the Lamb–Dicke regime

The interdependency of absorption or emission of a photon by a particle and its external, motional state is well known and essential for laser cooling. Due to energy and momentum conservation in free space, the transfer of a finite momentum from or to the photon gives rise to the Doppler and photon recoil shifts of the atomic resonance. In free space, as well as ODTs or even shallow optical lattices, the resulting broadening of the transition severely limits the resolution of precision spectroscopy using ultranarrow transitions. Deep optical lattices, however, allow strong confinement of atoms in the Lamb–Dicke regime[236] that is well known from ion traps.[288] Here, an atom is confined to an extent smaller than the wavelength of the transition and changes of its motional state are strongly supressed.

In a deep lattice without significant tunnelling, this effect may readily be understood by considering the discrete energy levels of an atom trapped at an individual lattice site. Changes of its motional state during a transition correspond to discrete sidebands in addition to the carrier that leaves the motional state unchanged. The probe laser couples to all of these sidebands, and their individual coupling strengths are determined by the photon recoil, which in turn broadens and shifts the resonance. In the case of the ultranarrow clock transition, the resolved-sideband regime ($\omega_{\mathrm{ho}} \gg \Gamma$ for a harmonic oscillator) is usually achieved. The spectrum then consists of a series of discrete peaks, and the resulting shifts are much smaller than in the unresolved sideband regime.* The carrier is hence affected mainly by line-pulling due to the asymmetry of the sidebands, which is especially pronounced in the ground state, since it does not have any red-detuned sidebands. In the Lamb–Dicke regime, the energy spacing of the motional states is much larger than the recoil energy of the photon. It is found that the coupling strengths of the sidebands asymptotically vanish, and only the carrier transition remains.[289] The first sidebands are suppressed proportionally to

*Note, however, that the anharmonicity of the potential wells in an optical lattice lifts the degeneracy of transitions with different initial motional states and causes an additional, much smaller splitting of the carrier and sidebands if multiple motional energy levels are occupied.

the square of the Lamb–Dicke parameter η which is given by[289]

$$\eta = \sqrt{\frac{E_{\mathrm{rec}}^{(\mathrm{s})}}{\hbar\omega_{\mathrm{ho}}}} \tag{7.2}$$

in the simple case of a harmonic oscillator, where $E_{\mathrm{rec}}^{(\mathrm{s})}$ is the recoil energy of the probe photon. A detailed, highly instructive discussion of the line shape of a confined atom is given *e.g.* by Ludlow.[290]

A more comprehensive understanding that also accounts for tunnelling between lattice sites may be obtained in the basis of the Bloch bands of the lattice potential.[72] In one dimension, the state $|^1\mathrm{S}_0, n, q\rangle$, *i.e.* an atom in its internal ground state in the n-th Bloch band and with quasi-momentum q, is coupled by the clock laser to internally excited states $|^3\mathrm{P}_0, n', q + k_{\mathrm{s}}\rangle$ in all Bloch bands n' and a quasi-momentum that is shifted by the photon momentum k_{s} of the coupling laser. Since the Bloch bands correspond to the energy levels at a single potential well in the previous picture, transitions to different Bloch bands obviously give rise to sidebands shifted by the respective band separations, *i.e.* several times the recoil energy $E_{\mathrm{rec}}^{(\mathrm{l})}$ of the lattice, which may be resolved spectrally in the case of the clock transition. For each of these transitions, even within the same Bloch band, the resonance frequency is shifted further due to the energy difference of the coupled quasi-momentum states, and the transition is broadened if multiple quasi-momentum states are occupied. However, both the shifts and the resulting broadening reduce with the widths of the Bloch bands at large lattice depths. In OLCs, this broadening needs to be suppressed to below the actual experimental line width, and it has been shown that lattice depths of at least several $10E_{\mathrm{rec}}^{(\mathrm{l})}$ are required in a one-dimensional lattice. Depending on the specific experimental situation, this suppression may or may not be necessary in studies of quantum-gases, since it is equivalent to Raman processes that are frequently used for alkali elements in optical lattices and yields information about the distribution of quasi-momenta.

Finally, it is worth mentioning that strong confinement by the optical lattice is required only along the axis of propagation of the probe laser. In fact, most OLCs are operated in one-dimensional lattices (see for example the review by Derevianko & Katori[74]), and usually a vertical orientation is used, for gravity lifts the degeneracy of neighbouring lattice sites, which greatly suppresses tunnelling and reduces the required lattice depth[36] (*cf.* also the spectroscopy of Wannier–Stark states proposed by Wolf *et al.*[187]). In our case, it is thus sufficient to set up a deep lattice along one axis (z), while the maximum lattice depth in the remaining directions may in principle be reduced in favour of a more homogeneous system, *i.e.* larger beams that create less harmonic confinement. Due to the layout of our apparatus, however, we cannot use a vertical one-dimensional lattice, although we may try and exploit the effect of gravity in a two-dimensional lattice in the x–y-plane.

7.2.2 Magic-wavelength optical lattices

Although an optical lattice allows the controlled suppression of frequency shifts caused by atomic motion, as discussed in the previous section 7.2.1, it induces substantial AC–Stark shifts of the internal atomic states. In general, these are of different magnitudes, *i.e.* there is a differential light shift that directly modifies the transition frequency. In particular, the two states of the clock transition, $^1\mathrm{S}_0$ and $^3\mathrm{P}_0$, experience different lattice depths and residual harmonic confinement. As discussed in section 2.8.2, however, the lattice may be tuned to a magic wavelength, where the differential

light shift of these states is cancelled, at least to leading order. This feature is essential to OLCs, as it removes an intensity-dependent shift of the clock transition. A magic-wavelength optical lattice certainly is the best choice for performing spectroscopy of quantum gases at optimal precision, as well. Nevertheless, its importance in this case needs to be re-evaluated carefully with respect to the intended spectral resolution. We are mostly interested in resolving the energy differences of individual states that may be induced by atom interactions, for instance, whereas systematic shifts of the absolute frequency may be ignored for the most part. Similar to the case of an OLC, there are several effects that ultimately limit the achievable precision, ranging from technical imperfections, such as fluctations of the lattice intensity, to more fundamental problems like the inhomogeneity of the residual differential light shift, *e.g.* due to residual harmonic confinement.

For the commonly used, NIR magic wavelength of the $^1S_0 \leftrightarrow {}^3P_0$ transition in ytterbium, the residual differential light shift in reasonably deep lattices is well below the hertz level even for a detuning of a few tens or hundreds of megahertz from the magic wavelength (see section 2.8.2 for details). Therefore, the well-known technique of composing multi-dimensional lattice potentials from several lower-dimensional lattices detuned from each other by at least several megahertz may be used in our case. In fact, while the first realisation[54] of a multi-dimensional optical lattice clock did use a single folded beam for the lattice, another recent experiment[184] on collisional shifts in an OLC using ^{171}Yb employed detuned one-dimensional lattices to create an effective two-dimensional lattice potential. The use of detuned lattices close to the magic wavelength hence allows great flexibility in realising different lattice geometries and significantly reduces the complexity of the experimental setup, even if sub-hertz precision is required. Phase-stable mono-frequent lattices on the other hand provide unique ways of dynamically tuning the lattice potential.[27]

In some cases, part of the optical lattice may even be set up at an entirely different wavelength, *e.g.* anti-magic or state-selective wavelengths (see section 2.8), in order to exploit the different light shifts of both states of the clock transition. A deep one-dimensional lattice near a magic wavelength is needed only along the axis of propagation of the probe beam to enable precision spectroscopy on this transition. As these non-magic optical lattice do create additional differential light shifts that may impede the observation of minute frequency shifts, careful design and optimisation are necessary to improve the sensitivity of spectroscopy in each case, *e.g.* by using large beams to reduce the inhomogeneity of these shifts or by lowering the depths of these lattices during spectroscopy.

If, in contrast, such differential frequency shifts of the clock transition are resolved spectrally, they give rise to a wealth of new opportunities. For example, strongly state-dependent lasers may be used to split the transition frequencies of individual lattice sites deliberately and address specific parts of the lattice, ranging from applying a large-scale intensity gradient across the lattice to selecting single sites by strongly focussed beams[20,21,291] or applying superlattices, to name only a few examples.

7.2.3 Residual shifts of the clock transition

As mentioned in the previous section 7.2.2, an optical lattice at the magic wavelength cancels the differential AC–Stark shift only to leading order. However, there are both higher-order contributions of the AC–Stark shift – most importantly the fourth-order shift commonly referred to as hyperpolarisability – and the terms of a multipole expansion for the fermionic isotopes that have a non-zero nuclear spin, *i.e.* the magic wavelength specifically cancels the scalar term of the second-

order AC–Stark shift. Finally, any magnetic fields that are applied, *e.g.* to separate the nuclear spin substates in the fermionic isotopes, give rise to additional shifts as well.

The effects related to the nuclear spin have been studied Boyd *et al.*[46] (see also Boyd[292]) in a strontium OLC; a detailed review of hyperpolarisability, specifically in the case of ytterbium, is given by Taichenachev *et al.*[293] and Barber *et al.*[133] Therefore, the following discussion is limited to a brief introduction of each effect and a discussion of its possible impact on studies of quantum gases.*

Hyperpolarisability

If the second-order AC–Stark shift is considered as the stimulated absorption and re-emission of a photon (or vice versa) on a single-photon transition, hyperpolarisability arises from two-photon transitions and it is thus proportional to the square of the laser intensity. Several two-photon resonances have been identified in the vicinity of the magic wavelength, but the resulting shifts are well below the hertz level for typical optical lattices as used for spectroscopy.[133] With respect to studies of quantum gases at wavelengths away from the magic wavelength, while such resonances need to be kept in mind, the can be avoided in most cases by detuning the lattice laser. However, the corresponding two-photon transitions may end in the continuum of states above the ionisation threshold for short lattice wavelengths – especially for the excited state $^3\mathrm{P}_0$, where this is the case *e.g.* in the vicinity of the resonance frequency of the intercombination transition $^1\mathrm{S}_0 \leftrightarrow {}^3\mathrm{P}_1$. In consequence, the effects of hyperpolarisability need to be evaluated carefully, *e.g.* in the case of state-selective potentials (see section 2.8.4).

Vector and tensor light shifts

The spin-dependence of the second-order AC–Stark shift for the fermionic isotopes may be expressed by a multipole expansion, where the leading order is the spin-independent scalar term. The first higher-order terms are the vector light shifts[292]

$$V^{(\mathrm{v})} \propto \varepsilon m_F I_\mathrm{L} \tag{7.3}$$

and tensor light shifts[292]

$$V^{(\mathrm{t})} \propto \frac{3\cos\theta_\mathrm{pol} - 1}{2}\left(3{m_F}^2 - F(F+1)\right) I_\mathrm{L} \tag{7.4}$$

where ε is the degree of elliptic polarisation† and θ_pol is the angle between the polarisation axis of the laser and the quantisation axis that is usually defined by a strong bias magnetic field.

Vector light shifts are readily described in terms of an effective magnetic field that is generated by an elliptically polarised lattice laser.‡ As in the case of the bias magnetic field (see below) the resulting linear splitting of the nuclear spin substates is not necessarily a problem for precision

*Of course, the same shifts exist for any laser, but other beams used in our experiments will typically be of much lower intensities than an optical lattice (*cf.* the additional light shift due to the probe beam discussed in section 7.4 for bosonic isotopes).

†Linear polarisation corresponds to $\varepsilon = 0$, whereas $\varepsilon = \pm 1$ corresponds to two states of circular polarisation.

‡In fact, vector light shifts are well known from alkali elements.[233] For instance, they have been used to generate spin-dependent optical lattice potentials,[259] albeit these lattices are operated much closer to resonance and the resulting shifts are thus much larger.

spectroscopy of quantum gases, provided that the shift is sufficiently stable and the individual spin states may be resolved spectrally, if required. Nevertheless, the orientation of the lattice-induced to the bias magnetic field may give rise to complications in some cases, *e.g.* a rotation of the quantisation axis or m_F–changing terms due to the effective magnetic field are conceivable. The interplay of bias and lattice-induced magnetic fields has been analysed[294] for the MIS scheme used in the bosonic isotopes (see section 7.4), and in a similar fashion the lattice-induced field may be oriented perpendicular to a strong bias magnetic field to minimise the shift.[292]

The magnitude of the vector shifts close to the magic wavelength has been studied both theoretically[132] and experimentally.[59] The vector polarisability of the excited state $^3\mathrm{P}_0$ is expected to be much larger than that of the ground state, and values of $\alpha^{(\mathrm{v})} = -0.10$ a.u. (0.075 a.u.) have been predicted for the $^3\mathrm{P}_0$ state of ^{171}Yb (^{173}Yb) at the NIR magic wavelength.[132] These predictions are in agreement with measurements in an ^{171}Yb-OLC, where vector shifts up to 220 Hz for circularly polarised light were observed in an optical lattice with a depth of $500E_{\mathrm{rec}}^{(\mathrm{l})}$.[59] In studies of quantum gases, however, typical lattice depths and hence the resulting vector shifts are at least an order of magnitude smaller than this. Therefore, a moderate intensity stabilisation of the lattice is sufficient to prevent these shifts from impeding precision spectroscopy at the hertz-level for the fermionic isotopes (*cf.* also the discussion of the bias magnetic field below).

Obviously, vector shifts can be avoided by using a linearly polarised lattice; but, while this is possible in two dimensions either by a phase-stable lattice or by two detuned one-dimensional lattices,[184] purely linear polarisation cannot be achieved in a three-dimensional lattice. Only a common plane of polarisation may be established. If multiple detuned lattices, *e.g.* in one and two dimensions, are used to create a three-dimensional optical lattice, the effects of the rapidly rotating, possibly spatially varying state of polarisation as well as the orientation of the bias magnetic field (see below) have to be considered carefully with respect to the specific experimental situation.

In contrast to vector shifts, the tensor shifts described by equation (7.4) exist for both linearly and circularly polarised light. Since they depend on the orientation of the lattice polarisation, they may be suppressed only for linear polarisation of the lattice at a specific orientation towards the quantisation axis where the first term vanishes. Thus there will be residual tensor shifts of the clock transition in a three-dimensional optical lattice. For studies of ultracold gases, fluctuations of these shifts need to be avoided, *i.e.* stable and well reproducible intensities are required, but their absolute values are of little consequence in most cases. As in the case of the vector shifts, potential spin rotation may need to be analysed in more detail, depending on the specific experimental conditions. Finally, it is interesting to note that there are no tensor shift in ^{171}Yb due to its small nuclear spin of $I = 1/2$.[295]

Bias magnetic field

In the fermionic isotopes, the states $^1\mathrm{S}_0$ and $^3\mathrm{P}_0$ have different Landé factors due to hyperfine interaction in the excited state,[46] although neither state has any net angular momentum ($J = 0$). Therefore, a bias magnetic field of magnitude B induces a differential Zeeman shift

$$\hbar\Delta\omega_{\mathrm{s}}^{(\mathrm{B})} = \left(g_I \cdot \Delta m_F + \delta g \cdot m_F'\right)\mu_N B \tag{7.5}$$

of the $|^1\mathrm{S}_0, m_F\rangle \rightarrow |^3\mathrm{P}_0, m_F'\rangle$ transition, where $g_F(^1\mathrm{S}_0) = g_I$ and $g_F(^3\mathrm{P}_0) = g_I + \delta g$, and may be used to separate the transitions of individual nuclear spin states. For ^{171}Yb a splitting of 420 Hz G^{-1} between the transitions from either nuclear spin state has been reported,[59] *i.e.* fields of a few gauss

are sufficient to spectrally resolve the nuclear spin states during spectroscopy. In OLCs, Zeeman and vector shifts are continuously monitored by probing opposite nuclear spin states $\pm m_F$ at opposite polarisations in an alternating pattern. In order to probe the clock transition and detect frequency shift at the hertz level, stable and reproducible magnetic fields are required. Based on the aforementoned results, a relative stability of 10^{-3} or better is required to achieve this level of sensitivity at a bias field of $B \sim 1$ G.

Moreover, the orientation of the bias magnetic field is naturally determined by transition that is to be driven by a specific probe laser. In our case, we plan to use a probe laser and a 1D optical lattice at the magic wavelength along the z-axis for most experiments, *i.e.* the bias field has to be applied along that axis to drive $\sigma^{\pm}$ transitions or in the x–y-plane to drive π transitions. Therefore, the orientation of the bias field, *e.g.* with respect to a deep one-dimensional lattice at the magic wavelength along z or a tow-dimensional lattice in the x–y-plane, is severely restricted, which has to be taken into account when evaluating the effects of the lattice polarisation discussed previously. The same argument applies if a probe laser propagating in the x–y-plane is used instead.

7.3 An ultrastable laser system

In order to probe the $^1S_0 \leftrightarrow {}^3P_0$ clock transition of ytterbium (see chapter 2), a frequency-doubled commercial diode-laser* is stabilised to an ultrastable resonator at the transition wavelength λ_s and provides a laser source of sufficient short-term stability for spectroscopy on this transition.

The ultrastable resonator is a high-finesse, vertically mounted cavity.† To insulate it from mechanical and thermal fluctuations and achieve the intended stability of the resonance frequency, the cavity is enclosed by two heat shields – a passive inner shield and an actively stabilised outer one – within a vacuum chamber at a residual pressure of about 10^{-7} mbar (see figure 7.4). The vacuum system has been mounted on a commercial passive vibration insulation system‡ surrounded by a soundproof box.

The laser is stabilised to the resonator by the Pound–Drever–Hall (PDH) method[297,298] with slow feedback to the PZT of the external-cavity diode-laser (ECDL) and fast feedback to an external AOM with a servo bandwidth of 1 MHz. Judging from the PDH error signal, the lock to the ultrastable cavity achieves residual line widths below 1 Hz. However, we have set up two identical ultrastable resonators for quantitative evaluation of the clock laser stability. Each has its own fast-feedback AOM, so the laser may be split and locked to each cavity independently. Residual −3 dB line widths of down to 5 Hz have been observed in the beat notes of the lasers recently. These results demonstrate that spectroscopy at sensitivities of a few hertz is within reach.

Further details on the ultrastable resonator setup and initial characterisation and locking of the laser are found in the diploma theses of Thomas Rützel[296] and Jan-Henrik Carstens.[299] A detailed discussion of improved locking schemes and stabilisation that have led to the aforementioned, preliminary results will be given along with future improvements in the doctoral thesis of Alexander Thobe.

*Toptica, DL-SHG pro. The system has been retrofitted with a tapered amplifier module recently, increasing its typical output power to 300 mW.

†AT Films, ATF-6030 (finesse $\mathscr{F} \approx 150\,000$, spacer: ULE glass, mirror substrates: fused silica). These cavities were originally developed for the ytterbium optical lattice clock at NIST, Boulder.[158]

‡MinusK Technologies, 150BM-1.

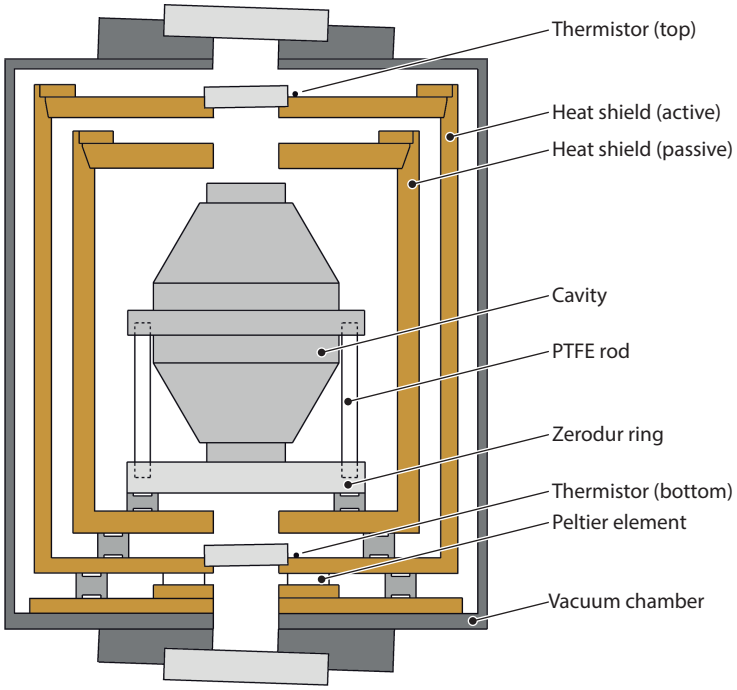

Figure 7.4 | Housing of the ultrastable resonator. As shown in this schematic drawing, each ultrastable resonator of the clock laser system is kept under vacuum for thermal and mechanical insulation. The resonator is mounted on three PTFE rods that rest on a Zerodur ring and enclosed by two gold-coated copper heat shields. The inner one is a passive shield, whereas the outer shield is actively stabilised by a Peltier element and monitored by a pair of thermistors. The resonator is accessed by the clock laser along the central vertical axis of the setup, but the access ports in the outer heat shield have been covered by quartz windows to reduce the leakage of black-body radiation from the vacuum chamber into the inner volume. All windows have been AR-coated for a wavelength of 578 nm and tilted, where possible, to avoid stray back-reflection. Drawing courtesy of Thomas Rützel,[296] see *ibid.* for further details.

7.4 Driving the clock transition

Driving the clock transition $^1S_0 \leftrightarrow {}^3P_0$ is straightforward for the fermionic isotopes, since it has a finite transition rate due to hyperfine interaction (see section 2.5). The on-resonance Rabi frequency is given by[137]

$$\Omega = \frac{\Gamma}{2}\sqrt{\frac{I_\mathrm{L}}{I_\mathrm{L,sat}}}. \tag{7.6}$$

Based on the decay rates Γ predicted by Porsev & Derevianko[174] (see table 2.6), a probe beam of $P^{(\mathrm{s})} = 10\,\mathrm{mW}$ focussed to a diameter of $w_0^{(\mathrm{s})} = 200\,\mu\mathrm{m}$ yields a peak Rabi frequency of about $\Omega/2\pi = 6.4\,\mathrm{kHz}$ (6.0 kHz) in the case of ^{171}Yb (^{173}Yb). Therefore, laser powers on the order of a few 100 mW (see section 7.3) are sufficient to produce either moderate, but spatially very homogeneous Rabi frequencies across the atomic sample or extremely large peak Rabi frequencies, *e.g.* much greater than the equivalent recoil energy of an optical lattice.

In contrast, the clock transition is more difficult to address in the bosonic isotope, for it is strictly

forbidden as a single-photon transition (see section 2.5 for details). Several schemes[67,68] to interrogate the clock transition indirectly by means of multi-photon resonances have been proposed. A number of other interrogation schemes aims at artificially reproducing the perturbation of eigenstates that creates a finite transition strength in the fermionic isotopes – either by an additional laser field at a magic wavelength[71] or by a static magnetic field.[69,70] These mixing schemes are generally much easier to implement, and more instructive, than the aforementioned multi-photon schemes. In particular, they allow interrogation of the clock transition of bosonic atoms in the same way as for fermionic atoms, *i.e.* directly by a single laser at the clock transition itself. This feature is especially advantageous if quantum-gases are studied, since bosonic and fermionic systems can be studied by almost the same methods. In our case, we plan to implement the latter scheme, using a static magnetic field, as it does not require an additional laser beam.

In this magnetically induced spectroscopy (MIS) scheme (see the article by Taichenachev *et al.*[70] for details), a weak static magnetic field $\boldsymbol{B} = B \cdot \boldsymbol{e}_z$ is applied. The corresponding Hamiltonian $H_{\mathrm{MIS}} = -\boldsymbol{\mu} \cdot \boldsymbol{B}$ does not modify the energy of the perturbed $^3\mathrm{P}_0$ eigenstate in first order perturbation theory, but the eigenstate itself acquires admixtures of other states, mostly $^3\mathrm{P}_1$, resulting in a perturbed eigenstate

$$|^3\mathrm{P}_0{}'\rangle \approx |^3\mathrm{P}_0\rangle + \frac{\Omega_\mathrm{B}}{\Delta_\mathrm{FS}} |^3\mathrm{P}_1, m_J = 0\rangle \tag{7.7}$$

where $\hbar\Omega_\mathrm{B} = -\langle ^3\mathrm{P}_1, m_J = 0|\boldsymbol{\mu} \cdot \boldsymbol{B}|^3\mathrm{P}_0\rangle$ and $\hbar\Delta_\mathrm{FS}$ is the fine-structure splitting of the two states. Obviously, the transition from $^1\mathrm{S}_0$ to this perturbed eigenstate has a finite transition amplitude

$$\Omega \approx -\hbar^{-1} \langle ^1\mathrm{S}_0|\boldsymbol{d} \cdot \boldsymbol{E}|^3\mathrm{P}_0{}'\rangle = \frac{\Omega_\mathrm{B}\Omega_\mathrm{L}}{\Delta_\mathrm{FS}} \tag{7.8}$$

where $\hbar\Omega_\mathrm{L} = -\langle ^1\mathrm{S}_0|\boldsymbol{d} \cdot \boldsymbol{E}|^3\mathrm{P}_1\rangle$ is the Rabi frequency with respect to the intercombination transition $^1\mathrm{S}_0 \leftrightarrow {}^3\mathrm{P}_1$. In terms of experimental parameters, the Rabi frequency reads

$$\Omega = \kappa\sqrt{I_\mathrm{L}}\,|B| \cos\theta_\mathrm{pol} \tag{7.9}$$

where θ_pol is the angle between the magnetic field $\boldsymbol{B}$ and the electric field vector $\boldsymbol{E}$ of a linearly polarised laser. In a detailed analysis, Taichenachev *et al.*[70] (see also the PhD thesis of Barber[158]) reported $\kappa = 2\pi \times 186\,\mathrm{Hz\,T^{-1}\,mW^{-1/2}\,cm^{-1}}$ in the case of ytterbium. For a magnetic field of $B = 10\,\mathrm{G}$ the same probe beam parameters as above hence result in a Rabi frequency of only $\Omega/2\pi = 23\,\mathrm{Hz}$.

This figure demonstrates well that large Rabi frequencies are much harder to achieve for the bosonic isotopes, especially since it scales only with the square root of the probe beam intensity, and the realisation of some proposals is impeded in the bosonic isotopes (see chapter 8). Moreover, large magnetic fields and probe beam intensities, which are required to achieve substantial Rabi frequencies, give rise to substantial second-order Zeeman shifts and differential AC-Stark shifts due to the probe beam itself. A detailed analysis[70,158] of the MIS scheme reveals that these shifts are of the same order of magnitude as the Rabi frequency even under optimal conditions. Therefore, although systematic shifts of the clock transition are of little consequence in our case, their fluctuations or spatial variation may still become a problem, if large Rabi frequencies are used. A careful survey of the stability – both short-term and shot-to-shot – of magnetic field and probe beam intensity is necessary.

Finally, additional shifts arise from the interplay of the MIS scheme and the optical lattice.[294] To leading order, an elliptically polarised lattice laser beam gives rise to a small additional magnetic field that modifies the quadratic Zeeman shift. The bias magnetic field in turn modifies the AC–Stark shifts induced by the lattice due to the linear Zeeman splitting of the contributing intermediary states. Even from this brief summary it is clear that these shifts can be suppressed if either a linearly polarised laser is used or the magnetic field $\boldsymbol{B}$ lies in the plane of polarisation of the lattice beam. In consequence, they are not going to pose any significant problem for applications of the clock transition in quantum gases, especially, if a deep optical lattice is applied only along one dimension during spectroscopy.

Chapter 8

Conclusion and outlook

In the framework of this thesis, an experimental apparatus for studies of quantum-degenerate Bose and Fermi gases of ytterbium and ultracold Yb-Rb mixtures by ultrahigh precision spectroscopy has been developed. I have presented a versatile experimental setup (see chapter 4) based on a novel 2D-/3D-MOT scheme and the subsequent all-optical production of quantum-degenerate gases as well as first experimental results obtained from this apparatus.

Laser cooling of ytterbium has been realised in a novel 2D-/3D-MOT for the first time (see chapter 5). I have shown that transverse loading of a 2D-MOT from an atomic beam, as first demonstrated for lithium,[99] can be implemented in a compact glass cell using dispenser sources and employed for efficient magneto-optical trapping of alkaline earth–like species.* The optimal parameters for cooling and trapping of ytterbium emitted by these dispensers are predicted accurately by numeric simulations of the 2D-MOT. Therefore, the techniques and experimental findings reported in this thesis may be applied to implement similar 2D-MOTs for other elements suffering from low vapour pressures at room temperature. Moreover, a second species, rubidium in the apparatus presented herein, may be laser cooled and trapped in a single 2D-MOT setup for studies of quantum-degenerate mixtures with ytterbium.

I have also demonstrated the subsequent loading of a 3D-MOT operating on the narrow $^1S_0 \leftrightarrow {}^3P_1$ intercombination transition of ytterbium from the 2D-MOT. Spectral broadening of the 3D-MOT cooling laser allows precise tailoring of its capture range to the velocity distribution of the flux emerging from the 2D-MOT, whereas temperatures of about 20 μK are achieved for narrow-line cooling. The use of additional pushing beam enhances the transfer rates further. In conclusion, the 2D-/3D-MOT setup developed in the framework of this thesis yields excellent loading rates of typically 1.5×10^7 s^{-1} for ^{174}Yb. Although the hyperfine structure of ^{173}Yb is not ideal for magneto-optical trapping on the broad $^1S_0 \leftrightarrow {}^1P_1$ principal transition, we have achieved substantial loading rates of this fermionic isotope as well. Our apparatus thus provides larger loading rates than reported[76,77,100] for ytterbium Zeeman slowers to date.

Starting from this 2D-/3D-MOT setup, I have presented forced evaporative cooling of ^{174}Yb and ^{173}Yb in a crossed optical dipole trap that has planned and implemented in the framework of this thesis (see chapter 6). We routinely generate Bose–Einstein condensates of 1×10^5 ^{174}Yb atoms† with no discernible thermal fraction or quantum-degenerate Fermi of typically 2×10^4 atom at

*We have learnt of another recent realisation of an ytterbium 2D-MOT in a joint experiment by the groups of S. L. Rolston and J. V. Porto. Moreover, Rathod *et al.*[300] have recently reported loading of a 2D-MOT from a Zeeman slower.

†Note that the VXDT has been planned conservatively and that the implementation of an optical lattice during the writing of this thesis allowed the production of even larger BECs with up to 2×10^5 ^{174}Yb atoms.

$T/T_F = 0.15$, but temperatures as low as $T/T_F = 0.09$ have been achieved.

Finally, I discussed several potential applications of the ultranarrow $^1S_0 \leftrightarrow {}^3P_0$ clock transition for probing and manipulation of ytterbium quantum gases in an optical lattice (see chapter 7), *e.g.* the detection multiple occupancies via interaction-induced shifts of the transition frequency or measurements of spin–spin correlations between particles at the same or neighbouring lattice sites. As I have shown in a brief summary, an ultrastable laser system has been set up and allows spectroscopy of the clock transition at sensitivities of a few hertz.

As of the writing of this thesis, an optical lattice composed of a strongly confining, one-dimensional lattice along z and a triangular/hexagonal lattice in the x–y-plane is being set up. Several theoretical proposals[232,244,245,301] have already pointed out the prospects of studying SU(N)-symmetric system with $N > 2$ in such a lattice. Preliminary proof-of-principle spectroscopy experiments with a resolution of several kilohertz have already been performed in the one-dimensional lattice, and the next experimental step will be to improve this sensitivity in the full three-dimensional optical lattice.

After studying *e.g.* the MI–SF transition in ^{174}Yb to refine the use of the clock transition for detection of interaction and correlations as well as the preparation of atoms in the metastable excited electronic state $^3P_0$, we plan to concentrate on the novel quantum phases, whiche arise from the nuclear spin decoupling and metastable electronic states, in future experiments. However, as mentioned briefly both in chapter 2 and section 7.1 the use of the clock transition for the creation of artificial gauge potentials (see the review paper by Dalibard *et al.*[85] for details) represents an interesting alternative to the well-established technique of lattice modulation in triangular optical lattice.[32]

Since our lattice setup is designed specifically to allow tuning of the lattice wavelength across a wide range around the magic wavelength, we plan to study mixed systems of fermionic ^{173}Yb in the $^1S_0$ and $^3P_0$ states which are excellent candidates to realise the Kondo-lattice model (KLM) in ultracold atoms. Several theoretical publications[92–96] have already discussed and pointed out the prospects of using ultracold AEL atoms in studying this model that is a long-standing issue in solid-state physics, *e.g.* in the investigation of heavy-fermion materials. Here, a mobile species of spin-1/2 particles interacts with a second species of localised spin-1/2 particles via contact exchange interaction in a periodic potential. Therefore, ytterbium is ideal for studying this model, and the localised species will be implemented by atoms in the metastable state $^3P_0$, in order to suppress losses due to the interaction of excited state atoms, whereas ground-state atoms can be used as the mobile species. As discussed in section 2.8, the lattice wavelength may then be used to tune the relative depths of the lattice potentials accordingly.

Owing to the harmonic confinement of the trap, the system is expected to exhibit a shell structure with an outer metallic phase followed by a Kondo-insulating phase. In this correlated state, each lattice site is occupied by one mobile and a localised atom whose spins are correlated,* and both spin–spin correlations between these species and a suppression of number flucuations should be observable. The Kondo insulator may be followed by another metallic phase and an inner band insulator phase (see the articles by Silva-Valencia & Souza[95,96] for further details).

Before systems like the KLM can be studied in ytterbium quantum gases, however, the interac-

*The Kondo-insulating phase is expected to occur for both ferromagnetic and antiferromagnetic coupling, resulting in correlation and anti-correlation of the spins, respectively.[95]

tion parameters of the metastable state $^3P_0$, which are largely unknown at this point, have to be studied in more detail, particularly for the fermionic isotopes. It remains to be studied to what extent direct interaction[92] $(U_{eg}^{+} + U_{eg}^{-})/\sqrt{2}$ of $^1S_0$ and $^3P_0$ atoms and interaction of ground-state atoms modify the systems that will eventually be realised in quantum gases of ultracold atoms.

In a long-term perspective, quantum gases of ytterbium may be used to study a variety of SU(N)-symmetric spin Hamiltonians, as discussed in the seminal paper by Gorshkov *et al.*[92] However, the expected nuclear spin decoupling in the fermionic AEL needs to be verified experimentally, and especially the residual nuclear spin–dependence in the excited state $^3P_0$ needs to be investigated.

Appendix A

Main vacuum chamber

The central vacuum chamber has only been discussed briefly in section 4.1. Conceptually, it is based on the chambers used by existing research projects of our group.[254–257] For our project, however, it was redesigned from scratch by the author for several reasons. Some modifications were made to adapt the vacuum system to our requirements or to improve the ultimate vacuum conditions and robustness of the apparatus, *e.g.* larger tube diameters to improve pumping speeds or the use of a single large-diameter electrical feedthrough. The main reason was the extremely complex construction of the older design, using a welded chamber with two internal compartments and additional tubes to connect feedthroughs *etc.*, to the individual glass cells, which resulted in extremely expensive offers – about twice as high a price per unit as for the final, redesigned chamber – by commercial manufacturers. Nevertheless, special attention was paid to keeping the chamber mechanically compatible with the previous iteration used by the experiment on K-Rb mixtures.

We decided to have the main chamber manufactured from a solid block of stainless steel. In our case, this results in a much simpler construction for a similar functional layout as in previous iterations. The internal structure, including all connections between the glass cells or to pumps, electrical feedthroughs *etc.*, has been milled or drilled, and only the peripheral flanges have been welded to the main body. Highly non-ferromagnetic steel (1.4429ESU, $\mu_r < 1.03$) was used for the body of the chamber as well as all of the flanges, whereas the tubes are made of 1.4404 steel.

The vacuum chamber is mounted to the superstructure frame shown in figure 4.7 by a mounting ring and four pylons (see figure 4.4). Additional threaded bores at the bottom of the chamber allow mounting of both the primary magnetic coils designed for our experiment (see section 4.2) and the hybrid 8-Dee coils[262] used by the projects on K-Rb mixtures. The graphite tubes* of the DPS are mounted in bores along the central axis and the lower tube is secured by a threaded aluminium ring.

The science cell is mounted to a CF flange at the bottom of the chamber, whose knife edge has been cut directly into the body. Two sets of threaded bores allow mounting of the science cell at various orientations in steps of 30°. In contrast, the 2D-MOT cell is mounted on top of the chamber via a pair of Helicoflex gaskets† and a counter-flange (see figure A.1). Two ring-shaped grooves have been cut into the top surface of the chamber to simplify centring of the gaskets and polished to establish a tight vacuum seal. However, the inner groove is only intended as a backup in case of damage to the primary, outer one.

Figure A.1 | Helicoflex sealing of the 2D-MOT cell illustrated by a CAD model.

*Goodfellow, custom-manufactured, drawing numbers GFD 0760 & GFD 0756.

†Garlock, HN100-type, reference number H15047 (mantle: aluminium). These gaskets consist of a spiral spring and a metallic outer mantle.

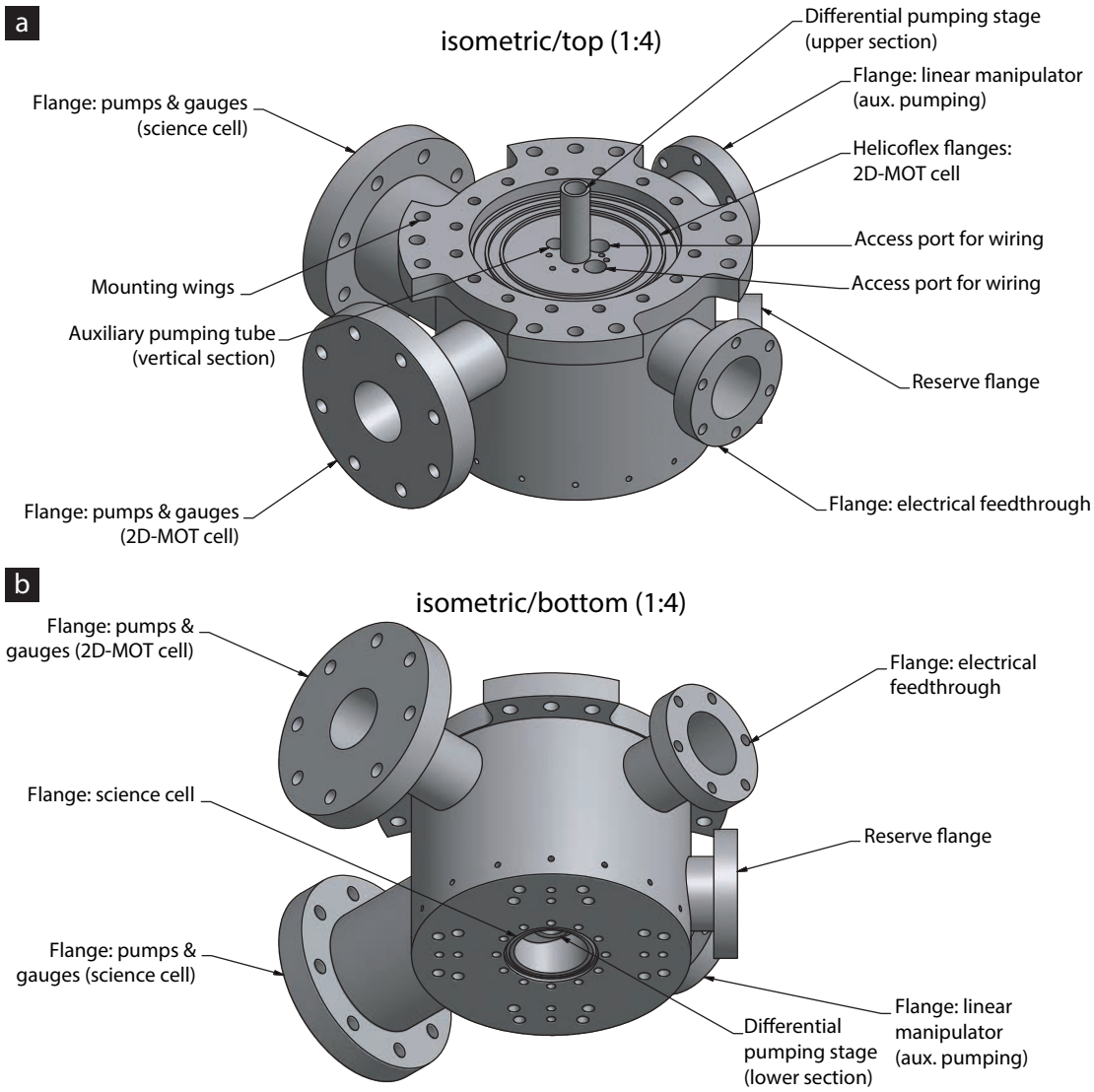

Figure A.2 | Overview of the vacuum chamber. External features of the vacuum chamber are shown in isometric views from above **(a)** and below **(b)** the chamber.

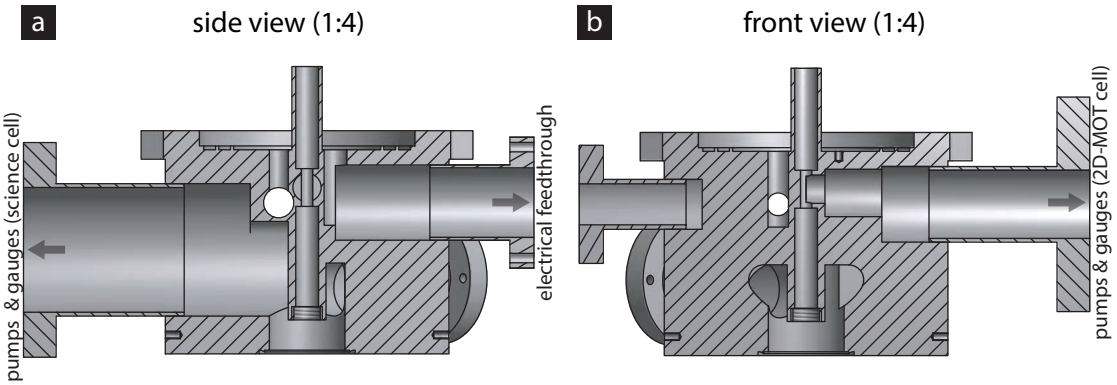

Figure A.3 | Pumping conduits in the central vacuum chamber. Cross sections of the vacuum chamber show conduits connecting the science cell **(a)** and the 2D-MOT cell **(b)** to lateral flanges used to connect vacuum pumps and gauges in orthogonal vertical planes.

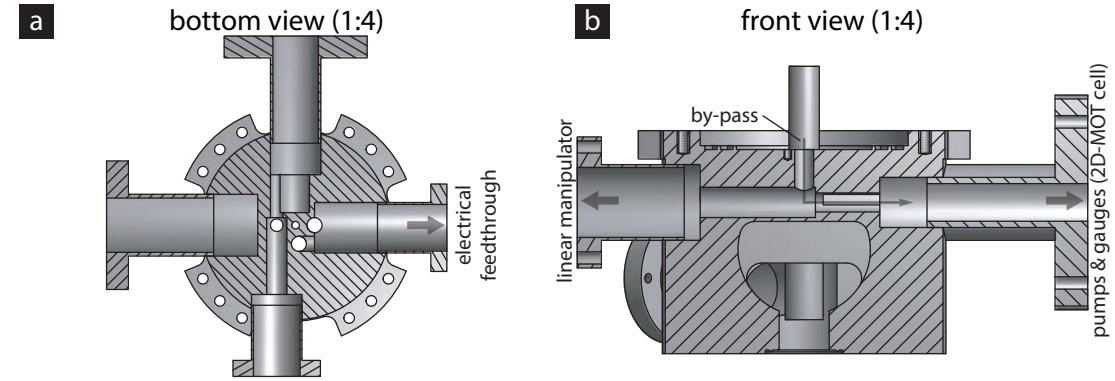

Figure A.4 | Auxiliary pumping stage and wire conduits. **(a)** A horizontal section view centered to the flange carrying the high-power electric feedthrough shows the conduits used to connect it to the dispensers in the 2D-MOT cell in more detail. **(b)** The auxiliary pumping stage is shown in more detail in another section view in a parallel plane of figure A.3b centred to the flange carrying the linear manipulator, which is used to block or unblock the by-pass of the upper DPS.

Appendix B

Numeric simulation of a transversely loaded 2D-MOT

In order to assess the feasibility of operating a transversely loaded 2D-MOT of ytterbium and characterise it in more detail, *e.g.* to determine optimal parameters of the MOTs, we performed a series of numerical simulations both prior to setting up the apparatus in the first place and during characterisation of the 2D-/3D-MOT system. Some of the results are shown in figures 5.2 and 5.6. In this appendix, the methods used in these numerical simulations are presented in more detail.

B.1 Simulation program

The simulation is initially provided with the parameters of a 2D-MOT geometry (*cf.* figure 3.1), *i.e.* the geometry and intensity of cooling laser beams, position and orientation of an emitter surface as well as the parameters of a differential pumping stage, as illustrated by figure B.1. Furthermore, the gradient of a two-dimensional magnetic quadrupole field $\boldsymbol{B}(\boldsymbol{r}) \propto x\boldsymbol{e}_x - z\boldsymbol{e}_z$ and other parameters, *e.g.* the emitter temperature, are specified. For the sake of simplicity, gradients along the vertical axis (y) are ignored and the lasers are implicitly assumed to have the correct circular polarisation for a 2D-MOT configuration. Moreover, a homogeneous intensity is used for the laser beams instead of the actual Gaussian profiles.

At its core, the simulation traces the trajectory of an atom in the 2D-MOT from a given initial position and velocity by numerically integrating the mean radiation force from the lasers in the magnetic field in time steps of 1 µs. The trajectory ends if any of three conditions is fulfilled:

1. The trajectory reaches the predefined horizontal exit plane containing the DPS.
2. The trajectory leaves a predefined boundary volume. In our case, a cylinder around the 2D-MOT axis with a radius of 30 mm is used.
3. The vertical velocity component is positive, *i.e.* the atom travels away from the exit plane. Since this velocity is preserved in a purely horizontal laser setup, the trajectory cannot reach the exit plane.

If condition 1 is fulfilled, the initial and final parameters of the trajectory are stored along with a status flag that indicates whether the trajectory enters and passes the differential pumping stage. The trajectory is discarded otherwise.

Trajectories are calculated successively for a three-dimensional grid of velocities, ranging from $0\,\mathrm{m\,s^{-1}}$ to $250\,\mathrm{m\,s^{-1}}$ along the normal vector of the emitter surface and $-250\,\mathrm{m\,s^{-1}}$ to $250\,\mathrm{m\,s^{-1}}$

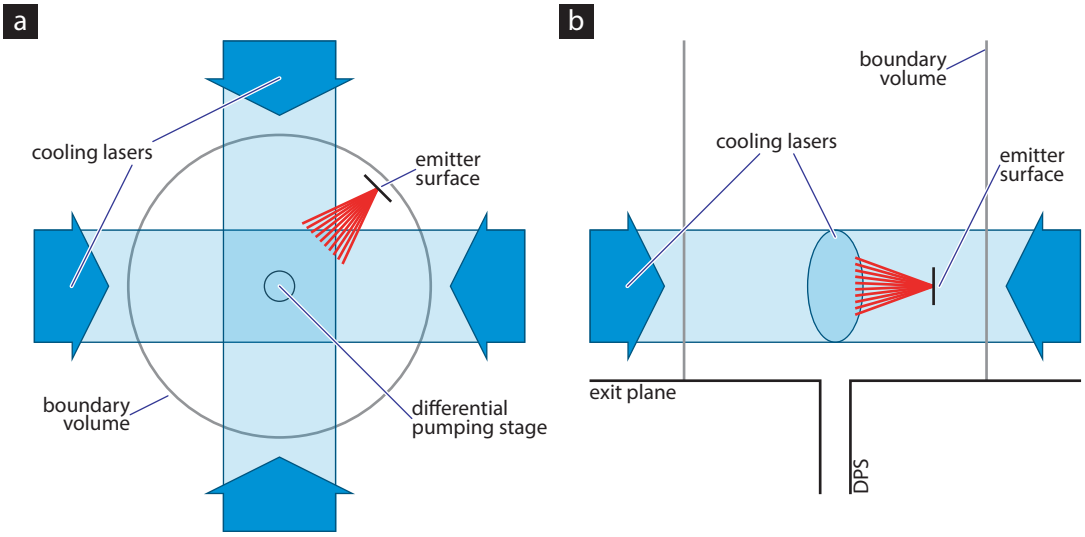

Figure B.1 | Geometry of the numeric simulation. The geometric setup of an ytterbium 2D-MOT for simulation of transverse loading is illustrated schematically in top view **(a)** and side **(c)**. It is discussed in more detail in the text below, including the configurable and hard-coded geometric parameters shown above.

along each of two lateral axes in steps of $1\,\mathrm{m\,s^{-1}}$, and originating from the centre of the emitter surface.*

In order to determine the distribution of atoms cooled by the 2D-MOT and entering the DPS, each trajectory is also assigned a flux based on its initial velocity, where the emission of ytterbium by the source is assumed to obey an effusive distribution

$$\Phi(\boldsymbol{v}) = \begin{cases} \bar{n}\boldsymbol{v}\cdot\boldsymbol{A}_\mathrm{e}\left(\frac{2\pi k_\mathrm{B}T_\mathrm{e}}{m}\right)^{-3/2}\exp\left(-mv^2/2k_\mathrm{B}T_\mathrm{e}\right) & \text{if } \boldsymbol{v}\cdot\boldsymbol{A}_\mathrm{e} > 0, \\ 0 & \text{otherwise,} \end{cases} . \tag{B.1}$$

i.e. atoms are emitted into a velocity segment of size d^3v around $\boldsymbol{v}$ at a rate of $\Phi(\boldsymbol{v})\mathrm{d}^3v$. Here $\boldsymbol{A}_\mathrm{e}$ and T_e are the normal vector of the emitter surface and its temperature as specified (see above). The mean density $\bar{n}$ may be determined from the vapour pressure curve of ytterbium (see section 2.1) using the emitter temperature T_e.

In conclusion, the simulation program returns a set of trajectories and associated flux rates produced by the 2D-MOT. The program itself is written in C++ and configured via input from a text file. Likewise, the output trajectories are written to a formatted text file, so the results may be evaluated with another program later. To retrieve the expected loading rate of a 3D-MOT from the output of the simulation program, the flux rates of all trajectories with final velocities $-\boldsymbol{v}\cdot\boldsymbol{e}_y/|v| \geq \cos\theta_\mathrm{c}$ and $|v| < v_\mathrm{c}$ have been accumulated to yield a net loading rate for a given critical angle θ_c and velocity v_c.

*Optionally, the emitter surface may be subdivided into multiple sampled points of origin. However, this option has not been used in the simulations presented here.

B.2 2D-MOT scenario

For the simulations presented in chapter 5, we have re-created the actual experimental setup as accurately as possible. The cooling force has been set to the parameters of Doppler cooling of ytterbium on the $^1S_0 \leftrightarrow {}^1P_1$ transition. 2D-MOT beams of an elliptical cross section with diameters of 10 mm (40 mm) along the horizontal (vertical) direction and a homogeneous intensity of $I_L = 0.6 I_{L,sat}$ have been setup to match the configuration of the actual beams, in particular they are truncated by the differential pumping stage and not centred to the emitter surface. The latter has been placed at the approximate position and orientation of the emitter slit of an ytterbium dispenser in our setup (see section 4.1.1). The emitter surface corresponds to a disc with a radius of 1 mm sampled at its centre, but is of no consequence for the results presented in chapter 5. Based on the operating parameters of our beam apparatus, we have assumed an emitter temperature of $T_e = 700$ K. Finally, the DPS has been set to the same initial radius and angle of acceptance as in our experimental setup, *i.e.* 5 mm and *ca.* 1.8°, respectively (see section 4.1.1).

B.3 Remarks

As shown in chapter 5 the simulations reproduce our experimental findings remarkably well. Nevertheless, numerous assumptions and simplifications have been made that need to be kept in mind during any analysis of their results.

Most importantly, only the mean radiation pressure on the atoms due to Doppler cooling has been taken into account, whereas the stochastic nature of absorption and re-emission of photons, effects of imperfect polarisation, interactions of atoms and so forth have been ignored, since the original, primary intention of performing these numeric simulations has been to gain a basic understanding of the 2D-MOT performance in order to assess the feasibility of the concept and coarsely identify suitable parameters.

Furthermore, the Gaussian intensity distributions of the beams have been ignored and replaced by flat distributions of equal mean intensities. This simplification was made to avoid the time-consuming calculation of the local intensities for each integration step. As discussed in section 5.5, this simplification may be one of the reasons causing the different dependence of the optimal 2D-MOT detuning on the magnetic field gradient away from the global optimum in the simulations as compared to the experimental results.

An effusive velocity distribution has been assumed for the ytterbium atoms emitted by the dispenser, which is justified by the lack of any exact knowledge of the actual emission pattern. Quantitative measurement of the velocity distribution of an actual dispenser is not only difficult in our setup, but we have also visually observed considerable qualitative differences from one dispenser to the next during initial testing. Since it is not our primary interest, we have refrained from characterising the dispenser in any more detail.

Finally, we have ignored the pushing beam in our numeric simulation, because its effect on the loading rate observed in our experiments depends intricately on its alignment (see section 5.4) and cannot be reproduced with sufficient accuracy in the simulations. Running a series of simulations for different pushing beam configuration, on the other hand, would be extremely time-consuming and has thus not been attempted.

Appendix C

AC–Stark shifts in ytterbium

The qualitative discussion of state-dependent optical potentials for the $^1S_0$ and $^3P_0$ states of ytterbium in section 2.8 uses a simplified expression of the AC–Stark shift induced by another state of a multi-level atom. Equation (2.6) neglects both possible decay rates of the contributing state into one or more third states and the influence of angular momentum coupling in the individual m_J substates. In contrast, the AC–Stark shifts of these states were revisited briefly in section 7.2.3 in order to discuss their dependence on magnetic substates and other effects exceeding the picture presented in chapter 2. The detailed discussion of AC-polarisabilities in multi-level atoms given in the subsequent section is intended to bridge this gap. Emphasis is placed on the calculation of AC–Stark shifts from experimental line data, which has been relevant for the design of the optical traps discussed in chapter 6.

The dynamic polarisability of a state $|\gamma J m_J\rangle$ in multi-level atoms by electron-magnetic radiation is given in dipole approximation by[142]

$$\alpha(\gamma J m_J, \varepsilon, \omega_\mathrm{L}) = \frac{2}{\hbar} \sum_{(\gamma' J') \neq (\gamma J)} \left[\frac{\omega_0}{{\omega_0}^2 - {\omega_\mathrm{L}}^2} \left| \langle J 1 m_J \varepsilon | J' m_J + \varepsilon \rangle \right|^2 \frac{\left| \langle \gamma J || \boldsymbol{d} || \gamma' J' \rangle \right|^2}{2J' + 1} \right] \tag{C.1}$$

where $\omega_0 = (E(\gamma' J') - E(\gamma J))/\hbar$ and ω_L are the angular frequencies of the respective transitions and the driving field, respectively. ω_0 is negative for contributions by states with a lower energy. $\langle J 1 m_J \varepsilon | J' m_J' \rangle$ are the Clebsch-Gordan coefficients,* where $\varepsilon = 0, \pm 1$ corresponds to π or $\sigma^\pm$ polarisation, and $\langle \gamma J || \boldsymbol{d} || \gamma' J' \rangle$ is the reduced dipole matrix element of the transition. Magnetic and higher-order electric transitions are neglected in dipole approximation.

The reduced matrix element may be inferred from the spontaneous transition rate[142,302]

$$W^{(s)}(\gamma' J' \to \gamma J) = \frac{4{\omega_0}^3}{3\hbar c^3} \left(\frac{1}{4\pi\varepsilon_0} \right) \frac{\left| \langle \gamma J || \boldsymbol{d} || \gamma' J' \rangle \right|^2}{2J' + 1} \tag{C.2}$$

of the excited state $|\gamma' J'\rangle$ into the individual state. We shall henceforth assume that all states $|\gamma' J'\rangle$ contributing to the dynamic dipole polarisability have higher energies than $|\gamma J\rangle$. Otherwise the reduced matrix elements for the relevant states may be inferred from the spontaneous decay rate $W^{(s)}(\gamma J \to \gamma' J')$. In this case, the negative sign of the resonance frequency ω_0 requires an overall negative sign, and the denominator in the last term reads $2J + 1$. These changes result in a corresponding modification of equation (C.4) below.

*A useful summary of analytic expressions for this case is given *e.g.* in the textbook by Bransden & Joachain[142] in table A4.1 on page 1005.

The AC–Stark shift of $|\gamma J m_J\rangle$ is given in lowest non-vanishing order perturbation theory by[142]

$$V_{\mathrm{D}}(\gamma J m_J, \varepsilon, \omega_{\mathrm{L}}, \boldsymbol{r}) = -\frac{1}{2\varepsilon_0 c}\alpha(\gamma J m_J, \varepsilon, \omega_{\mathrm{L}}) I_{\mathrm{L}}(\boldsymbol{r}), \tag{C.3}$$

and the first higher-order contribution is the fourth-order hyperpolarisability (see section 7.2.3). Inserting equation (C.1) and replacing the reduced matrix elements using equation (C.2) then yields the expression

$$V_{\mathrm{D}}(\gamma J m_J, \varepsilon, \omega_{\mathrm{L}}, \boldsymbol{r}) = -\sum_{(\gamma' J')\neq(\gamma J)} \left[\frac{3\pi c^2}{2{\omega_0}^3} \left|\langle J 1 m_J \varepsilon | J' m_J + \varepsilon\rangle\right|^2 \left(\frac{W^{(s)}(\gamma' J' \to \gamma J)}{\omega_0 - \omega_{\mathrm{L}}} + \frac{W^{(s)}(\gamma' J' \to \gamma J)}{\omega_0 + \omega_{\mathrm{L}}}\right)\right] I_{\mathrm{L}}(\boldsymbol{r}) \tag{C.4}$$

for the dipole potential, which may readily be evaluated using experimental data. Replacing the spontaneous rate $W^{(s)}(\gamma' J' \to \gamma J)$ of the individual transition by the total decay rate Γ of its excited state as in equation (2.6) is obviously justified if and only if said excited state $|\gamma' J'\rangle$ decays almost exclusively into the state $|\gamma J\rangle$. While this is certainly the case for the relevant D-lines in alkali elements and some of the ground-state transitions in ytterbium, many other states in ytterbium, including most of those accessible from the metastable states, have multiple decay channels and equation (2.6) does not describe their contributions to the AC–Stark shifts in ytterbium correctly.

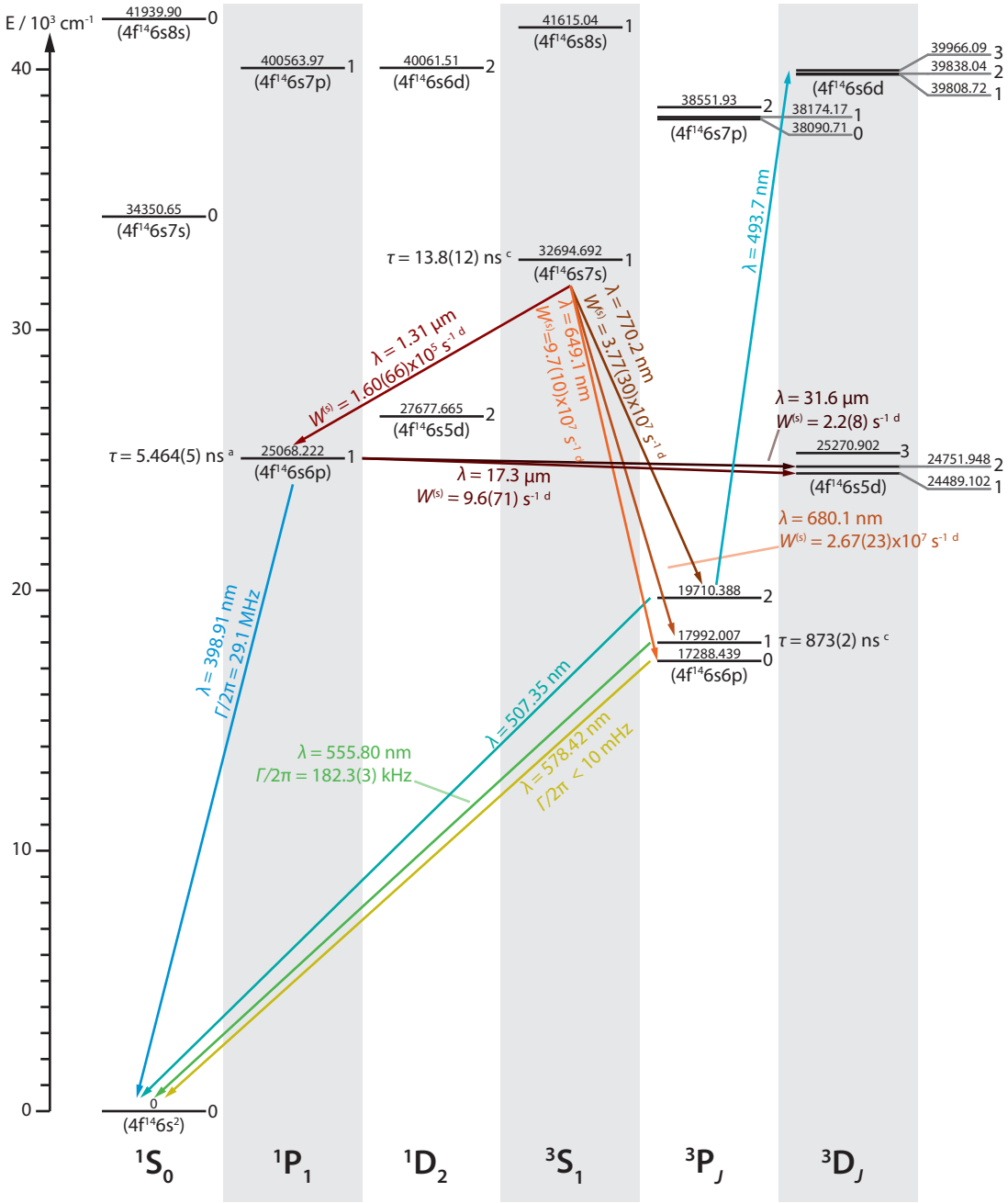

Figure C.1 | Term diagram of neutral ytterbium (Yb I) including energy levels up to 42 000 cm^{-1} and the most relevant transitions and decay channels. The ionisation threshold to Yb II is 50 443.2(1) cm^{-1}.

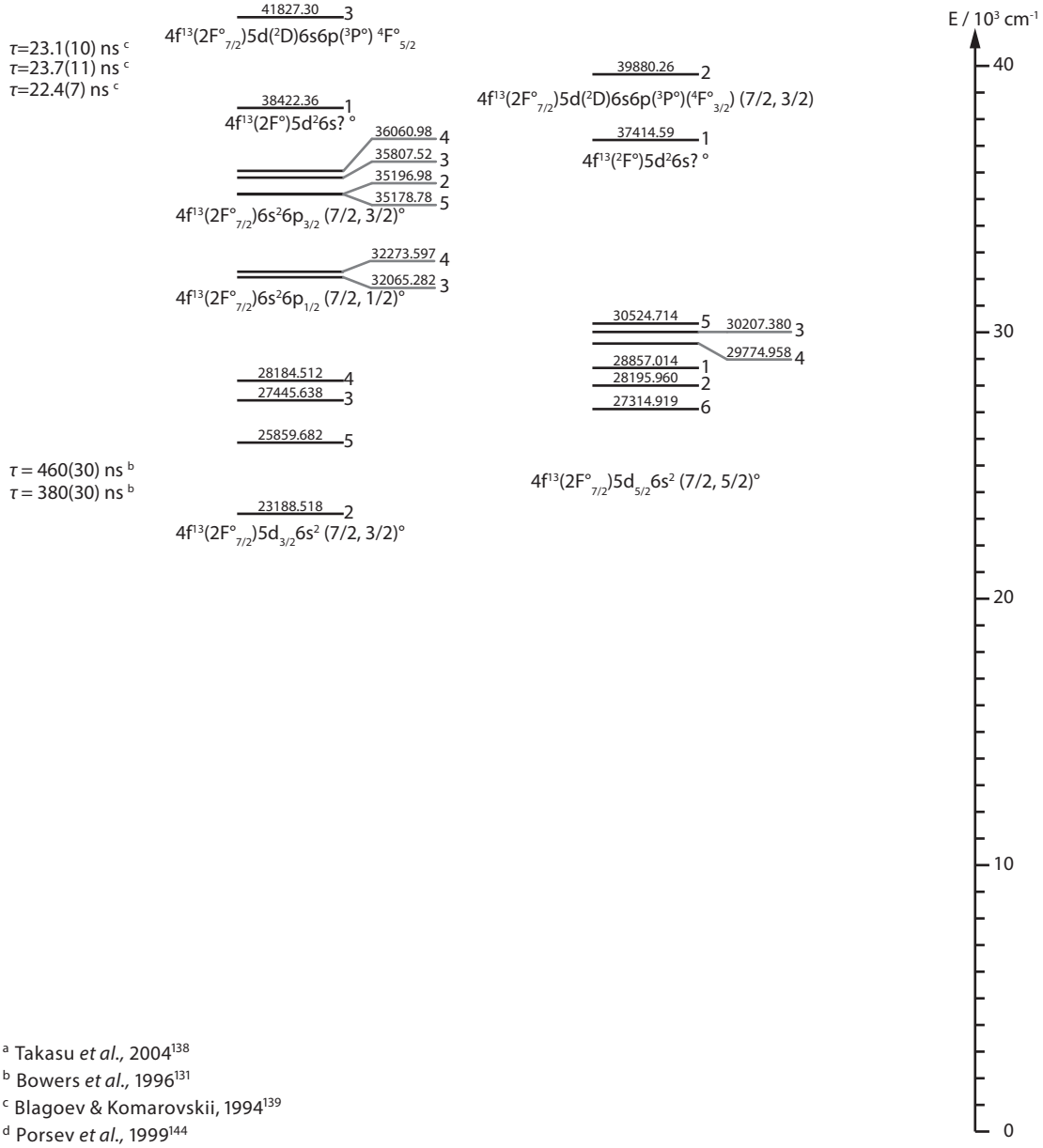

[a] Takasu *et al.,* 2004[138]
[b] Bowers *et al.,* 1996[131]
[c] Blagoev & Komarovskii, 1994[139]
[d] Porsev *et al.,* 1999[144]

f-shell excitations

Level and configuration data courtesy of: Kramida, A., Ralchenko, Yu., Reader, J., and NIST ASD Team (2012). NIST Atomic Spectra Database (ver. 5.0), [Online]. Available: http://physics.nist.gov/asd [2013, August 10]. National Institute of Standards and Technology, Gaithersburg, MD.

Appendix D

Optical dipole traps

Optical dipole traps are well known and widely used tools in experiments on quantum gases. Some basic equations to describe these traps and their properties are given below to establish a consistent notation and cover the general case of elliptic beam. Furthermore, the influence of gravity is discussed briefly. Detailed introductions may be found in review articles[233] or doctoral theses, *e.g.* the thesis of Christoph Becker.[258]

D.1 Dipole potential of a Gaussian beam

The dipole potential (see equation (C.3)) created by an elliptic Gaussian beam propagating along z may be written as[303]

$$V_{\mathrm{D}}(\boldsymbol{r}) = -V_0 f(z) \exp\left[-2\left(\frac{x}{w_x(z)}\right)^2 - 2\left(\frac{y}{w_y(z)}\right)^2\right] \tag{D.1}$$

where

$$V_0 = \frac{\alpha(\omega_{\mathrm{L}})}{2\varepsilon_0 c}\frac{2P}{\pi\chi w_0^2}, \tag{D.2}$$

$$f(z) = \frac{w_x(0)w_y(0)}{w_x(z)w_y(z)}, \tag{D.3}$$

$$w_y(z) = w_0\sqrt{1+\left(\frac{z}{z_{\mathrm{R}}}\right)^2}, \tag{D.4}$$

$$w_x(z) = \chi w_0\sqrt{1+\left(\frac{z}{\chi^2 z_{\mathrm{R}}}\right)^2}, \text{ and} \tag{D.5}$$

$$z_{\mathrm{R}} = \frac{\pi {w_0}^2}{\lambda}. \tag{D.6}$$

The beam is characterised by its power P, wavelength λ, its minimal waist w_0 in y-direction, and its aspect ratio χ, *i.e.* the ratio of the waist along the x- and y-directions. As discussed in appendix C, the polarisability $\alpha(\omega_{\mathrm{L}}) = \alpha(\gamma J, \varepsilon, \omega_{\mathrm{L}})$ expresses the response of an atomic state to the laser as a function of its frequency and polarisation. Obviously, the depth of the trapping potential is given by V_0.

D.2 Harmonic approximation

In the vicinity of the focus, *i.e.* for $y, x/\chi \ll w_0$, $z/z_\mathrm{R} \ll \min(1, \chi^2)$, the potential may be approximated by a harmonic potential with trapping frequencies

$$\omega_y = \chi\omega_x = \sqrt{\frac{4V_0}{m{w_0}^2}}, \tag{D.7}$$

$$\omega_z = \sqrt{(1+\chi^{-4})\frac{V_0}{m{z_\mathrm{R}}^2}} \tag{D.8}$$

where m is the atomic mass of the trapped species. Usually, $z_\mathrm{R}/w_0 \gg \max(1, \chi)$ is fulfilled, and a single beam creates very little axial confinement as compared to its radial trapping frequencies. If multiple beams are focussed to the same spot in a crossed optical dipole trap, their squared frequencies are of course additive. Hence, the total trapping frequencies are readily determined in harmonic approximation.

In many experiments, this harmonic approximation of the trapping potential is sufficient; however, the anharmonicity of the potential may often not be neglected in the case of tightly focussed beams.

D.3 Influence of gravity

Under the influence of gravity, the effective properties of an optical dipole trap are modified substantially at low trap depths. The additional linear potential term

$$V_g(\boldsymbol{r}) = -m\boldsymbol{g}\boldsymbol{r}$$

effectively tilts the optical dipole potential and reduces the effective trap depth. Obviously, the maximum restoring force of the trapping potential must exceed gravity and the trapping potential will not support an atomic cloud against gravity at all below a critical depth V_c. Due to the weak confinement along the direction of propagation (see section D.2), the effective potential depth decreases rapidly if the beam is tilted out of the horizontal plane, and vertically oriented traps are usually incapable of trapping atoms under the influence of gravity even at high power. Moreover, the effective trap centre is displaced as the dipole potential compensates gravity, and the harmonic trap frequencies, especially along the direction of gravity, are therefore reduced. In symmetric horizontally crossed traps, the reduced trap frequency along the vertical axis is frequently used to create spherical confinement at a characteristic power.[258]

The effects of gravity can be treated analytically in the case of a single horizontal beam as presented in section D.1. For the sake of simplicity, the following discussion only covers the experimentally most relevant case of gravity along either x or y, and without further loss of generality the negative y-direction is chosen as the direction of gravity $\boldsymbol{g} = -g\boldsymbol{e}_y$. The maximum restoring force of the trap is obviously achieved at a displacement of $\pm w_0/2$ from the centre along the y-axis, and this yields a critical depth

$$V_\mathrm{c} = \frac{mgw_0}{2}\exp(1/2) \tag{D.9}$$

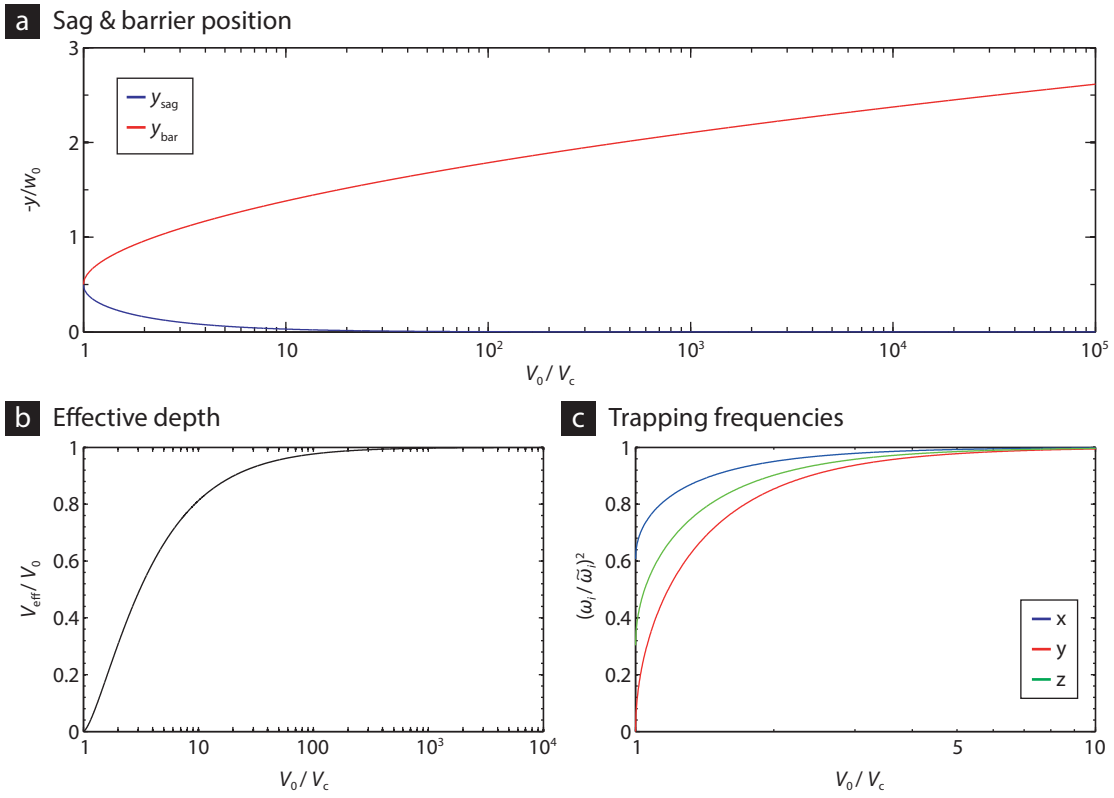

Figure D.1 | The influence of gravity on a horizontal dipole trap composed of a single beam is illustrated by the dependence of sag y_{sag} and barrier position y_{bar} **(a)**, effective trap depth V_{eff} **(b)** as well as the relative trapping frequencies ω_i **(c)** with respect to their values in the absence of gravity. For the axial trapping frequency ω_z, a circular beam ($\chi = 1$) has been assumed.

that is required to support atoms of mass m against gravity. Sag y_{sag} and barrier position y_{bar} at trap depths $V_0 \geq V_c$, *i.e.* the positions of the local minimum and maximum of the tilted potential along the vertical axis, are given by

$$y_{sag} = -\frac{w_0}{2}\sqrt{-W_0\left(-\left[\frac{mgw_0}{2V_0}\right]^2\right)} \tag{D.10}$$

$$y_{bar} = -\frac{w_0}{2}\sqrt{-W_{-1}\left(-\left[\frac{mgw_0}{2V_0}\right]^2\right)} \tag{D.11}$$

(D.12)

where $W_{0,-1}$ are branches of the Lambert W function. Therefore, the effective trap depth is reduced to

$$V_{eff} = V_0\left[\exp\left(-2\frac{{y_{sag}}^2}{{w_0}^2}\right) - \exp\left(-2\frac{{y_{bar}}^2}{{w_0}^2}\right)\right] + \frac{2V_c}{\exp(1/2)}\frac{y_{bar} - y_{sag}}{w_0}. \tag{D.13}$$

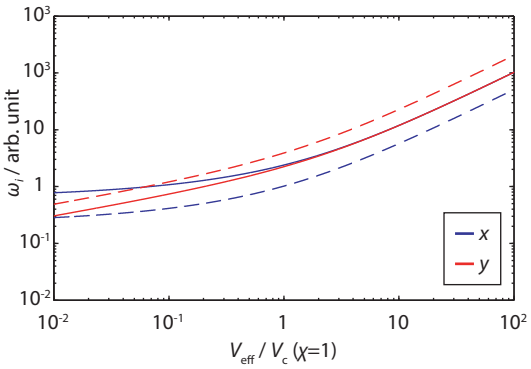

Figure D.2 | Elliptic and circular traps. The lateral trapping frequencies $\omega_{x,y}$ of a circular (solid line) and an elliptic trap with $\chi = 2$ (dashed line) are plotted as a function of their effective potential depth under the influence of gravity. As explained in the text, the waist $w_0(\chi) = w_0/\sqrt{\chi}$ has been chosen to yield a constant peak intensity.

The reduced trapping frequencies at the displaced trap centre are given by

$$\omega_x/\tilde{\omega}_x = \exp\left(-{y_{\mathrm{sag}}}^2/{w_0}^2\right), \tag{D.14}$$

$$\omega_y/\tilde{\omega}_y = \sqrt{1-(2y_{\mathrm{sag}}/w_0)^2}\cdot\exp\left(-{y_{\mathrm{sag}}}^2/{w_0}^2\right), \text{ and} \tag{D.15}$$

$$\omega_z/\tilde{\omega}_z = \sqrt{1-\frac{(2y_{\mathrm{sag}}/w_0)^2}{1+\chi^{-4}}}\cdot\exp\left(-{y_{\mathrm{sag}}}^2/{y_{\mathrm{sag}}}^2\right), \tag{D.16}$$

$$\tag{D.17}$$

where $\tilde{\omega}_i$ ($i = x, y, z$) are the free trapping frequencies given in section D.2. Especially the vertical trap frequency decreases rapidly to zero for $V_0 \rightarrow V_c$. All of these relations are illustrated by figure D.1.

The consequences of different aspect ratios at equal peak intensities, *i.e.* $w_0(\chi) = w_0/\sqrt{\chi}$, on the trapping frequencies at a given trap depth V_{eff} are shown in figure D.2. At large trap depths ($V_{\mathrm{eff}} \gg V_c$), the influence of gravity is negligible, and the trap frequencies $\omega_{x,y}^2 \propto \chi^{\mp 1}$ scale as expected from equation (D.7). In contrast, the stronger restoring forces of an elliptic traps with $\chi > 1$ has a significant effect at small effective trap depths. Less power is required to achieve the same trap depth in an elliptical trap with $\chi > 1$. At small effective trap depths, the horizontal frequency ω_x is reduced more strongly as a function of χ than expected from equation (D.7), whereas the vertical frequency ω_y increases less than expected from equation (D.7).

In general, the sag in a crossed dipole trap is determined by the combined restoring forces of all beams. Therefore, it usually depends intricately on its geometry and power distribution. This situation is simplified greatly in vertical crossed dipole traps as discussed in chapter 6. Because the atomic cloud is supported against gravity almost exclusively by the horizontal beam, the results for a single beam may be applied to this beam. The trapping frequencies of the vertical beam remain nearly unchanged, since $y_{\mathrm{sag}}/z_R \ll \min(1, \chi^2)$ is usually well fulfilled.

Finally, gravity may become a problem in mixture experiments where the overlap of different species may be lost due to different displacements in the dipole trap (*cf.* the "magic" dipole traps used in K-Rb mixture experiments[254,255]).

Bibliography

1. Dörscher, S., Thobe, A., Hundt, B., Kochanke, A., Le Targat, R., Windpassinger, P., Becker, C. & Sengstock, K. Creation of quantum-degenerate gases of ytterbium in a compact 2D-/3D-magneto-optical trap setup. *Review of Scientific Instruments* **84,** 043109 (Apr. 2013) (cit. on pp. xi, 2, 5, 16, 37, 71, 92).
2. De Angelis, M., Angonin, M. C., Beaufils, Q., Becker, C., Bertoldi, A., Bongs, K., Bourdel, T., Bouyer, P., Boyer, V., Dörscher, S., Duncker, H., Ertmer, W., Fernholz, T., Fromhold, T. M., Herr, W., Krüger, P., Kürbis, C., Mellor, C. J., Pereira dos Santos, F., Peters, A., Poli, N., Popp, M., Prevedelli, M., Rasel, E. M., Rudolph, J., Schreck, F., Sengstock, K., Sorrentino, F., Stellmer, S., Tino, G. M., Valenzuela, T., Wendrich, T. J., Wicht, A., Windpassinger, P. & Wolf, P. iSense: A Portable Ultracold-Atom-Based Gravimeter. *Procedia Computer Science* **7,** 334–336 (2011) (cit. on p. xi).
3. Becker, C., Soltan-Panahi, P., Kronjäger, J., Dörscher, S., Bongs, K. & Sengstock, K. Ultracold quantum gases in triangular optical lattices. *New Journal of Physics* **12,** 065025 (June 2010) (cit. on p. xi).
4. Mohr, P. J., Taylor, B. N. & Newell, D. B. CODATA recommended values of the fundamental physical constants: 2010. *Reviews of Modern Physics* **84,** 1527–1605 (Oct. 2012) (cit. on pp. xviii, xx, xxii, xxiii).
5. Wieser, M. E. & Coplen, T. B. Atomic weights of the elements 2009 (IUPAC Technical Report). *Pure and Applied Chemistry* **83,** 359–396 (2011) (cit. on pp. xix, 6).
6. Davis, K. B., Mewes, M. O., Andrews, M. R., van Druten, N. J., Durfee, D. S., Kurn, D. M. & Ketterle, W. Bose-Einstein condensation in a gas of sodium atoms. *Physical Review Letters* **75,** 3969–3973 (Nov. 1995) (cit. on pp. 1, 52).
7. Anderson, M. H., Ensher, J. R., Matthews, M. R., Wieman, C. E. & Cornell, E. A. Observation of Bose-Einstein Condensation in a Dilute Atomic Vapor. *Science* **269,** 198–201 (July 1995) (cit. on p. 1).
8. DeMarco, B. & Jin, D. S. Onset of Fermi Degeneracy in a Trapped Atomic Gas. *Science* **285,** 1703–1706 (Sept. 1999) (cit. on p. 1).
9. Feynman, R. P. Simulating Physics with Computers. *International Journal of Theoretical Physics* **21,** 467–488 (June 1982) (cit. on p. 1).
10. Jaksch, D., Bruder, C., Cirac, J. I., Gardiner, C. W. & Zoller, P. Cold Bosonic Atoms in Optical Lattices. *Physical Review Letters* **81,** 3108–3111 (Oct. 1998) (cit. on p. 1).
11. Greiner, M., Mandel, O., Esslinger, T., Hänsch, T. W. & Bloch, I. Quantum phase transition from a superfluid to a Mott insulator in a gas of ultracold atoms. *Nature* **415,** 39–44 (Jan. 2002) (cit. on p. 1).

12. Jördens, R., Strohmaier, N., Günter, K., Moritz, H. & Esslinger, T. A Mott insulator of fermionic atoms in an optical lattice. *Nature* **455,** 204–207 (Sept. 2008) (cit. on p. 1).

13. Ospelkaus, S., Ospelkaus, C., Wille, O., Succo, M., Ernst, P., Sengstock, K. & Bongs, K. Localization of Bosonic Atoms by Fermionic Impurities in a Three-Dimensional Optical Lattice. *Physical Review Letters* **96,** 180403 (May 2006) (cit. on p. 1).

14. Ospelkaus, C., Ospelkaus, S., Humbert, L., Ernst, P., Sengstock, K. & Bongs, K. Ultracold Heteronuclear Molecules in a 3D Optical Lattice. *Physical Review Letters* **97,** 120402 (Sept. 2006) (cit. on p. 1).

15. Lang, F., Winkler, K., Strauss, C., Grimm, R. & Hecker Denschlag, J. Ultracold Triplet Molecules in the Rovibrational Ground State. *Physical Review Letters* **101,** 133005 (Sept. 2008) (cit. on p. 1).

16. Ni, K.-K., Ospelkaus, S., de Miranda, M. H. G., Pe'er, A., Neyenhuis, B., Zirbel, J. J., Kotochigova, S., Julienne, P. S., Jin, D. S. & Ye, J. A High Phase-Space-Density Gas of Polar Molecules. *Science* **322,** 231–235 (Oct. 2008) (cit. on p. 1).

17. Ospelkaus, S., Ni, K.-K., Wang, D., de Miranda, M. H. G., Neyenhuis, B., Quéméner, G., Julienne, P. S., Bohn, J. L., Jin, D. S. & Ye, J. Quantum-State Controlled Chemical Reactions of Ultracold Potassium-Rubidium Molecules. *Science* **327,** 853–857 (Feb. 2010) (cit. on p. 1).

18. Fölling, S., Trotzky, S., Cheinet, P., Feld, M., Saers, R., Widera, A., Müller, T. & Bloch, I. Direct observation of second-order atom tunnelling. *Nature* **448,** 1029–1032 (Aug. 2007) (cit. on p. 1).

19. Trotzky, S., Cheinet, P., Fölling, S., Feld, M., Schnorrberger, U., Rey, A. M., Polkovnikov, A., Demler, E. A., Lukin, M. D. & Bloch, I. Time-Resolved Observation and Control of Superexchange Interactions with Ultracold Atoms in Optical Lattices. *Science* **319,** 295–299 (Jan. 2008) (cit. on p. 1).

20. Sherson, J. F., Weitenberg, C., Endres, M., Cheneau, M., Bloch, I. & Kuhr, S. Single-atom-resolved fluorescence imaging of an atomic Mott insulator. *Nature* **467,** 68–72 (Feb. 2010) (cit. on pp. 1, 104).

21. Bakr, W. S., Peng, A., Tai, M. E., Ma, R., Simon, J., Gillen, J. I., Fölling, S., Pollet, L. & Greiner, M. Probing the Superfluid-to-Mott Insulator Transition at the Single-Atom Level. *Science* **329,** 547–550 (July 2010) (cit. on pp. 1, 104).

22. Fölling, S., Gerbier, F., Widera, A., Mandel, O., Gericke, T. & Bloch, I. Spatial quantum noise interferometry in expanding ultracold atom clouds. *Nature* **434,** 481–484 (Mar. 2005) (cit. on p. 1).

23. Rom, T., Best, T., van Oosten, D., Schneider, U., Fölling, S., Paredes, B. & Bloch, I. Free fermion antibunching in a degenerate atomic Fermi gas released from an optical lattice. *Nature* **444,** 733–736 (Dec. 2006) (cit. on p. 1).

24. Lühmann, D.-S., Bongs, K., Sengstock, K. & Pfannkuche, D. Self-Trapping of Bosons and Fermions in Optical Lattices. *Physical Review Letters* **101,** 050402 (July 2008) (cit. on p. 1).

25. Best, T., Will, S., Schneider, U., Hackermüller, L., van Oosten, D., Bloch, I. & Lühmann, D. S. Role of Interactions in ^{87}Rb-^{40}K Bose-Fermi Mixtures in a 3D Optical Lattice. *Physical Review Letters* **102,** 030408 (Jan. 2009) (cit. on p. 1).

26. Will, S., Best, T., Schneider, U., Hackermüller, L., Lühmann, D.-S. & Bloch, I. Time-resolved observation of coherent multi-body interactions in quantum phase revivals. *Nature* **465,** 197–201 (May 2010) (cit. on p. 1).

27. Wirth, G., Ölschläger, M. & Hemmerich, A. Evidence for orbital superfluidity in the P-band of a bipartite optical square lattice. *Nature Physics* **7,** 147–153 (Dec. 2010) (cit. on pp. 1, 104).

28. Ölschläger, M., Wirth, G. & Hemmerich, A. Unconventional Superfluid Order in the *F* Band of a Bipartite Optical Square Lattice. *Physical Review Letters* **106,** 015302 (Jan. 2011) (cit. on p. 1).

29. Soltan-Panahi, P., Lühmann, D.-S., Struck, J., Windpassinger, P. & Sengstock, K. Quantum phase transition to unconventional multi-orbital superfluidity in optical lattices. *Nature Physics* **8,** 71–75 (Oct. 2011) (cit. on p. 1).

30. Lühmann, D.-S., Jürgensen, O. & Sengstock, K. Multi-orbital and density-induced tunneling of bosons in optical lattices. *New Journal of Physics* **14,** 033021 (Mar. 2012) (cit. on p. 1).

31. Jürgensen, O., Sengstock, K. & Lühmann, D.-S. Density-induced processes in quantum gas mixtures in optical lattices. *Physical Review A* **86,** 043623 (Oct. 2012) (cit. on p. 1).

32. Struck, J., Ölschläger, C., Le Targat, R., Soltan-Panahi, P., Eckardt, A., Lewenstein, M., Windpassinger, P. & Sengstock, K. Quantum Simulation of Frustrated Classical Magnetism in Triangular Optical Lattices. *Science* **333,** 996–999 (Aug. 2011) (cit. on pp. 1, 101, 112).

33. Katori, H. in *Proceedings of the 6th Symposium on Frequency Standards and Metrology* (ed Gill, P.) (World Scientifc, Singapore, 2002), 323–330 (cit. on pp. 1, 32, 101).

34. Takamoto, M. & Katori, H. Spectroscopy of the $^1S_0$-$^3P_0$ Clock Transition of ^{87}Sr in an Optical Lattice. *Physical Review Letters* **91,** 223001 (Nov. 2003) (cit. on p. 1).

35. Takamoto, M., Hong, F.-L., Higashi, R. & Katori, H. An optical lattice clock. *Nature* **435,** 321–324 (May 2005) (cit. on pp. 1, 95, 96, 101).

36. Lemonde, P. & Wolf, P. Optical lattice clock with atoms confined in a shallow trap. *Physical Review A* **72,** 033409 (Sept. 2005) (cit. on pp. 1, 99, 103).

37. Hong, T., Cramer, C., Cook, E., Nagourney, W. & Fortson, E. N. Observation of the $^1S_0$-$^3P_0$ transition in atomic ytterbium for optical clocks and qubit arrays. *Optics Letters* **30,** 2644–2646 (Oct. 2005) (cit. on p. 1).

38. Ludlow, A. D., Boyd, M. M., Zelevinsky, T., Foreman, S. M., Blatt, S., Notcutt, M., Ido, T. & Ye, J. Systematic Study of the ^{87}Sr Clock Transition in an Optical Lattice. *Physical Review Letters* **96,** 033003 (Jan. 2006) (cit. on p. 1).

39. Brusch, A., Le Targat, R., Baillard, X., Fouché, M. & Lemonde, P. Hyperpolarizability Effects in a Sr Optical Lattice Clock. *Physical Review Letters* **96,** 103003 (Mar. 2006) (cit. on pp. 1, 10).

40. Le Targat, R., Baillard, X., Fouché, M., Brusch, A., Tcherbakoff, O., Rovera, G. D. & Lemonde, P. Accurate Optical Lattice Clock with ^{87}Sr Atoms. *Physical Review Letters* **97,** 130801 (Sept. 2006) (cit. on p. 1).

41. Takamoto, M., Hong, F.-L., Higashi, R., Fujii, Y., Imae, M. & Katori, H. Improved Frequency Measurement of a One-Dimensional Optical Lattice Clock with a Spin-Polarized Fermionic ^{87}Sr Isotope. *Journal of the Physical Society of Japan* **75,** 104302 (Oct. 2006) (cit. on p. 1).

42. Boyd, M. M., Zelevinsky, T., Ludlow, A. D., Foreman, S. M., Blatt, S., Ido, T. & Ye, J. Optical Atomic Coherence at the 1-Second Time Scale. *Science* **314,** 1430–1433 (Dec. 2006) (cit. on p. 1).

43. Zelevinsky, T., Boyd, M. M., Ludlow, A. D., Foreman, S. M., Blatt, S., Ido, T. & Ye, J. Optical clock and ultracold collisions with trapped strontium atoms. *Hyperfine Interactions* **174,** 55–64 (Jan. 2007) (cit. on p. 1).

44. Boyd, M. M., Ludlow, A. D., Blatt, S., Foreman, S. M., Ido, T., Zelevinsky, T. & Ye, J. ^{87}Sr Lattice Clock with Inaccuracy below 10^{-15}. *Physical Review Letters* **98,** 083002 (Feb. 2007) (cit. on p. 1).

45. Baillard, X., Fouché, M., Le Targat, R., Westergaard, P. G., Lecallier, A., Le Coq, Y., Rovera, G. D., Bize, S. & Lemonde, P. Accuracy evaluation of an optical lattice clock with bosonic atoms. *Optics Letters* **32,** 1812–1814 (July 2007) (cit. on p. 1).

46. Boyd, M. M., Zelevinsky, T., Ludlow, A. D., Blatt, S., Zanon-Willette, T., Foreman, S. M. & Ye, J. Nuclear spin effects in optical lattice clocks. *Physical Review A* **76,** 022510 (Aug. 2007) (cit. on pp. 1, 35, 105, 106).

47. Baillard, X., Fouché, M., Le Targat, R., Westergaard, P. G., Lecallier, A., Chapelet, F., Abgrall, M., Rovera, G. D., Laurent, P., Rosenbusch, P., Bize, S., Santarelli, G., Clairon, A., Lemonde, P., Grosche, G., Lipphardt, B. & Schnatz, H. An optical lattice clock with spin-polarized ^{87}Sr atoms. *European Physical Journal D* **48,** 11–17 (Dec. 2007) (cit. on p. 1).

48. Hachisu, H., Miyagishi, K., Porsev, S. G., Derevianko, A., Ovsiannikov, V. D., Pal'chikov, V. G., Takamoto, M. & Katori, H. Trapping of Neutral Mercury Atoms and Prospects for Optical Lattice Clocks. *Physical Review Letters* **100,** 053001 (Feb. 2008) (cit. on p. 1).

49. Ludlow, A. D., Zelevinsky, T., Campbell, G. K., Blatt, S., Boyd, M. M., de Miranda, M. H. G., Martin, M. J., Thomsen, J. W., Foreman, S. M., Ye, J., Fortier, T. M., Stalnaker, J. E., Diddams, S. A., Le Coq, Y., Barber, Z. W., Poli, N., Lemke, N. D., Beck, K. M. & Oates, C. W. Sr Lattice Clock at 1×10^{-16} Fractional Uncertainty by Remote Optical Evaluation with a Ca Clock. *Science* **319,** 1805–1808 (Mar. 2008) (cit. on p. 1).

50. Blatt, S., Ludlow, A. D., Campbell, G. K., Thomsen, J. W., Zelevinsky, T., Boyd, M. M., Ye, J., Baillard, X., Fouché, M., Le Targat, R., Brusch, A., Lemonde, P., Takamoto, M., Hong, F.-L., Katori, H. & Flambaum, V. V. New Limits on Coupling of Fundamental Constants to Gravity Using ^{87}Sr Optical Lattice Clocks. *Physical Review Letters* **100,** 140801 (Apr. 2008) (cit. on p. 1).

51. Poli, N., Barber, Z. W., Lemke, N. D., Oates, C. W., Ma, L. S., Stalnaker, J. E., Fortier, T. M., Diddams, S. A., Hollberg, L., Bergquist, J. C., Brusch, A., Jefferts, S., Heavner, T. & Parker, T. Frequency evaluation of the doubly forbidden $^1S_0 \rightarrow {}^3P_0$ transition in bosonic ^{174}Yb. *Physical Review A* **77,** 050501(R) (May 2008) (cit. on p. 1).

52. Porsev, S. G., Ludlow, A. D., Boyd, M. M. & Ye, J. Determination of Sr properties for a high-accuracy optical clock. *Physical Review A* **78,** 032508 (Sept. 2008) (cit. on p. 1).

53. Campbell, G. K., Ludlow, A. D., Blatt, S., Thomsen, J. W., Martin, M. J., de Miranda, M. H. G., Zelevinsky, T., Boyd, M. M., Ye, J., Diddams, S. A., Heavner, T. P., Parker, T. E. & Jefferts, S. R. The absolute frequency of the ^{87}Sr optical clock transition. *Metrologia* **45,** 539–548 (Oct. 2008) (cit. on p. 1).

54. Akatsuka, T., Takamoto, M. & Katori, H. Optical lattice clocks with non-interacting bosons and fermions. *Nature Physics* **4,** 954–959 (Dec. 2008) (cit. on pp. 1, 104).

55. Takamoto, M. & Katori, H. Coherence of Spin-Polarized Fermions Interacting with a Clock Laser in a Stark-Shift-Free Optical Lattice. *Journal of the Physical Society of Japan* **78,** 013301 (Dec. 2008) (cit. on p. 1).

56. Takamoto, M., Katori, H., Marmo, S. I., Ovsiannikov, V. D. & Pal'chikov, V. G. Prospects for Optical Clocks with a Blue-Detuned Lattice. *Physical Review Letters* **102,** 063002 (Feb. 2009) (cit. on pp. 1, 34).

57. Hong, F.-L., Musha, M., Takamoto, M., Inaba, H., Yanagimachi, S., Takamizawa, A., Watabe, K., Ikegami, T., Imae, M., Fujii, Y., Amemiya, M., Nakagawa, K., Ueda, K. & Katori, H. Measuring the frequency of a Sr optical lattice clock using a 120 km coherent optical transfer. *Optics Letters* **34,** 692–694 (Feb. 2009) (cit. on p. 1).

58. Campbell, G. K., Boyd, M. M., Thomsen, J. W., Martin, M. J., Blatt, S., Swallows, M. D., Nicholson, T. L., Fortier, T., Oates, C. W., Diddams, S. A., Lemke, N. D., Naidon, P., Julienne, P., Ye, J. & Ludlow, A. D. Probing Interactions Between Ultracold Fermions. *Science* **324,** 360–363 (Apr. 2009) (cit. on p. 1).

59. Lemke, N. D., Ludlow, A. D., Barber, Z. W., Fortier, T. M., Diddams, S. A., Jiang, Y., Jefferts, S. R., Heavner, T. P., Parker, T. E. & Oates, C. W. Spin-1/2 Optical Lattice Clock. *Physical Review Letters* **103,** 063001 (Aug. 2009) (cit. on pp. 1, 23, 33, 106).

60. Katori, H., Hashiguchi, K., Il'Inova, E. Y. & Ovsiannikov, V. D. Magic Wavelength to Make Optical Lattice Clocks Insensitive to Atomic Motion. *Physical Review Letters* **103,** 153004 (Oct. 2009) (cit. on p. 1).

61. Jiang, Y. Y., Ludlow, A. D., Lemke, N. D., Fox, R. W., Sherman, J. A., Ma, L.-S. & Oates, C. W. Making optical atomic clocks more stable with 10^{-16}-level laser stabilization. *Nature Photonics* **5,** 158–161 (Mar. 2011) (cit. on p. 1).

62. Takamoto, M., Takano, T. & Katori, H. Frequency comparison of optical lattice clocks beyond the Dick limit. *Nature Photonics* **5,** 288–292 (May 2011) (cit. on p. 1).

63. Bishof, M., Lin, Y.-J., Swallows, M. D., Gorshkov, A. V., Ye, J. & Rey, A. M. Resolved Atomic Interaction Sidebands in an Optical Clock Transition. *Physical Review Letters* **106,** 250801 (June 2011) (cit. on pp. 1, 96).

64. Nicholson, T. L., Martin, M. J., Williams, J. R., Bloom, B. J., Bishof, M., Swallows, M. D., Campbell, S. L. & Ye, J. Comparison of Two Independent Sr Optical Clocks with 1×10^{-17} Stability at 10^3 s. *Physical Review Letters* **109,** 230801 (Dec. 2012) (cit. on p. 1).

65. Le Targat, R., Lorini, L., Le Coq, Y., Zawada, M., Guéna, J., Abgrall, M., Gurov, M., Rosenbusch, P., Rovera, D. G., Nagórny, B., Gartman, R., Westergaard, P. G., Tobar, M. E., Lours, M., Santarelli, G., Clairon, A., Bize, S., Laurent, P., Lemonde, P. & Lodewyck, J. Experimental realization of an optical second with strontium lattice clocks. *Nature Communications* **4,** 2109 (July 2013) (cit. on p. 1).

66. Hinkley, N., Sherman, J. A., Phillips, N. B., Schioppo, M., Lemke, N. D., Beloy, K., Pizzocaro, M., Oates, C. W. & Ludlow, A. D. An atomic clock with 10^{-18} instability. *arXiv.org,* 1305.5869 (May 2013) (cit. on pp. 1, 101).

67. Hong, T., Cramer, C., Nagourney, W. & Fortson, E. N. Optical Clocks Based on Ultranarrow Three-Photon Resonances in Alkaline Earth Atoms. *Physical Review Letters* **94,** 050801 (Feb. 2005) (cit. on pp. 1, 109).

68. Santra, R., Arimondo, E., Ido, T., Greene, C. H. & Ye, J. High-Accuracy Optical Clock via Three-Level Coherence in Neutral Bosonic ^{88}Sr. *Physical Review Letters* **94,** 173002 (May 2005) (cit. on pp. 1, 109).

69. Barber, Z. W., Hoyt, C. W., Oates, C. W., Hollberg, L., Taichenachev, A. V. & Yudin, V. I. Direct Excitation of the Forbidden Clock Transition in Neutral ^{174}Yb Atoms Confined to an Optical Lattice. *Physical Review Letters* **96,** 083002 (Mar. 2006) (cit. on pp. 1, 109).

70. Taichenachev, A. V., Yudin, V. I., Oates, C. W., Hoyt, C. W., Barber, Z. W. & Hollberg, L. Magnetic Field-Induced Spectroscopy of Forbidden Optical Transitions with Application to Lattice-Based Optical Atomic Clocks. *Physical Review Letters* **96,** 083001 (Mar. 2006) (cit. on pp. 1, 109).

71. Ovsiannikov, V. D., Pal'chikov, V. G., Taichenachev, A. V., Yudin, V. I., Katori, H. & Takamoto, M. Magic-wave-induced $^1S_0$-$^3P_0$ transition in even isotopes of alkaline-earth-metal-like atoms. *Physical Review A* **75,** 020501(R) (Feb. 2007) (cit. on pp. 1, 109).

72. Lemonde, P. Optical lattice clocks. *The European Physical Journal Special Topics* **172,** 81–96 (June 2009) (cit. on pp. 1, 101, 103).

73. Hong, F.-L. & Katori, H. Frequency Metrology with Optical Lattice Clocks. *Japanese Journal of Applied Physics* **49,** 080001 (Aug. 2010) (cit. on p. 1).

74. Derevianko, A. & Katori, H. Colloquium: Physics of optical lattice clocks. *Reviews of Modern Physics* **83,** 331–348 (Apr. 2011) (cit. on pp. 1, 101, 103).

75. Diddams, S. A., Jones, D. J., Ye, J., Cundiff, S. T., Hall, J. L., Ranka, J. K., Windeler, R. S., Holzwarth, R., Udem, T. & Hänsch, T. W. Direct Link between Microwave and Optical Frequencies with a 300 THz Femtosecond Laser Comb. *Physical Review Letters* **84,** 5102–5105 (May 2000) (cit. on p. 1).

76. Takasu, Y., Maki, K., Komori, K., Takano, T., Honda, K., Kumakura, M., Yabuzaki, T. & Takahashi, Y. Spin-Singlet Bose-Einstein Condensation of Two-Electron Atoms. *Physical Review Letters* **91,** 040404 (July 2003) (cit. on pp. 2, 5, 16, 24, 59, 74, 111).

77. Hansen, A. H., Khramov, A., Dowd, W. H., Jamison, A. O., Ivanov, V. V. & Gupta, S. Quantum degenerate mixture of ytterbium and lithium atoms. *Physical Review A* **84,** 011606(R) (July 2011) (cit. on pp. 2, 5, 16, 30, 59, 73, 74, 88, 111).

78. Miranda, M., Nakamoto, A., Okuyama, Y., Noguchi, A., Ueda, M. & Kozuma, M. All-optical transport and compression of ytterbium atoms into the surface of a solid immersion lens. *Physical Review A* **86,** 063615 (Dec. 2012) (cit. on pp. 2, 5, 16).

79. Kraft, S., Vogt, F., Appel, O., Riehle, F. & Sterr, U. Bose-Einstein Condensation of Alkaline Earth Atoms: ^{40}Ca. *Physical Review Letters* **103,** 130401 (Sept. 2009) (cit. on pp. 2, 74).

80. Halder, P., Yang, C.-Y. & Hemmerich, A. Alternative route to Bose-Einstein condensation of two-electron atoms. *Physical Review A* **85,** 31603 (Mar. 2012) (cit. on p. 2).

81. Stellmer, S., Tey, M. K., Huang, B., Grimm, R. & Schreck, F. Bose-Einstein Condensation of Strontium. *Physical Review Letters* **103,** 200401 (Nov. 2009) (cit. on pp. 2, 15).

82. Martinez de Escobar, Y. N., Mickelson, P. G., Yan, M., DeSalvo, B. J., Nagel, S. B. & Killian, T. C. Bose-Einstein Condensation of ^{84}Sr. *Physical Review Letters* **103,** 200402 (Nov. 2009) (cit. on p. 2).

83. Bhongale, S. G., Mathey, L., Zhao, E., Yelin, S. F. & Lemeshko, M. Quantum Phases of Quadrupolar Fermi Gases in Optical Lattices. *Physical Review Letters* **110,** 155301 (Apr. 2013) (cit. on pp. 2, 22).

84. Gerbier, F. & Dalibard, J. Gauge fields for ultracold atoms in optical superlattices. *New Journal of Physics* **12,** 033007 (Mar. 2010) (cit. on pp. 2, 17, 21, 22, 30, 34, 100).

85. Dalibard, J., Gerbier, F., Juzeliūnas, G. & Öhberg, P. Colloquium: Artificial gauge potentials for neutral atoms. *Reviews of Modern Physics* **83,** 1523–1543 (Oct. 2011) (cit. on pp. 2, 17, 21, 30, 34, 100, 101, 112).

86. Cooper, N. R. Optical Flux Lattices for Ultracold Atomic Gases. *Physical Review Letters* **106,** 175301 (Apr. 2011) (cit. on p. 2).

87. Cooper, N. R. & Dalibard, J. Optical flux lattices for two-photon dressed states. *Europhysics Letters* **95,** 66004 (Sept. 2011) (cit. on p. 2).

88. Daley, A. J., Boyd, M. M., Ye, J. & Zoller, P. Quantum Computing with Alkaline-Earth-Metal Atoms. *Physical Review Letters* **101,** 170504 (Oct. 2008) (cit. on pp. 2, 21, 22, 30, 34, 36, 100).

89. Shibata, K., Kato, S., Yamaguchi, A., Uetake, S. & Takahashi, Y. A scalable quantum computer with ultranarrow optical transition of ultracold neutral atoms in an optical lattice. *Applied Physics B* **97,** 753–758 (Dec. 2009) (cit. on pp. 2, 21, 22).

90. Gorshkov, A. V., Rey, A. M., Daley, A. J., Boyd, M. M., Ye, J., Zoller, P. & Lukin, M. D. Alkaline-Earth-Metal Atoms as Few-Qubit Quantum Registers. *Physical Review Letters* **102,** 110503 (Mar. 2009) (cit. on pp. 2, 22, 36, 100).

91. Daley, A. J., Ye, J. & Zoller, P. State-dependent lattices for quantum computing with alkaline-earth-metal atoms. *European Physical Journal D* **65,** 207–217 (Nov. 2011) (cit. on pp. 2, 21, 22, 30, 34, 36, 101).

92. Gorshkov, A. V., Hermele, M., Gurarie, V., Xu, C., Julienne, P. S., Ye, J., Zoller, P., Demler, E., Lukin, M. D. & Rey, A. M. Two-orbital *SU(N)* magnetism with ultracold alkaline-earth atoms. *Nature Physics* **6,** 289–295 (Apr. 2010) (cit. on pp. 2, 22, 25, 30, 35, 112, 113).

93. Foss-Feig, M., Hermele, M. & Rey, A. M. Probing the Kondo lattice model with alkaline-earth-metal atoms. *Physical Review A* **81,** 051603(R) (May 2010) (cit. on pp. 2, 22, 30, 35, 112).

94. Foss-Feig, M., Hermele, M., Gurarie, V. & Rey, A. M. Heavy fermions in an optical lattice. *Physical Review A* **82,** 053624 (Nov. 2010) (cit. on pp. 2, 22, 30, 35, 112).

95. Silva-Valencia, J. & Souza, A. M. C. Ground state of alkaline-earth fermionic atoms in one-dimensional optical lattices. *European Physical Journal B* **85,** 5 (Jan. 2012) (cit. on pp. 2, 22, 35, 112).

96. Silva-Valencia, J. & Souza, A. M. C. Entanglement of alkaline-earth-metal fermionic atoms confined in optical lattices. *Physical Review A* **85,** 033612 (Mar. 2012) (cit. on pp. 2, 22, 35, 112).

97. Dieckmann, K., Spreeuw, R. J. C., Weidemüller, M. & Walraven, J. T. M. Two-dimensional magneto-optical trap as a source of slow atoms. *Physical Review A* **58,** 3891–3895 (Nov. 1998) (cit. on pp. 2, 38, 67).

98. Phillips, W. D. & Metcalf, H. Laser Deceleration of an Atomic Beam. *Physical Review Letters* **48,** 596–599 (Mar. 1982) (cit. on pp. 2, 38).

99. Tiecke, T. G., Gensemer, S. D., Ludewig, a. & Walraven, J. T. M. High-flux two-dimensional magneto-optical-trap source for cold lithium atoms. *Physical Review A* **80,** 013409 (July 2009) (cit. on pp. 2, 37, 39, 111).

100. Fukuhara, T., Takasu, Y., Kumakura, M. & Takahashi, Y. Degenerate Fermi Gases of Ytterbium. *Physical Review Letters* **98,** 030401 (Jan. 2007) (cit. on pp. 5, 16, 24, 71, 111).

101. Fukuhara, T., Takasu, Y., Sugawa, S. & Takahashi, Y. Quantum Degenerate Fermi Gases of Ytterbium Atoms. *Journal of Low Temperature Physics* **148,** 441–445 (Aug. 2007) (cit. on pp. 5, 16, 24).

102. Fukuhara, T., Sugawa, S. & Takahashi, Y. Bose-Einstein condensation of an ytterbium isotope. *Physical Review A* **76,** 051604 (R) (Nov. 2007) (cit. on pp. 5, 24).

103. Sugawa, S., Yamazaki, R., Taie, S. & Takahashi, Y. Bose-Einstein condensate in gases of rare atomic species. *Physical Review A* **84,** 011610(R) (July 2011) (cit. on pp. 5, 24).

104. Takeuchi, M., Takano, T., Ichihara, S., Takasu, Y., Kumakura, M., Yabuzaki, T. & Takahashi, Y. Paramagnetic Faraday rotation with spin-polarized ytterbium atoms. *Applied Physics B* **83,** 107–114 (Apr. 2006) (cit. on p. 5).

105. Takano, T., Fuyama, M., Namiki, R. & Takahashi, Y. Spin Squeezing of a Cold Atomic Ensemble with the Nuclear Spin of One-Half. *Physical Review Letters* **102,** 033601 (Jan. 2009) (cit. on p. 5).

106. Inoue, R., Tanaka, S.-I.-R., Namiki, R., Sagawa, T. & Takahashi, Y. Unconditional Quantum-Noise Suppression via Measurement-Based Quantum Feedback. *Physical Review Letters* **110,** 163602 (Apr. 2013) (cit. on p. 5).

107. DeMille, D. Parity Nonconservation in the $6s^2\ ^1S_0 \rightarrow 6s5d\ ^3D_1$ Transition in Atomic Ytterbium. *Physical Review Letters* **74,** 4165–4168 (May 1995) (cit. on pp. 5, 17).

108. Das, B. P. Computation of correlation effects on the parity-nonconserving electric-dipole transition in atomic ytterbium. *Physical Review A* **56,** 1635–1637 (Aug. 1997) (cit. on pp. 5, 17).

109. Porsev, S. G., Rakhlina, Y. G. & Kozlov, M. G. Calculation of hyperfine structure constants for ytterbium. *Journal of Physics B* **32,** 1113–1120 (Mar. 1999) (cit. on pp. 5, 17).

110. Bowers, C. J., Budker, D., Freedman, S. J., Gwinner, G., Stalnaker, J. E. & DeMille, D. Experimental investigation of the $6s^2\ ^1S_0 \rightarrow 5d6s\ ^3D_{1,2}$ forbidden transitions in atomic ytterbium. *Physical Review A* **59,** 3513–3526 (May 1999) (cit. on pp. 5, 17).

111. Kimball, D. F., Clyde, D., Budker, D., DeMille, D., Freedman, S. J., Rochester, S., Stalnaker, J. E. & Zolotorev, M. Collisional perturbation of states in atomic ytterbium by helium and neon. *Physical Review A* **60,** 1103–1112 (Aug. 1999) (cit. on pp. 5, 17, 19).

112. Stalnaker, J. E., Budker, D., Demille, D. P., Freedman, S. J. & Yashchuk, V. V. Measurement of the forbidden $6s^2\ ^1S_0 \rightarrow 5d6s\ ^3D_1$ magnetic-dipole transition amplitude in atomic ytterbium. *Physical Review A* **66,** 031403(R) (Sept. 2002) (cit. on pp. 5, 17).

113. Tsigutkin, K., Dounas-Frazer, D., Family, A., Stalnaker, J. E., Yashchuk, V. V. & Budker, D. Observation of a Large Atomic Parity Violation Effect in Ytterbium. *Physical Review Letters* **103,** 071601 (Aug. 2009) (cit. on pp. 5, 17).

114. Romalis, M. V. & Fortson, E. N. Zeeman frequency shifts in an optical dipole trap used to search for an electric-dipole moment. *Physical Review A* **59,** 4547–4558 (June 1999) (cit. on pp. 5, 17).

115. Natarajan, V. Proposed search for an electric-dipole moment using laser-cooled ^{171}Yb atoms. *European Physical Journal D* **32,** 33–38 (Jan. 2005) (cit. on pp. 5, 17).

116. Dzuba, V. A., Flambaum, V. V. & Ginges, J. S. M. Atomic electric dipole moments of He and Yb induced by nuclear Schiff moments. *Physical Review A* **76,** 034501 (Sept. 2007) (cit. on pp. 5, 17).

117. Hudson, J. J., Sauer, B. E., Tarbutt, M. R. & Hinds, E. A. Measurement of the Electron Electric Dipole Moment Using YbF Molecules. *Physical Review Letters* **89,** 023003 (June 2002) (cit. on pp. 5, 17, 30).

118. Meyer, E. R. & Bohn, J. L. Electron electric-dipole-moment searches based on alkali-metal- or alkaline-earth-metal-bearing molecules. *Physical Review A* **80,** 042508 (2009) (cit. on pp. 5, 17).

119. Atkins, P. W. *Physikalische Chemie* 3rd ed. (ed Höpfner, A.) (Wiley-VCH, Weinheim, 2001) (cit. on p. 6).

120. Habermann, C. E. & Daane, A. H. Vapor Pressures of the Rare-Earth Metals. *Journal of Chemical Physics* **41,** 2818–2827 (Nov. 1964) (cit. on p. 6).

121. Maruyama, R. *Optical trapping of ytterbium atoms* PhD thesis (University of Washington, Seattle, 2003) (cit. on pp. 6, 9, 16).

122. Audi, G., Bersillon, O., Blachot, J. & Wapstra, A. H. The Nubase evaluation of nuclear and decay properties. *Nuclear Physics A* **729,** 3–128 (Dec. 2003) (cit. on p. 6).

123. Adams, C., Lee, H., Davidson, N., Kasevich, M. & Chu, S. Evaporative Cooling in a Crossed Dipole Trap. *Physical Review Letters* **74,** 3577–3580 (May 1995) (cit. on p. 6).

124. Sansonetti, J. E. & Martin, W. C. Handbook of Basic Atomic Spectroscopic Data. *Journal of Physical and Chemical Reference Data* **34,** 1559–2259 (Sept. 2005) (cit. on pp. 7, 8, 11, 28).

125. Audi, G., Wapstra, A. H. & Thibault, C. The Ame2003 atomic mass evaluation. *Nuclear Physics A* **729,** 337–676 (Dec. 2003) (cit. on p. 7).

126. Berglund, M. & Wieser, M. E. Isotopic compositions of the elements 2009 (IUPAC Technical Report). *Pure and Applied Chemistry* **83,** 397–410 (Jan. 2011) (cit. on p. 7).

127. Lu, M., Burdick, N. Q., Youn, S. H. & Lev, B. L. Strongly Dipolar Bose-Einstein Condensate of Dysprosium. *Physical Review Letters* **107,** 190401 (Nov. 2011) (cit. on p. 7).

128. Aikawa, K., Frisch, A., Mark, M., Baier, S., Rietzler, A., Grimm, R. & Ferlaino, F. Bose-Einstein Condensation of Erbium. *Physical Review Letters* **108,** 210401 (May 2012) (cit. on p. 7).

129. Degenhardt, C., Stoehr, H., Lisdat, C., Wilpers, G., Schnatz, H., Lipphardt, B., Nazarova, T., Pottie, P.-E., Sterr, U., Helmcke, J. & Riehle, F. Calcium optical frequency standard with ultracold atoms: Approaching 10^{-15} relative uncertainty. *Physical Review A* **72,** 062111 (Dec. 2005) (cit. on p. 8).

130. Martin, W. C., Zalubas, R. & Hagan, L. *Atomic Energy Levels—The Rare-Earth Elements* National Standard Reference Data System. Apr. 1978 (cit. on pp. 8, 11, 15, 22).

131. Bowers, C. J., Budker, D., Commins, E. D., DeMille, D., Freedman, S. J., Nguyen, A.-T., Shang, S.-Q. & Zolotorev, M. Experimental investigation of excited-state lifetimes in atomic ytterbium. *Physical Review A* **53,** 3103–3109 (May 1996) (cit. on pp. 8, 127).

132. Porsev, S. G., Derevianko, A. & Fortson, E. N. Possibility of an optical clock using the $6^1S_0 \rightarrow 6^3P_0^o$ transition in ^{171,173}Yb atoms held in an optical lattice. *Physical Review A* **69,** 021403 (R) (Feb. 2004) (cit. on pp. 9, 17, 18, 106).

133. Barber, Z. W., Stalnaker, J. E., Lemke, N. D., Poli, N., Oates, C. W., Fortier, T. M., Diddams, S. A., Hollberg, L., Hoyt, C. W., Taichenachev, A. V. & Yudin, V. I. Optical Lattice Induced Light Shifts in an Yb Atomic Clock. *Physical Review Letters* **100,** 103002 (Mar. 2008) (cit. on pp. 9, 33, 105).

134. Lett, P. D., Watts, R. N., Westbrook, C. I., Phillips, W. D., Gould, P. L. & Metcalf, H. J. Observation of Atoms Laser Cooled below the Doppler Limit. *Physical Review Letters* **61,** 169–172 (July 1988) (cit. on p. 9).

135. Dalibard, J. & Cohen-Tannoudji, C. Laser cooling below the Doppler limit by polarization gradients: simple theoretical models. *Journal of the Optical Society of America B* **6,** 2023–2045 (Nov. 1989) (cit. on p. 9).

136. Batär, A. *Erzeugung und Charakterisierung ultrakalter Rubidium-und Ytterbiumatome-Auf dem Weg zu einem gemischten Quantengas* PhD thesis (Heinrich-Heine-Universität Düsseldorf, Düsseldorf, 2005) (cit. on pp. 9, 28).

137. Metcalf, H. J. & van der Straten, P. *Laser cooling and trapping* (Springer, New York, 1999) (cit. on pp. 9, 108).

138. Takasu, Y., Komori, K., Honda, K., Kumakura, M., Yabuzaki, T. & Takahashi, Y. Photoassociation Spectroscopy of Laser-Cooled Ytterbium Atoms. *Physical Review Letters* **93,** 123202 (Sept. 2004) (cit. on pp. 11, 15, 127).

139. Blagoev, K. B. & Komarovskii, V. A. Lifetimes of Levels of Neutral and Singly Ionized Lanthanide Atoms. *Atomic Data and Nuclear Data Tables* **56,** 1–40 (Jan. 1994) (cit. on pp. 11, 15, 127).

140. Das, D., Barthwal, S., Banerjee, A. & Natarajan, V. Absolute frequency measurements in Yb with 0.08 ppb uncertainty: Isotope shifts and hyperfine structure in the 399-nm $^1S_0 \rightarrow {}^1P_1$ line. *Physical Review A* **72,** 032506 (Sept. 2005) (cit. on pp. 11, 12).

141. Pandey, K., Singh, A. K., Kumar, P. V. K., Suryanarayana, M. V. & Natarajan, V. Isotope shifts and hyperfine structure in the 555.8-nm $^1S_0 \rightarrow {}^3P_1$ line of Yb. *Physical Review A* **80,** 022518 (Aug. 2009) (cit. on pp. 12, 15).

142. Bransden, B. H. & Joachain, C. J. *Physics of Atoms and Molecules* 2nd ed. (Pearson Education, Harlow, June 2003) (cit. on pp. 11, 31, 123, 124).

143. Reichenbach, I. & Deutsch, I. H. Sideband Cooling while Preserving Coherences in the Nuclear Spin State in Group-II-like Atoms. *Physical Review Letters* **99,** 123001 (Sept. 2007) (cit. on pp. 13, 22, 100).

144. Porsev, S. G., Rakhlina, Y. G. & Kozlov, M. G. Electric-dipole amplitudes, lifetimes, and polarizabilities of the low-lying levels of atomic ytterbium. *Physical Review A* **60,** 2781–2785 (Oct. 1999) (cit. on pp. 13, 15, 17, 18, 22, 127).

145. Loftus, T., Bochinski, J. R. & Mossberg, T. W. Magnetic trapping of ytterbium and the alkaline-earth metals. *Physical Review A* **66,** 013411 (July 2002) (cit. on p. 15).

146. Cho, J. W., Lee, H.-g., Lee, S., Ahn, J., Lee, W.-K., Yu, D.-H., Lee, S. K. & Park, C. Y. Optical repumping of triplet-*P* states enhances magneto-optical trapping of ytterbium atoms. *Physical Review A* **85,** 035401 (Mar. 2012) (cit. on p. 13).

147. Loftus, T., Bochinski, J. R., Shivitz, R. & Mossberg, T. W. Power-dependent loss from an ytterbium magneto-optic trap. *Physical Review A* **61,** 051401 (May 2000) (cit. on p. 13).

148. Honda, K., Takahashi, Y., Kuwamoto, T., Fujimoto, M., Toyoda, K., Ishikawa, K. & Yabuzaki, T. Magneto-optical trapping of Yb atoms and a limit on the branching ratio of the $^1P_1$ state. *Physical Review A* **59,** R934–R937 (Feb. 1999) (cit. on pp. 13, 39).

149. Nagel, S. B., Simien, C. E., Laha, S., Gupta, P., Ashoka, V. S. & Killian, T. C. Magnetic trapping of metastable $^3P_2$ atomic strontium. *Physical Review A* **67,** 011401(R) (Jan. 2003) (cit. on pp. 15, 22).

150. Hansen, D. P., Mohr, J. R. & Hemmerich, A. Magnetic trapping of metastable calcium atoms. *Physical Review A* **67,** 021401(R) (Feb. 2003) (cit. on pp. 15, 22).

151. Grünert, J. & Hemmerich, A. Sub-Doppler magneto-optical trap for calcium. *Physical Review A* **65,** 041401(R) (Mar. 2002) (cit. on pp. 15, 23).

152. Migdalek, J. & Baylis, W. E. Relativistic transition probabilities and lifetimes of low-lying levels in ytterbium. *Journal of Physics B* **24,** L99–L102 (Feb. 1991) (cit. on pp. 16–19).

153. Kuwamoto, T., Honda, K., Takahashi, Y. & Yabuzaki, T. Magneto-optical trapping of Yb atoms using an intercombination transition. *Physical Review A* **60,** R745–R748 (Aug. 1999) (cit. on pp. 16, 40, 65).

154. Zhao, P.-Y., Xiong, Z.-X., Long, Y., He, L.-X. & Lu, B.-L. Realization of Green MOT for Ytterbium Atoms. *Chinese Physics Letters* **26,** 083702 (Aug. 2009) (cit. on p. 16).

155. Takasu, Y. & Takahashi, Y. Quantum Degenerate Gases of Ytterbium Atoms. *Journal of the Physical Society of Japan* **78,** 012001 (Jan. 2009) (cit. on p. 16).

156. Ivanov, V. V., Khramov, A., Hansen, A. H., Dowd, W. H., Münchow, F., Jamison, A. O. & Gupta, S. Sympathetic Cooling in an Optically Trapped Mixture of Alkali and Spin-Singlet Atoms. *Physical Review Letters* **106,** 153201 (Apr. 2011) (cit. on p. 16).

157. Hoyt, C. W., Barber, Z. W., Oates, C. W., Fortier, T. M., Diddams, S. A. & Hollberg, L. Observation and Absolute Frequency Measurements of the $^1S_0$-$^3P_0$ Optical Clock Transition in Neutral Ytterbium. *Physical Review Letters* **95,** 083003 (Aug. 2005) (cit. on p. 16).

158. Barber, Z. *Ytterbium Optical Lattice Clock* PhD thesis (University of Colorado, Boulder, 2007) (cit. on pp. 16, 31, 39, 107, 109).

159. Honda, K., Takasu, Y., Kuwamoto, T., Kumakura, M., Takahashi, Y. & Yabuzaki, T. Optical dipole force trapping of a fermion-boson mixture of ytterbium isotopes. *Physical Review A* **66,** 021401(R) (Aug. 2002) (cit. on p. 16).

160. Takasu, Y., Honda, K., Komori, K., Kuwamoto, T., Kumakura, M., Takahashi, Y. & Yabuzaki, T. High-Density Trapping of Cold Ytterbium Atoms by an Optical Dipole Force. *Physical Review Letters* **90,** 023003 (Jan. 2003) (cit. on pp. 16, 87, 88).

161. Tojo, S., Kitagawa, M., Enomoto, K., Kato, Y., Takasu, Y., Kumakura, M. & Takahashi, Y. High-Resolution Photoassociation Spectroscopy of Ultracold Ytterbium Atoms by Using the Intercombination Transition. *Physical Review Letters* **96,** 153201 (Apr. 2006) (cit. on p. 16).

162. Yamaguchi, A., Uetake, S., Kato, S., Ito, H. & Takahashi, Y. High-resolution laser spectroscopy of a Bose-Einstein condensate using the ultranarrow magnetic quadrupole transition. *New Journal of Physics* **12,** 103001 (Oct. 2010) (cit. on pp. 16, 25, 96).

163. Okano, M., Hara, H., Muramatsu, M., Doi, K., Uetake, S., Takasu, Y. & Takahashi, Y. Simultaneous magneto-optical trapping of lithium and ytterbium atoms towards production of ultracold polar molecules. *Applied Physics B* **98,** 691–696 (Mar. 2010) (cit. on p. 16).

164. Tassy, S., Nemitz, N., Baumer, F., Höhl, C., Batär, A. & Görlitz, A. Sympathetic cooling in a mixture of diamagnetic and paramagnetic atoms. *Journal of Physics B* **43,** 205309 (Oct. 2010) (cit. on pp. 16, 28, 29).

165. Yasuda, M., Kohno, T., Inaba, H., Nakajima, Y., Hosaka, K., Onae, A. & Hong, F.-L. Fiber-comb-stabilized light source at 556 nm for magneto-optical trapping of ytterbium. *Journal of the Optical Society of America B* **27,** 1388–1393 (2010) (cit. on p. 16).

166. Katori, H., Ido, T., Isoya, Y. & Kuwata-Gonokami, M. Magneto-Optical Trapping and Cooling of Strontium Atoms down to the Photon Recoil Temperature. *Physical Review Letters* **82,** 1116–1119 (Feb. 1999) (cit. on pp. 16, 70).

167. Xu, X., Loftus, T. H., Smith, M. J., Hall, J. L., Gallagher, A. & Ye, J. Dynamics in a two-level atom magneto-optical trap. *Physical Review A* **66,** 011401(R) (July 2002) (cit. on p. 16).

168. Maruyama, R., Wynar, R. H., Romalis, M. V., Andalkar, A., Swallows, M. D., Pearson, C. E. & Fortson, E. N. Investigation of sub-Doppler cooling in an ytterbium magneto-optical trap. *Physical Review A* **68,** 011403 (R) (July 2003) (cit. on p. 16).

169. Hopkins, S. A. & Durrant, A. V. Parameters for polarization gradients in three-dimensional electromagnetic standing waves. *Physical Review A* **56,** 4012–4022 (Nov. 1997) (cit. on p. 16).

170. Schadwinkel, H., Reiter, U., Gomer, V. & Meschede, D. Magneto-optical trap as an optical lattice. *Physical Review A* **61,** 013409 (Jan. 2000) (cit. on p. 16).

171. Chanelière, T., Meunier, J.-L., Kaiser, R., Miniatura, C. & Wilkowski, D. Extra-heating mechanism in Doppler cooling experiments. *Journal of the Optical Society of America B* **22,** 1819–1828 (Sept. 2005) (cit. on p. 16).

172. Curtis, E. A., Oates, C. W. & Hollberg, L. Quenched narrow-line laser cooling of ^{40}Ca to near the photon recoil limit. *Physical Review A* **64,** 031403(R) (Sept. 2001) (cit. on p. 16).

173. Kimball, D. F. Parity-nonconserving optical rotation on the $6s6p\ ^3P_0 \rightarrow 6s6p\ ^1P_1$ transition in atomic ytterbium. *Physical Review A* **63,** 052113 (May 2001) (cit. on p. 17).

174. Porsev, S. G. & Derevianko, A. Hyperfine quenching of the metastable $^3P_{0,2}$ states in divalent atoms. *Physical Review A* **69,** 042506 (Apr. 2004) (cit. on pp. 17–19, 108).

175. Derevianko, A. Feasibility of Cooling and Trapping Metastable Alkaline-Earth Atoms. *Physical Review Letters* **87,** 023002 (July 2001) (cit. on p. 18).

176. Yasuda, M. & Katori, H. Lifetime Measurement of the $^3P_2$ Metastable State of Strontium Atoms. *Physical Review Letters* **92,** 153004 (Apr. 2004) (cit. on p. 19).

177. Derevianko, A., Porsev, S. G., Kotochigova, S., Tiesinga, E. & Julienne, P. S. Ultracold Collision Properties of Metastable Alkaline-Earth Atoms. *Physical Review Letters* **90,** 063002 (Feb. 2003) (cit. on pp. 20, 22, 25, 27).

178. Santra, R. & Greene, C. Tensorial analysis of the long-range interaction between metastable alkaline-earth-metal atoms. *Physical Review A* **67,** 062713 (June 2003) (cit. on pp. 20, 22, 25, 27).

179. Kokoouline, V., Santra, R. & Greene, C. H. Multichannel Cold Collisions between Metastable Sr Atoms. *Physical Review Letters* **90,** 253201 (June 2003) (cit. on pp. 20, 22, 25, 27).

180. Hansen, D. & Hemmerich, A. Observation of Multichannel Collisions of Cold Metastable Calcium Atoms. *Physical Review Letters* **96,** 073003 (Feb. 2006) (cit. on p. 20).

181. Yamaguchi, A., Uetake, S., Hashimoto, D., Doyle, J. M. & Takahashi, Y. Inelastic Collisions in Optically Trapped Ultracold Metastable Ytterbium. *Physical Review Letters* **101,** 233002 (Dec. 2008) (cit. on p. 20).

182. Traverso, A., Chakraborty, R., Martinez de Escobar, Y. N., Mickelson, P. G., Nagel, S. B., Yan, M. & Killian, T. C. Inelastic and elastic collision rates for triplet states of ultracold strontium. *Physical Review A* **79,** 060702(R) (June 2009) (cit. on pp. 20, 21).

183. Uetake, S., Murakami, R., Doyle, J. M. & Takahashi, Y. Spin-dependent collision of ultracold metastable atoms. *Physical Review A* **86,** 032712 (Sept. 2012) (cit. on p. 20).

184. Lemke, N. D., von Stecher, J., Sherman, J. A., Rey, A. M., Oates, C. W. & Ludlow, A. D. *p*-Wave Cold Collisions in an Optical Lattice Clock. *Physical Review Letters* **107,** 103902 (Sept. 2011) (cit. on pp. 20, 104, 106).

185. Lisdat, C., Vellore Winfred, J. S. R., Middelmann, T., Riehle, F. & Sterr, U. Collisional Losses, Decoherence, and Frequency Shifts in Optical Lattice Clocks with Bosons. *Physical Review Letters* **103,** 090801 (Aug. 2009) (cit. on pp. 20, 21).

186. Wilkowski, D. Runaway evaporation for optically dressed atoms. *Journal of Physics B: Atomic, Molecular and Optical Physics* **43,** 205306 (Oct. 2010) (cit. on p. 21).

187. Wolf, P., Lemonde, P., Lambrecht, A., Bize, S., Landragin, A. & Clairon, A. From optical lattice clocks to the measurement of forces in the Casimir regime. *Physical Review A* **75,** 063608 (June 2007) (cit. on pp. 21, 99, 103).

188. Kato, S., Shibata, K., Yamamoto, R., Yoshikawa, Y. & Takahashi, Y. Optical magnetic resonance imaging with an ultra-narrow optical transition. *Applied Physics B* **108,** 31–38 (Feb. 2012) (cit. on p. 21).

189. Derevianko, A. & Cannon, C. C. Quantum computing with magnetically interacting atoms. *Physical Review A* **70,** 062319 (Dec. 2004) (cit. on p. 22).

190. Hayes, D., Julienne, P. S. & Deutsch, I. H. Quantum Logic via the Exchange Blockade in Ultracold Collisions. *Physical Review Letters* **98,** 070501 (Feb. 2007) (cit. on pp. 22, 100).

191. Daley, A. J. Quantum computing and quantum simulation with group-II atoms. *Quantum Information Processing* **10,** 865–884 (Sept. 2011) (cit. on pp. 22, 36, 100).

192. Olmos, B., Yu, D., Singh, Y., Schreck, F., Bongs, K. & Lesanovsky, I. Long-Range Interacting Many-Body Systems with Alkaline-Earth-Metal Atoms. *Physical Review Letters* **110,** 143602 (Apr. 2013) (cit. on p. 23).

193. Stellmer, S. *Degenerate quantum gases of strontium* PhD thesis (University of Innsbruck, Jan. 2013) (cit. on p. 23).

194. Kitagawa, M., Enomoto, K., Kasa, K., Takahashi, Y., Ciuryło, R., Naidon, P. & Julienne, P. S. Two-color photoassociation spectroscopy of ytterbium atoms and the precise determinations of *s*-wave scattering lengths. *Physical Review A* **77,** 012719 (Jan. 2008) (cit. on pp. 23–25).

195. Kasamatsu, K. & Tsubota, M. Static and Dynamic Properties of Multicomponent Bose Einstein Condensates of Ytterbium Atoms. *Journal of Low Temperature Physics* **150,** 599–604 (Feb. 2008) (cit. on p. 24).

196. Ketterle, W. & Zwierlein, M. W. in *Ultracold Fermi Gases, Proceedings of the International School of Physics "Enrico Fermi"* (eds Inguscio, M., Ketterle, W. & Salomon, C.) 95–287 (IOS Press, 2007) (cit. on pp. 24, 92).

197. Kato, S., Sugawa, S., Shibata, K., Yamamoto, R. & Takahashi, Y. Control of Resonant Interaction between Electronic Ground and Excited States. *Physical Review Letters* **110,** 173201 (Apr. 2013) (cit. on pp. 25, 27, 29).

198. Chin, C., Grimm, R., Julienne, P. & Tiesinga, E. Feshbach resonances in ultracold gases. *Reviews of Modern Physics* **82,** 1225–1286 (Apr. 2010) (cit. on pp. 26, 27).

199. Ciuryło, R., Tiesinga, E. & Julienne, P. S. Optical tuning of the scattering length of cold alkaline-earth-metal atoms. *Physical Review A* **71,** 030701(R) (Mar. 2005) (cit. on p. 26).

200. Fedichev, P. O., Kagan, Y., Shlyapnikov, G. V. & Walraven, J. T. M. Influence of Nearly Resonant Light on the Scattering Length in Low-Temperature Atomic Gases. *Physical Review Letters* **77,** 2913–2916 (Sept. 1996) (cit. on p. 26).

201. Fatemi, F. K., Jones, K. M. & Lett, P. D. Observation of Optically Induced Feshbach Resonances in Collisions of Cold Atoms. *Physical Review Letters* **85,** 4462–4465 (Nov. 2000) (cit. on p. 26).

202. Theis, M., Thalhammer, G., Winkler, K., Hellwig, M., Ruff, G., Grimm, R. & Hecker Denschlag, J. Tuning the Scattering Length with an Optically Induced Feshbach Resonance. *Physical Review Letters* **93,** 123001 (Sept. 2004) (cit. on p. 26).

203. Thalhammer, G., Theis, M., Winkler, K., Grimm, R. & Denschlag, J. H. Inducing an optical Feshbach resonance via stimulated Raman coupling. *Physical Review A* **71,** 33403 (Mar. 2005) (cit. on p. 26).

204. Enomoto, K., Kasa, K., Kitagawa, M. & Takahashi, Y. Optical Feshbach Resonance Using the Intercombination Transition. *Physical Review Letters* **101,** 203201 (Nov. 2008) (cit. on p. 26).

205. Borkowski, M., Ciuryło, R., Julienne, P. S., Tojo, S., Enomoto, K. & Takahashi, Y. Line shapes of optical Feshbach resonances near the intercombination transition of bosonic ytterbium. *Physical Review A* **80,** 012715 (July 2009) (cit. on p. 26).

206. Yan, M., DeSalvo, B. J., Ramachandhran, B., Pu, H. & Killian, T. C. Controlling Condensate Collapse and Expansion with an Optical Feshbach Resonance. *Physical Review Letters* **110,** 123201 (Mar. 2013) (cit. on p. 26).

207. Yamazaki, R., Taie, S., Sugawa, S. & Takahashi, Y. Submicron Spatial Modulation of an Interatomic Interaction in a Bose-Einstein Condensate. *Physical Review Letters* **105,** 050405 (July 2010) (cit. on p. 26).

208. Reichenbach, I., Julienne, P. S. & Deutsch, I. H. Controlling nuclear spin exchange via optical Feshbach resonances in ^{171}Yb. *Physical Review A* **80,** 020701(R) (Aug. 2009) (cit. on p. 26).

209. Goyal, K., Reichenbach, I. & Deutsch, I. *p*-wave optical Feshbach resonances in ^{171}Yb. *Physical Review A* **82,** 062704 (Dec. 2010) (cit. on p. 26).

210. Yamazaki, R., Taie, S., Sugawa, S., Enomoto, K. & Takahashi, Y. Observation of a *p*-wave optical Feshbach resonance. *Physical Review A* **87,** 010704(R) (Jan. 2013) (cit. on p. 26).

211. LeBlanc, L. J. & Thywissen, J. H. Species-specific optical lattices. *Physical Review A* **75,** 053612 (May 2007) (cit. on pp. 27, 30).

212. Hansen, A. H., Khramov, A. Y., Dowd, W. H., Jamison, A. O., Plotkin-Swing, B., Roy, R. J. & Gupta, S. Production of quantum-degenerate mixtures of ytterbium and lithium with controllable interspecies overlap. *Physical Review A* **87,** 013615 (Jan. 2013) (cit. on pp. 28, 88).

213. Catani, J., Barontini, G., Lamporesi, G., Rabatti, F., Thalhammer, G., Minardi, F., Stringari, S. & Inguscio, M. Entropy Exchange in a Mixture of Ultracold Atoms. *Physical Review Letters* **103,** 140401 (Sept. 2009) (cit. on pp. 28, 35).

214. Tassy, S. *Sympathetische Kühlung von Ytterbium mit Rubidium* PhD thesis (Heinrich-Heine-Universitat Düsseldorf, Düsseldorf, 2007) (cit. on pp. 28, 29).

215. Aoki, T., Yamanaka, Y., Takeuchi, M., Sakemi, Y. & Torii, Y. Photoionization loss in simultaneous magneto-optical trapping of Rb and Sr. *arXiv.org,* 1302.6414 (Feb. 2013) (cit. on p. 28).

216. Nemitz, N., Baumer, F., Münchow, F., Tassy, S. & Görlitz, A. Production of heteronuclear molecules in an electronically excited state by photoassociation in a mixture of ultracold Yb and Rb. *Physical Review A* **79,** 061403(R) (June 2009) (cit. on pp. 28, 30).

217. Baumer, F., Münchow, F., Görlitz, A., Maxwell, S. E., Julienne, P. S. & Tiesinga, E. Spatial separation in a thermal mixture of ultracold ^{174}Yb and ^{87}Rb atoms. *Physical Review A* **83,** 040702(R) (Apr. 2011) (cit. on pp. 29, 58).

218. Baumer, F. *Isotope dependent interactions in a mixture of ultracold atoms* PhD thesis (Heinrich-Heine-Universitat Düsseldorf, Düsseldorf, Mar. 2010) (cit. on p. 29).

219. Münchow, F. *2-Photon-Photoassociation spectroscopy in a mixture of Ytterbium and Rubidium* PhD thesis (Heinrich-Heine-Universität Düsseldorf, Düsseldorf, 2012) (cit. on p. 29).

220. Brue, D. A. & Hutson, J. M. Prospects of forming ultracold molecules in $^2\Sigma$ states by magnetoassociation of alkali-metal atoms with Yb. *Physical Review A* **87,** 052709 (May 2013) (cit. on p. 29).

221. Micheli, A., Brennen, G. K. & Zoller, P. A toolbox for lattice-spin models with polar molecules. *Nature Physics* **2,** 341–347 (Apr. 2006) (cit. on p. 30).

222. Sørensen, L. K., Knecht, S., Fleig, T. & Marian, C. M. Four-Component Relativistic Coupled Cluster and Configuration Interaction Calculations on the Ground and Excited States of the RbYb Molecule. *The Journal of Physical Chemistry A* **113,** 12607–12614 (Nov. 2009) (cit. on p. 30).

223. Zhang, P., Sadeghpour, H. R. & Dalgarno, A. Structure and spectroscopy of ground and excited states of LiYb. *Journal of Chemical Physics* **133,** 044306 (2010) (cit. on p. 30).

224. Gopakumar, G., Abe, M., Das, B. P., Hada, M. & Hirao, K. Relativistic calculations of ground and excited states of LiYb molecule for ultracold photoassociation spectroscopy studies. *Journal of Chemical Physics* **133,** 124317 (Sept. 2010) (cit. on p. 30).

225. Sandars, P. G. H. in *Atomic Physics 4* (eds zu Putlitz, G., Weber, E. W. & Winnacker, A.) 71–92 (Plenum Press, New York, 1975) (cit. on p. 30).

226. Sandars, P. G. H. & Lipworth, E. Electric Dipole Moment of the Cesium Atom. A New Upper Limit to the Electric Dipole Moment of the Free Electron. *Physical Review Letters* **13,** 718–720 (Dec. 1964) (cit. on p. 30).

227. Hara, H., Takasu, Y., Yamaoka, Y., Doyle, J. M. & Takahashi, Y. Quantum Degenerate Mixtures of Alkali and Alkaline-Earth-Like Atoms. *Physical Review Letters* **106,** 205304 (May 2011) (cit. on pp. 30, 73).

228. Pasquiou, B., Bayerle, A., Tzanova, S., Stellmer, S., Szczepkowski, J., Parigger, M., Grimm, R. & Schreck, F. Quantum degenerate mixtures of strontium and rubidium atoms. *arXiv.org,* 1305.5935 (May 2013) (cit. on p. 30).

229. D'Incao, J. P. D. & Esry, B. D. Mass dependence of ultracold three-body collision rates. *Physical Review A* **73,** 030702 (R) (Mar. 2006) (cit. on p. 30).

230. Kartavtsev, O. I. & Malykh, A. V. Low-energy three-body dynamics in binary quantum gases. *Journal of Physics B* **40,** 1429–1441 (Apr. 2007) (cit. on p. 30).

231. Petrov, D. S., Astrakharchik, G. E., Papoular, D. J., Salomon, C. & Shlyapnikov, G. V. Crystalline Phase of Strongly Interacting Fermi Mixtures. *Physical Review Letters* **99,** 130407 (Sept. 2007) (cit. on p. 30).

232. Szirmai, G., Szirmai, E., Zamora, A. & Lewenstein, M. Gauge fields emerging from time-reversal symmetry breaking for spin-5/2 fermions in a honeycomb lattice. *Physical Review A* **84,** 011611(R) (July 2011) (cit. on pp. 30, 112).

233. Grimm, R., Weidemüller, M. & Ovchinnikov, Y. B. Optical Dipole Traps for Neutral Atoms. *Advances In Atomic, Molecular, and Optical Physics* **42,** 95–170 (2000) (cit. on pp. 31, 32, 105, 129).

234. Dzuba, V. A. & Derevianko, A. Dynamic polarizabilities and related properties of clock states of the ytterbium atom. *Journal of Physics B* **43,** 074011 (Apr. 2010) (cit. on pp. 32, 33).

235. Guo, K., Wang, G. & Ye, A. Dipole polarizabilities and magic wavelengths for a Sr and Yb atomic optical lattice clock. *Journal of Physics B* **43,** 135004 (July 2010) (cit. on pp. 32, 33).

236. Dicke, R. H. The Effect of Collisions upon the Doppler Width of Spectral Lines. *Physical Review* **89,** 472–473 (Jan. 1953) (cit. on pp. 32, 102).

237. Weinstein, J. D., Beloy, K. & Derevianko, A. Entangling the lattice clock: Towards Heisenberg-limited timekeeping. *Physical Review A* **81,** 030302(R) (Mar. 2010) (cit. on p. 33).

238. Yi, W., Daley, A. J., Pupillo, G. & Zoller, P. State-dependent, addressable subwavelength lattices with cold atoms. *New Journal of Physics* **10,** 073015 (July 2008) (cit. on p. 34).

239. Harper, P. G. Single Band Motion of Conduction Electrons in a Uniform Magnetic Field. *Proceedings of the Physical Society. Section A* **68,** 874–878 (Apr. 1955) (cit. on p. 34).

240. Hofstadter, D. R. Energy levels and wave functions of Bloch electrons in rational and irrational magnetic fields. *Physical Review B* **14,** 2239–2249 (Sept. 1976) (cit. on p. 34).

241. Xu, C. Liquids in multiorbital SU(N) magnets made up of ultracold alkaline-earth atoms. *Physical Review B* **81,** 144431 (Apr. 2010) (cit. on p. 35).

242. Manmana, S. R., Hazzard, K. R. A., Chen, G., Feiguin, A. E. & Rey, A. M. SU(N) magnetism in chains of ultracold alkaline-earth-metal atoms: Mott transitions and quantum correlations. *Physical Review A* **84,** 043601 (Oct. 2011) (cit. on p. 35).

243. Corboz, P., Läuchli, A. M., Penc, K., Troyer, M. & Mila, F. Simultaneous Dimerization and SU(4) Symmetry Breaking of 4-Color Fermions on the Square Lattice. *Physical Review Letters* **107,** 215301 (Nov. 2011) (cit. on p. 35).

244. Bauer, B., Corboz, P., Läuchli, A. M., Messio, L., Penc, K., Troyer, M. & Mila, F. Three-sublattice order in the SU(3) Heisenberg model on the square and triangular lattice. *Physical Review B* **85,** 125116 (Mar. 2012) (cit. on pp. 35, 112).

245. Lajkó, M. & Penc, K. Tetramerization in a SU(4)-Heisenberg model on the honeycomb lattice. *arXiv.org,* 1303.6297 (Mar. 2013) (cit. on pp. 35, 112).

246. Raab, E. L., Prentiss, M., Cable, A., Chu, S. & Pritchard, D. E. Trapping of Neutral Sodium Atoms with Radiation Pressure. *Physical Review Letters* **59,** 2631–2634 (Dec. 1987) (cit. on p. 38).

247. Ertmer, W., Blatt, R., Hall, J. L. & Zhu, M. Laser manipulation of atomic beam velocities: Demonstration of stopped atoms and velocity reversal. *Physical Review Letters* **54,** 996–999 (Mar. 1985) (cit. on p. 38).

248. Monroe, C., Swann, W., Robinson, H. & Wieman, C. Very cold trapped atoms in a vapor cell. *Physical Review Letters* **65,** 1571–1574 (Sept. 1990) (cit. on p. 38).

249. Kurosu, T. & Shimizu, F. Laser Cooling and Trapping of Calcium and Strontium. *Japanese Journal of Applied Physics* **29,** L2127–L2129 (Nov. 1990) (cit. on p. 39).

250. Dinneen, T. P., Vogel, K. R., Arimondo, E., Hall, J. L. & Gallagher, A. Cold collisions of Sr*-Sr in a magneto-optical trap. *Physical Review A* **59,** 1216–1222 (Feb. 1999) (cit. on p. 39).

251. Petersen, M., Chicireanu, R., Dawkins, S. T., Magalhães, D. V., Mandache, C., Le Coq, Y., Clairon, A. & Bize, S. Doppler-Free Spectroscopy of the $^1S_0$-$^3P_0$ Optical Clock Transition in Laser-Cooled Fermionic Isotopes of Neutral Mercury. *Physical Review Letters* **101,** 183004 (Oct. 2008) (cit. on p. 39).

252. Petersen, M. *Laser-cooling of Neutral Mercury and Laser-spectroscopy of the $^1S_0$-$^3P_0$ optical clock transition* PhD thesis (Université Pierre et Marie Curie-Paris VI, Paris, 2009) (cit. on p. 39).

253. Brickman, K. A., Chang, M.-S., Acton, M., Chew, A., Matsukevich, D., Haljan, P. C., Bagnato, V. S. & Monroe, C. Magneto-optical trapping of cadmium. *Physical Review A* **76,** 043411 (Oct. 2007) (cit. on p. 39).

254. Ospelkaus, C. *Fermi-Bose mixtures — From mean-field interactions to ultracold chemistry* PhD thesis (Universität Hamburg, Hamburg, 2006) (cit. on pp. 43, 115, 132).

255. Ospelkaus-Schwarzer, S. *Quantum Degenerate Fermi-Bose Mixtures of ^{40}K and ^{87}Rb in 3D Optical Lattices* PhD thesis (Universität Hamburg, Hamburg, 2006) (cit. on pp. 43, 115, 132).

256. Erhard, M. *Experimente mit mehrkomponentigen Bose-Einstein-Kondensaten* PhD thesis (Universität Hamburg, Hamburg, 2004) (cit. on pp. 43, 115).

257. Schmaljohann, H. *Spindynamik in Bose-Einstein Kondensaten* PhD thesis (Universität Hamburg, Hamburg, 2004) (cit. on pp. 43, 45, 115).

258. Becker, C. *Multi component Bose-Einstein condensates – From mean-field physics to strong correlations* PhD thesis (Universität Hamburg, Hamburg, 2008) (cit. on pp. 43, 129, 130).

259. Soltan-Panahi, P. *Multi–Component Quantum Gases in Hexagonal Lattices* PhD thesis (Universität Hamburg, Hamburg, 2010) (cit. on pp. 43, 105).

260. Jousten, K. *Wutz Handbuch Vakuumtechnik: Theorie und Praxis* 9th ed. (Vieweg, Wiesbaden, 2006) (cit. on p. 47).

261. Ketterle, W., Durfee, D. S. & Stamper-Kurn, D. M. in *Ultracold Fermi Gases, Proceedings of the International School of Physics "Enrico Fermi"* (eds Inguscio, M., Stringari, S. & Wieman, C. E.) 4034 (IOS Press, Amsterdam, Apr. 1999) (cit. on p. 52).

262. Kottke, M. *Magnetfallen und Signaturen der Eindimensionalität für Bose-Einstein-Kondensate* PhD thesis (Leibniz-Universität Hannover, Hannover, 2004) (cit. on pp. 52, 115).

263. Comparat, D., Fioretti, A., Stern, G., Dimova, E., Laburthe Tolra, B. & Pillet, P. Optimized production of large Bose-Einstein condensates. *Physical Review A* **73,** 043410 (Apr. 2006) (cit. on p. 52).

264. Lin, Y.-J., Perry, A. R., Compton, R. L., Spielman, I. B. & Porto, J. V. Rapid production of ^{87}Rb Bose-Einstein condensates in a combined magnetic and optical potential. *Physical Review A* **79,** 063631 (June 2009) (cit. on p. 52).

265. Keßler, H. *Aufbau eines blauen Lasersystems als Lichtquelle für eine Ytterbium 2D-MOT* Diploma thesis (Universität Hamburg, Hamburg, May 2011) (cit. on pp. 60, 61, 63).

266. Sleator, T., Pfau, T., Balykin, V., Carnal, O. & Mlynek, J. Experimental demonstration of the optical Stern-Gerlach effect. *Physical Review Letters* **68,** 1996–1999 (Mar. 1992) (cit. on p. 62).

267. Taie, S., Takasu, Y., Sugawa, S., Yamazaki, R., Tsujimoto, T., Murakami, R. & Takahashi, Y. Realization of a SU(2)×SU(6) System of Fermions in a Cold Atomic Gas. *Physical Review Letters* **105,** 190401 (Nov. 2010) (cit. on p. 62).

268. Stellmer, S., Grimm, R. & Schreck, F. Detection and manipulation of nuclear spin states in fermionic strontium. *Physical Review A* **84,** 043611 (Oct. 2011) (cit. on p. 62).

269. Lefevre, H. C. Single-mode fibre fractional wave devices and polarisation controllers. *Electronics Letters* **16,** 778–780 (1980) (cit. on p. 62).

270. Mukaiyama, T., Katori, H., Ido, T., Li, Y. & Kuwata-Gonokami, M. Recoil-Limited Laser Cooling of ^{87}Sr Atoms near the Fermi Temperature. *Physical Review Letters* **90,** 113002 (Mar. 2003) (cit. on p. 71).

271. Taie, S., Yamazaki, R., Sugawa, S. & Takahashi, Y. An SU(6) Mott insulator of an atomic Fermi gas realized by large-spin Pomeranchuk cooling. *Nature Physics* **8,** 825–830 (Nov. 2012) (cit. on p. 73).

272. Barrett, M. D., Sauer, J. A. & Chapman, M. S. All-Optical Formation of an Atomic Bose-Einstein Condensate. *Physical Review Letters* **87,** 10404 (July 2001) (cit. on p. 74).

273. Kinoshita, T., Wenger, T. & Weiss, D. S. All-optical Bose-Einstein condensation using a compressible crossed dipole trap. *Physical Review A* **71,** 011602(R) (Jan. 2005) (cit. on p. 74).

274. Granade, S. R., Gehm, M. E., O'Hara, K. M. & Thomas, J. E. All-Optical Production of a Degenerate Fermi Gas. *Physical Review Letters* **88,** 120405 (Mar. 2002) (cit. on p. 74).

275. Clément, J.-F., Brantut, J.-P., Robert-de-Saint-Vincent, M., Nyman, R. A., Aspect, A., Bourdel, T. & Bouyer, P. All-optical runaway evaporation to Bose-Einstein condensation. *Physical Review A* **79,** 061406(R) (June 2009) (cit. on p. 74).

276. O'Hara, K. M., Gehm, M. E., Granade, S. R. & Thomas, J. E. Scaling laws for evaporative cooling in time-dependent optical traps. *Physical Review A* **64,** 051403(R) (Nov. 2001) (cit. on pp. 74, 92).

277. Pu, J. & Zhang, H. Intensity distribution of Gaussian beams focused by a lens with spherical aberration. *Optics Communications* **151,** 331–338 (June 1998) (cit. on pp. 82, 83).

278. Brinkmann, M. *Optimierung der Detektion und Auswertung von* ^{87}*Rb-Spinor-Kondensaten* MA thesis (Universität Hamburg, Hamburg, Aug. 2005) (cit. on p. 86).

279. Kronjäger, J. *Coherent dynamics of spinor Bose-Einstein condensates* PhD thesis (Universität Hamburg, Hamburg, 2007) (cit. on p. 86).

280. Dalfovo, F., Giorgini, S., Pitaevskii, L. P. & Stringari, S. Theory of Bose-Einstein condensation in trapped gases. *Reviews of Modern Physics* **71,** 463–512 (Apr. 1999) (cit. on pp. 90, 91).

281. Campbell, G. K., Mun, J., Boyd, M., Medley, P., Leanhardt, A. E., Marcassa, L. G., Pritchard, D. E. & Ketterle, W. Imaging the Mott Insulator Shells by Using Atomic Clock Shifts. *Science* **313,** 649–652 (Aug. 2006) (cit. on p. 96).

282. Fukuhara, T., Sugawa, S., Sugimoto, M., Taie, S. & Takahashi, Y. Mott insulator of ultracold alkaline-earth-metal-like atoms. *Physical Review A* **79,** 041604 (Apr. 2009) (cit. on p. 97).

283. Kuklov, A. B. & Svistunov, B. V. Counterflow Superfluidity of Two-Species Ultracold Atoms in a Commensurate Optical Lattice. *Physical Review Letters* **90,** 100401 (Mar. 2003) (cit. on p. 99).

284. Duan, L.-M., Demler, E. & Lukin, M. D. Controlling Spin Exchange Interactions of Ultracold Atoms in Optical Lattices. *Physical Review Letters* **91,** 090402 (Aug. 2003) (cit. on p. 99).

285. Van Oosten, D., van der Straten, P. & Stoof, H. T. C. Quantum phases in an optical lattice. *Physical Review A* **63,** 053601 (Apr. 2001) (cit. on p. 99).

286. Glück, M., Kolovsky, A. R. & Korsch, H. J. Wannier–Stark resonances in optical and semiconductor superlattices. *Physics Reports* **366,** 103–182 (Aug. 2002) (cit. on p. 99).

287. Nenciu, G. Dynamics of band electrons in electric and magnetic fields: rigorous justification of the effective Hamiltonians. *Reviews of Modern Physics* **63,** 91–127 (Jan. 1991) (cit. on p. 99).

288. Margolis, H. S. Trapped ion optical clocks. *The European Physical Journal Special Topics* **172,** 97–107 (June 2009) (cit. on p. 102).

289. Stenholm, S. The semiclassical theory of laser cooling. *Reviews of Modern Physics* **58,** 699–739 (July 1986) (cit. on pp. 102, 103).

290. Ludlow, A. D. *The strontium optical lattice clock: Optical spectroscopy with Sub-Hertz accuracy* PhD thesis (University of Colorado, Boulder, 2008) (cit. on p. 103).

291. Weitenberg, C., Endres, M., Sherson, J. F., Cheneau, M., Schauß, P., Fukuhara, T., Bloch, I. & Kuhr, S. Single-spin addressing in an atomic Mott insulator. *Nature* **471,** 319–324 (Mar. 2011) (cit. on p. 104).

292. Boyd, M. M. *High Precision Spectroscopy of Strontium in an Optical Lattice: Towards a New Standard for Frequency and Time* PhD thesis (University of Colorado, Boulder, 2007) (cit. on pp. 105, 106).

293. Taichenachev, A. V., Yudin, V. I., Ovsiannikov, V. D. & Pal'chikov, V. G. Optical Lattice Polarization Effects on Hyperpolarizability of Atomic Clock Transitions. *Physical Review Letters* **97,** 173601 (Oct. 2006) (cit. on p. 105).

294. Taichenachev, A. V., Yudin, V. I. & Oates, C. W. Optical lattice polarization effects on magnetically induced optical atomic clock transitions. *Physical Review A* **76,** 023806 (Aug. 2007) (cit. on pp. 106, 110).

295. Angel, J. R. P. & Sandars, P. G. H. The Hyperfine Structure Stark Effect. I. Theory. *Proceedings of the Royal Society A: Mathematical, Physical and Engineering Sciences* **305,** 125–138 (May 1968) (cit. on p. 106).

296. Rützel, T. *Konzeption und Aufbau eines hochstabilen Lasers für Präzisionsmessungen an ultrakalten Quantengasen* Diploma thesis (Universität Hamburg, Hamburg, Jan. 2010) (cit. on pp. 107, 108).

297. Drever, R. W. P., Hall, J. L., Kowalski, F. V., Hough, J., Ford, G. M., Munley, A. J. & Ward, H. Laser phase and frequency stabilization using an optical resonator. *Applied Physics B* **31,** 97–105 (June 1983) (cit. on p. 107).

298. Black, E. D. An introduction to Pound–Drever–Hall laser frequency stabilization. *American Journal of Physics* **69,** 79–87 (Jan. 2001) (cit. on p. 107).

299. Carstens, J.-H. *Stabilization of a Clock Laser for High Precision Spectroscopy on Ultracold Quantum Gases* Diploma thesis (Universität Hamburg, Hamburg, May 2011) (cit. on p. 107).

300. Rathod, K. D., Singh, A. K. & Natarajan, V. Continuous beam of laser-cooled Yb atoms. *Europhysics Letters* **102,** 43001 (June 2013) (cit. on p. 111).

301. Corboz, P., Lajkó, M., Läuchli, A. M., Penc, K. & Mila, F. Spin-Orbital Quantum Liquid on the Honeycomb Lattice. *Physical Review X* **2,** 41013 (Oct. 2012) (cit. on p. 112).

302. Budker, D., Kimball, D. F. & DeMille, D. P. *Atomic Physics* 2nd ed. (Oxford University Press, Oxford, 2008) (cit. on p. 123).

303. Svelto, O. *Principles of lasers* 5th ed. (Springer, 2010) (cit. on p. 129).

Danksagung

Der Aufbau des Ytterbiumexperiments, von der bloßen Idee bis zur tatsächlichen Erzeugung von Quantengasen im Labor, im Rahmen dieser Arbeit wäre ohne die Unterstützung einer Vielzahl von Personen so nicht möglich gewesen. Mein besonderer Dank gilt daher:

- Prof. Dr. Klaus Sengstock für die Gelegenheit, meine Dissertation in seiner Arbeitsgruppe durchzuführen, und sein Vertrauen, mich mit der Gestaltung und Umsetzung eines neuen Projekts zu solch einem komplexen und herausfordernden Thema zu betrauen. Stets fand er dabei das rechte Maß zwischen Förderung und Forderung, um mich und das Projekt voranzubringen.

- Prof. Dr. Henning Moritz für die Übernahme des Zweitgutachten ebenso wie die Leihgabe eines seiner Labors vor dem Umzug ins ZOQ.

- Dr. Christoph Becker für sein in allen Lebenslagen offenes Ohr bei kleineren wie größeren Problemen ebenso wie für seine Unterstützung mit Rat und Tat.

- Prof. Dr. Patrick Windpassinger, der durch sein Wissen sowie, gerade in der Anfangsphase, tatkräftige Unterstützung und manches elektronische Bauteil nachhaltig zum Gelingen des Projekt beigesteuert hat.

- Dr. Rodolphe Le Targat für seine Erfahrungen zu optischen Uhren, die er mit uns geteilt hat, und die vielen Stunden, in denen wir über Plänen für das Experiment oder der Welt der Strahlapparaturen gebrütet haben.

- Alexander Thobe, der als mein langjähriger Mitdoktorand das Projekt ebenfalls auf dem langen Weg von einem leeren Labor zum funktionierenden Quantengasexperiment begleitet und mitgeprägt hat.

- Bastian Hundt für eine angenehme Arbeitsatmosphäre und die wertvollen Beiträge, die er seit seinem Hinzustoßen zum Team Yb kurz vor der Realisierung der ersten 3D-MOT leistet.

- André Kochanke für viele produktive physikalische Diskussionen und die gute Zusammenarbeit.

- Thomas Rützel, Hans Keßler und Jan Carstens, "meinen" Diplomanden, sowie David Perconte für ihre Beiträge zum Projekt und eine denkwürdige Zeit.

- Ortwin Hellmig für seine Unterstützung beim Aufbau der Dipolfallen durch die Erprobung und Anpassung der verwendeten Fasern für hohe Leistungen.

- der gesamten Arbeitsgruppe Sengstock sowie allen weiteren Mitarbeitern des ILP und des ZOQ für ein stets hilfsbereites und kollegiales Arbeitsumfeld sowie ihre Bereitschaft, uns während der Aufbauphase wo immer nötig unter die Arme zu greifen.
- Stefan Fleig und dem gesamten Team der Standortwerkstatt Bahrenfeld, die einen Großteil der Komponenten für das Experiment gefertigt und mir stets mit handwerklichem Rat zur Seite gestanden haben.
- dem technischen und Verwaltungspersonal für ihre Unterstützung in allen weltlichen Belangen. Namentlich sei hier Reinhard Mielck genannt, der uns nicht nur sein umfangreiches Know-How zur Verfügung stellte, sondern auch wesentlich dazu beigetragen hat, dass wir im neugebauten ZOQ hervorragendes Laborbedingungen vorfanden.
- Christoph Becker, Alexander Thobe, Bastian Hundt und André Kochanke für geduldiges Korrekturlesen.

Schlußendlich möchte ich noch meinen Eltern und meinen Freunden danken, ohne deren Unterstützung, Vertrauen und Geduld diese Arbeit nicht möglich gewesen wäre.